Developments in Photon Absorption Remote Sensing Microscopy and Deep Learning–Based Virtual Histochemical Staining

by

James Tweel

A thesis
presented to the University of Waterloo
in fulfillment of the
thesis requirement for the degree of
Doctor of Philosophy
in
Systems Design Engineering

Waterloo, Ontario, Canada, 2026

© James Tweel 2026

Examining Committee Membership

The following served on the Examining Committee for this thesis. The decision of the Examining Committee is by majority vote.

External Examiner:	Shuo Tang Professor, Dept. of Electrical & Computer Engineering University of British Columbia
Supervisor:	Parsin Haji Reza Associate Professor, Dept. of Systems Design Engineering University of Waterloo
Internal Members:	Nima Maftoon Associate Professor, Dept. of Systems Design Engineering University of Waterloo
	John Zelek Professor, Dept. of Systems Design Engineering University of Waterloo
Internal-External Member:	Omar Ramahi Professor, Dept. of Electrical & Computer Engineering University of Waterloo

Author's Declaration

I hereby declare that this thesis consists of material all of which I either authored or co-authored: see Statement of Contributions. This is a true copy of the thesis, including any required final revisions, as accepted by my examiners.

I understand that my thesis may be made electronically available to the public.

Statement of Contributions

James Tweel is the sole author of Chapters 1, 2, and 7 and first author of Chapters 3, 4, 5, and 6 which have been adapted from published peer-reviewed articles, preprints, or manuscripts currently under review.

Chapter 3 consists of material from a published and peer-reviewed paper [1].

James Tweel, Benjamin Ecclestone, Marian Boktor, Deepak Dinakaran, John Mackey, and Parsin Haji Reza. "Automated whole slide imaging for label-free histology using photon absorption remote sensing microscopy". IEEE Transactions on Biomedical Engineering, 71(6):1901–1912, June 2024.

J.T. designed and implemented the whole-slide scanning framework, conducted experiments, collected TA whole-slide scans, prepared the figures, and wrote the main manuscript. B.E. also contributed to the development of the whole slide scanning framework and contrast-leveling algorithm and helped scan TA samples. J.T. and B.E. implemented the transmission-mode PARS architecture. M.B. performed the pix2pix virtual H&E whole-slide colourization. D.D. and J.M. prepared and collected tissue specimens and provided clinical feedback and consultation in the assessment of the results. P.H.R. directed and organized the project and oversaw experimental work and manuscript preparation as the principal investigator.

Chapter 4 consists of material from a published preprint paper [2].

James Tweel, Benjamin Ecclestone, Marian Boktor, James Alexander Tummon Simmons, Paul Fieguth, and Parsin Haji Reza. "Virtual histology with photon absorption remote sensing using a cycle-consistent generative adversarial network with weakly registered pairs". arXiv preprint arXiv:2306.08583, 2023.

J.T. implemented the CycleGAN model and whole-slide virtual staining inference pipeline, collected the TA whole-slide imaging dataset, analyzed the results, prepared the figures, and was the primary author to manuscript writing. B.E. assisted with dataset collection, developed and implemented the denoising and jitter-correction algorithms, and contributed to manuscript writing. H.G. performed all tissue processing and H&E staining procedures and digitally scanned the reference H&E images. M.B. assisted in training the pix2pix virtual H&E model. J.A.T.S. supported study conceptualization and assisted with manuscript writing. P.F. provided feedback on the study design and manuscript preparation. All authors read, provided edits, and approved the final manuscript. P.H.R. directed and organized

the project and oversaw experimental work and manuscript preparation as the principal investigator.

Chapter 5 consists of material from a published and peer-reviewed paper [3].

James Tweel, Benjamin Ecclestone, Hager Gaouda, Deepak Dinakaran, Michael Wallace, Gilbert Bigras, John Mackey, and Parsin Haji Reza. "Photon absorption remote sensing Imaging of breast needle core biopsies is diagnostically equivalent to gold standard H&E histologic assessment". Current Oncology, 30(11):9760–9771, November 2023. Publisher: MDPI.

J.T. processed the PARS images for model training, applied the virtual H&E staining, and organized the images using a custom web-based histology visualization platform. J.T. and B.E. built the PARS optical system and imaged all breast needle core biopsy tissue sections. H.G. performed all tissue processing and H&E staining procedures and digitally scanned the reference H&E images. J.M., D.D., and G.B. designed the survey questionnaire and provided clinical feedback and consultation in the assessment of the results. J.M. launched the final survey and recruited pathologists for participation. M.W. performed the statistical analysis and assisted in writing the results section of the manuscript. J.T. and J.M. were the primary contributors to manuscript writing. All authors read, provided edits, and approved the final manuscript. P.H.R. directed and organized the project and oversaw experimental work and manuscript preparation as the principal investigator.

Chapter 6 consists of material from a paper under peer-review [4].

James Tweel, Benjamin Ecclestone, James Alexander Tummon Simmons, and Parsin Haji Reza. "Label-free whole slide virtual multi-staining using dual-excitation photon absorption remote sensing microscopy". arXiv preprint arXiv:2509.05085, 2025.

J.T. collected data, performed histochemical staining, analyzed results, prepared the figures, developed the system and model code, and wrote the manuscript. J.T. and B.E. designed and built the dual-excitation optical system. B.E. and J.A.T.S. both collected data, contributed to image acquisition code, assisted with manuscript writing, and supported study conceptualization. P.H.R. served as principal investigator, acquired funding, and helped review and edit the manuscript.

Abstract

Histological staining remains the gold standard of diagnostic pathology, enabling visualization of tissue structure and cellular morphology. However, traditional staining workflows are time-consuming, destructive, and chemically intensive, limiting the number of stains that can be applied to valuable biopsy samples. These processes also introduce delays, variability in stain quality, and high resource demands. To address these limitations, this thesis presents a label-free histology framework that combines Photon Absorption Remote Sensing (PARS) microscopy with deep learning–based virtual staining to replicate commonly used histochemical stains without altering or consuming the tissue.

The first component of this work focuses on the development of an automated whole slide PARS system designed for imaging thin, transmissible tissue sections. The system captures sub-micron resolution radiative and non-radiative absorption contrasts using 266 nm UV excitation, targeting endogenous chromophores such as DNA and extracellular matrix components to reveal nuclear and connective tissue structures. Whole slide imaging is achieved through automated focusing, tiling, and contrast leveling, producing gigapixel-scale images directly comparable to standard hematoxylin and eosin (H&E) slides.

The second component introduces a deep learning virtual staining pipeline based on the unpaired CycleGAN architecture, with direct comparison to the paired Pix2Pix model. These models are trained on one-to-one whole slide images of PARS data and chemically stained H&E slides. The first masked clinical concordance study is conducted using breast needle core biopsies, where board-certified pathologists independently diagnose and assess the virtual and real H&E slides. The study demonstrates substantial diagnostic agreement, validating the clinical viability of the PARS-based virtual staining approach.

The final component expands the PARS imaging system through the integration of a secondary long-wave UV excitation wavelength (355 nm), enabling sensitivity to additional biomolecular absorbers and thereby expanding the captured label-free contrasts. The additional label-free contrast contributes to improved emulation of histochemical stains beyond H&E, including Masson's Trichrome, Periodic acid–Schiff, and Jones methenamine silver. To further improve performance, a more advanced registration-guided GAN model (Reg-GAN) is adopted, outperforming both Pix2Pix and CycleGAN. The resulting whole slide virtual images closely match their ground truth counterparts in qualitative appearance, quantitative metrics, and masked pathology review.

Together, this work presents a non-destructive histology pipeline capable of generating high-resolution, multi-stain images of commonly used stains without chemical labeling, representing a step toward integrating label-free microscopy and deep learning virtual staining into routine pathology workflows.

Acknowledgements

Firstly, I would like to thank my friends and colleagues at the Photomedicine Labs, in particular Ben Ecclestone and James Alexander Tummon Simmons, with whom I shared an office and worked closely throughout my PhD. I am deeply grateful that I could always turn to them for critical discussion of my work, and that they consistently engaged with enthusiasm, candid feedback, and rigorous critique.

I would also like to thank my girlfriend, Abigail Conner, for her unwavering support throughout my PhD, including always helping to proofread my written work, presentations, and this thesis. As a far better writer than I am, she consistently provided critical evaluation of my writing and a valuable outside perspective that helped me better communicate my ideas and results. I am also deeply grateful to my parents for their love and support throughout my PhD journey.

I would like to thank the members of my examining committee, Prof. Shuo Tang, Prof. Nima Maftoon, Prof. John Zelek, and Prof. Omar Ramahi, for taking the time to review this work and my contributions. Their feedback and suggestions have helped improve this thesis. I would also like to thank my supervisor, Prof. Parsin Haji Reza, for providing the resources that enabled me to pursue and develop my own research ideas, and for reviewing my work and contributions throughout my PhD.

This thesis was supported by the expertise and generosity of multiple clinical collaborators, for which I am extremely grateful. In particular, I would like to thank Dr. Deepak Dinakaran and Dr. John Mackey for their availability and willingness to review my work, discuss the clinical aspects of the results, and provide guidance to ensure accuracy and appropriate interpretation.

I would also like to thank Dr. Hector Li-Chang and Dr. Jamie Lee for their review of the multi-stain work presented in Chapter 6, including review of the associated manuscript for clinical and histological accuracy.

I would like to thank Hager Gaouda and Sabeena Giri for their assistance in preparing and staining tissue samples used across multiple studies in this thesis. I am also grateful for their guidance in teaching and supporting me in performing histochemical staining to support later chapters of this work.

I would like to thank Dr. Ally-Khan Somani and Dr. Marie Abi Daoud for providing human skin tissue samples, and Dr. Gilbert Bigras for providing human breast tissue samples used in this work.

I would like to thank Dr. Ellen Cai, Dr. Julinor Bacani, Dr. Judith Hugh, Dr. Murray Savard, Dr. Richard Berendt, Dr. Erene Farag, and Dr. Nadia Giannakopoulos for their

participation in the questionnaire-based masked clinical concordance study of breast needle core biopsy samples presented in Chapter 5.

I would also like to thank Dr. Hector Li-Chang, Dr. Will Chen, and Dr. Bibi Naghibi Torbati for completing the stain quality assessment survey presented in Chapter 6.

I am grateful for personal funding support that contributed to the completion of this research, including the NSERC Postgraduate Doctoral Scholarship, the W.S. Rickert Graduate Student Fellowship in Science, the Ontario Graduate Scholarship, the Queen Elizabeth II Graduate Scholarship in Science and Technology, the Engineering Excellence Fellowship, and the President's Graduate Scholarship.

This research was supported by funding from the Natural Sciences and Engineering Research Council of Canada (DGECR-2019-00143, RGPIN-2019-06134, DH-2023-00371), the Canada Foundation for Innovation (JELF #38000), Mitacs Accelerate (IT13594), University of Waterloo startup funds, the Centre for Bioengineering and Biotechnology (CBB Seed Fund), illumiSonics Inc. (SRA #083181), the New Frontiers in Research Fund – Exploration (NFRFE-2019-01012), and the Canadian Institutes of Health Research (CIHR PJT 185984, PJT 195962), all of which provided financial support for the laboratory, equipment, and research activities underlying this work.

Biological materials (human kidney samples) were provided by the Ontario Tumour Bank, which is supported by the Ontario Institute for Cancer Research through funding provided by the Government of Ontario. The views expressed in this thesis are those of the author and do not necessarily reflect those of the Government of Ontario.

Dedication

To my mother and father, for their unconditional support and belief in me; my siblings and grandparents; my girlfriend, for her patience and encouragement; and my younger self, who thought he knew what he was signing up for but didn't really, yet was tenacious enough to see it through.

Table of Contents

Examining Committee Membership ii

Author's Declaration iii

Statement of Contributions iv

Abstract vi

Acknowledgements vii

Dedication ix

List of Figures xv

List of Tables xix

List of Abbreviations xx

1 Introduction 1

1.1 Overview and Motivation 1

1.2 Thesis Scope, Objectives, and Contributions 3

1.2.1 Summary of Contributions 4

2 Literature Review **6**

2.1 Background . . . 6

2.1.1 Introduction to Histology and Histopathology . . . 6

2.1.2 Common Histological Stains and Brightfield Microscopy . . . 9

2.1.3 Overview of Label-Free Microscopy . . . 11

2.1.4 Photon Absorption Remote Sensing (PARS) Microscopy . . . 14

2.1.5 Deep Learning-Based Virtual Histological Staining . . . 18

2.2 Related Label-Free Methods for Virtual Staining . . . 25

2.2.1 Overview . . . 25

2.2.2 Scattering-Based Approaches . . . 27

2.2.3 Radiative Absorption-Based Approaches . . . 32

2.2.4 Non-Radiative Absorption-Based Approaches . . . 36

2.2.5 Nonlinear and Multimodal Methods . . . 38

2.2.6 Summary and Research Motivation . . . 38

3 Automated Whole Slide Imaging for Label-Free Histology using PARS Microscopy **42**

3.1 Introduction and Motivations . . . 42

3.1.1 Study Overview and Contributions . . . 43

3.2 Methods . . . 45

3.2.1 PARS Histology System Architecture . . . 45

3.2.2 Whole Slide Scanning Workflow . . . 46

3.2.3 Focus Criterion Function and Autofocus Algorithm . . . 47

3.2.4 Section Scanning and Image Reconstruction . . . 49

3.2.5 Whole Slide Stitching and Contrast levelling Algorithm . . . 49

3.2.6 Quantitative Analysis of Image Similarity . . . 50

3.2.7 Sample Preparation . . . 52

3.3 Results and Discussion . . . 53

3.3.1 System Improvements and Power Correction . . . 53
3.3.2 Sample Autofocusing and Whole Slide Stitching . . . 55
3.3.3 Label-Free Whole Slide Images . . . 59
3.3.4 Whole Slide Virtual H&E Staining . . . 65
3.4 Conclusion . . . 68

4 Virtual Whole Slide H&E Histology with PARS using CycleGAN with Weakly Registered Pairs 70
4.1 Introduction and Motivations . . . 70
4.1.1 Study Overview and Contributions . . . 72
4.2 Materials and Methods . . . 72
4.2.1 Description of PARS Tissue Imaging Process . . . 72
4.2.2 PARS Data Preprocessing . . . 73
4.2.3 Dataset Preparation for Model Training . . . 75
4.2.4 Sample Preparation . . . 77
4.3 Results and Discussion . . . 78
4.4 Conclusion . . . 88

5 Clinical Concordance and Masked Validation of PARS Virtual H&E with Gold-Standard Pathology in Breast Needle Core Biopsies 89
5.1 Introduction and Motivations . . . 89
5.1.1 Specific Background . . . 90
5.1.2 Study Overview and Contributions . . . 91
5.2 Methods . . . 92
5.2.1 Patient Materials . . . 92
5.2.2 Sample Preparation Prior to PARS Imaging and Gold Standard H&E Staining . . . 92
5.2.3 PARS Microscope Imaging . . . 93
5.2.4 Gold Standard H&E Staining and Digital Image Acquisition . . . 93

5.2.5 PARS Virtual H&E Colourization . . . 94
5.2.6 Evaluation by Expert Pathologists . . . 94
5.2.7 Statistical Analysis . . . 97
5.3 Results . . . 97
5.3.1 Example Whole Slide Image Pairs . . . 97
5.3.2 Image Origin . . . 100
5.3.3 Primary Diagnosis . . . 100
5.3.4 Evaluation of Tissue Gradings . . . 101
5.4 Discussion . . . 102
5.4.1 Study Summary and Key Findings . . . 102
5.4.2 Interpretation of Findings in Context . . . 103
5.4.3 Strengths and Limitations . . . 104
5.5 Conclusion . . . 104

6 Label-Free Whole Slide Virtual Multi-Staining Using Dual-Excitation Photon Absorption Remote Sensing Microscopy 106
6.1 Introduction and Motivations . . . 106
6.2 Study Overview and Contributions . . . 108
6.3 Methods . . . 109
6.3.1 Dual-Excitation PARS System Architecture and Configuration . . . 109
6.3.2 Interlaced Scanning, Signal Acquisition, and Image Reconstruction 112
6.3.3 Deep Learning Based Virtual Staining . . . 113
6.3.4 Sample Preparation . . . 119
6.3.5 Masked Pathologist Evaluation . . . 120
6.4 Results and Discussion . . . 120
6.4.1 Expanded Contrast and Biomolecular Specificity with Addition of 355 nm Excitation . . . 120
6.4.2 High-Fidelity Virtual Staining of Diverse Histochemical Stains . . . 124

6.4.3 Pathologist Validation Results 135
6.4.4 Contribution of Individual Excitation Channels to Virtual Staining Performance 136
6.4.5 Comparative Performance of Virtual Staining Models 142
6.5 Conclusion 147

7 Conclusions and Future Work **148**

Letter of Copyright Permission **153**

References **154**

List of Figures

2.1 Overview of histological processing steps from tissue excision to microscopic vieweing. . . . 8

2.3 Absorption spectrum of common biomolecules 13

2.4 The PARS radiative and non-radiative measurement process, shown alongside the excitation, absorption, and subsequent relaxation pathways within a biomolecule. . . . 16

2.5 Pix2Pix paired training scheme for virtual staining with PARS as the input and H&E as the target stain 20

2.6 CycleGAN unpaired training scheme for virtual staining with PARS as the input and H&E as the target stain 22

2.7 RegGAN training scheme for virtual staining with PARS as the input and H&E as the target stain 23

2.8 Example virtual staining using brightfield microscopy. . . . 28

2.9 Example virtual staining using QPI and qOBM microscopy 30

2.10 Example virtual staining using Reflectance Confocal Microscopy. . . . 31

2.11 Example virtual staining using autofluorescence microscopy. . . . 33

2.12 Example virtual staining using FLIM microscopy. . . . 35

2.13 Example virtual H&E image of FFPE mouse brain section using UV-PAM. 36

2.14 Example virtual H&E image of mouse brain using SRS input compared with chemical H&E of frozen tissue section. . . . 39

3.1 Simplified PARS histology optical architecture with labeled components. . 45

3.2 Overview of the PARS whole slide scanning workflow. . . . 47

3.3 'Snake'-like stage scanning pattern and signal compression into pixel intensities. . . . 49
3.4 Illustration of the two-part algorithm used to level and blend the contrast and shading between sections. . . . 51
3.5 Overview of the tissue sample preparation workflow from excision to H&E staining. . . . 53
3.6 Label-free PARS image contrasts before and after reference power correction. 54
3.7 Relationship between scattering focus and non-radiative image SNR. . . . 56
3.8 Whole slide scattering images before and after bulk and gradient levelling. 57
3.9 Comparison of the proposed contrast levelling algorithm with ImageJ stitching plugins. . . . 58
3.10 Stitched and leveled PARS WSIs of malignant human breast tissue. . . . 60
3.11 Comparison of PARS total absorption images with H&E of breast biopsy. . 62
3.12 Whole slide PARS TA images of malignant breast and skin tissue with H&E. 63
3.13 Quantitative comparison of PARS and H&E images based on nuclear features. 64
3.14 Comparison of PARS TA, virtual H&E, and ground truth H&E whole slide images. . . . 66
3.15 Quantitative comparison of virtual and ground truth H&E whole slide images. 67

4.1 Algorithm for jitter correction of denoised images. . . . 74
4.2 Data preparation, inversion, and virtual colourization model training workflow. 76
4.3 Denoising and jitter correction results on PARS non-radiative and radiative channels. . . . 79
4.4 Before and after results of affine transform registration between H&E and inverted TA WSIs. . . . 80
4.5 Comparison of Pix2Pix and CycleGAN virtual staining with H&E and PARS TA of skin tissue. . . . 82
4.6 Comparison of Pix2Pix and CycleGAN virtual staining with H&E and PARS TA of malignant breast tissue. . . . 84
4.7 Whole slide virtual staining of malignant skin tissue with representative cropped areas. . . . 85

4.8 Comparison of intrinsic PARS contrast with H&E staining, highlighting arterial features. 87

5.1 Example PARS TA WSI with corresponding H&E and training image pairs. 95

5.2 Example PARS TA, virtual H&E, and true H&E images with closely matched staining colours. 98

5.3 Example PARS TA, virtual H&E, and true H&E images showing epithelial and stromal contrast. 99

6.1 Dual-excitation PARS architecture with interlaced scanning and signal extraction. 111

6.2 Workflow for training data preparation and whole slide virtual staining. Example shown in H&E mouse gastrointestinal tissue. 114

6.3 Overview of the RegGAN-based virtual staining framework and associated network architectures. 115

6.4 Label-free contrasts from 266 nm and 355 nm PARS showing correspondence with H&E and specialized stains in skin and kidney tissues. 122

6.5 Edge-based spatial resolution measurements for the three wavelengths used in the system. 123

6.6 Virtual staining with dual-excitation PARS input and RegGAN model across multiple tissues, compared with H&E and specialized histochemical stains. 125

6.7 Virtual staining with dual-excitation PARS input and RegGAN model across healthy mouse tissues and multiple histochemical stains. 127

6.8 Simultaneous virtual H&E, Masson's trichrome, PAS, and JMS stains of mouse kidney tissue. 129

6.9 Virtual multi-staining of mouse intestine tissue (H&E, Masson's trichrome, and PAS) from a single PARS input. 130

6.10 Virtual multi-staining of human kidney with ccRCC using PARS input to generate H&E and Masson's trichrome. 131

6.11 Representative failure cases observed in the virtual staining results across tissue types and histochemical stains. 133

6.12 L*a*b* color distribution comparison between virtual and chemical stains. 134

6.13 Dual-excitation models improve histological feature staining across multiple stains, including collagen, nuclei, RBCs, and fungal hyphae. 140

6.14 Visual and quantitative comparison of RegGAN, Pix2Pix, and CycleGAN virtual staining across multiple stains and disease cases. 143

List of Tables

5.1 Survey questionnaire given to pathologists for each of the 14 total images. . 96

5.2 Summary of pathologist responses to question "the primary tissue diagnosis is". 101

5.3 Inter-rater reliability of invasive cancer scores. 102

5.4 Distribution of "not assessable" responses. 103

6.1 Training and validation sample summary by tissue type and stain. 118

6.2 Summary of masked pathologist evaluation of chemical and virtual stains. . 135

6.3 Results of masked pathologist evaluation showing responses for diagnostic quality (DQ) and image origin (IO). 137

6.4 DISTS (↓) scores across datasets for different excitation wavelength input combinations. Each cell reports the Avg. ± Std results. 138

6.5 MS-SSIM (↑) scores across datasets for different excitation wavelength input combinations. Each cell reports the Avg. ± Std results. 139

6.6 Quantitative comparison of RegGAN, Pix2Pix, and CycleGAN for each dataset using DISTS (↓). Each cell reports the Avg. ± Std results. 144

6.7 Quantitative comparison of RegGAN, Pix2Pix, and CycleGAN for each dataset using MS-SSIM (↑). Each cell reports the Avg. ± Std results. . . . 145

List of Abbreviations

CARS Coherent Anti-Stokes Raman Scattering 14, 25, 38

ccRCC Clear Cell Renal Cell Carcinoma 108, 117, 119, 122, 123, 125, 126, 128, 130, 131, 140–143

CNN Convolutional Neural Network 71, 73, 74, 78, 79

CycleGAN Cycle-Consistent Generative Adversarial Network 3–5, 18, 20–24, 29, 37, 70, 72, 75, 77, 81–84, 86, 88, 89, 94, 106, 108, 109, 116, 142, 143, 146, 149

DCIS Ductal Carcinoma In Situ 91, 92, 100, 103

DISTS Deep Image Structure and Texture Similarity 34, 136, 142, 143, 146, 151

DNA Deoxyribonucleic Acid 2, 7, 13–15, 17, 34, 40, 42, 45, 70

ECM Extracellular Matrix 3, 7, 10, 13, 15, 32, 45, 61, 107, 110, 121

ESF Edge Spread Function 112, 123

FFPE Formalin-Fixed Paraffin-Embedded 7, 8, 17, 26, 36–38, 43, 52, 53, 70, 77, 89, 90, 92, 100, 119, 121, 148

FID Fréchet Inception Distance 26

FLIM Fluorescence Lifetime Imaging Microscopy 25, 34–36, 38

FWHM Full Width Half Maximum 46, 55, 112, 120, 123

GAN Generative Adversarial Network 19, 20, 22, 24, 25, 27, 32, 34, 108, 151

GI Gastrointestinal 109, 117, 126, 130, 133

H&E Hematoxylin and Eosin 1, 3–5, 7, 9, 10, 18, 20, 22, 23, 27–39, 42, 44, 50, 52–54, 61–68, 70–72, 75–78, 80–91, 93–95, 97–109, 114, 116, 117, 119, 121–131, 133, 134, 140–143, 146–150

I2I Image-to-Image 19, 20, 24, 25, 71, 81, 108, 116, 117

IDC Invasive Ductal Carcinoma 59, 91, 92, 100, 103

ILC Invasive Lobular Carcinoma 91, 92, 100, 103

JMS Jones Methenamine Silver 4, 5, 9–11, 106, 108, 117, 119, 125, 126, 128–130, 134, 142, 143, 146, 147, 149

LSF Line Spread Function 112, 123

MPF Multi-Photon Fluorescence 25, 38

MS-SSIM Multi-Scale Structural Similarity Index Measure 44, 52, 67, 68, 136, 142, 143, 146, 151

MSE Mean Squared Error 26, 78

N2V Noise2Void 73, 78, 79

NA Numerical Aperture 46, 48, 53, 73, 93, 110

NCB Needle Core Biopsy 4, 59, 62, 66, 89–91, 103, 106, 149

OCT Optical Coherence Tomography 12

OR-PAM Optical-Resolution Photoacoustic Microscopy 13

PA Photoacoustic 13

PAM Photoacoustic Microscopy 36, 37

PARS Photon Absorption Remote Sensing 2–5, 15–18, 20, 22–24, 36, 40–47, 50, 52–54, 60–66, 68–75, 77, 78, 81, 82, 84, 86–91, 93–95, 97–109, 111–114, 116, 118–133, 142, 143, 147–151

PAS Periodic Acid–Schiff 4, 5, 9, 10, 106, 108, 117, 119, 122–130, 132–134, 140–143, 146, 147, 149

PLM Polarized Light Microscopy 12

PSNR Peak Signal-to-Noise Ratio 26, 27

QER Quantum Efficiency Ratio 15

qOBM Quantitative Oblique Back-Illumination Microscopy 29, 30

QPI Quantitative Phase Imaging 2, 12, 25, 27, 29, 30

RBC Red Blood Cell 10, 15, 34, 35, 81, 108–110, 121–124, 126, 127, 132, 133, 140–142, 146, 147

RCM Reflectance Confocal Microscopy 25, 29, 31, 32

RNA Ribonucleic Acid 7, 13, 34

ROI Region of Interest 43, 46, 59

SHG Second Harmonic Generation 14, 25, 38

SNR Signal-to-Noise Ratio 43, 55, 56, 70, 113, 152

SRS Stimulated Raman Scattering 14, 25, 38, 39

SSIM Structural Similarity Index Measure 26, 27, 37, 78, 89

TA Total Absorption 15, 61–66, 68, 75–78, 80–84, 87, 94, 95, 97–99

THG Third Harmonic Generation 14, 38

UV Ultraviolet 13, 14, 18, 32, 43–46, 54, 55, 65, 73, 87, 93, 110, 112, 120, 147, 150, 151

WSI Whole Slide Image 3–5, 11, 18, 20, 43, 44, 49, 50, 52, 56, 59–61, 63, 65–70, 72–75, 77, 78, 80, 83, 88–91, 93–95, 100, 108, 109, 113, 114, 117, 118, 124, 126, 131, 147–149, 151

Chapter 1

Introduction

1.1 Overview and Motivation

Microscopes are essential tools in modern medicine, widely used in hospitals for disease diagnosis and monitoring, as well as in biomedical research and drug development to study both healthy and pathological biological processes. The study of microscopic cell structure and function, known as histology, relies on histochemical stains that apply colour to tissue microanatomy by binding to specific molecular targets [5, 6]. These stains differentiate cellular and extracellular components such as nuclei, proteins, lipids, and carbohydrates, providing contrast in otherwise transparent tissue sections. Stained samples are examined using light microscopy, often with brightfield whole slide scanners to capture high-resolution, sub-cellular detail across the sample for digital viewing, navigation, and computational analysis [7], [8]. The gold-standard stain is Hematoxylin and Eosin (H&E), which stains nuclei purple and cytoplasmic and extracellular components pink [9]. It is the first and most routinely used stain in almost any diagnostic workflow. Nuclear staining is important because nuclear morphology reflects the cell's state, revealing growth patterns, proliferation, and structural abnormalities that allow pathologists to grade the presence, nature, and extent of disease such as cancer [10, 11, 12]. In addition to H&E, there are a variety of other stains are used for more specific diagnostic purposes.

While invaluable, histochemical staining has many drawbacks. Prior to staining, fresh biopsy samples must first undergo chemical fixation, dehydration, and paraffin embedding to preserve the specimen and allow thin sectioning onto microscope slides [6, 9]. The subsequent staining and labeling process is destructive, and the same section cannot always be re-stained or used for ancillary diagnostic assays [13]. Multiple stains require

additional cutting and consumption of limited biopsy tissue, and adjacent cuts inevitably have misalignments or mismatched structures. Beyond tissue loss, staining protocols are complex, multi-step procedures that require trained histotechnologists and dedicated laboratory infrastructure, and stain quality can be highly variable [14]. These workflows also generate chemical waste, add cost, and, when additional stains are required, can lengthen turnaround times and delay diagnosis and treatment [15].

To address these challenges and complement traditional staining, a range of label-free microscopes have been developed that capture endogenous tissue contrast without the need for destructive chemical markers. These methods exploit scattering, absorption, or nonlinear optical interactions in the tissue, using techniques such as Quantitative Phase Imaging (QPI) [16], autofluorescence [17], photoacoustic [18] and photothermal microscopy [19], multiphoton fluorescence [20], coherent Raman scattering [21, 22], and more, to reveal structural and biochemical features of tissue. Recent advances in deep learning have extended the utility of these modalities through *virtual staining*, which learns to transform raw label-free contrasts into brightfield representations of familiar histochemical stains [15, 23]. This approach enables the visualization of multiple stains on a single tissue section, without the time, cost, or tissue loss associated with chemical staining, while preserving the same tissue sample for downstream histological or molecular analyses [15].

Various label-free modalities have been used for deep learning–based virtual staining, several of which are discussed in greater detail in Section 2.2. Among these, absorption-based methods are particularly well suited because they are relatively simple and can target biomolecules through their characteristic absorption spectra [24, 25]. However, existing absorption modalities measure only a single relaxation pathway: either radiative (e.g., autofluorescence microscopy), or non-radiative (e.g., photoacoustic and photothermal microscopy). As a result, each method provides contrast from only a subset of absorbing biomolecules, limiting the biochemical information available to virtual staining models and reducing their ability to accurately reproduce stain-specific features [26]. For example, autofluorescence imaging, the most widely used technique for virtual staining [15], lacks nuclear contrast because Deoxyribonucleic Acid (DNA) relaxes primarily non-radiatively [27], requiring the model to predict nuclear structure and increasing the risk of inaccurate reconstructions.

In general, label-free inputs that provide greater biochemical specificity or complementary contrast allow the network to better distinguish tissue components and reconstruct the features of the target stain [26, 28, 29]. For this reason, Photon Absorption Remote Sensing (PARS) microscopy is particularly well suited for virtual staining, as it simultaneously captures radiative and non-radiative absorption signals from a single excitation event, providing a more complete picture of absorbing biomolecules, effectively combining

the contrast information of autofluorescence (radiative) and photoacoustic or photothermal methods (non-radiative) [30, 31, 32]. For label-free histology, PARS has been implemented using a 266 nm excitation source [32]. In this configuration, Ecclestone et al. demonstrated that non-radiative absorption provides strong nuclear contrast, while radiative relaxation autofluorescence highlights cytoplasmic and Extracellular Matrix (ECM) structures through endogenous fluorophores [32]. Together, these complementary PARS contrasts yield image features highly analogous to conventional H&E staining. Boktor et al. subsequently presented the first application of virtual staining on raw PARS images using a Pix2Pix model to emulate H&E in skin tissues [33].

1.2 Thesis Scope, Objectives, and Contributions

Building on recent developments, this thesis aims to develop and validate a whole slide scanning PARS microscope and virtual staining workflow capable of emulating multiple histochemical stains from a single unstained tissue section. The system captures Whole Slide Images (WSIs) compatible with clinical diagnostic workflows and directly comparable to conventional H&E and special stains, enabling one-to-one masked concordance with gold-standard histopathology. The following summarizes the key aims and scope of each research module, with detailed motivations, technical gaps, and specific contributions described in the respective chapter introductions and summaries.

In **Chapter 3**, an automated whole slide scanning PARS histology system was developed with a refined optical architecture for imaging standard thin, transmissible tissue sections at sub-micron resolution suitable for diagnostic assessment. Previous PARS embodiments lacked whole slide imaging capabilities, which is a critical functionality for a histology microscopes. Visual and quantitative similarity of diagnostically relevant features (e.g., nuclear characteristics) is demonstrated between the developed PARS system and gold-standard H&E staining in human breast and skin cancer samples.

In **Chapter 4**, a deep learning–based virtual staining algorithm was implemented for gold-standard H&E using the unpaired image translation model Cycle-Consistent Generative Adversarial Network (CycleGAN). The first virtual H&E staining across entire whole slide PARS images is demonstrated, and CycleGAN is compared to the strictly paired Pix2Pix model implemented in previous work [33]. The CycleGAN model is trained with loosely paired data and equal feature representation across domains to ensure high-fidelity virtual H&E staining, demonstrated in human skin and breast cancer samples.

In **Chapter 5**, the the diagnostic fidelity of PARS virtual H&E is evaluated using the imaging system from Chapter 3 and the H&E model from Chapter 4. The first masked

clinical concordance study is conducted on one-to-one WSI pairs of breast Needle Core Biopsies (NCBs), where board-certified pathologists independently assessed the virtual and real H&E slides. The results show strong diagnostic agreement across a spectrum of histologic findings, confirming that PARS virtual H&E provides sufficient quality and detail for clinical interpretation.

In **Chapter 6**, the PARS virtual staining workflow is extended beyond H&E to multiple specialized stains, including Masson's Trichrome, Periodic Acid–Schiff (PAS), and Jones Methenamine Silver (JMS). To achieve this, a secondary 355 nm UVA excitation source is introduced for the first time in a PARS system, providing complementary radiative and non-radiative contrasts that enhance visualization of diverse tissue structures. An improved registration-guided virtual staining model, RegGAN [34], is also applied for the first time in this domain, outperforming both Pix2Pix and CycleGAN from Chapter 4 by achieving a more effective balance between strictly paired and unpaired translation methods. Virtual staining is demonstrated across a range of diseased human and murine tissues, and masked evaluations by expert pathologists confirms that the resulting virtual stains achieved the same diagnostic quality as their chemical counterparts, and pathologists could not reliably distinguish real from virtual stains.

Overall, this work advances PARS histology toward integration with standard pathology workflows, producing clinically interpretable virtual stains while preserving the original specimen for downstream analysis and expanding the diagnostic utility of valuable biopsy samples.

1.2.1 Summary of Contributions

The main contributions of this thesis can be summarized as follows:

- Designed and published the first automated whole slide PARS system and workflow for diagnostic-resolution imaging of entire standard thin, transmissible tissue sections in clinically compatible WSI formats suitable for clinical interpretation (Chapter 3).
- Showcased the first whole slide virtual H&E staining of PARS images using the unpaired CycleGAN model, enabling virtual PARS histology at clinical resolutions suitable for standard diagnostic review (Chapter 4).
- Published the first masked clinical concordance study comparing PARS virtual H&E with gold-standard chemical H&E in breast NCBs, demonstrating substantial diagnostic concordance across standard clinical assessments performed by board-certified pathologists (e.g., cancer subtyping) and overall diagnostic equivalence (Chapter 5).

- The first demonstration of PARS virtual multi-staining, achieving virtual emulation of multiple histochemical stains including H&E, Masson's Trichrome, PAS, and JMS, and showcasing their simultaneous application on a single unstained tissue section (Chapter 6).
- Presented a new dual-excitation PARS imaging system representing the first application of long-wave 355 nm UVA excitation alongside the established 266 nm UVC source, extending PARS contrast and sensitivity to additional tissue structures (Chapter 6).
- Explored the use of the RegGAN image-translation model for the first time in PARS virtual staining, demonstrating superior performance over well-established Pix2Pix and CycleGAN methods through a comprehensive comparison across large datasets spanning multiple organs, stains, and disease cases (Chapter 6).
- To the best of our knowledge, this work is the first to make publicly available one-to-one chemical and virtual WSIs, comprising entire slides held out from all training and validation sets, across all tissue stains presented in this thesis and covering representative healthy and diseased cases. The datasets, provided in standard OME-TIFF formats compatible with common pathology software, are available through the BioImage Archive at https://doi.org/10.6019/S-BIAD2232 (Chapter 6).

Chapter 2

Literature Review

2.1 Background

2.1.1 Introduction to Histology and Histopathology

Histology is the anatomical and physiological study of tissues and cells at microscopic, cellular, and subcellular levels, and it is critical for understanding the biological processes that underlie health and disease [5, 6]. It is employed across diverse domains including medicine, research, agriculture, veterinary science, environmental science, and pharmaceutical industries. By examining thinly sliced and stained tissue sections under high magnification microscopes, histologists and pathologists can visualize structural details invisible to the naked eye.

While histology encompasses the study of normal tissue, histopathology is specifically concerned with structural changes in tissue associated with disease or disorder [35]. It plays a vital role in drug development, treatment testing, and most importantly in clinical practice for the diagnosis and monitoring of diseases such as cancer [35, 36].

Histopathologists use a wide range of stains, labels or dyes to impart contrast in otherwise transparent, thinly cut biopsy samples to reveal tissue structure and composition, and to localize different biomolecules such as proteins, lipids, and carbohydrates [5]. The most important feature assessed in histopathology is the cell nucleus. Pathologists rely on nuclear staining because nuclei provide critical information about the cell state and behavior. Nuclear morphology (e.g., size, shape), chromatin patterns, and nucleolar prominence can indicate whether a cell is healthy, proliferating, precancerous, or malignant [10, 11, 12].

Irregular nuclear contours, enlarged nuclei, or abnormal chromatin distribution are signs of cancerous tissue. With this information, pathologists can grade disease severity, distinguish benign from malignant tissue, and assess tumor aggressiveness [12].

The gold standard stain in histopathology is H&E. Hematoxylin stains nuclear structures purple, while eosin stains cytoplasm and ECM structures pink [9]. There are also a variety of more specialized stains capable of targeting more specific tissue structures [37]. In addition, more advanced techniques such as immunohistochemical staining and in-situ hybridization are available for localization of specific proteins and DNA/Ribonucleic Acid (RNA) sequences, respectively [37].

Limitations of Conventional Histology Workflows

While staining methods and advanced labeling techniques continue to prove invaluable in providing insights for medicine and disease, they are not without their limitations. Histochemical stains must be applied to preserved, thinly cut tissue sections ($\sim 5\mu$m). Before creating thin tissue section, the freshly resected biopsy must undergo a series of laborious processing steps [5], which are outlined in Figure 2.1. Following excision, the fresh tissue sample is first preserved with a formalin fixative for a period of up to 48 hours. Water is then removed from the sample (i.e., dehydrated) through exposure to ethanol. Following this, the tissue is 'cleared', wherein xylene is used to eliminate ethanol and any remaining residual fats to prepare the sample for wax infiltration. The sample is then embedded with paraffin, creating standard Formalin-Fixed Paraffin-Embedded (FFPE) tissue blocks. The paraffin both preserves and structurally supports the sample so that it may be thinly sliced, using a microtome, and placed onto glass microscope slides. The tissue sections are then ready for staining, which requires further chemical processing, which varies depending on the stain applied [6].

Overall, this procedure can take anywhere from days to weeks to complete [38, 39] and can delay critical diagnostic feedback. Delays in diagnosis may lead to repeat biopsies ($\sim$30% of patients [40]), prolonging the process and adversely affecting patients' mental and physical well-being [41, 42]. In surgical oncology, it prohibits 'real-time' cancer margin assessment. In some cases, patients may require further surgery weeks later, risking disease progression or metastasis. In addition to being time-consuming, the processing steps and staining protocols are chemically harsh and permanently alter the tissue specimen. The labeling process is generally irreversible or challenging to undo [13], and 'destaining' is not always practical or achievable [43]. In practice, a new tissue section must be cut for each staining protocol applied. Repeated cutting of tissue sections may not always be feasible, especially in valuable biopsy samples (e.g., brain tissue) which should be used and

taken sparingly. Even when stains are applied to adjacent tissue sections, the sections are inherently misaligned, preventing true cell-to-cell comparison of histological features across different stains.

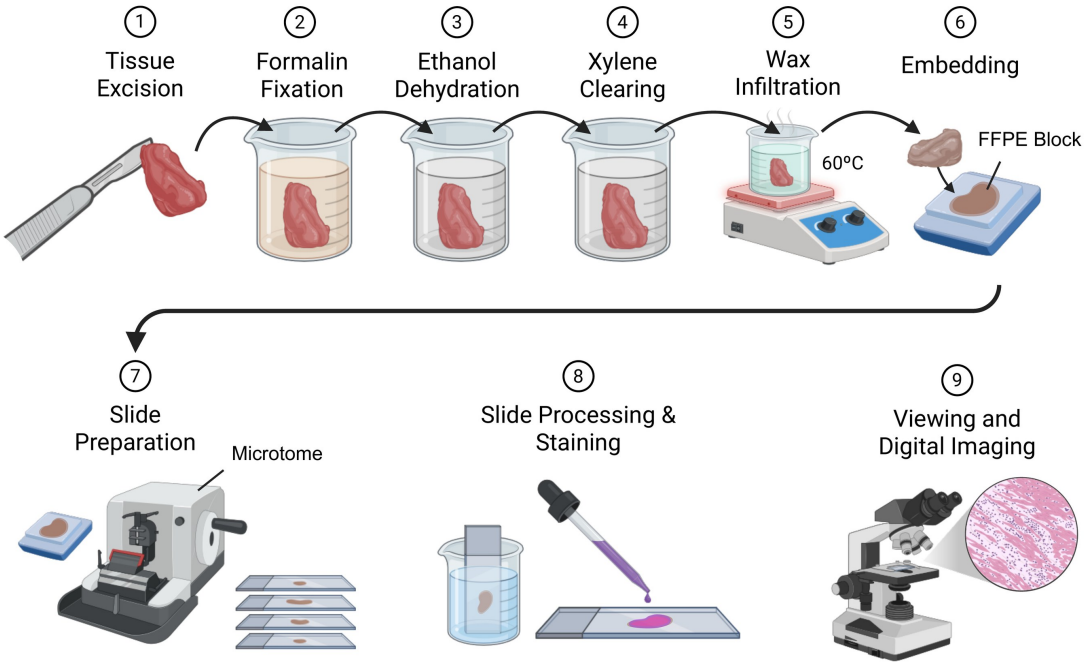

Figure 2.1: Standard histological tissue processing workflow. Steps 1–6 show preparation of a FFPE block (excision, fixation, dehydration, clearing, wax infiltration, embedding). Steps 7–9 show sectioning with a microtome, slide mounting, staining, and microscopic evaluation.

Furthermore, tissue preparation steps are tedious, and sophisticated staining protocols must be carried out by expertly trained histotechnicians [15]. Even with an experienced histotechnician, pre-analytical variables (i.e., all steps prior to visualization) are difficult to control and standardize across labs, countries, and continents [15]. This results in wide variability in staining results, and in some instances, failed stains [26]. When staining fails, more tissue material (i.e., repeat biopsy) may be required from the patient. As well, variability in stain quality presents a major challenge for downstream computerized analysis of stained images (e.g., AI assistive diagnosis) [14]. Lastly, histochemical staining is resource intensive, requires expensive lab infrastructure, and makes up the majority of cost burdens in a lab [15]. As well, stains and biomarkers are expensive and usually highly toxic [15].

As such, for all the aforementioned limitations, there is a clear need for improvements in

century-old histology workflows. Ideally, a microscope imaging platform would be capable of acquiring rich, histology-like contrast in tissue specimen, without the need for exogenous stains or dyes and laborious tissue processing.

2.1.2 Common Histological Stains and Brightfield Microscopy

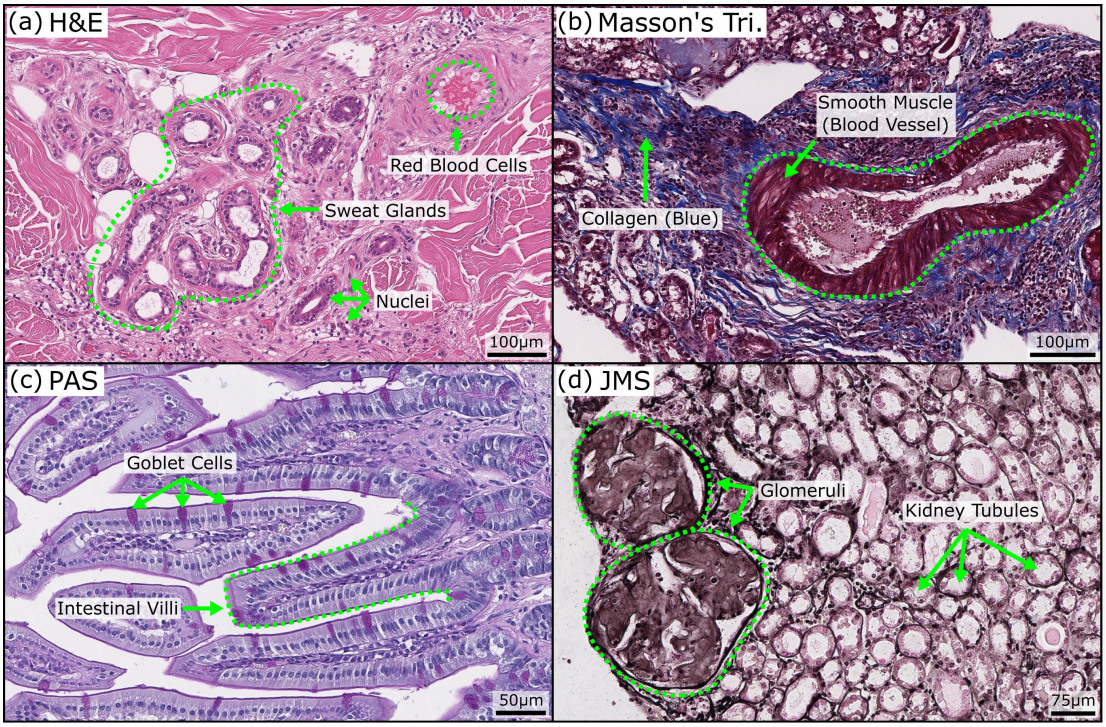

Figure 2.2: Examples of common histological stains with annotated structures: (a) H&E-stained skin tissue, (b) Masson's trichrome-stained kidney tissue, (c) PAS-stained intestine tissue, and (d) JMS-stained kidney tissue.

There exist a variety of histological stains which selectively bind to different tissue structures and cellular components. The following section provide examples of some of the most commonly used stains in histopathology, including H&E, Masson's trichrome, PAS, and JMS. Visual examples of these stains are provided in Figure 2.2.

Hematoxylin and Eosin (H&E): H&E is the most widely used histological stain and is regarded as the gold standard in histopathology [5, 9]. It is considered the gold standard due to its reliability, reproducibility, cost-effectiveness, and its ability to consistently

provide a comprehensive overview of tissue architecture across a broad range of tissue types and pathological conditions. It combines two dyes with complementary properties. Hematoxylin binds strongly to negatively charged, basophilic structures such as nucleic acids, imparting a deep blue-purple colour to nuclei. Eosin is an acidic dye that binds to positively charged, eosinophilic structures such as proteins in the cytoplasm and ECM, and Red Blood Cells (RBCs), staining them in shades of pink to red. Together, these contrasting stains provide nuclear detail within the context of overall tissue architecture and is therefore almost always the first stain applied. Pathologists rely on it to evaluate tissue organization, detect cancerous changes, assess inflammation, and grade disease severity [44]. An example of H&E staining of skin tissue is shown in Figure 2.2a, showing sweat glands outlined in pink, numerous nuclei stained dark purple, and RBCs stained red.

Masson's Trichrome: Masson's trichrome uses three separate dyes to separate key structural elements, providing contrast of muscle fibers (dark red), cell nuclei (dark brown or black), and collagen fibers (typically blue) [5, 9]. Its main purpose is to highlight collagen, making useful for evaluating connective tissue, stromal composition, and fibrosis. Pathologists frequently use this stain to assess diseases such as liver cirrhosis, and tumor-associated tissue remodeling. An example of masson's trichrome stained kidney tissue is shown in Figure 2.2b, showing the smooth muscle of a blood vessel in dark red and the surrounding collagen fibers stained blue, providing a sharp contrast that emphasizes the wall of the vessel and the distribution of connective tissue.

Periodic acid–Schiff (PAS): The PAS stain targets complex carbohydrates, including polysaccharides (e.g., glycogen), mucosubstances, glycoproteins, and basement membranes [5, 9]. It oxidizes carbohydrate structures to aldehydes, which then react with Schiff's reagent to yield a magenta coloration [9]. PAS is used in a wide range of tissues types to highlight carbohydrate-rich structures, but is widely applied in renal pathology, where it delineates the glomerular basement membrane and tubular structures, aiding in the diagnosis of kidney diseases such as diabetic nephropathy [45]. Another specialized use case is in skin tissue, where PAS highlights polysaccharides in fungal cell walls (e.g., chitin), helping diagnosis skin fungal infections (e.g., dermatophytosis) [46]. An example of PAS-stained intestine tissue is shown in Figure 2.2c, highlighting mucin-producing goblet cells in magenta, and also outlining the basement membranes surrounding the intestinal villi in pink.

Jones Methenamine Silver (JMS): The JMS stain is primarily used in renal pathology, where it outlines basement membranes and produces sharp black borders around glomerular and tubular structures [5, 45]. These outlines are useful for assessing glomerular architecture, detecting thickening or splitting of basement membranes, and evaluating

structural damage in non-cancerous kidney biopsies. JMS is often interpreted alongside other stains, providing complementary information for the diagnosis of a wide range of kidney diseases [45]. An example of a JMS-stained kidney sample is shown in Figure 2.2d, where glomeruli are sharply outlined in black and the basement membranes of surrounding tubules are also highlighted.

Brightfield Imaging and Digital Pathology

After slides are stained and coverslipped, they are typically examined using a brightfield microscope, which illuminates the sample with transmitted white light, providing visualization of tissue architecture and cellular detail across a range of magnifications [5]. They are commonly equipped with objective lenses at 5×, 10×, 20×, and 40×. The 5× and 10× magnifications are considered "low power" and are used for overall tissue assessment and identifying regions of interest, whereas 20× and 40× are considered "high power" and are used to visualize cellular and subcellular details within those regions.

Over the past ∼15 years, digital brightfield imaging has become increasingly common. Modern brightfield microscopes are equipped with high-resolution camera sensors that digitize specimens at the same magnifications described above, enabling the transition from conventional optical viewing to digital pathology. An important capability of these scanners is whole slide imaging, where the entire tissue area (e.g., ∼1 cm^2) is scanned at diagnostic resolutions (∼250 nm/pixel [47]), producing gigapixel-sized images of the entire sample. These WSIs can then be visualized on a computer, shared electronically, and integrated into pathology workflows. Today, digital pathology is used as a primary diagnostic method. The digitization of WSIs has also opened up an entire field of computational pathology, enabling a variety of downstream analyses and quantitative algorithms for tasks like cell counting, nuclear segmentation, and tumor grading [48]. More recently, this has led to the development of advanced artificial intelligence–assisted diagnostic tools that aim to support pathologist decision making [49, 48].

2.1.3 Overview of Label-Free Microscopy

Many biological samples inherently lack strong intrinsic contrast, and as a result, important biological structures are difficult to visualize using standard optical methods. For this reason, exogenous labeling strategies have been developed over the past century, in which dyes, stains, or fluorescent probes, with specific chemical affinities, bind to cellular or extracellular targets to provide contrast in the specimen (e.g., histochemical stains) [35, 50].

While effective, these exogenous labels are destructive, perturb natural biological processes and tissue dynamics, and introduce confounding factors [51].

Label-free microscopy is a class of imaging modalities that are able to generate contrast directly from intrinsic light–matter interactions within biological tissues, without the need for external labeling agents. By using endogenous sources of contrast, label-free methods better preserve the native state of the specimen, provided the required optical energy is non-damaging, while still providing structural and functional information and visualizations [51].

Broadly speaking, scattering and absorption processes are the two major physical interactions which label-free methods use to visualize contrast in biological specimens. There are also a variety of nonlinear counterparts to these techniques.

Scattering Modalities for Label-Free Histology: Scattering is the deflection or redistribution of light after interacting with matter, where a photon may change its direction, phase, or energy upon encountering particles or refractive index variations. There are a large variety of label-free imaging approaches that exploit scattering to form contrast. For example, QPI measures phase shifts to acquire refractive index distributions across a tissue sample and provide nanoscale visualizations of tissue and cellular structures [16, 52, 43, 53]. Polarized Light Microscopy (PLM) derives contrast from birefringent structures in tissue samples, such as collagen fibers or filament arrays, and has been used visualize connective tissue organization in tissue samples [54, 55]. Optical Coherence Tomography (OCT) employs interferometric-based detection of backscattered light to acquire depth-resolved images and, while widely used for non-invasive eye imaging, it has also been used for histology applications to assess tissue morphology [56, 57, 58]. These scattering methods are highly useful in a variety of applications, but they generally lack the biomolecular specificity of absorption-based approaches, as their contrast arises mainly from morphological features in the sample rather than chemical composition.

Absorption Modalities for Label-Free Histology: When the incident photon energy is close to the energy difference between two electron states of a molecule, absorption may occur. During an absorption event, the electron is raised to a higher energy level and orbital. Following the absorption event and subsequent electronic transition, there are two main relaxation pathways for the excited electron. One way the electron dissipates energy is through non-radiative relaxation processes, wherein the energy is transferred as heat or vibration to the surrounding area [61, 62]. The second way the energy dissipates is through radiative relaxation, where a lower energy photon is emitted or radiative, otherwise known as autofluorescence [63]. A given molecule may exhibit a combination of both non-radiative and radiative relaxation events.

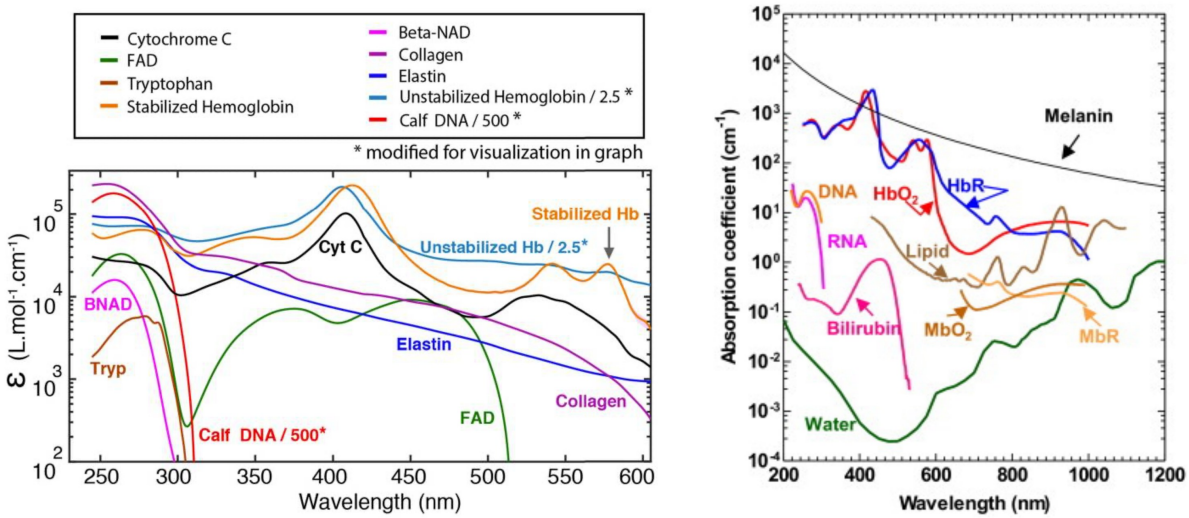

Figure 2.3: Absorption spectrum of common biomolecules. Left [59], right [60].

In general, absorption-based microscopy techniques are better able to target biomolecules given their unique absorption spectra [24, 25], as shown in Figure 2.3. In recent years, radiative-based or autofluorescence microscopy techniques have shown potential in label-free histology [17, 26, 64, 65, 66, 67, 68]. Many biologically relevant molecules and tissue structures become autofluorescent (radiative emissions) when excited by an appropriate wavelength, typically in the Ultraviolet (UV) or shorter wavelength visible range [69]. The emission from these endogenous fluorophores contains valuable information which correlates to structural and functional characteristics of biological specimen [17, 69, 70]. However, while these contrasts map well to cytoplasm and ECM structures, chromatin (DNA, RNA) has relatively low quantum yield [71]. As a result, important nuclear contrast is generally missing with such techniques.

Non-radiative optical absorption contrast has also been realized in photothermal [19, 72] and Photoacoustic (PA) [73, 18, 74] imaging techniques for label-free histology-like visualizations. In particular, Optical-Resolution Photoacoustic Microscopy (OR-PAM) methods have shown high-resolution visualizations of nuclear and cytoplasmic structures [73, 18, 74]. In addition, photoacoustic remote sensing, a non-contact optical absorption-based method, was first used for label-free nuclear imaging in unstained tissues by Haven et al. [75] and Abassi et al. [76] in 2019. It has also been used to image a variety of biomolecules label-free including hemoglobin [77, 78, 79, 80, 81], cytochromes [82, 83], DNA/RNA and lipids [84, 85].

Nonlinear Modalities for Label-Free Histology: In addition to first-order scattering and absorption techniques, there are also a variety of nonlinear optical modalities. These techniques rely on higher-order light–matter interactions to provide intrinsic sources of contrast. Examples include multiphoton fluorescence methods, such as two-photon and three-photon autofluorescence microscopy, which offer good optical sectioning and deep tissue penetration in thick specimens and generate contrast from endogenous fluorophores, including structural proteins (e.g., elastin, keratin, collagen) and metabolic cofactors (e.g., NADH, FAD) [20, 86]. Harmonic generation approaches include Second Harmonic Generation (SHG), which produces signals from non-centrosymmetric structures such as filamentous proteins (e.g., collagen fibrils, microtubules) [87, 88], and Third Harmonic Generation (THG), which highlights sharp optical interfaces such as lipid– or protein–water boundaries [89, 90], together provide visualization of connective tissue and structural organization [91]. Coherent Raman scattering methods, such as Stimulated Raman Scattering (SRS) [21] and Coherent Anti-Stokes Raman Scattering (CARS) [22], target the vibrational modes of molecular bonds to provide label-free "chemical imaging" of lipids, proteins, and other biomolecules.

It should be noted that the label-free imaging field is broad, and within and across each of these categories there exist many sub-variants, multimodal configurations, and hybrid implementations. This section provides a high-level overview of common label-free methods; specific examples of the most relevant techniques for this work and for virtual histology will be discussed in more detail in Section 2.2.

2.1.4 Photon Absorption Remote Sensing (PARS) Microscopy

Absorption-based imaging methods are particularly effective label-free techniques because they leverage the intrinsic absorption spectra of biomolecules to capture specific tissue contrast. By choosing a specific excitation wavelength, one can select molecular absorbers to provide contrast of different tissue components (Figure 2.3). For example, exciting nucleic acids (e.g. DNA) using deep-UV wavelengths reveal histologically relevant nuclear structures [76, 18, 92], while exciting hemoglobin with longer-wave UV or visible spectrum (e.g. 532 nm) can provide visualization of blood-rich areas [93, 60]. However, most label-free absorption modalities capture only one of the two primary relaxation pathways after photon absorption: radiative emissions, such as autofluorescence microscopy, or non-radiative effects, such as photothermal and photoacoustic microscopy. Consequently, their contrast depends on the quantum yield of the biomolecule, defined as the fraction of absorbed photons that relax radiatively [94], with radiative methods limited to high quantum yield

biomolecules and non-radiative methods to low-yield targets.

Photon Absorption Remote Sensing (PARS) microscopy (previously photoacoustic remote sensing) addresses this limitation by simultaneously measuring signals from both radiative and non-radiative de-excitation pathways following a single excitation event [32]. Following absorption, PARS employs a secondary confocal probe laser, alongside the excitation source, to detect non-radiative induced material changes and optical modulations while radiative emissions are directly measured using a photodetector. Uniquely, these signals are intrinsically linked to the same absorption event, rather than being acquired separately with distinct modalities. In this way, PARS provides a more complete mapping of absorbers in the sample, often described as a Total Absorption (TA) signal, and also captures the relative balance between radiative and non-radiative relaxation fractions, referred to as the Quantum Efficiency Ratio (QER), which varies across biomolecular targets [32, 31].

By circumventing mechanism-specific contrast limitations, PARS enables a broader range of biomolecules to be visualized. Low quantum yield absorbers, such as DNA, RBCs, and melanin [95, 96, 97], can be detected through their strong non-radiative signatures, while high quantum yield structures, such as fluorophores in the ECM and connective tissues [17, 69, 70], can be simultaneously imaged via their radiative emissions. In this way, regardless of their quantum yield properties, biomolecules that absorb light have the potential to contribute to a PARS signal, providing a more complete endogenous contrast than is accessible with independent radiative or non-radiative methods alone. These combined advantages make PARS particularly well suited for label-free histology and tissue diagnostics.

Operational Principles of PARS Imaging

The specific PARS optical architectures designed and presented in this work will be detailed in later chapters; however, all systems share the same base configuration: a continuous-wave detection beam and a pulsed excitation beam co-aligned and co-focused onto the specimen, which image the sample in a point-scanning fashion. The PARS contrast measurement process can be described in three sequential steps, illustrated in Figure 2.4.

Firstly, prior to excitation, the detection beam's transmission or reflection intensity from the specimen is recorded as a baseline scattering measurement, establishing the sample's unexcited optical properties. This baseline serves as a reference for later measurements and provides an independent scattering contrast channel that highlights tissue morphology and microstructure.

Following this, the pulsed excitation beam targets the sample, inducing electronic transitions within the interrogated biomolecule(s). After absorption, the two dominant de-excitation pathways are measured simultaneously as distinct channels. Radiative relaxation is measured by isolating the Stokes-shifted emission photons and quantifying their intensity with a photodetector device. In the PARS architectures presented in this work, the entire radiative emission spectrum is broadly collected with an objective lens, spectrally filtered to remove residual excitation or detection light, and then directed to a detector as a single intensity measurement.

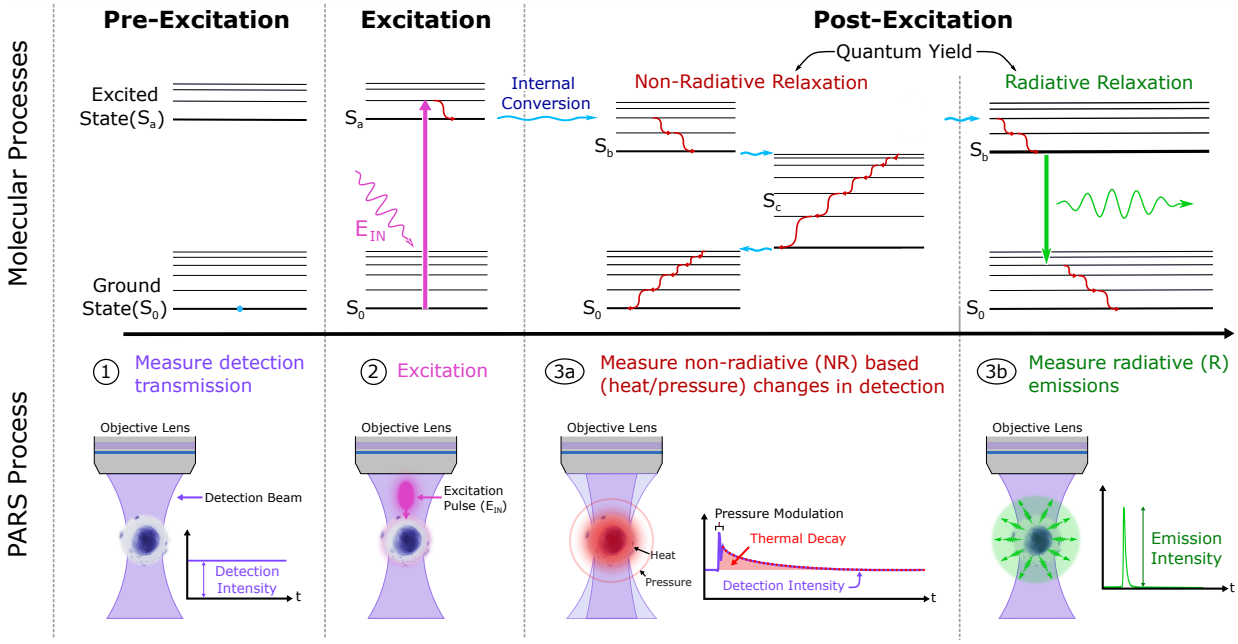

Figure 2.4: The PARS radiative and non-radiative measurement process, shown alongside the excitation, absorption, and subsequent relaxation pathways within a biomolecule. (1) A baseline transmission or reflection of the detection beam (scattering contrast) is measured. (2) A co-focused pulsed excitation beam targets the sample, inducing absorption which results in an electron transition from the ground state (S_0) to an excited state (S_a, S_b, S_c). (3) The two dominant relaxation pathways are then measured: (3a) Non-radiative relaxation produces localized heating that modulates the surrounding optical properties, detected as transmissivity changes in the detection beam. (3b) Radiative relaxation produces Stokes-shifted photons which are subsequently measured. Modified from [30].

Measuring the non-radiative relaxation process is more complex and less direct than in the radiative case, and instead relies on the continuous-wave detection beam to probe secondary effects generated by localized non-radiative heating. This heating produces thermoelastic expansion within the excited volume. If the heating is sufficiently rapid (picosec-

onds to nanoseconds), thermal expansion can outpace the relaxation of the surrounding material, generating photoacoustic pressure [98, 99]. Together, these photothermal and photoacoustic perturbations create transient density fluctuations that modulate the local refractive index of the specimen, in turn perturbing the transmitted or reflected detection beam intensity relative to its baseline (pre-excitation) and providing a measurable non-radiative signal [30]. The non-radiative signal is illustrated in part (3a) of Figure 2.4, where the modulations would appear as an initial sharp pressure peak followed by a longer thermal decay. The photoacoustic pressure wave propagates outward at the speed of sound and exits the probe region more quickly, while the thermal perturbation dissipates more gradually through diffusion, and remains measurable within the probe region for a longer duration. The temporal evolution of these modulations is governed by the material properties of the specimen [30]. To give a rough idea of these timescales, in the FFPE histology slides used in this work and with detection and excitation beams focused at sub-micron resolutions, the photoacoustic signal persists in the probe region for a few nanoseconds, while the thermal decay (i.e., the period over which 98% of the deposited heat dissipates) extends over several microseconds ($\sim$5 μs) [30].

Different strategies can be applied to extract non-radiative contrast from this signal in part (3a) of Figure 2.4 [31, 93, 100]. The most common approach is to integrate the thermal decay curve to calculate the non-radiative signal energy, typically reported as a percentage modulation normalized to the baseline scattering level pre-excitation. The specific extraction methods implemented in this work are described in later chapters.

Previous and Concurrent Work in PARS Label-Free Tissue Imaging

As previously mentioned, PARS evolved from photoacoustic remote sensing, first introduced by Haji Reza et al. in 2017 [77]. This initial implementation measured non-radiative relaxation mechanisms and was applied to imaging blood and vasculature through hemoglobin absorption, like conventional photoacoustic methods but with the advantages of a fully optical and non-contact architecture [77]. Building on this, the first demonstration of label-free histology was reported in 2019, where a 266 nm excitation beam was used to target the optical absorption peak of DNA, enabling nuclear contrast in unstained tissue sections [75, 76], consistent with earlier photoacoustic studies employing 266 nm excitation [18, 92]. Subsequent work further established proof-of-concept non-radiative imaging across a wider range of sample formats, including FFPE slides, FFPE blocks, frozen sections, and freshly resected tissues, using a variety of architectures [82, 83, 101, 102].

These previous systems only captured non-radiative contrast, until Ecclestone et al. [32] advanced the field by adding simultaneous radiative relaxation contrast as well as

improvements to non-radiative nuclear contrast, in what is now termed Photon Absorption Remote Sensing (PARS). The radiative channel supplied missing connective tissue contrast, and together with the non-radiative nuclear contrast, PARS captured label-free images analogous to gold-standard H&E staining. Following this, Boktor et al. showed the first application of virtual staining on raw PARS images using Pix2Pix for emulation of H&E in skin tissues [33].

In addition to the contributions in this thesis, many concurrent studies from our group have advanced the role of PARS in label-free diagnostic pathology. A number of these works have directly built on the contributions presented here, such as the automated whole slide scanning architecture described in Chapter 3 and the PARS virtual staining approaches demonstrated in Chapters 4 and 6. These include a clinical concordance study in skin tissues [103], which followed the initial breast tissue concordance study in Chapter 5 and employed the WSI scanning system from Chapter 3. Other related studies have pursued improved signal extraction and contrast separation techniques for enhanced biomolecular mapping and contrast extraction [104, 31]. More recently, a new optical scanning head with a substantially faster design for higher imaging speeds has been introduced [105]. This system has built on the automation framework, autofocusing process, software tools, and many of the design elements and downstream data processing developed in Chapter 3 and directly employing the virtual staining methods from Chapter 6 for H&E staining. In addition, while this work builds on the initial PARS histology studies mentioned earlier, it has also employed software tools from parallel studies in other PARS applications (e.g., in-vivo vascular imaging) [93], including high-speed data acquisition code adapted to support the developments presented here.

In parallel to the work presented in this thesis, other groups have also investigated UV-PARS-based approaches for histology, including a reflection-mode UV-PARS implementations employing voice-coil hardware stages and alternative scanning patterns for increased imaging speed [106], as well as a subsequent study applying strictly unpaired deep learning methods (CycleGAN) for virtual H&E staining in thicker tissue samples [107].

2.1.5 Deep Learning-Based Virtual Histological Staining

Virtual staining is the process of computationally transforming a label-free microscopy image into the appearance of a chemically stained tissue section [15, 23]. This approach bypasses many of the time- and resource-intensive, destructive chemical processing steps required for traditional staining, while keeping the familiar stain patterns (e.g., H&E) that pathologists are trained to interpret. Virtual staining offers several advantages over

conventional methods. Because it is a purely digital process, the same tissue section can be rendered in multiple virtual stains simultaneously (i.e., multi-staining), expanding diagnostic utility without consuming additional biopsy material. Importantly, the tissue remains preserved for standard or advanced downstream assays that would otherwise be precluded by chemical staining. While the focus of this work is the virtual staining of label-free microscopy images, stain-to-stain translations have also been demonstrated by various groups [108, 109, 110] and represent another branch of virtual staining research.

Beyond enabling a non-destructive analysis, virtual staining offers potential workflow and economic advantages. Chemical staining represents one of the most labor-intensive and resource-dependent components of histology, requiring reagents, consumables, trained personnel, quality control procedures, and hazardous waste handling [15]. Eliminating or reducing these steps can shorten specimen preparation time prior to microscopic review, which may translate into meaningful reductions in turnaround time (TAT), particularly in high-volume laboratories. Furthermore, digital stain generation reduces slide-to-slide variability and avoids technically failed stains that require reprocessing [15]. While precise costs for the staining alone are not publicly itemized, histopathology services collectively represent a multi-billion-dollar global market, highlighting the potential impact of efficiency gains within this workflow.

Deep learning is particularly well suited to virtual staining because it can learn complex, nonlinear mappings between label-free image contrasts and histological stain patterns. These models capture not only fine-scale cellular detail but also larger-scale contextual information necessary for accurately replicating hierarchical tissue structures. Among deep learning approaches, generative adversarial networks (Generative Adversarial Networks (GANs)), specifically Image-to-Image (I2I) translation frameworks, have emerged as the most widely adopted due to their ability to generate high-quality, perceptually realistic stained images [15].

Generative Adversarial Network (GAN) Frameworks for Virtual Staining

GANs were first proposed by Goodfellow et al. in 2014 for natural image synthesis [111] and have since been applied to a wide range of generative tasks. The GAN architectures most commonly used for virtual staining are I2I translation frameworks, in which a generator learns to map an input image from one domain to another while a discriminator enforces perceptual realism. Therefore, the GAN framework consists of two deep networks, a Generator (G; U-Net or similar [112]) and Discriminator (D; classifier network), which are simultaneously trained in a competitive fashion. In the context of virtual staining, the generator network works to produce a realistic-looking, but virtually stained image

based on the label-free input data, while the discriminator network learns to accurately classify what is a virtual versus real histochemically stained image. Throughout training, the discriminator judges the generated images, and provides an adversarial loss to the generator. This adversarial loss helps guide the generator towards its goal of producing realistic-looking virtually stained images which are capable of fooling the discriminator. Ideally, training progresses towards a balanced state where the discriminator is unable to reliably distinguish between real and virtually stained images, indicating that the generated images are perceptually realistic. Virtual staining I2I networks are a type of conditional GANs (cGANs) because they are conditioned on the input label-free image, as opposed to random noise.

There are two main training strategies for GAN-based virtual staining models, depending on whether paired training samples are available. If one-to-one images in each domain can be acquired and WSI registration is feasible, then supervised approaches are possible, with Pix2Pix and its variants being the most widely used [113]. However, in most scenarios, obtaining perfectly pixel-aligned datasets is challenging, and training is performed with unpaired images [15]. In these cases, CycleGAN and its variants are the most commonly employed [114].

Pix2Pix (Supervised)

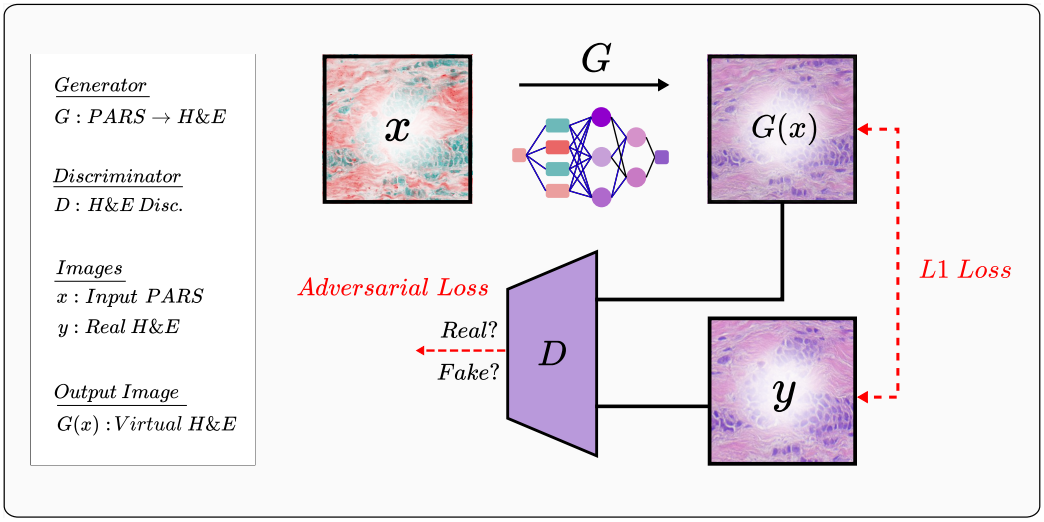

Figure 2.5: Pix2Pix paired training scheme for virtual staining with PARS as the input and H&E as the target stain. Losses are shown in red; the legend (left) defines all components and image types.

For Pix2Pix, the training dataset $\{(x_i, y_i)\}_{i=1}^{N}$ consists of N paired images from domains X (label-free) and Y (histochemical stain). The generator is trained to learn the mapping $G : X \rightarrow Y$ (i.e., Label-Free $\rightarrow$ Histochemical). The Pix2Pix model combines two losses: the conditional adversarial loss ($\mathcal{L}_{cGAN}$) and a pixel-wise loss ($\mathcal{L}_{L1}$). The adversarial loss is derived from the binary cross-entropy formulation in [111, 115] and is expressed as:

$$\mathcal{L}_{cGAN}(G, D) = \mathbb{E}_{x,y}\left[logD(x, y)\right] + \mathbb{E}_{x,z}\left[log(1 - D(x, G(x, z)))\right] \tag{2.1}$$

In equation 2.1, $\mathbb{E}$ denotes the expectation operator, representing the average over samples drawn from the joint data distribution of paired images (x, y). The discriminator D is a neural network that outputs the probability that an input image pair is real (i.e., a true histochemical stain) rather than generated. The generator G produces a virtual stain conditioned on the input label-free image x. The variable z denotes a random noise vector used to add stochasticity into the generation process; however, in standard Pix2Pix implementations this explicit noise term is omitted, and dropout layers within the generator are instead employed for regularization. In this adversarial loss, the generator G aims to minimizes the loss while the discriminator D attempts to maximize it. Next, the $\mathcal{L}_{L1}$ pixel-wise loss is expressed below:

$$\mathcal{L}_{L1}(G) = \mathbb{E}_{x,y,z}\left[\|y - G(x, z))\|_1\right] \tag{2.2}$$

Equation 2.2 measures the pixel-level difference between the virtually stained image and its corresponding ground truth histochemical stain. It is calculated as the average absolute difference between the two images. The generator minimizes this loss by learning to produce increasingly realistic virtual images with pixel-level detail. The overall Pix2Pix objective function combines both losses and is given as:

$$G^* = \arg\min_G \max_D \left[\mathcal{L}_{cGAN}(G, D) + \lambda \mathcal{L}_{L1}(G)\right] \tag{2.3}$$

where the hyperparameter λ controls the relative weighting of the two losses.

CycleGAN (Unsupervised)

When pixel-aligned training pairs are unavailable, virtual staining models are trained in an unpaired fashion, most commonly using CycleGAN. Like Pix2Pix, CycleGAN aims to learn the image mapping function $G : X \rightarrow Y$ through the adversarial loss. However,

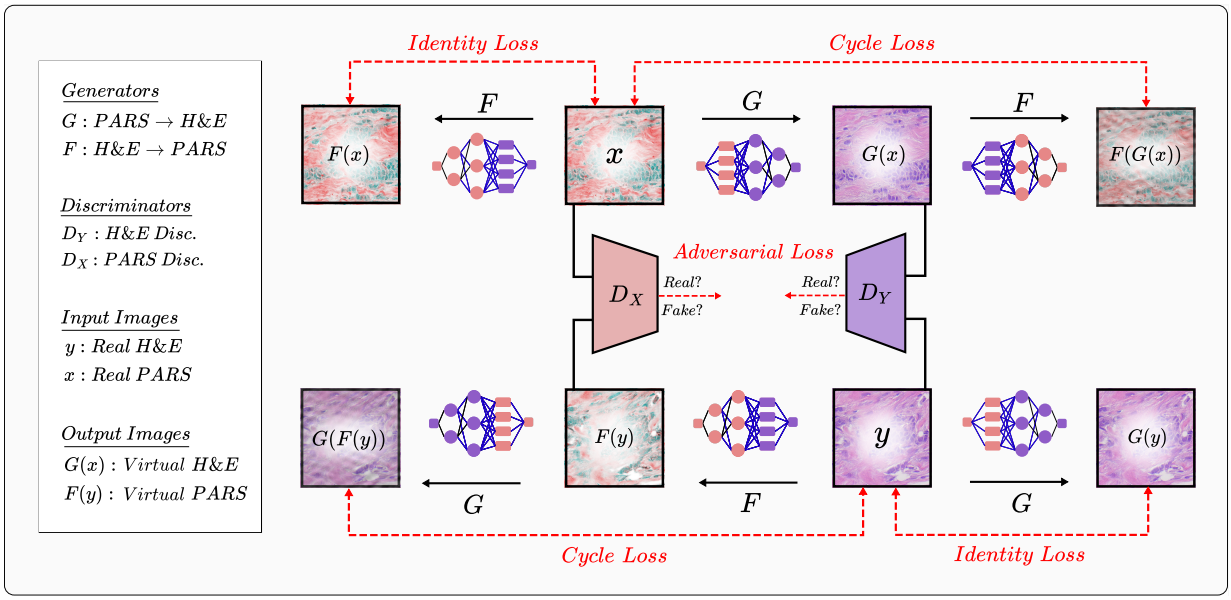

Figure 2.6: CycleGAN unpaired training scheme for virtual staining with PARS as the input and H&E as the target stain. Losses are shown in red; the legend (left) defines all components and image types.

in unpaired data scenarios, this goal becomes highly under-constrained. To address this, CycleGAN simultaneously learns an inverse mapping $F : Y \rightarrow X$ (i.e., Histochemical $\rightarrow$ Label-Free) to enforce that $F(G(X)) \approx X$ and $G(F(Y)) \approx Y$ throughout training. This is called the 'cycle-consistency' loss and it ensures that a translated image (i.e., virtual stain) can be reverted back to its original form (i.e., label-free), enhancing the robustness of the learned transformations. The framework therefore employs two generators, G and F, along with two adversarial discriminators, D_X and D_Y. Specifically, D_X discriminates between images x and $F(y)$, while D_Y distinguishes between y and $G(x)$. We also have training samples $\{x_i\}_{i=1}^{N}$ in domain X and $\{y_i\}_{i=1}^{M}$ in domain Y. The cycle-consistency loss is expressed as:

$$\mathcal{L}_{cyc}(G, F) = \mathbb{E}_x \left[\|F(G(x)) - x\|_1\right] + \mathbb{E}_y \left[\|G(F(y)) - y\|_1\right] \tag{2.4}$$

We then also have the standard GAN adversarial loss, expressed as:

$$\mathcal{L}_{GAN}(G, D_Y) = \mathbb{E}_y \left[log D_Y(y)\right] + \mathbb{E}_x \left[log(1 - D_Y(G(x)))\right] \tag{2.5}$$

This same adversarial loss in equation 2.5 is repeated for the inverse mapping $F : Y \rightarrow X$. Again, the generators aim to minimize this loss while the discriminators work to maximize

it. Lastly, an additional identity loss [116] is often incorporated during CycleGAN training to encourage preservation of essential image features (e.g., color composition) between input and output domains. This loss regularizes the generators toward an identity mapping when a real histochemically stained image is inputted to G and a real label-free image in inputted to F. It is expressed as follows:

$$\mathcal{L}_{identity}(G, F) = \mathbb{E}_y \left[\|G(y) - y\|_1 \right] + \mathbb{E}_x \left[\|F(x) - x\|_1 \right] \tag{2.6}$$

With this, the overall objective function for CycleGAN is can be expressed as:

$$\begin{aligned} G^*, F^* = \arg\min_{G,F} \max_{D_Y, D_X} \big[& \mathcal{L}_{GAN}(G, D_Y) \\ & + \mathcal{L}_{GAN}(F, D_X) \\ & + \lambda \mathcal{L}_{cyc}(G, F) \\ & + 0.5\lambda \mathcal{L}_{identity}(G, F) \big] \end{aligned} \tag{2.7}$$

where the hyperparameter λ is used to control relative loss weightings.

RegGAN (Supervised with Noisy Labels)

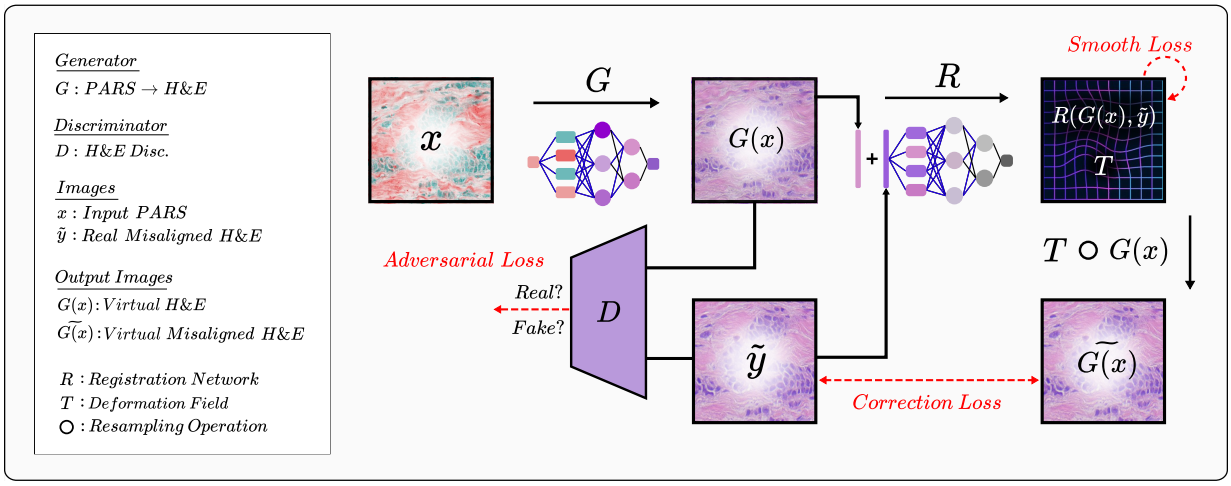

Figure 2.7: RegGAN training scheme for virtual staining with PARS as the input and H&E as the target stain. Losses are shown in red; the legend (left) defines all components and image types.

While Pix2Pix and CycleGAN remain the most widely employed frameworks for virtual staining, this work employs a more recent I2I translation model called RegGAN ('registration' GAN) [34]. RegGAN is a supervised approach that is robust to misaligned or 'noisy' labels and is designed for scenarios where perfectly paired samples are not available. The model uses a registration network to adaptively correct for these errors during training. To the best of our knowledge, RegGAN has not yet been applied to virtual staining, and this work explores its applicability in this domain. The underlying principles of RegGAN are overviewed here, while its application and results are presented later in Chapter 6.

RegGAN is a supervised learning process, wherein the model is trained with misaligned or 'noisy' target images. The training dataset is denoted as $\{(x_n, \tilde{y_n})\}_{n=1}^{N}$ with N sample pairs, where x_n corresponds to an input PARS image and $\tilde{y_n}$ is the corresponding misaligned, 'noisy' chemically stained image. The unknown, perfectly registered target image for x_n is denoted as y_n. Using the noisy labeled dataset $\{(x_n, \tilde{y_n})\}_{n=1}^{N}$, the goal is to train the virtual staining generator $G(x_n)$ to achieve performance as close as possible to a staining model trained on a perfectly registered dataset $\{(x_n, y_n)\}_{n=1}^{N}$.

The noise distribution can be expressed as a displacement error, $\tilde{y_n} = y \circ T$, where T is a random deformation field with a displacement for each pixel in the image, and $\circ$ denotes the resampling operation. As shown in Figure 2.7, RegGAN introduces a registration network (R) following the stain generator (G), which models the displacement transformation to correct the generated stained image. The resulting correction loss is defined as:

$$\arg\min_{G,R} \mathcal{L}_{corr}(G, R) = \mathbb{E}_{x,\tilde{y}} \left[\| \tilde{y} - G(x) \circ R(G(x), \tilde{y}) \|_1 \right] \tag{2.8}$$

In equation 2.8, $R(G(x), \tilde{y})$ represents the deformation field. Furthermore, as with most existing deformable registration algorithms [117], a smoothness loss, equation 2.9, is included to enforce a spatially smooth deformation field and minimize the gradient of the deformation field.

$$\arg\min_{R} \mathcal{L}_{smooth}(R) = \mathbb{E}_{x,\tilde{y}} \left[\| \nabla R(G(x), \tilde{y}) \|^2 \right] \tag{2.9}$$

Lastly, a least squares adversarial loss is used for the generator and discriminator networks:

$$\arg\min_{D} \mathcal{L}_{ls}(D) = \mathbb{E}_y \left[(1 - D(y))^2 \right] + \mathbb{E}_x \left[D(G(x))^2 \right] \tag{2.10}$$

$$\arg\min_{G} \mathcal{L}_{ls}(G) = \mathbb{E}_x \left[(1 - D(G(x)))^2 \right] \tag{2.11}$$

The total loss is therefore expressed in equation 2.12 as follows.

$$\mathcal{L}_{total}(G, R, D) = \lambda_{corr}\mathcal{L}_{corr} + \lambda_{smooth}\mathcal{L}_{smooth} + \lambda_{adv}\left[\mathcal{L}_{ls}(D) + \mathcal{L}_{ls}(G)\right] \tag{2.12}$$

where the hyperparameters λ_{corr}, λ_{smooth}, λ_{adv} are used as relative loss weightings for the correction, smooth, and adversarial losses, respectively.

2.2 Related Label-Free Methods for Virtual Staining

2.2.1 Overview

Virtual staining offers the ability to generate histology-like contrast in tissue samples without the need for stains, chemical reagents, or time-consuming processing steps. Broadly, virtual staining approaches can be divided into two categories: stain-to-stain transformations and label-free-to-stain transformations [15]. While stain-to-stain methods have demonstrated value, label-free approaches offer several key advantages. Such techniques rely on intrinsic optical contrast in the sample and can image tissue in a non-destructive manner, and therefore the same specimen is preserved for advanced downstream analyses and standard histology workflows are not disrupted [15]. Because this work focuses on label-free microscopy with virtual staining, this review is limited to studies within the label-free category.

A variety of label-free imaging modalities have been employed for virtual staining, each capturing unique forms of contrast with their own strengths and limitations. The success of a virtual staining model is in large part, dependent on the quality and biomolecular specificity of the input data, since the ability to emulate the features of the target stain relies on the contrast information available in the input. Examples of scattering-based methods include brightfield [118, 119], QPI [43, 120, 53], and Reflectance Confocal Microscopy (RCM) [121]. Absorption-based approaches make use of signals such as autofluorescence [26, 64, 67, 122, 123, 68, 124], Fluorescence Lifetime Imaging Microscopy (FLIM) [28] or photoacoustics [125, 73, 126], while non-linear methods include techniques like CARS, SHG, and Multi-Photon Fluorescence (MPF) [127], as well as SRS [128, 129] for virtual staining. As mentioned previously, the vast majority of these works use GANs [15], due to their strength in I2I translation and ability to learn complex mappings between input contrasts and the target stain. Consequently, the examples highlighted in this review largely involve GAN-based implementations.

Among the label-free microscopes used for virtual staining, the point at which they intervene in the histology pipeline differs. Some methods target pre-fixation, performing "slide-free" or fresh tissue imaging, where samples are imaged without requiring fixation or sectioning [53, 121, 127]. Slide-free imaging is an active area of research with clear potential to be highly valuable, offering the possibility of faster diagnostic turnaround times among other benefits. However, beyond technical considerations, it faces key barriers to adoption: there is no established diagnostic gold standard for comparison, and the field of histopathological analysis has largely been built around preserved specimens in standardized slide formats. As a result, interpretation of fresh tissue images is unfamiliar to pathologists. In addition, paired training data are difficult or impossible to obtain, further complicating model development for virtual staining [15].

In contrast, many label-free virtual staining approaches focus on imaging standard unstained FFPE tissue slides [15], where stained counterparts exist. This provides a direct gold-standard reference, making validation more straightforward and model training more feasible. Beyond this practical advantage, there are benefits to preserving tissue specimens as slides, and large collections of archival material spanning diverse disease cases are maintained in biobanks and hospitals. The standard FFPE slide format is widely used not only in diagnostic workflows but also in research and development, including academic studies, pharmaceutical research, and drug development, where specimens corresponding to specific disease states are required. As such, slide-based approaches align naturally with current diagnostic and research practices.

When evaluating the performance of virtual staining methods, several benchmarking strategies are commonly used. For paired datasets, standard quantitative metrics such as Mean Squared Error (MSE), Structural Similarity Index Measure (SSIM) [130], and Peak Signal-to-Noise Ratio (PSNR) provide a measure of similarity to the reference image. In unpaired settings, reference-free metrics like Fréchet Inception Distance (FID) [131] are often applied, though these are more general measures of generative image quality. There are also algorithm-driven histological feature comparisons. For example, segmenting nuclei in both real and virtual images and comparing counts, morphology, or other cellular features [15, 4, 1]. However, many clinically meaningful features remain difficult to quantify algorithmically. For this reason, some studies incorporate pathologist surveys as an additional benchmark, to judge whether the virtual stains preserve diagnostic information [4, 3]. These surveys are valuable but less common, as they require significant time and are therefore usually limited in scope to small tissue areas with simplified questions rather than full diagnostic evaluations.

With these considerations in mind, the following section will review the range of label-free imaging modalities that have been used for virtual staining, generally categorized into

scattering-based, absorption-based, and nonlinear or multimodal techniques.

2.2.2 Scattering-Based Approaches

Brightfield Imaging: Brightfield microscopy is a straightforward and common microscopy method which records the transmitted intensity of white light illumination through tissue sample. In stained specimens, brightfield contrast arises from absorption of transmitted light by the applied stains. As light passes through the sample, stained regions absorb portions of the illumination, reducing transmitted intensity and creating contrast. In unstained tissue sections, intrinsic absorption is minimal and therefore absorption-based contrast is typically weak. Instead, contrast arises from refractive index variations within the tissue that scatter and redirect the transmitted light. Because the objective lens collects only a finite range of angles, light scattered outside the collection cone is not detected, resulting in localized intensity reductions that reflect underlying microstructural features. Although this mechanism provides substantially weaker contrast than histochemical staining, brightfield imaging of unstained sections has nevertheless been explored for virtual staining applications [118, 119].

Li *et al.* developed a deep learning–based virtual staining approach that transformed brightfield images of unlabeled rat carotid artery sections into H&E, picrosirius red (PSR), and orcein stains using a conditional GAN and the multi-domain StarGAN network (unpaired), achieving close agreement with true stains in pathologist evaluations [118]. An example output of all three stains is shown in Figure 2.8. Zhang *et al.* extended this concept to human carotid atherosclerotic tissue, training a paired multi-stain Pix2Pix GAN with pseudo-labels to simultaneously generate H&E, PSR, and Verhoeff van Gieson (EVG) stains from a single brightfield image, showing improved SSIM and PSNR compared to other multi-domain methods like StarGAN, and similar pathologist agreement on key plaque features such as necrotic core, collagen, and elastin [119].

While brightfield microscopes are widely available and simple to operate, their main limitation is the inherently low contrast of unstained tissue sections, which are largely transparent and show minimal differentiation of structural features without additional staining or contrast-enhancing methods. As such, virtual staining model have limited contrast information to learn from, making it challenging to accurately emulate the biochemical specificity of chemical stains.

Quantitative Phase Imaging (QPI): QPI is a label-free technique that measures the phase delay of light transmitted through a sample, which comes from spatial variations

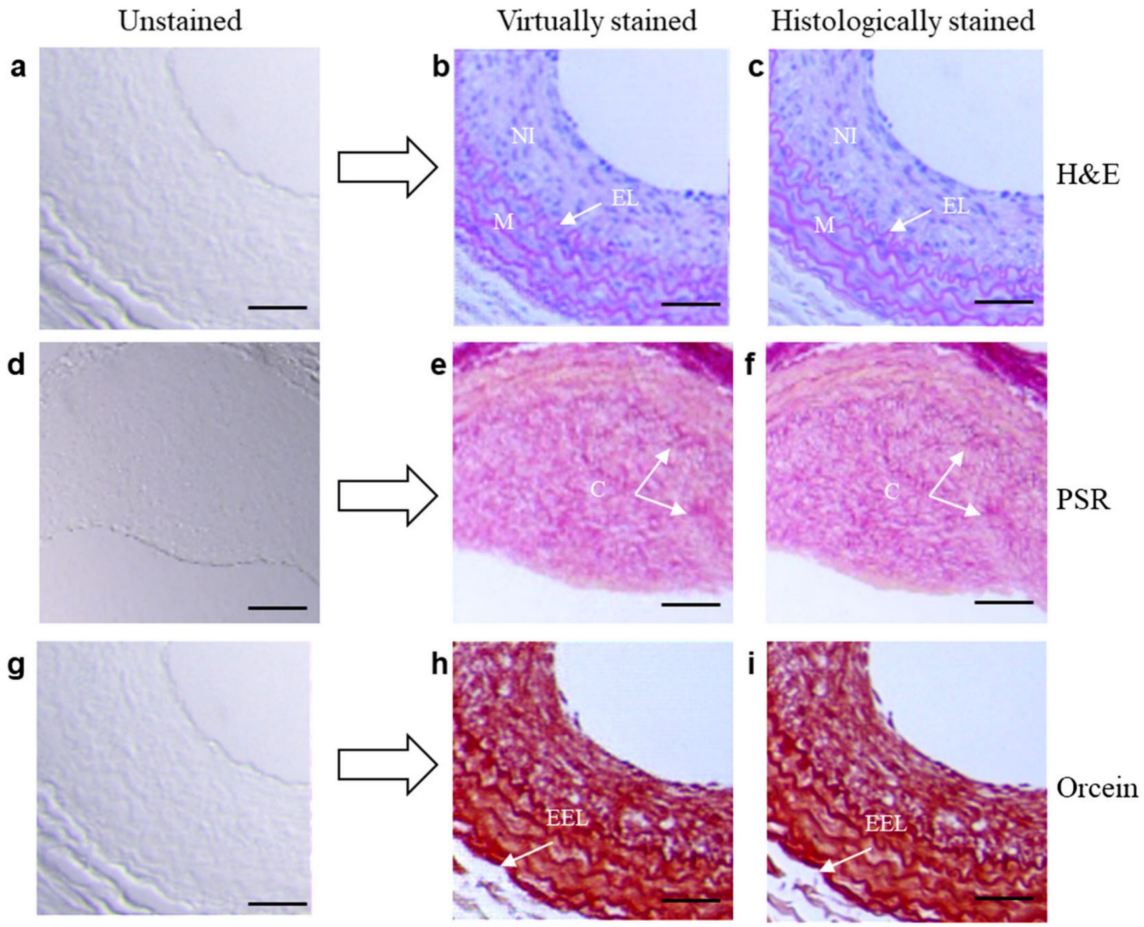

Figure 2.8: Example virtual staining from brightfield microscopy of unstained carotid artery tissue sections. Virtual H&E, picrosirius red (PSR), and orcein stains are shown alongside their corresponding histologically stained references (adapted from Li *et al.* [118]).

in the refractive index and optical path length. Because these variations are tied to the structural and organizational features of the tissue, QPI provides a visualization of cellular and microstructural morphology without the need for stains. A variety of QPI implementations exist, and have found extensive use in live-cell imaging, studying the dynamics of biological processes (e.g., cell growth), and more [132]. In addition, QPI has also been investigated for virtual staining of histology samples.

Rivenson *et al.* demonstrated one of the first applications of QPI for virtual staining, where a deep learning model was trained in a paired fashion to generate virtual H&E, Masson's trichrome, and Jones stained images from label-free tissue sections of human skin, kidney, and liver tissue [43]. Their approach, called 'PhaseStain', showed that QPI could reproduce tissue morphology in a virtual histology format, enabling interpretation of nuclear and cytoplasmic features without physical staining or damage to the tissue. An example QPI to virtual H&E translation can be seen in the top part of Figure 2.9. Following this, Nygate *et al.* demonstrated QPI virtual cytological staining of individual cells, allowing for standardized but non-toxic evaluation of human sperm cells for fertility evaluation [120]. More recently, Abraham *et al.* employed a 3D QPI method, Quantitative Oblique Back-Illumination Microscopy (qOBM) combined with an unpaired CycleGAN-based virtual staining network to generate virtual H&E images from label- and slide-free fresh tissues [53]. Healthy and tumor tissue images were validated using a classifier and a neuropathologist study, showing that QPI can be adapted to slide-free imaging contexts with potential value for intraoperative applications. An example virtually stained qOBM 3D volumetric stack of a rat brain tumor margin can be see in the bottom part of Figure 2.9.

Overall, QPI has been established as an effective input for virtual staining. However, its main limitation is the models rely purely on structural contrast in the tissue, meaning they differentiate features only by morphology and refractive index differences in the specimen. As a result, they may fail to capture biomolecular differences, making translation to stains that highlight biochemical content more challenging.

Reflectance Confocal Microscopy (RCM): RCM is a label-free optical imaging technique that captures backscattered light from tissue and uses confocal sectioning to generate en face images of microstructural tissue features [121]. It is most prominently used in dermatology as a noninvasive, in vivo imaging tool capable of visualizing the epidermis through the papillary and superficial dermis at near-histological resolution, enabling real-time assessment of skin architecture without a biopsy. However, RCM images differ from traditional histology, lacking the familiar nuclear contrast seen in skin cells, which

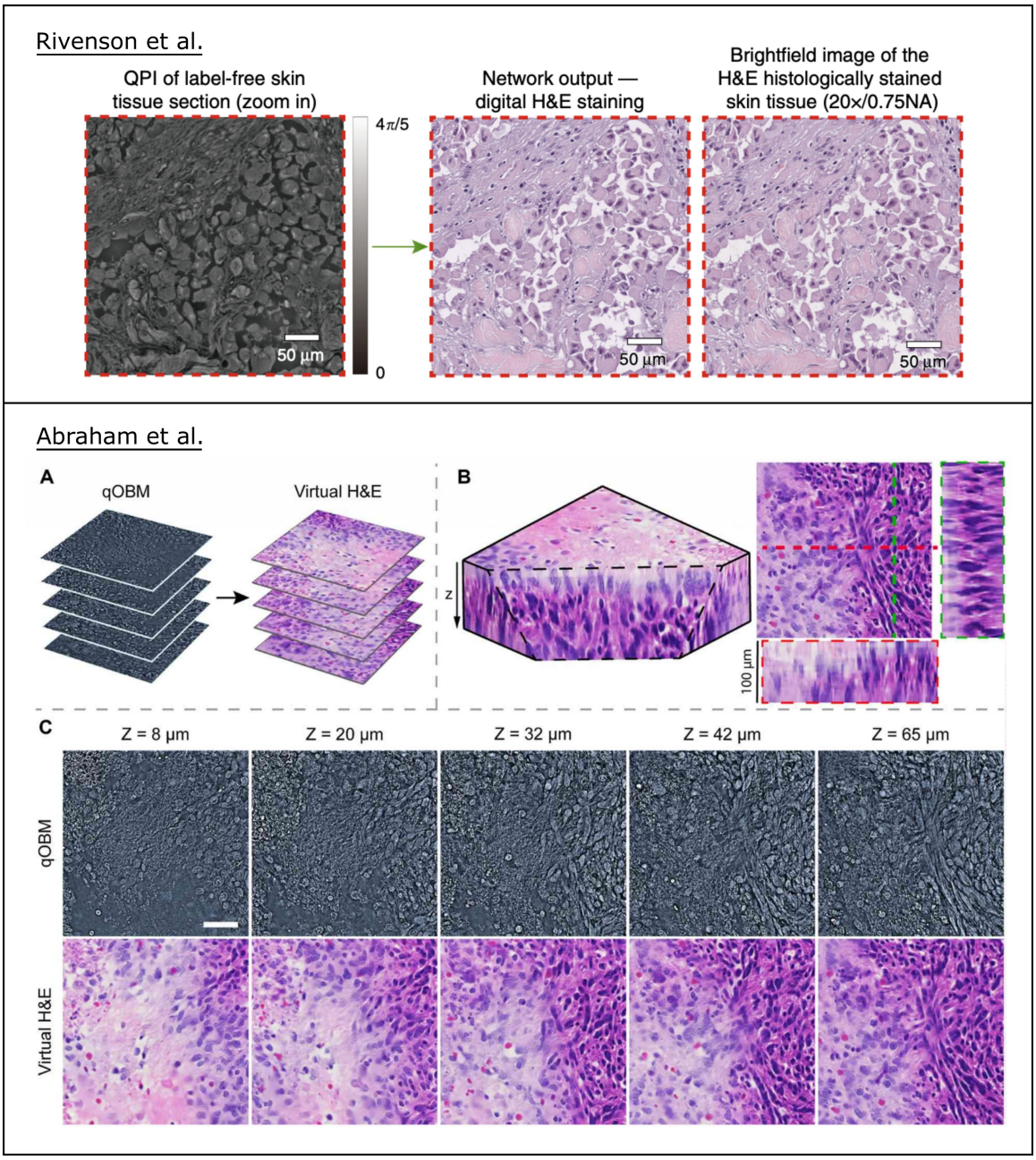

Figure 2.9: Example virtual staining using QPI and qOBM microscopy. Top: QPI image of label-free human skin tissue translated into virtual H&E, compared with the corresponding true H&E image (adapted from Rivenson *et al.* [43]). Bottom: qOBM image and corresponding virtual H&E 3D volumetric stack of a rat brain tumor margin (adapted from Abraham *et al.* [53]).

makes them more challenging to interpret. As a result, virtual staining has been explored to enhance interpretability.

Li *et al.* developed a deep learning framework to generate virtual H&E images from RCM data of human skin [121]. The model was trained in a paired fashion using ex vivo RCM images of unstained tissue and corresponding images of the same tissue after acetic-acid staining to highlight nuclear structures. Through this pairing, the network learned to map structural RCM contrast to H&E-like color representations. When applied to normal and cancerous skin, the model reproduced morphological features comparable to traditional H&E histology, demonstrating the potential of RCM for noninvasive, label-free virtual histology. An example RCM virtual H&E staining result of ex-vivo skin tissue is shown in Figure 2.10.

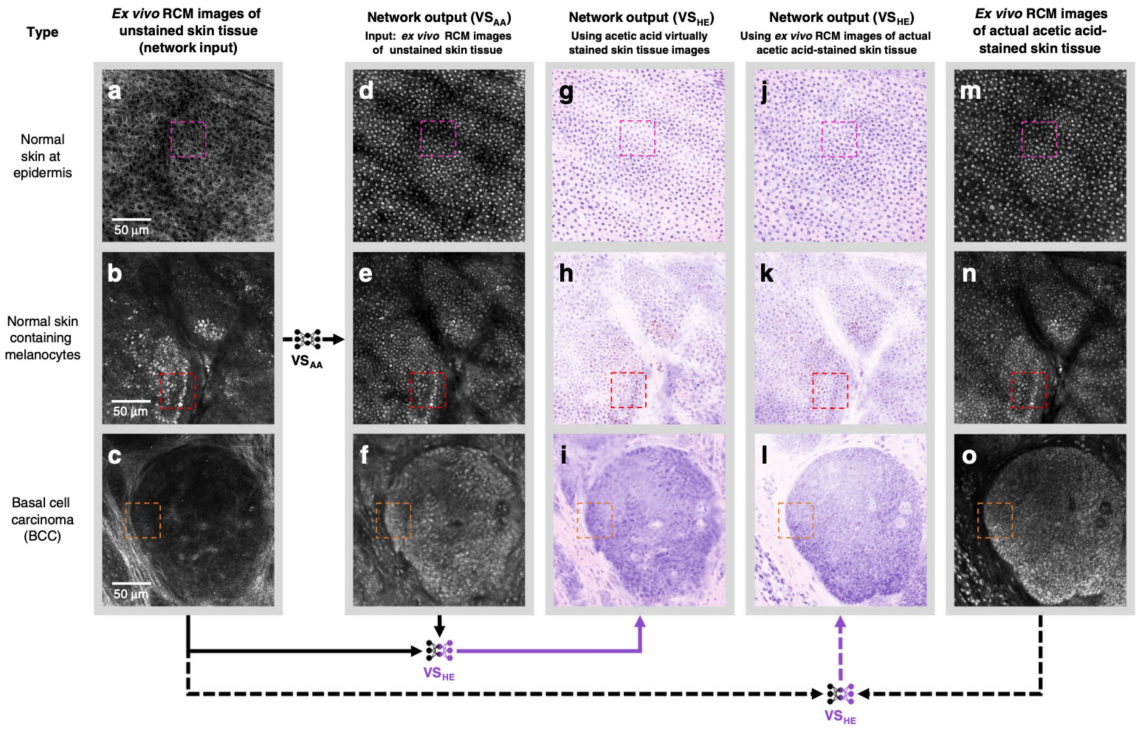

Figure 2.10: Example virtual H&E staining from RCM images of human skin areas including: normal skin at the epidermis, normal skin containing melanocytes, and basal cell carcinoma (BCC). The first network produces virtual acetic-acid–stained images to enhance nuclear contrast, while the second produces H&E-like virtual stains from the combined inputs. Results are shown alongside the corresponding ground truth acetic-acid–stained RCM images for comparison (adapted from Li *et al.* [121]).

While RCM has demonstrated feasibility in generating histology-like images noninva-

sively, its appearance differs from traditional slide-based histology, though it may have complementary clinical uses. RCM provides high-resolution, en face imaging based on refractive index variations, generating primarily morphological contrast rather than stain-specific biochemical contrast. As a result, while cellular detail can be visualized, the contrast mechanism differs fundamentally from histochemical staining, and interpretability remains largely confined to dermatologic applications.

2.2.3 Radiative Absorption-Based Approaches

Autofluorescence Imaging: Autofluorescence microscopy is an absorption-based imaging method that captures intrinsic emissions (radiative relaxation) from tissue following light excitation [69]. Unlike the aforementioned scattering-based techniques, which primarily visualize structural morphology of the sample, autofluorescence directly images endogenous biomolecules such as proteins, cofactors, and ECM components, based on their absorption and emission properties. Many biologically relevant proteins and tissue structures become autofluorescent when excited by an appropriate wavelength, typically in the UV or shorter visible range [69]. The emission of these endogenous fluorophores contains valuable information that correlates with the structural and functional characteristics of the biological specimen and has therefore been explored for various diagnostic and research purposes [17, 69, 70]. Autofluorescence images of unstained tissue can be acquired using a standard wide-field fluorescent microscope with a set of standard near-UV excitation and emission filters. Because autofluorescence contrast aligns more closely with the targets of histological stains, it has become the most widely explored input for virtual staining, enabling the generation of virtual H&E and other histochemical stains [26, 64, 67, 122, 123, 68, 124].

Rivenson *et al.* introduced the first deep learning–based virtual staining framework using autofluorescence microscopy of unlabeled tissue. In this work, a Pix2Pix-like GAN model was trained in a paired fashion to map label-free autofluorescence images of unsectioned human skin, kidney, and liver tissue to H&E, Masson's trichrome, and Jones stains [26]. Zhang *et al.* from the same group later introduced a framework that takes an autofluorescence image and a user-defined digital staining matrix as inputs, enabling spatial control over stain assignment and the digital blending of multiple histological stains within a single tissue section [64]. Example results from these two works is shown in Figure 2.11.

More recent studies have applied autofluorescence-based virtual staining to specific clinical contexts, including ovarian cancer tissue [67], HER2 immunohistochemical staining of breast tissue [124], lung and heart transplant biopsies [123], and post-mortem autopsy

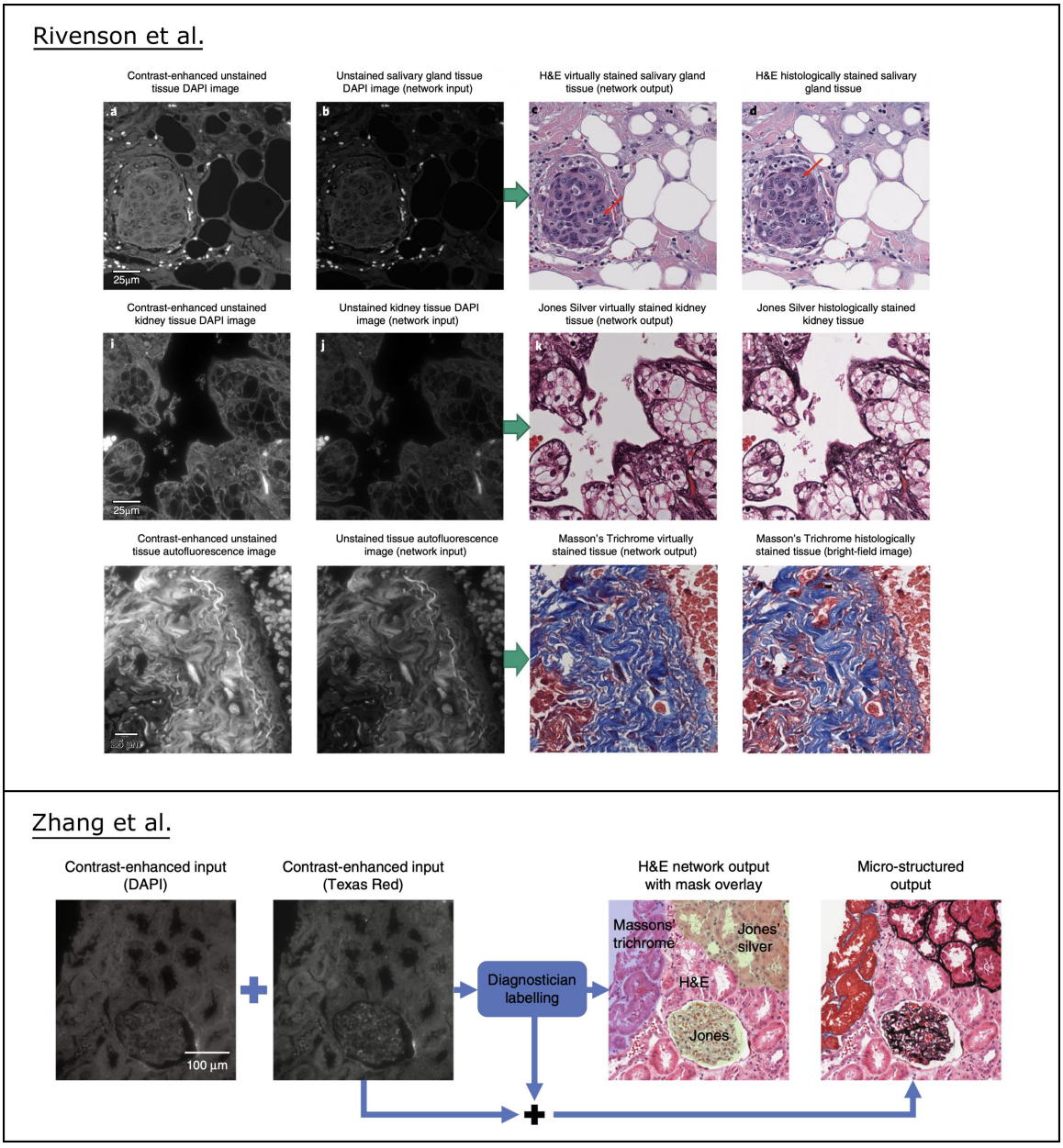

Figure 2.11: Example virtual staining using autofluorescence microscopy. Top: Autofluorescence image of unstained salivary gland (row 1), kidney (row 2), and lung (row 3) translated to virtual H&E, Jones, and Masson's trichrome, respectively (adapted from Rivenson *et al.* [26]). Fluorescence channels were acquired using filter cubes commonly labeled "DAPI" and "Texas Red," referring to the excitation/emission bandpass settings rather than exogenous staining. Bottom: Example of micro-structured virtual staining applied to autofluorescence image of unstained kidney given user-defined staining matrix (adapted from Zhang *et al.* [64]).

specimens [122]. While most existing models use GAN-based architectures, Zhang *et al.* recently introduced a diffusion-based approach that performs super-resolution virtual staining from low-resolution autofluorescence images [68]. Their model outperformed GANs for 2×–5× resolution enhancement, however performance was comparable at native resolution.

While autofluorescence enables virtual staining across diverse tissue and stain types, its main limitation is the lack of nuclear contrast. Chromatin (DNA and RNA) has a very low quantum yield, with most of its excited-state relaxation occurring non-radiatively, meaning nuclei contribute little to the autofluorescent signal [27]. As a result, autofluorescence imaging does not directly capture nuclear morphology, which is a fundamental source of contrast in histology used to assess cellular organization, growth, proliferation, and disease state [10, 12, 11]. The absence of this signal means that virtual staining models need to infer nuclear features from surrounding structures, increasing the risk of hallucinated or misplaced nuclei. More broadly, autofluorescence represents only the radiative relaxation component of optical absorption, leaving out much of the biochemical information carried by non-radiative pathways.

Fluorescence Lifetime Imaging (FLIM): FLIM as a label-free method works by measuring the temporal decay of autofluorescence emissions from the excited state to the ground state following pulsed excitation. The fluorescence lifetime is independent of signal intensity but is highly sensitive to the surrounding tissue microenvironment [133, 134]. FLIM has been shown to reveal information about metabolic state, pH, ion concentration, and molecular interactions, providing insight into tissue composition and pathology [134, 28]. As such, FLIM has been widely applied in cancer diagnosis, metabolic imaging, and drug response monitoring across both research and clinical settings [134]. Overall, FLIM offers richer biochemical information and specificity for virtual staining and delivers more robust contrast than intensity-based autofluorescence.

Wang *et al.* used label free FLIM data of human lung adenocarcinoma tissue to generate virtual H&E images using a paired Pix2Pix style GAN trained on registered FLIM and brightfield histology images [28]. Their model incorporated the Deep Image Structure and Texture Similarity (DISTS) [135] perceptual loss to better preserve structural and textural fidelity in the reconstructed output. The work showed that incorporating the fluorescence lifetime dimension, rather than intensity images alone, improved virtual staining performance, particularly for reconstruction of macrophages and other immune cells. Using the resulting virtual H&E images, distinct lifetime signatures were identified for seven major cell types (tumor, fibroblast, lymphocyte, plasma cell, neutrophil, macrophage, and RBC). A result from this work can be see in Figure 2.12. The ability to generate an aligned virtual

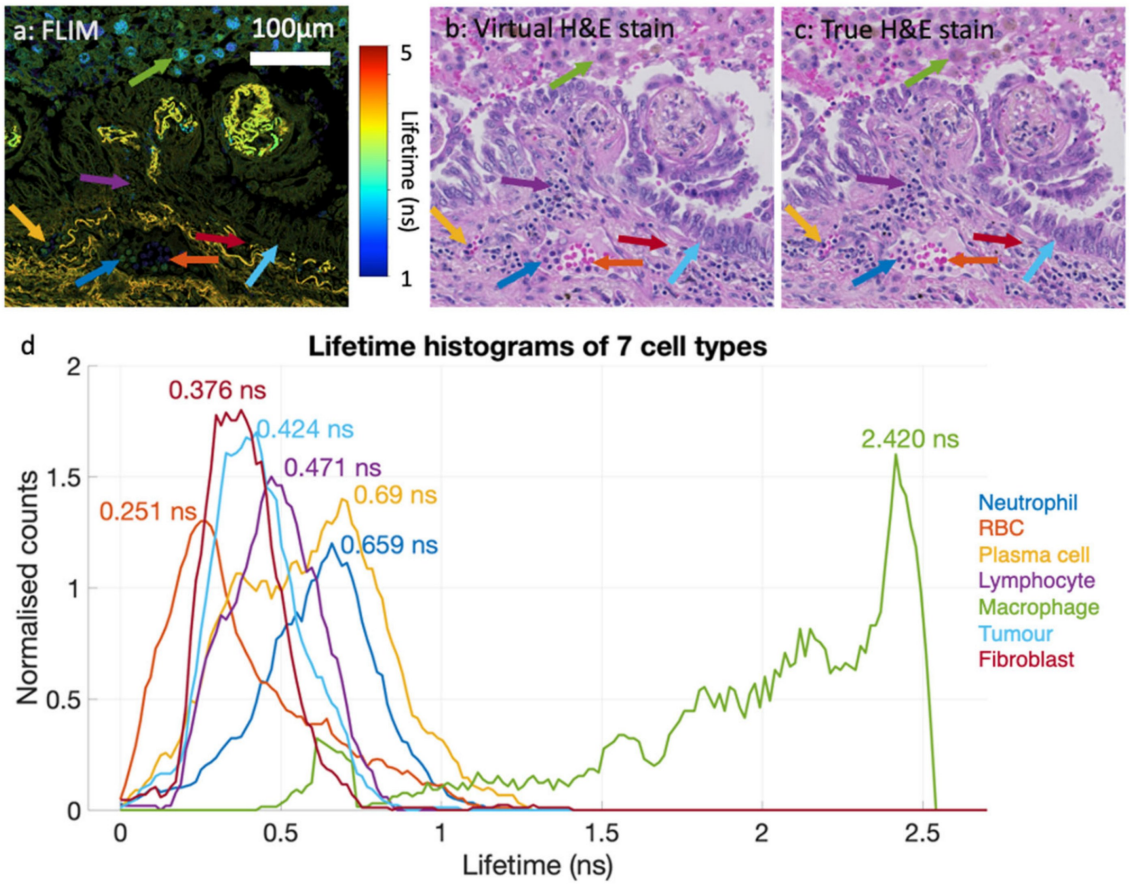

Figure 2.12: Example virtual H&E staining using FLIM microscopy of unstained cancerous lung tissue. Result shows seven distinct lifetime signatures of cellular components including tumours, lymphocytes, plasma cells, macrophages, neutrophils, fibroblasts, and RBCs (adapted from Wang *et al.* [28]).

H&E reference directly from the FLIM data helps facilitate interpretation of the lifetime data without the need for physical staining and the complexities of co-registering FLIM and histology images.

FLIM offers enhanced biomolecular specificity and outperforms intensity based autofluorescence. However, its major limitations are the complexity of acquisition and relatively longer imaging times compared to other methods. FLIM requires collection of sufficient photon statistics to estimate fluorescence decay lifetimes, typically necessitating multiple excitation events per pixel and therefore longer dwell times compared to PARS, which makes scaling to large tissue sections challenging. Additionally, similar to intensity based autofluorescence, it lacks direct nuclear contrast and captures only the radiative relaxation components of absorption.

2.2.4 Non-Radiative Absorption-Based Approaches

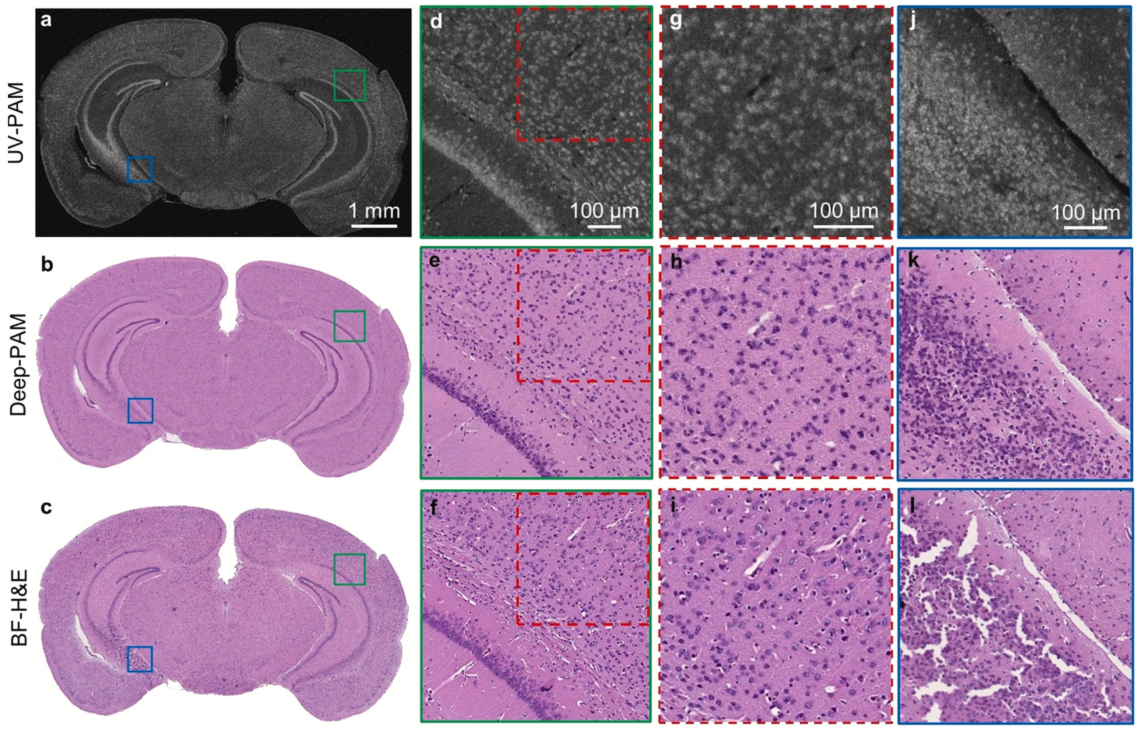

Figure 2.13: Comparison of the UV-PAM image and the Deep-PAM virtual H&E image with the corresponding brightfield H&E image of an FFPE mouse brain section (adapted from Kang *et al.* [125]).

Photoacoustic Microscopy (PAM): PAM is a non-radiative, absorption-based imaging modality that detects pressure waves generated by thermoelastic expansion following the absorption of pulsed excitation light [136]. Biomolecules that relax non-radiatively will deposit heat into the surrounding tissue, and when the excitation pulse is sufficiently short, the rapid thermal expansion will produces acoustic waves which can be detected via surface contact with a high-frequency ultrasound transducer. Photoacoustic Microscopy (PAM) is able to achieve high-resolution imaging at greater depths than conventional optical microscopy because ultrasonic scattering is much weaker than optical scattering. As well, it provides sensitivity to absorbers inaccessible to radiative or autofluorescence-based methods, including nuclear contrast through UV excitation of nucleic acids and other key biomolecules such as hemoglobin, melanin, lipids, and glucose [136]. As such, PAM offers complementary contrast for virtual staining.

Kang *et al.* presented one of the first demonstrations of virtual H&E staining using UV-PAM. In this work, results were demonstrated in mouse brain tissue in several formats, including deparaffinized FFPE sections, frozen sections, and fresh tissue embedded in agarose [125]. The model was trained using an unpaired CycleGAN-like network with an added SSIM loss between the input UV-PAM and virtual output (Deep-PAM) images to better constrain the transformation. An example from this work is shown in Figure 2.13, illustrating virtual H&E staining of deparaffinized FFPE mouse brain tissue and highlighting UV-PAM's ability to directly capture nuclear contrast through non-radiative absorption, a key advantage over autofluorescence-based methods which supports more accurate nuclear reconstruction in the virtual stain. Following this, Cao *et al.* applied a reflection-mode UV-PAM setup for label-free histology of bone tissue without sectioning [73]. An unsupervised CycleGAN model was trained to virtually stain the UV-PAM bone tissue images, improving pathologists' ability to distinguish cancerous features toward rapid intraoperative margin assessment. Another work by Yoon *et al.* demonstrated UV-PAM imaging of human liver specimens, integrating virtual staining, segmentation, and cancer vs. non-cancer classification within a unified framework [126].

In general, UV-PAM provides complementary non-radiative contrast which enables important nuclear visualization, an advantage over autofluorescence methods; however, it lacks sensitivity to many biomolecules that relax radiatively. Furthermore, it is limited by the complexity of the instrumentation, which requires optical and acoustic alignment, and the need for contact or physical coupling (via water or gel) between the sample and the ultrasonic transducer, which complicates preparation and reduces compatibility with standard slide-based histology workflows.

2.2.5 Nonlinear and Multimodal Methods

Nonlinear optical imaging techniques exploit higher-order light–matter interactions to generate intrinsic contrast in tissue. Examples include SHG and THG, SRS, CARS, MPF. These methods can highlight structural proteins (e.g., collagen via SHG [87]), molecular vibrations (via CARS [22] or SRS [21]), and intrinsic fluorophores (via MPF [20]) and in general they offer complementary contrast to the aforementioned linear scattering and absorption methods. Because they deliver distinct biochemical and structural information, multimodal and nonlinear imaging datasets are attractive for virtual staining.

A few groups have demonstrated virtual H&E staining using multimodal and nonlinear imaging techniques. Pradhan *et al.* combined CARS, SHG, and two-photon fluorescence to generate virtual H&E images of gastrointestinal tissue, comparing both supervised and unsupervised approaches [127]. Falahkheirkhah *et al.* employed SRS microscopy to acquire depth-resolved images of fresh-frozen prostate samples, training a paired model to convert the SRS data into frozen H&E images, followed by an unpaired model to translate from frozen to fresh H&E formats [128]. Building on this, Liu *et al.* developed an unsupervised virtual staining algorithm using SRS microscopy to generate virtual H&E images of fresh brain tissue, demonstrating that label-free SRS can achieve FFPE-like contrast without fixation or sectioning [129]. An example from this work is shown in Figure 2.14, where the virtual brain H&E is validated against the corresponding frozen-stained section. In another study, Borhani *et al.* combined two-photon microscopy and FLIM to produce virtual H&E images, showing that integrating both modalities provided complementary structural and functional contrast for more faithful reconstruction of the target stain [137].

Together, these studies highlight the potential of nonlinear and multimodal methods to provide both structural and biochemical specificity for virtual staining. While promising, such approaches are generally more complex to implement than linear absorption or scattering methods. Nonlinear optical interactions typically have cross-sections several orders of magnitude smaller than linear absorption processes, resulting in comparatively weak signal generation [138, 139, 140]. As a result, longer pixel dwell times, signal averaging, or specialized detection schemes (e.g., lock-in amplifier for SRS) are often required to achieve sufficient signal-to-noise ratios, which can limit acquisition speed when imaging large tissue areas.

2.2.6 Summary and Research Motivation

Overall, the label-free imaging methods discussed in this section each offer distinct forms of contrast and collectively demonstrate strong potential for virtual histology. Among these,

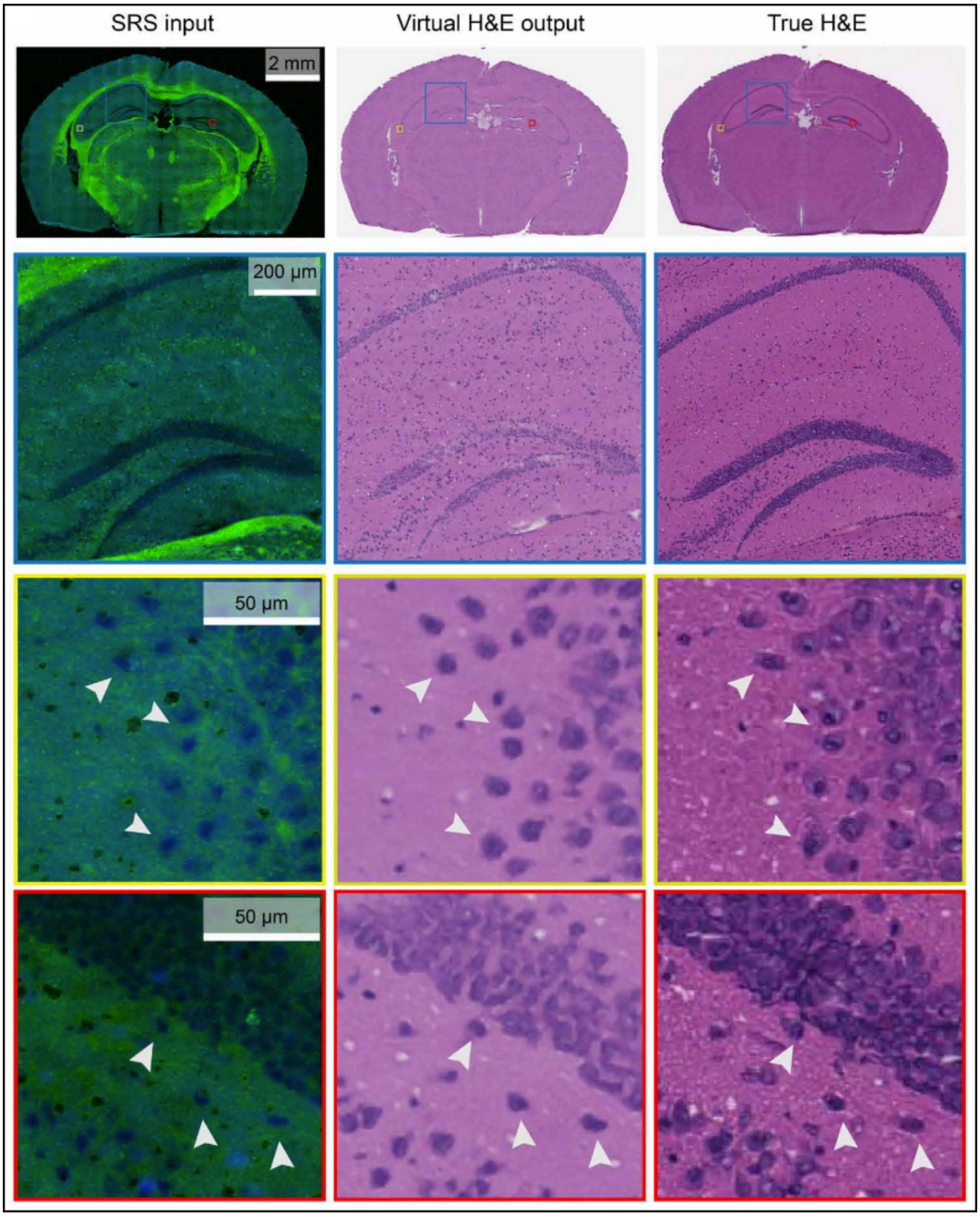

Figure 2.14: Example virtual H&E image of mouse brain using SRS input compared with chemical H&E of frozen tissue section (adapted from Liu *et al.* [129]).

linear absorption–based methods, particularly autofluorescence imaging, have emerged as the most developed and widely applied approaches for virtual staining, as they strike a practical balance between system complexity and biochemical contrast. Scattering-based methods are generally straightforward to implement but offer limited molecular specificity compared to absorption-based techniques. In contrast, nonlinear optical methods can provide highly selective contrast but require considerably more complex instrumentation and typically operate at slower imaging speeds. Consequently, linear absorption approaches represent a valuable middle ground, offering broad biochemical sensitivity with relatively low experimental complexity.

However, autofluorescence microscopy is unable to provide reliable nuclear contrast due to the low quantum yield of DNA [27], which is an essential feature for histological interpretation [10, 11, 12]. In addition to this limitation, these methods capture only the radiative relaxation component of absorption and miss the complementary non-radiative processes that carry additional biochemical information. While non-radiative absorption can be accessed through photoacoustic methods, these techniques introduce challenges due to their contact-based operation and, likewise, are unable to capture signals from biomolecules that relax through radiative pathways, thereby limiting the completeness of the resulting contrast. Consequently, the contrast in both techniques depends on the quantum yield of a given biomolecule.

For this reason, this thesis employs PARS microscopy, which addresses this limitation by simultaneously measuring signals from both radiative and non-radiative relaxation pathways following a single absorption event. This approach combines the biochemical contrast accessible to autofluorescence and photoacoustic modalities, enabling a more complete mapping of optical absorbers within the sample and improved contrast for virtual staining algorithms.

PARS microscopy nevertheless shares some practical considerations with other advanced optical imaging techniques, including the use of multiple co-aligned laser sources and point-by-point scanning. However, in contrast to nonlinear and lifetime-based approaches that often require signal averaging or multiple excitation events per pixel to accumulate sufficient photon statistics, PARS signals are generated from a single excitation event and can therefore be acquired with substantially shorter pixel dwell times. In practice, imaging speed is primarily constrained by the excitation pulse repetition rate and the scanning architecture. In the system presented in this work, imaging speed was limited by a 50 kHz excitation source and mechanical stage scanning; however, PARS implementations operating at MHz-scale repetition rates have been reported concurrent with this work [105], demonstrating the potential for significantly faster acquisition when appropriate scanning hardware is employed.

As detailed in Section 1.2, this thesis builds on recent developments in PARS microscopy to develop and validate a whole slide scanning PARS microscope and virtual staining workflow capable of emulating multiple histochemical stains from a single unstained tissue section.

Chapter 3

Automated Whole Slide Imaging for Label-Free Histology using PARS Microscopy

3.1 Introduction and Motivations

In this chapter, we present the first demonstration of an automated whole slide PARS imaging platform for histopathology. Building on prior PARS developments, this work advances the modality toward compatibility with standard pathology workflows, which require whole slide imaging capabilities in thin, transmissible tissue sections.

PARS has previously been applied in a variety of histology studies using 266 nm excitation to target nuclear contrast through DNA absorption and subsequent non-radiative relaxation [75, 76, 82]. Building on prior work, Ecclestone et al. in 2022 demonstrated a second-generation PARS architecture [32], capable of capturing radiative relaxation processes in addition to non-radiative and scattering contrast from a single excitation event. In this work, PARS demonstrated improved nuclear contrast through non-radiative absorption, while the newly introduced radiative channel provided complementary contrast from surrounding connective tissues structures, creating label-free images analogous to gold-standard H&E staining.

Despite this progress, current PARS embodiments lack whole slide imaging capabilities. Brightfield and fluorescent whole slide scanning microscopes represent the current gold standard in histology [8]. A critical functionality of these devices is their ability to capture

the entire tissue area, generating gigapixel-sized WSIs viewable at both low and high magnifications [8]. This multi-scale capability is essential for diagnosis, allowing pathologists to survey global tissue architecture and then drill into Regions of Interest (ROIs) [7, 141]. Moreover, reviewing the entire specimen enables identification of dispersed disease patterns and subtle abnormalities that would be missed when examining only isolated fields of view. As a result, WSI functionality is indispensable for any imaging modality intended for clinical histology.

The absence of WSI capabilities in current PARS systems severely limits their clinical applicability. Without seamless WSIs, PARS cannot be used to benchmark diagnostic performance or establish concordance with gold standards. Currently, the PARS field of view (FOV) is restricted (typically $0.5\,\text{mm} \times 0.5\,\text{mm}$) to ensure in-focus scans. Out-of-focus regions not only degrade resolution but also reduce the Signal-to-Noise Ratio (SNR) of the non-radiative channel, as the detection beam cannot effectively probe the excited volume. To cover larger areas, the system must compensate for variations in surface morphology and tilt across the tissue plane. At present, generating a whole slide PARS image requires manual focusing and mosaicing of hundreds of tiles (e.g., $\sim$400 for a $1\,\text{cm} \times 1\,\text{cm}$ sample). These manual steps are prohibitively time-consuming, introduce inconsistencies in focus, resolution, and SNR which compromise downstream image processing algorithms (e.g., virtual staining). Consequently, there is a pressing need for an automated whole slide PARS platform capable of producing diagnostic-quality images across entire tissue sections.

In addition to whole slide imaging, there is also motivation to modify the PARS optical design for the types of samples used in routine histology. Previous UV-PARS optical architectures have demonstrated proof-of-concept imaging across multiple formats, including fresh tissue samples, frozen sections, and FFPE tissue sections [82, 32]. However, these optical architectures are confined to reflection-mode operation to accommodate imaging of thicker samples. In contrast, the clinical gold standard for pathology is thinly sliced FFPE tissue sections. These sections are thin and allow for transmission imaging, which offers several advantages over reflection designs, including stronger forward-scattered signal (i.e., improved SNR) and reduced susceptibility to surface artifacts. This approach also aligns more closely with the operating principles of transmission brightfield whole slide scanners routinely used in clinical practice.

3.1.1 Study Overview and Contributions

The PARS whole slide scanning workflow introduced in this study uses all three PARS contrasts, with the scattering channel playing a crucial role in enabling the acquisition

of in-focus, high quality images across an entire tissue sample. Samples are automatically scanned in parts and precision focus is achieved for each section using an autofocusing algorithm. This strategy ensures the maintenance of accurate focus across the entire sample. The individually scanned sections are then seamlessly stitched together using a novel contrast levelling algorithm, forming a comprehensive WSI. Additionally, the study demonstrates the first whole slide virtual H&E staining of PARS images, achieved using the previously published Pix2Pix-based framework [33]. To reinforce the visual similarities between the PARS and H&E WSIs, a feature-based quantitative comparison between the modalities was performed, wherein nuclear features such as nuclear count, area, and eccentricity were compared. Furthermore, a Multi-Scale Structural Similarity Index Measure (MS-SSIM) was used to compare the virtual and real H&E WSI pairs at increasing pathology magnifications.

In addition to this WSI workflow, a transmission PARS optical architecture was introduced that takes advantage of forward scattering in thin, transmissible samples. A free-space, non-confocal detection pathway was implemented to capture forward scattered light and radiative emissions from the entire depth of the thin tissue sections. A spectral filter was added to separate the forward detection beam and radiative emission spectrum. Beam samplers were incorporated into the PARS optical system to measure incident detection power and excitation pulse energies. These measurements enabled image noise reduction by correcting for power instabilities during imaging.

These optical refinements facilitate histology-like label-free whole slide imaging and, importantly, allow for a significant reduction in detection powers and UV excitation energy compared to recent PARS histology implementations [106, 107]. With these reduced powers, the unstained tissue sections remain unaltered and available for subsequent standard histochemical staining, enabling both PARS and H&E WSIs to be acquired from the same tissue section in malignant human breast and skin samples. This ability to obtain one-to-one WSIs of both modalities is crucial for benchmarking diagnostic performance and concordance with gold standards.

Overall, the WSIs presented here allow for examination of tissue structures at resolutions sufficient for the recovery of diagnostically relevant subcellular details. Crucially, they provide pathologists with the necessary magnification range (up to 40×) to allow for comprehensive analysis of entire tissue samples, at both low and high magnifications, for informed and accurate diagnosis. The label-free slide images exhibit contrasts analogous to gold standard H&E stained slides and are viewable using the same or similar existing digital pathology tools.

3.2 Methods

3.2.1 PARS Histology System Architecture

The PARS histology imaging system architecture is shown in Figure 3.1. For the excitation laser, a 50 kHz 400 ps pulsed 266 nm UV laser (Wedge XF 266, RPMC) was chosen. This excitation wavelength is used to target the optical absorption of DNA, facilitating label-free nuclear contrast through non-radiative relaxation [142]. Additionally, it offers contrast for various structures of the ECM through the radiative relaxation process [17], [69], [70].

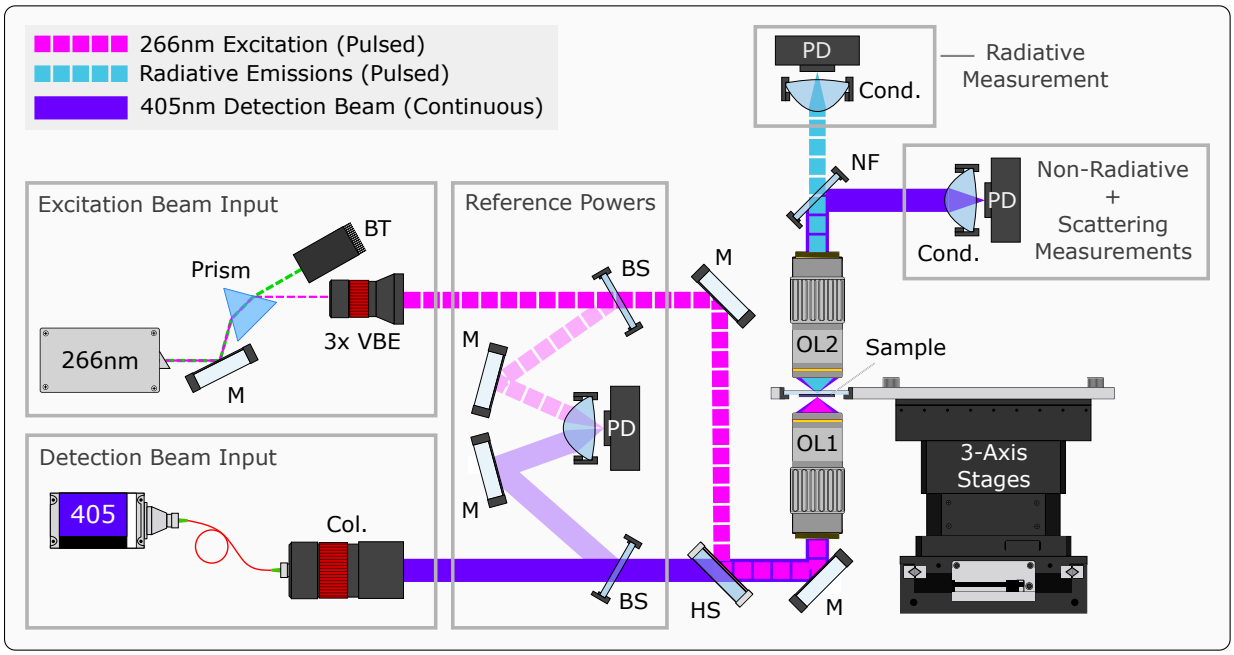

Figure 3.1: Simplified PARS histology optical architecture. Component labels are defined as follows: mirror, *M*; Nd:YAG Harmonic Separator, *HS*; variable beam expander, *VBE*; collimator, *Col.*; condenser lens, *Cond.*; notch filter, *NF*; beam sampler, *BS*; photodiode, PD; objective lens, OL; beam trap, *BT*.

At the output of the 266 nm source, a CaF_2 prism (Prism: PS862, Thorlabs) is used to remove residual 532 nm light and send it to a beam trap (BT: BT610, Thorlabs). The UV beam is then expanded (VBE: BE03-266, Thorlabs) and combined with the detection pathway using a long-pass dichroic mirror (DM: 37-721, Edmund optics).

For the detection path, a continuous wave 405 nm laser (OBIS-LS 405, Coherent), first reported in [32], was chosen. The 405 nm wavelength tightly overlaps with the excitation

source focus spot, enabling effective probing of the excited area [32]. Furthermore, the 405 nm wavelength has good chromatic compatibility with the UV excitation source. The output of the fiber-coupled detection source is collimated (Col: C40APC-A, Thorlabs) and then directed through the dichroic mirror to join the UV beam.

The co-aligned detection and excitation beams are then focused onto the sample with a 0.42 Numerical Aperture (NA) UV objective lens (OL1: NPAL-50-UV-YSTF, OptoSigma). The transmitted detection light and forward emissions from the radiative relaxation process are collected using a 0.7 NA objective lens (OL2: 278-806-3, Mitutoyo) and then separated with a 405 nm notch filter (SF: NF405-13, Thorlabs). The detection intensity modulations and radiative emissions are then each recorded on an avalanche photodiode (PD: APD130A2) following condenser lenses (Cond: ACL25416 U-A, Thorlabs). Prior to excitation and detection co-alignment, beam samplers (BSF10-UV/A, Thorlabs) are used to sample a portion of both the detection power and excitation pulse energy for reference and post-acquisition correction purposes. Based on the Abbe diffraction-limited resolution, Full Width Half Maximum (FWHM) of the focused beam waist, the 266 nm radiative and non-radiative channels exhibit approximate lateral and axial resolutions of 316.7 nm and 3.02 μm, respectively. The 405 nm scattering channel exhibits corresponding lateral and axial resolutions of approximately 482.1 nm and 4.59 μm.

3.2.2 Whole Slide Scanning Workflow

The PARS histology system first captures a preview image of the whole slide to allow the user to trace a border around the entire sample or draw a smaller ROI. These ROI coordinates are mapped to mechanical stage positions to inform the scanning algorithm of the tissue boundaries. To calibrate the mapping between the preview image's pixel coordinates and the stage coordinates, images of a USAF resolution target are captured from both the preview camera and the PARS system. Alignment points between the images are used to determine a linear transform between the two coordinate spaces.

The optimal focus plane must be maintained across the entire sample in order to acquire consistent high quality raw data. To do so, the selected area is split into smaller (typically 0.5 mm^2) square sections (S_n) as shown in Figure 3.2(a). Before scanning each section, the axial (z) stage is adjusted to pinpoint the sharpest imaging plane. This involves scanning a small portion of the section across depth and assessing sharpness using the Tenengrad focus measure. Once the optimal position is identified, the entire section is scanned at this axial depth. With this approach, the system is able to compensate for variances in the sample's surface morphology and is robust to any tilt in the sample and scanning plane.

Some sections positioned at the edge of the sample may cover more glass area than tissue area. This may cause the optimal focus to skew towards particles on the glass surface rather than tissue layer. As such, these sections are flagged (blue in Figure 3.2(a)) and will be scanned at the optimal focus of the closest adjacent section with sufficient tissue coverage (red in Figure 3.2(a)).

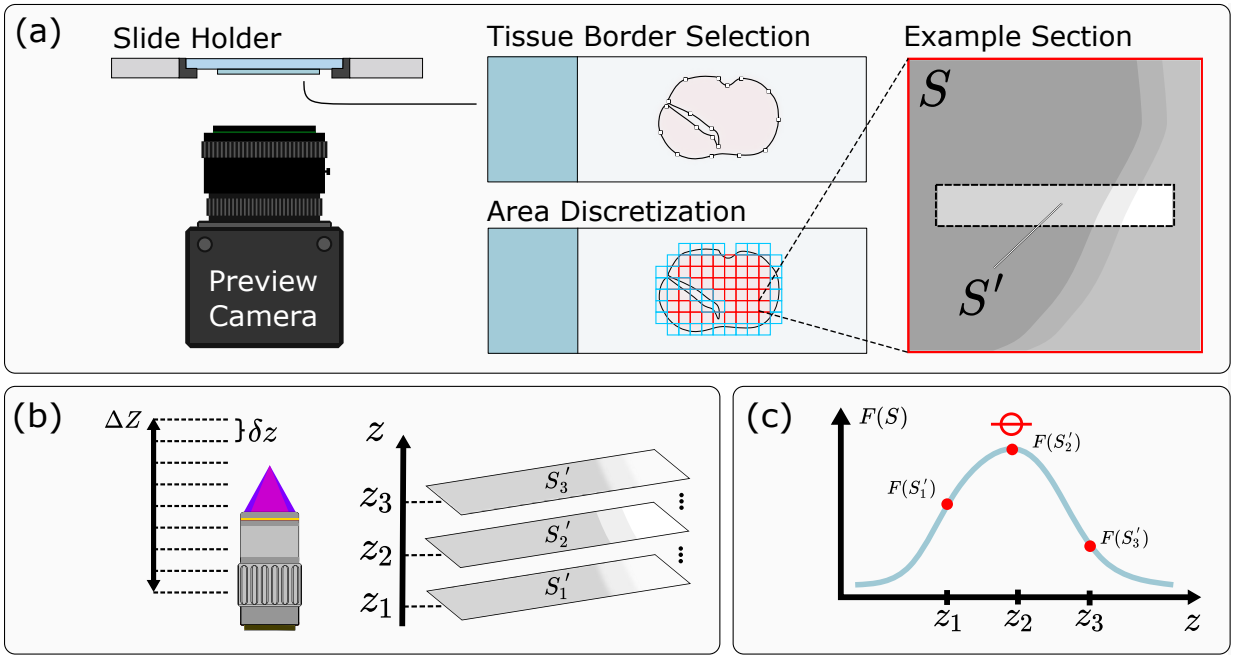

Figure 3.2: Overview of the PARS whole slide scanning workflow. (a) A preview camera is used to capture an image of the slide so the tissue border can be selected, and its area split into small sections, each to be independently scanned. (b) Before imaging S_n, scattering images of subset S'_n are taken across a depth ΔZ at a step size δz. (c) A relative focus metric is plotted for each scattering image from (b), and an optimal focus metric is determined.

3.2.3 Focus Criterion Function and Autofocus Algorithm

To find the optimal plane of focus for each section, a small sampling of the section area (S'_n) is imaged multiple times across a depth of ΔZ at step sizes of δz, as shown in Figure 3.2(b). With a smaller step size (δz), the selected maximum focus will better approximate the exact peak location. With a greater search depth (ΔZ), a larger focal shift can be accommodated between neighbouring sections. In this study, the search depth (ΔZ) was set at 4.5 μm, which is both close to the thickness of the tissue sections ($\sim$5 μm) and the

Abbe theoretical axial resolution (∼4.591 μm) for the 405 nm detection beam and 0.42 NA objective lens. The step size (δz) was set to 0.5 μm to provide sufficient step resolution to approximate the peak. While finer step sizes could be set, it would significantly increase autofocusing time with minimal benefit. Overall, with these selected values, each autofocus search required a total of N=10 focus points (0 μm to 4.5 μm inclusive).

For the subsections imaged across depth, the detection beam alone is sufficient for finding peak focus for all image channels (scattering, radiative and non-radiative). The Tenengrad focus criterion function is then used to evaluate the relative sharpness of the scattering images acquired across depth. The Tenengrad function was chosen because it provides a sharp peak for fine focusing and is relatively noise robust [143]. It first computes the horizontal (G_x) and vertical gradients (G_y) of an input image (I) at point (x, y) using the Sobel kernels:

$$G_x = \begin{bmatrix} 1 & 0 & -1 \\ 2 & 0 & -2 \\ 1 & 0 & -1 \end{bmatrix} * I \quad and \quad G_x = \begin{bmatrix} 1 & 2 & 1 \\ 0 & 0 & 0 \\ -1 & -2 & -1 \end{bmatrix} * I \tag{3.1}$$

From here the gradient magnitude, $G(x, y)$, is computed:

$$G(x, y) = \sqrt{G_x^2(x, y) + G_y^2(x, y)} \tag{3.2}$$

The focus criterion function, $F(I)$, is then evaluated as the sum of squared gradient magnitude values which exceed a given threshold T:

$$F(I) = \sum_x \sum_y [G(x, y)]^2 \tag{3.3}$$

The Tenengrad function quantifies the magnitude of the edges present in the scene. Across depth, it will produce a plot similar to Figure 3.2(c), with a single peak which monotonically decreases as the sample moves above or below this point. At the beginning of the whole slide scan, a coarse focus search is deployed over a large range to determine a rough starting point for the slide. Following this, subsequent section foci are found by quadratically interpolating the evaluated depth stack (N=10) centered at the optimal focus point of the closest neighbouring section. The computation time for the Tenengrad function depends on the size of the evaluated image. Here the subsections (S_n') are 0.5 mm x 15 μm or 3 % of the full 0.5 mm x 0.5 mm section area. For this size, the Tenengrad function takes ∼5 ms per depth scan or 0.05 s across all 10 depth scans.

3.2.4 Section Scanning and Image Reconstruction

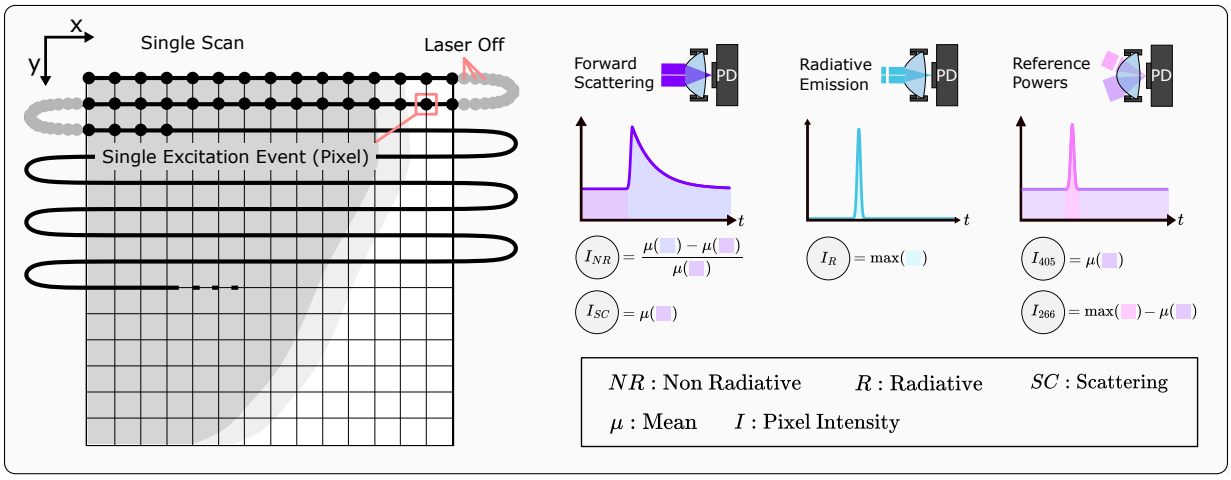

Figure 3.3: Illustration of the 'snake'-like stage scanning pattern for a single section of the WSI. Time-series data from each system photodiode is compressed to into scalar pixel intensity values for each image contrast.

During imaging, mechanical stages continually move the sample over the objective lens in an 's' or 'snake'-like scan pattern. Sample points are spaced out laterally to achieve the desired 40× equivalent magnification (∼250 nm/pixel). At each excitation event, a high-speed digitizer (CSE1442, RZE-004-200, Gage Applied) captures the stage position information as well as ∼500 ns of time resolved data from each system photodiode. These signals are then compressed into single amplitude values for the non-radiative, radiative, and scattering image channels. In addition, the 266 nm excitation pulse energy and 405 nm detection power are also simultaneously collected at this location. To form the non-radiative, radiative, and scattering images, the raw data points are arranged as pixels on a cartesian grid based on their stage position. The radiative and non-radiative images are then power corrected using the 266 nm pulse energy measurement. Similarly, the scattering image is power corrected using the 405 nm detection power measurement.

3.2.5 Whole Slide Stitching and Contrast levelling Algorithm

After all sections are scanned, they can be stitched together into a WSI using their relative stage positions. However, prior to stitching, a contrast and brightness levelling algorithm is needed to blend the shading differences between adjacent sections. The algorithm is two

part, consisting of a bulk levelling stage (Figure 3.4(a)) and gradient levelling stage (Figure 3.4(b)). Both parts use a small amount of overlap (∼100 pixels per direction) between sections to help with the blending. The bulk levelling algorithm brings all sections into the same overall brightness and contrast range while the gradient levelling algorithm blends the sharp transitions between sections due mismatched gradients of illuminations.

In bulk levelling, the inner and outer overlap areas are used to determine a transform ($T_{\mu\sigma_{o/i}}$) to level the inner section. This transform is based on the mean and standard deviation of the inner (μ_i, σ_i) and outer overlap pixels (μ_o), σ_o).

$$S_{LVL} = T_{\mu\sigma_{o/i}}(S) = \frac{\sigma_o}{\sigma_i} * (S - \mu_i) + \mu_o \tag{3.4}$$

Equation 3.4 scales the inner section's pixel intensity spread to better match the outer section based on the ratio of the outer and inner overlap standard deviations. It then shifts the average pixel intensity of the inner section (S) to the average pixel intensity of the outer section overlap. This is then repeated for every section in the WSI before moving on to the gradient levelling algorithm. For gradient levelling, a kernel with a size equal to the overlap, computes a local mean and standard deviation value at each point along the inner and outer overlaps. Values in non-overlap locations are interpolated using values from surrounding overlap areas. These local statistic values are used to create a point transform, $T_{\mu\sigma_{i/o}}(x, y)$, which has the same form as equation 3.4 but varies at each pixel location. The transform values are then gaussian blurred and applied to the inner section. This is then repeated for every section in the WSI. In some cases, the bulk or gradient levelling algorithm may be repeated more than once until the mosaic artifacts are corrected.

3.2.6 Quantitative Analysis of Image Similarity

To quantitatively compare the similarity between the PARS and H&E images, nuclear features, including nuclei count, nuclear area, and nuclear eccentricity were computed. The nuclear features were extracted from N=1793 PARS and H&E sample pairs (each of size 512×512 pixels) sourced from the skin and breast whole slide tissue samples used in this study. Nuclear segmentation was performed in each image type using the StartDist python library [144]. For the PARS images, nuclear segmentation was done on the non-radiative channel, which primarily highlights nuclear structures. For the brightfield H&E images, a colour deconvolution algorithm [145] was first used to isolate the hematoxylin channel and facilitate nuclear segmentation. The hematoxylin channel was then inverted, and

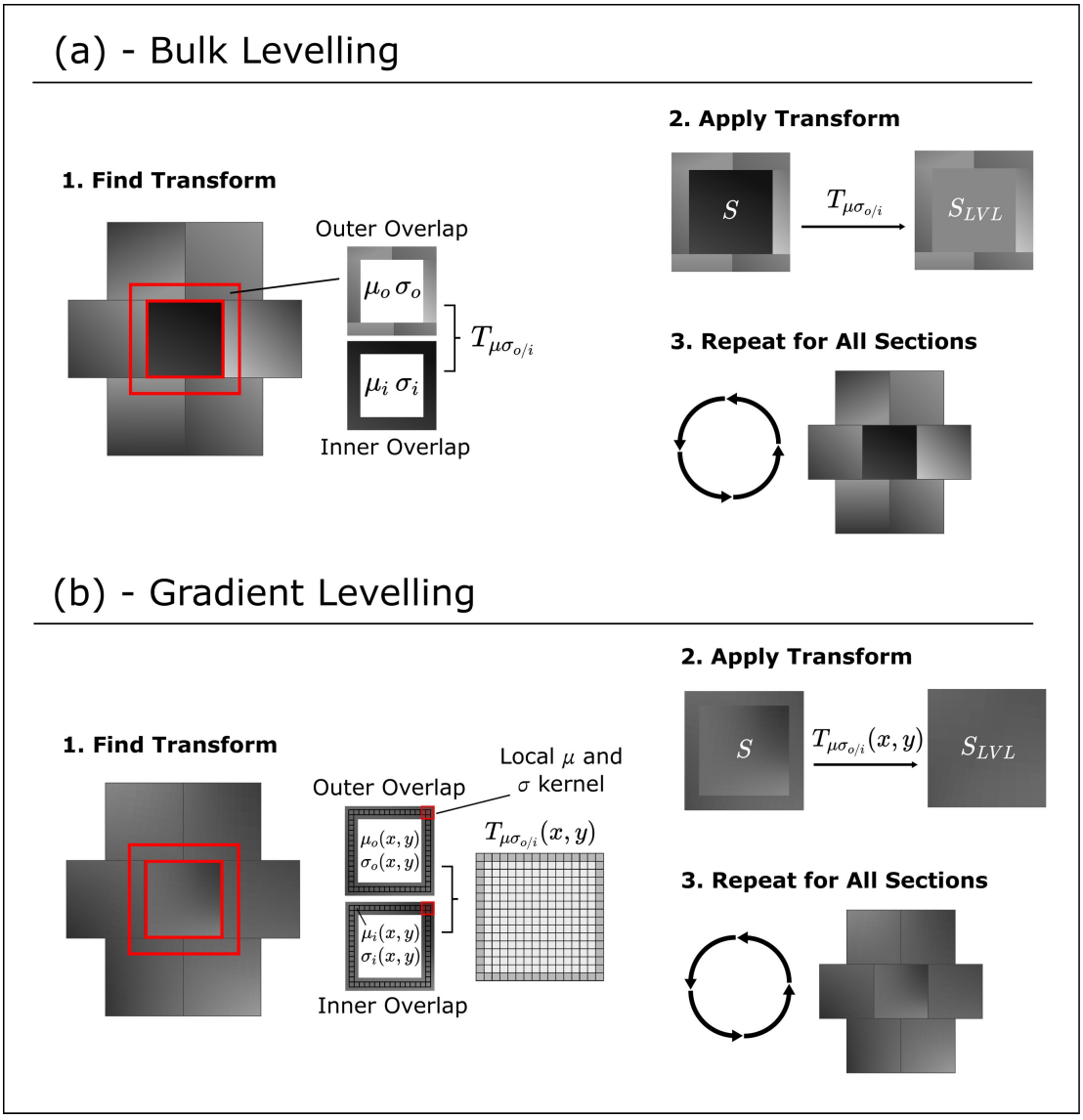

Figure 3.4: Illustration of the two-part algorithm used to level and blend the contrast and shading between sections. (a) Bulk levelling algorithm aims to bring all sections into the same general contrast range. Here a single transform ($T_{\mu\sigma_{o/i}}$) for the entire inner section is derived based on the overlap area between the inner and outer sections. (b) A gradient levelling algorithm aimed at continuously blending the boundaries between neighboring sections. Here a point transform ($T_{\mu\sigma_{o/i}}(x,y)$) for the inner section is derived based on a comparison between the local statistics of the grayscale values of inner and outer overlap regions.

contrast enhanced by rescaling pixel intensities. The minimum and maximum threshold bounds for this rescaling were determined manually for each WSI. The nuclei count, average nuclear area, and average nuclear eccentricity were then extracted from the 512×512 pixel segmentation maps using the *regionprops* function from the skimage Python library.

This same feature-based evaluation was applied to compare the virtual and real H&E WSI pair (N=383). Additionally, the MS-SSIM was employed as a pixel-level quantitative measure of agreement. Following the methodology in [107], RGB images were converted to the YC_bC_r colour space, and the MS-SSIM metric was computed for each channel and summed together with the following weights: 0.8 (Y), 0.1 (C_b), and 0.1 (C_r). This process was performed for the native PARS 40× magnification and was repeated for 20x, 10x, and 5x equivalent viewing magnifications. These lower magnifications were achieved by low pass filtering the original image pairs. For the pixel wise alignment, the WSIs were registered using an affine transformation.

3.2.7 Sample Preparation

In this study, a variety of unstained paraffin embedded human skin and breast tissue sections were imaged on glass microscope slides. Figure 3.5 outlines the steps involved in preparing the samples for PARS imaging. Fresh tissue samples are first excised and placed in a formalin fixative solution within 20 minutes of excision. The samples are fixed for a period of 24 to 48 hours and subsequently dehydrated following exposure to ethanol. After removing water from the specimen, xylene is used to clear the tissue, eliminating any remaining ethanol and residual fats in preparation for wax infiltration. The specimen is then placed in liquid paraffin at 60°C where it is thoroughly infiltrated with wax. The tissue samples are then embedded in a paraffin block, creating standard FFPE blocks. Using a microtome, thin tissue sections ($\sim$4-5 μm) are sliced from the FFPE block surface and placed onto glass microscope slides. The tissue slides are then baked at 60°C for $\sim$60 minutes to remove excess paraffin prior to imaging with the PARS system. Following PARS imaging the exact same tissue sections were stained with H&E and imaged at 40× magnification using a standard brightfield microscope (MorphoLens 1). This provided a direct one to one comparison between the PARS image data and the gold standard H&E stain.

Tissues were provided by clinical collaborators at the Cross-Cancer Institute (Edmonton, Alberta, Canada) from anonymous patient donors with all patient identification removed from the samples. Samples were archival tissues no longer required for patient diagnostic and thus patient consent was waived by the ethics committee. No information

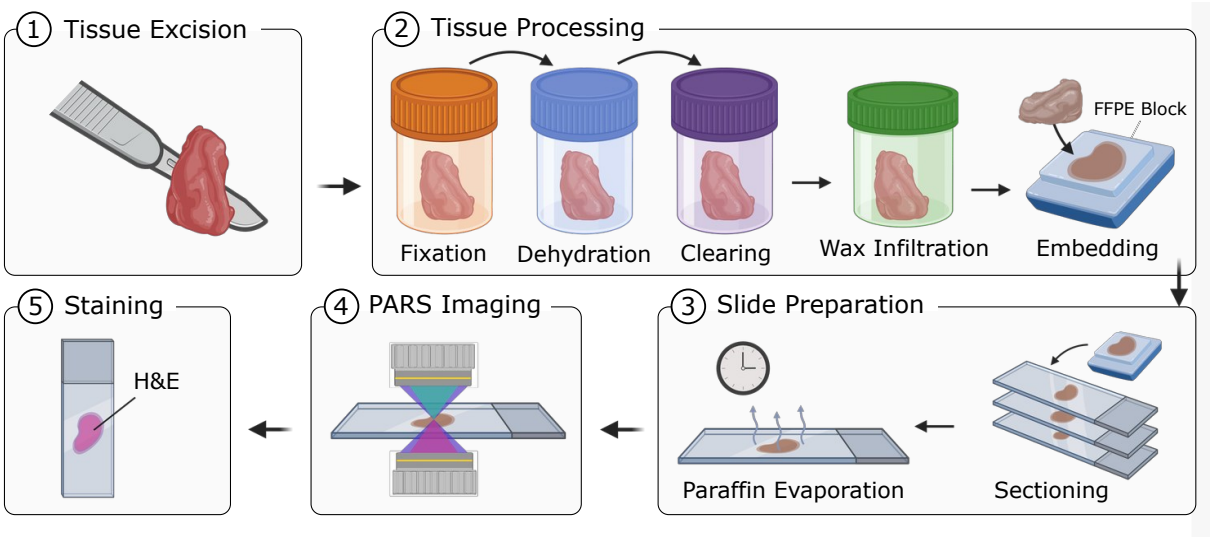

Figure 3.5: Overview of the sample preparation workflow: Fresh tissue samples are first excised, processed into FFPE blocks, prepared onto microscope slides, imaged using PARS, and subsequently stained with H&E. Created with BioRender.com

was provided to the researchers about the patient identity. Samples were collected under protocols approved by the Research Ethics Board of Alberta (Protocol ID: HREBA.CC-18-0277) and the University of Waterloo Health Research Ethics Committee (Photoacoustic Remote Sensing Microscopy of Surgical Resection, Needle Biopsy, and Pathology Specimens; Protocol ID: 40275). All human tissue experiments were conducted in accordance with the government of Canada guidelines and regulations, such as "Ethical Conduct for Research Involving Humans (TCPS 2)".

3.3 Results and Discussion

3.3.1 System Improvements and Power Correction

The PARS optical architecture presented here has been designed for whole slide imaging of thin, transmissible samples. As such, we have added a high 0.7 NA secondary objective lens overtop the sample to capture and take advantage of the stronger forward 405 nm detection scattering. As well, the free-space, non-confocal detection scheme, following the secondary objective lens, allows us to capture the forward scattered light and radiative signal from the entire depth of the sample. The stronger forward scattering allows for lower

detection power while maintaining similar recovery of the modulated detection signal from the non-radiative relaxation process. Specifically, in this configuration, the detection power incident on the sample during an acquisition was in the range of ∼2-5 μW compared to the previously reported value of 156 μW [32]. In addition, the pulse energies from UV source were in the range of 150-200pJ compared to the 5nJ excitation energies used in the most recent UV-PARS histology system [106], [107]. These pulse energies and detection powers permit standard H&E staining and clinical diagnosis following PARS imaging without any visual damage to the sample.

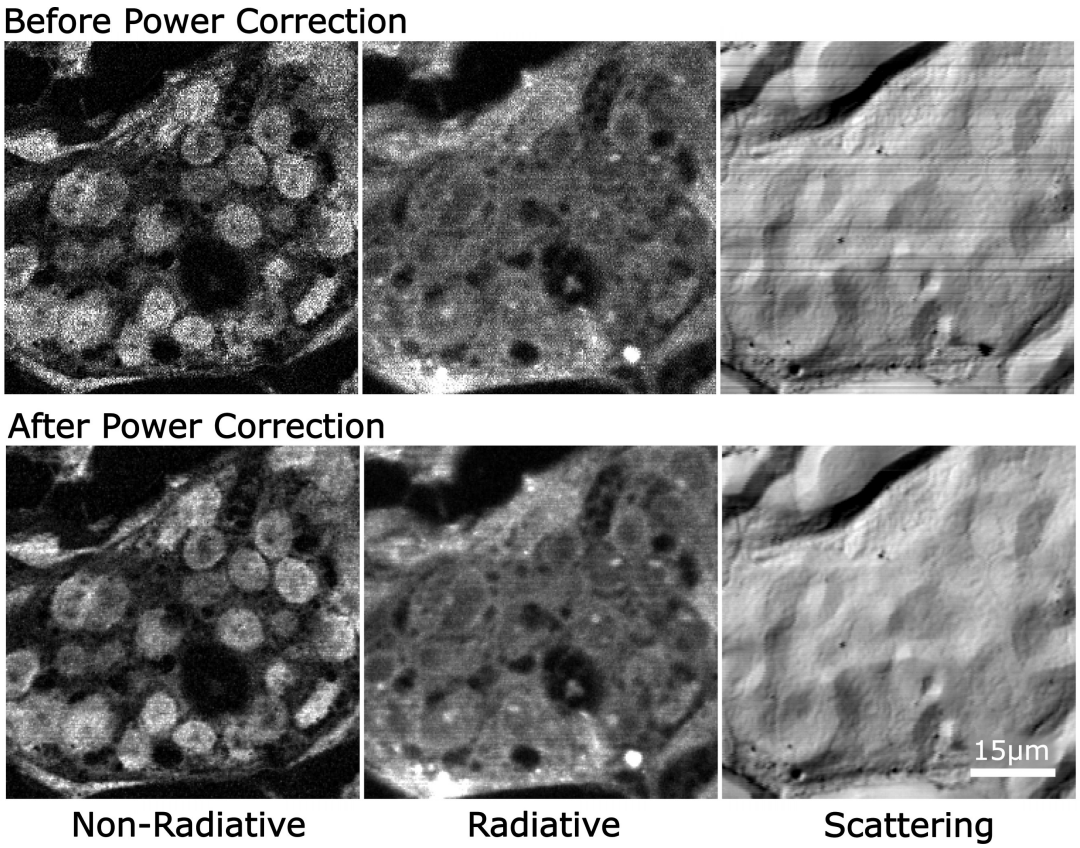

Figure 3.6: Non-radiative, radiative, and scattering label-free PARS image contrasts before and after correction from the measured reference power, demonstrated on a cluster of cell nuclei.

Separation of the 266 nm UV excitation pulse is not required in the forward path as it is absorbed by the borosilicate glass slide. For the radiative relaxation pathway, a 405 nm notch filter has been added to spectrally separate the forward detection path from the radiative emission spectrum. Another important addition to the system were the beam

samplers used to record the excitation pulse energy and detection power as the samples were point scanned. Figure 3.6 highlights improvements in image quality for the non-radiative, radiative, and scattering channels after power compensating the images. In the non-radiative and radiative image channels, each pixel is derived from a single excitation event. As such, pulse energy variability directly produces proportional fluctuations in absorbed energy, which manifest as pixel-to-pixel intensity variations. In this system, the excitation pulse energy exhibited a standard deviation of approximately 77 pJ for mean pulse energies of 150–200 pJ (40–50% relative variation). Because each pixel is derived from a single excitation event, these fluctuations appear as grain-like noise. This effect is not attributable to coherent optical speckle, as the non-radiative signal depends on absorbed energy rather than interference of coherent scattered fields. Furthermore, the noise pattern follows scan order and excitation variability rather than underlying sample microstructure. After compensating each pixel using the recorded pulse energy measurements, the grain-like texture is largely suppressed, supporting pulse energy instability as the dominant source.

In the case of the scattering image, which are collected with a continuous wave laser, power instabilities result in slow varying intensity streaks as the sample is scanned. The non-radiative and radiative resolutions here are measured at ∼400 nm (FWHM), which roughly corresponds to standard 40× magnification in standard histopathology [47]. By using the collected excitation pulse energy and detection power measurements these artifacts can largely be removed and the 40× magnification is well maintained. Furthermore, power compensation in the detection scattering image allowed for more robust focus finding algorithm, which was important for the automated whole slide scanning reported here.

3.3.2 Sample Autofocusing and Whole Slide Stitching

In the ideal case, the highest SNR and in-focus non-radiative and radiative acquisitions occurs at the optimal focus point of the detection beam. This way, the detection beam alone can be relied on for focus finding and the sample need not be exposed multiple times to UV excitation. To accomplish this, the optimal scattering focus is first determined using the methods described in section 3.2.3. At this peak focus, the excitation spot is moved to the optimal axial position where the largest refractive index modulation is observed. Following this axial alignment strategy, a tight correspondence between the detection focus and peak SNR of the non-radiative channel can be seen in Figure 3.7(a). Here a series of scattering images are acquired across a ± 35 μm depth range at 1 μm steps. The SNR is also evaluated for a series of non-radiative images captured over a ± 18 μm range at 1 μm steps. Figure 3.7(b) shows a stack of non-radiative images captured at and on either side (±1.5 μm and 3 μm) of the peak detection focus. Clear visual degradation of the non-radiative channel

can be seen with scans taken on either side of the focus spot, which corresponds well with the sharp SNR drop on either side of the focus. Overall, Figure 3.7 emphasizes and confirms the importance of maintaining focus across the entire sample. For this reason, the WSIs are captured in discrete in-focus sections which are stitched back together.

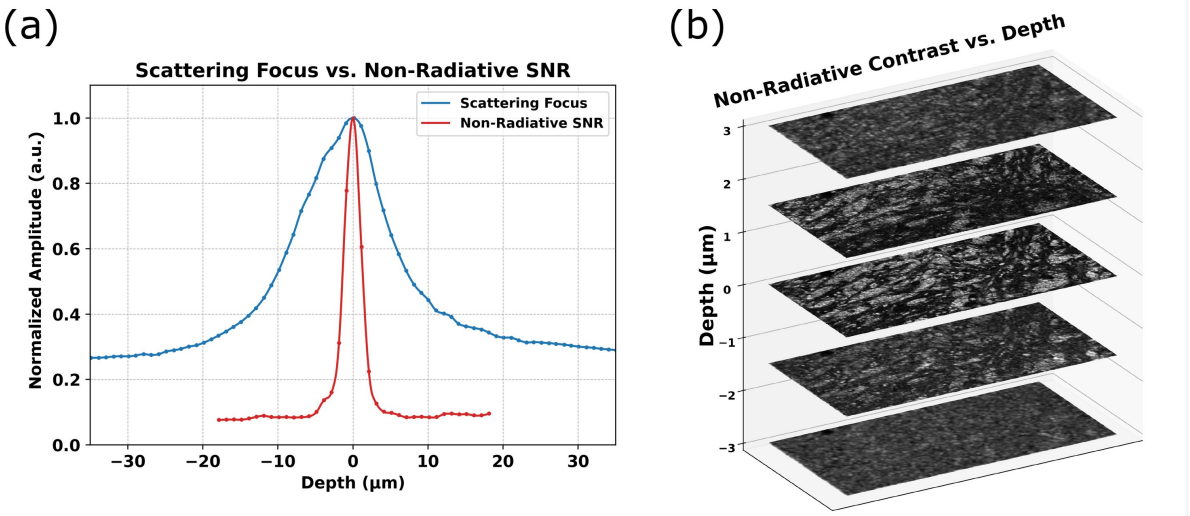

Figure 3.7: Relationship between scattering focus and the non-radiative image SNR. (a) Plot of the scattering focus across depth (blue) compared with non-radiative images SNR across depth (red). Each curve is independently normalized to its maximum value to enable relative comparison of focal trends. (b) Visualizations of non-radiative contrast quality across a $\pm\,3\,\mu$m depth.

However, the final stitched WSI often contains tiling artifacts between the edges of the sections. This arises from subtle variations in tissue surface height and morphology across the slide. Although the autofocus routine determines an optimal focal plane for each section, histological samples are not perfectly planar and may exhibit local thickness variations, folds, or compression artifacts. Because the system has a finite depth of field, small axial deviations from the optimal focus reduce collection efficiency and scattering amplitude, leading to slight intensity differences between independently acquired sections. When these sections are stitched together, these focus-dependent intensity variations manifest as visible tiling artifacts. These artifacts can be corrected using the contrast levelling algorithm discussed in section 3.2.5, allowing for better image interpretation. Figure 3.8 shows whole slide scattering images of a small breast tissue section ($\sim 3.5 \times 1.2\,\mathrm{mm}^2$) before and after the bulk and gradient levelling algorithms.

Figure 3.8(a) provides an example of the raw (pre-leveled) stitched WSI. In this raw

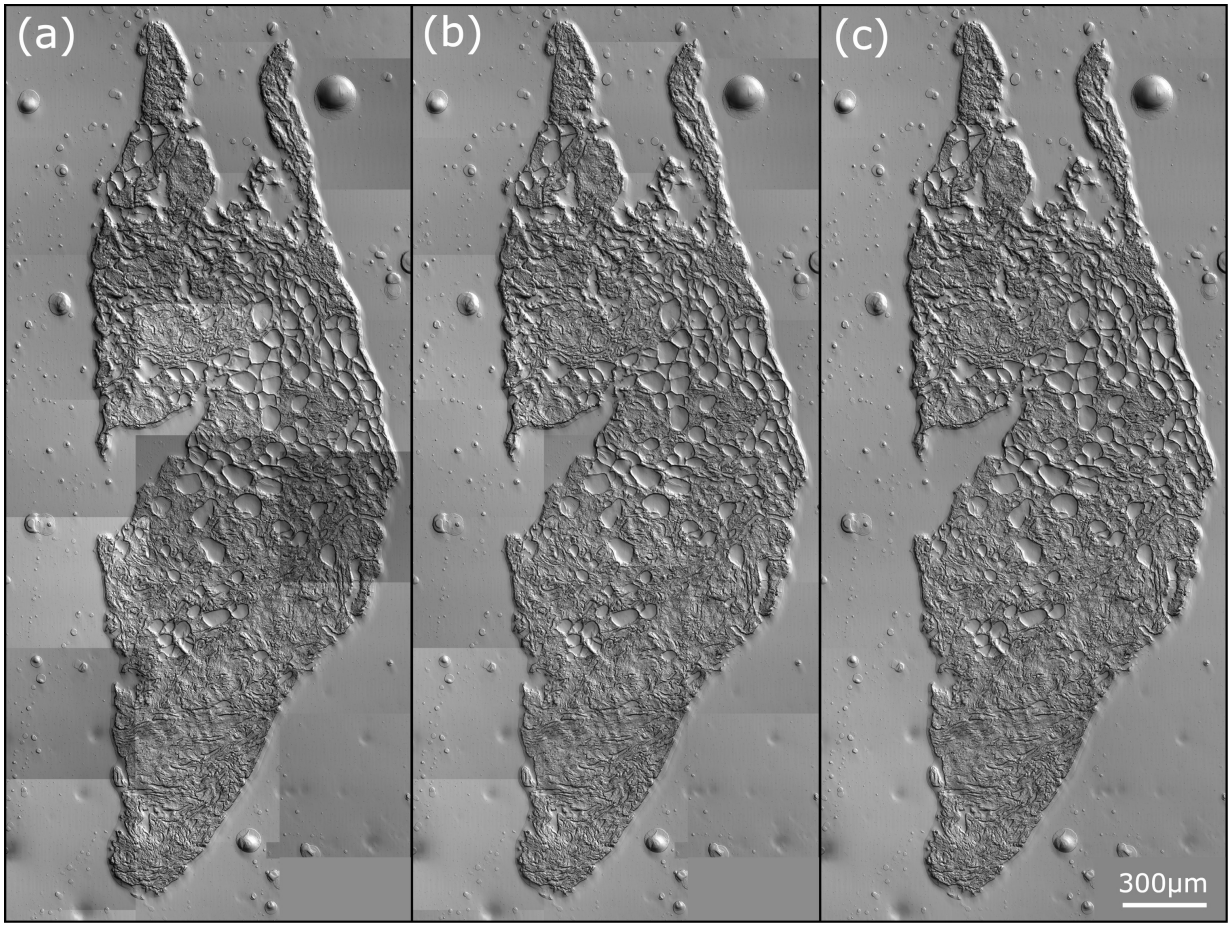

Figure 3.8: Whole slide scattering image at each stage of the brightness levelling algorithm. (a) Shows the raw stitched scattering image before levelling sections. (b) Shows the stitched scattering image after bulk levelling. (c) Shows the stitched scattering image after both bulk levelling and gradient levelling.

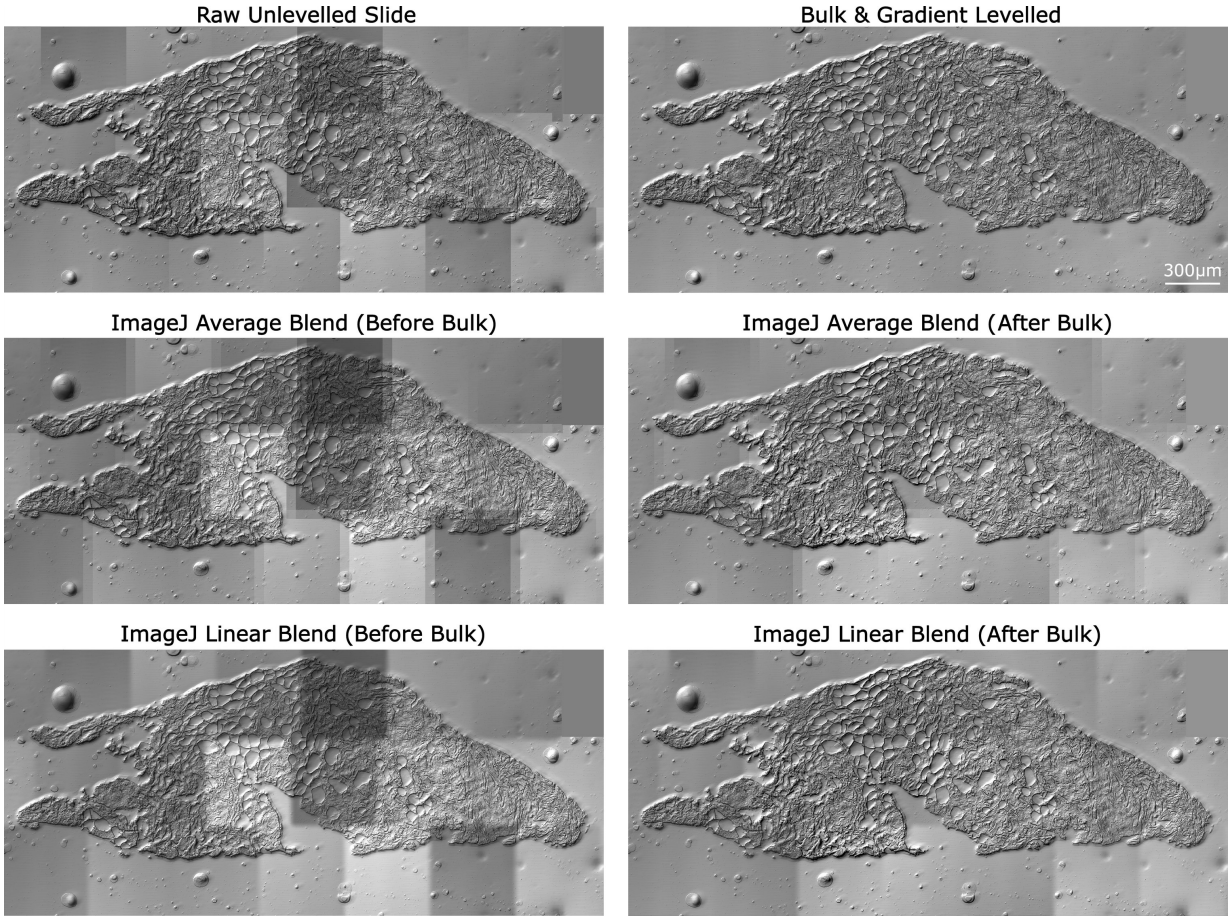

Figure 3.9: Comparison between the proposed contrast levelling algorithm and the ImageJ stitching plugins. Both the average blend and linear blend options are shown before and after the sections are bulk contrast leveled.

image, clear brightness variations can be seen between sections and the uneven shading at section boundaries results in sharp stitching artifacts. After bulk levelling the whole slide, the obvious brightness variations between sections have largely been removed and all sections have been normalized to the same brightness range (Figure 3.8(b)). However, stitching artifacts are still visible due to mismatched shading gradients between sections. After applying the gradient levelling algorithm, these sharp section transitions have been corrected giving the impression of a homogenous WSI (Figure 3.8(c)). Overall, levelling the WSI is important for improving image appearance, diagnostic value, and is a critical preprocessing step for virtual staining. While tools such as ImageJ offer powerful stitching plugins under the "Grid/Collection stitching" extension tab [146], they primarily address overlap alignment and blending (e.g., averaging or linear blending) rather than correcting global brightness mismatches. As a result, even after blending, significant contrast differences between sections remain. Figure 3.9 compares these ImageJ stitching results with the presented contrast levelling algorithm. Only after bulk and gradient levelling do the stitched WSIs appear homogeneous.

3.3.3 Label-Free Whole Slide Images

When screening a biopsy sample, pathologists leverage the multi-viewing capability of WSIs to identify diagnostically relevant ROIs [7], [141]. Pathologists typically adopt a combination of two viewing strategies: 'drilling', involving zooming in and out of an area of interest, and 'scanning', where pathologists use a fixed zoom while panning and searching over a larger area [7]. Low magnifications allow pathologists to survey the tissue structure and cell distribution, providing the necessary context for the detailed examination of specific tissue structures at high magnification. It is therefore important to provide pathologists with entire WSIs.

Figure 3.10 shows an example WSI of a breast NCB with Invasive Ductal Carcinoma (IDC). A heat map of the sample's relative focus positions is shown in Figure 3.10(a), indicating the topology of the sample's surface. Each section is outlined in white and has an optimal focus assigned to its center. All other focus values are interpolated between sections. In some instances, there may be artifacts in the sample preparation process, such as dust or other particles settling on the specimen, cracks in the tissue or a small clumps of paraffin. These artifacts, while infrequent, may disrupt the autofocusing algorithm, resulting in poor image quality. However, when a focus scan fails, the algorithm will referencing the optimal focus plane of the nearest unaffected section.

Figure 3.10(b) shows zoomed-out WSIs of the non-radiative and radiative channels while Figure 3.10(c) shows several higher magnification sections taken across the length

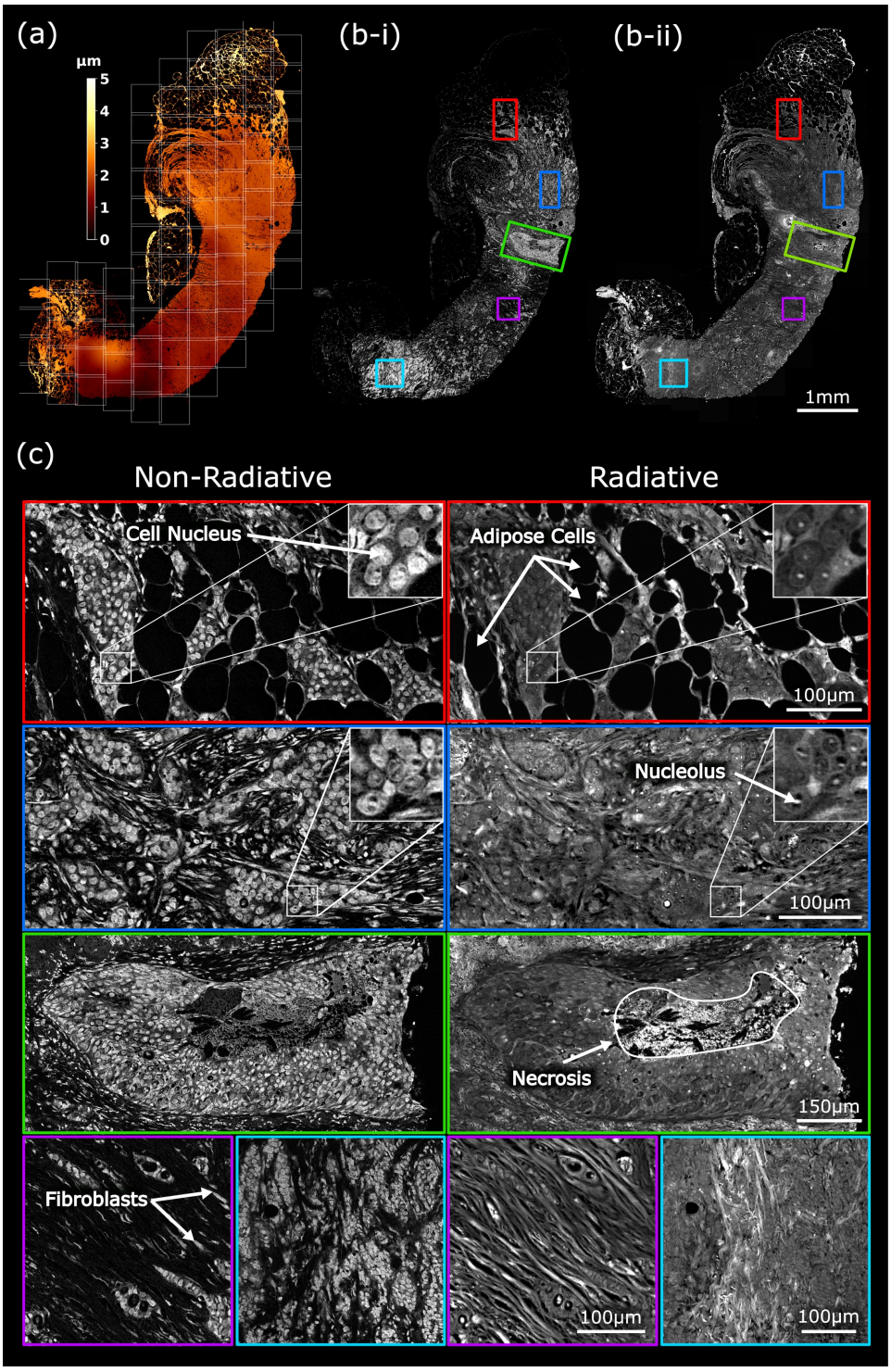

Figure 3.10: Stitched and leveled PARS non-radiative and radiative WSIs of malignant human breast tissue. (a) Shows a heat map of the relative focus positions across the sample. (b-i) and (b-ii) Show WSIs of both non-radiative and radiative channels, respectively. (c) Shows the non-radiative and radiative contrasts at high magnification. Sections are taken from across the sample and show clinically relevant features.

of the tissue. The non-radiative channel predominantly highlights nuclear contrast while the radiative channel shows complimentary contrast of structures in the ECM. The non-radiative channel shows a high degree of variance in nuclear size, shape, and appearance, which are indicative of neoplastic features often used in the evaluation of a cancer specimen [10]. The non-radiative channel also highlights irregular loosely arranged glandular structures with a high degree of disorganisation, which are important features in grading malignancies (Figure 3.10(c) blue box) [12]. The abnormal cells are seen invading and infiltrating into the surrounding stroma and adipose tissue (Figure 3.10(c) red box). These visualizations, provided by the non-radiative channel, help pathologists determine the aggressiveness of the cancer that guides management recommendations. Furthermore, at high magnifications, subnuclear details such as nucleoli and chromatin/chromatid arrangement are seen in the radiative channel (Figure 3.10(c) blue box). Such structures help show the degree of nuclear aberration and cell division (mitotic figures) in the tissue, which are important for cancer diagnosis [11]. Necrosis of breast tissue can also be seen in the radiative channel, inside a region of neoplastic cells, indicating high grade disease (Figure 3.10(c), green box) [147]. Fibroblasts, which contribute to the creation of connective tissue, are also seen in the non-radiative channel. In the corresponding radiative image, these fibroblasts are embedded in long diagonal strands of connective tissue (Figure 3.10(c) purple box). It's clear these label-free contrasts provide visualizations of clinically relevant features at both low and high magnifications.

To further demonstrate their utility, these contrasts were combined into a single Total Absorption (TA) coloured image and compared against gold standard H&E staining. This one-to-one correspondence is shown in Figure 3.11 for the same high magnification sections shown previously. The TA image here has the radiative channel in blue and non-radiative in red. In general, the non-radiative channel provides analogous contrast to the hematoxylin stain while the radiative channel provides analogous contrast to the eosin stain. Correspondence of the nuclear structure, shape, and size and subnuclear details is clearly seen between the TA and H&E images. Much like the combined H&E stains, the combined radiative and non-radiative contrasts allow clear differentiation of various tissue types and cell structures. The potential for label-free H&E emulation is clear. The H&E images were reviewed with clinicians and found to be of diagnostic quality with no artifacts apparent from the prior PARS scanning.

Next, whole slide TA visualizations were produced to demonstrate their potential as a stain-free alternative to H&E WSIs. Figure 3.12 shows a set of four TA WSIs with corresponding one-to-one H&E at high magnification. Pathologists are able to analyze these label-free slides at the same magnifications, using the same or similar digital pathology tools as they would with gold standard H&E stained slides. Figure 3.12(a) and (b) show

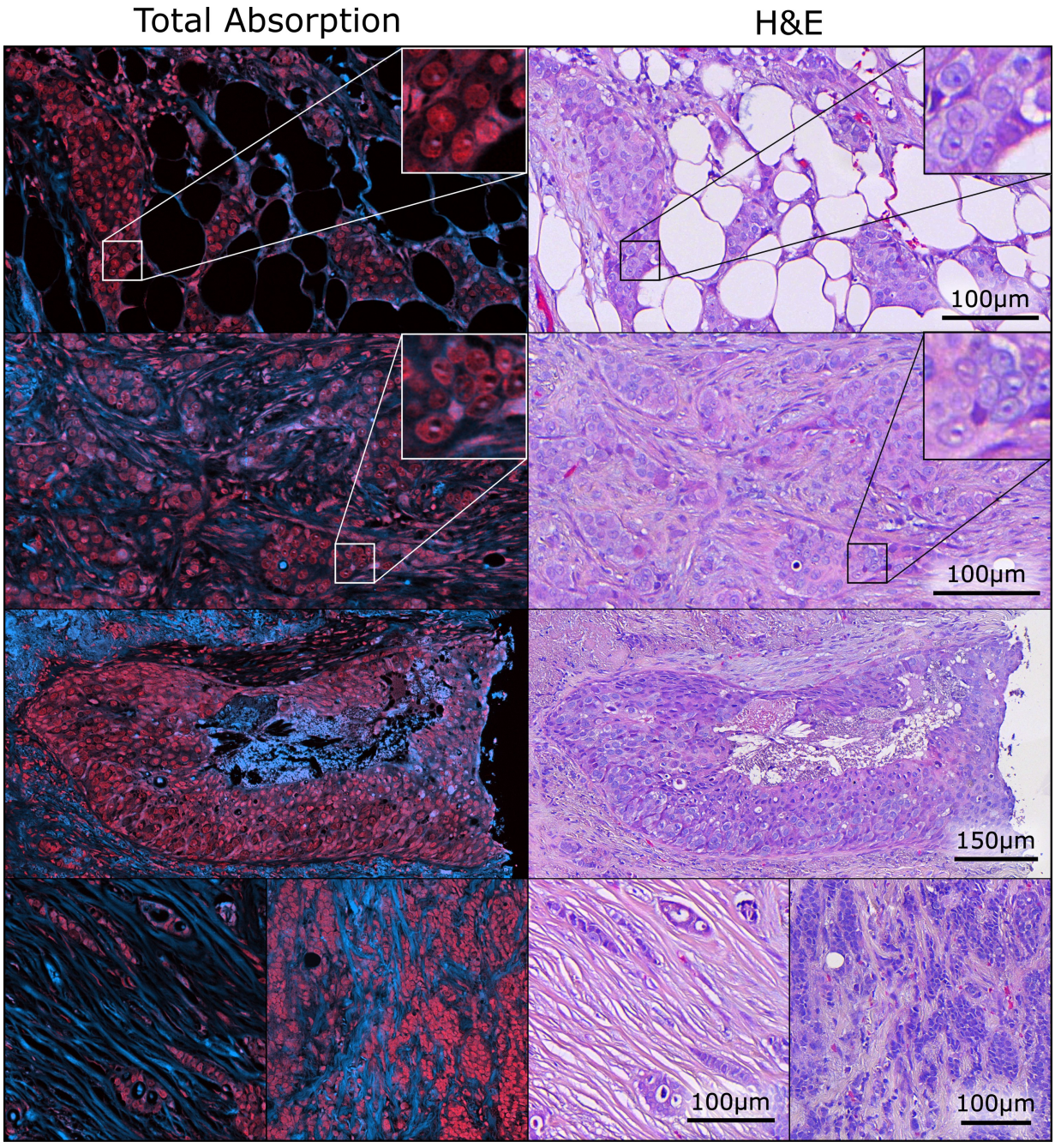

Figure 3.11: One to one comparison of PARS Total Absorption (TA) images with the gold standard H&E stain of a breast NCB. In the coloured TA image, the radiative contrast is blue and the non-radiative is red.

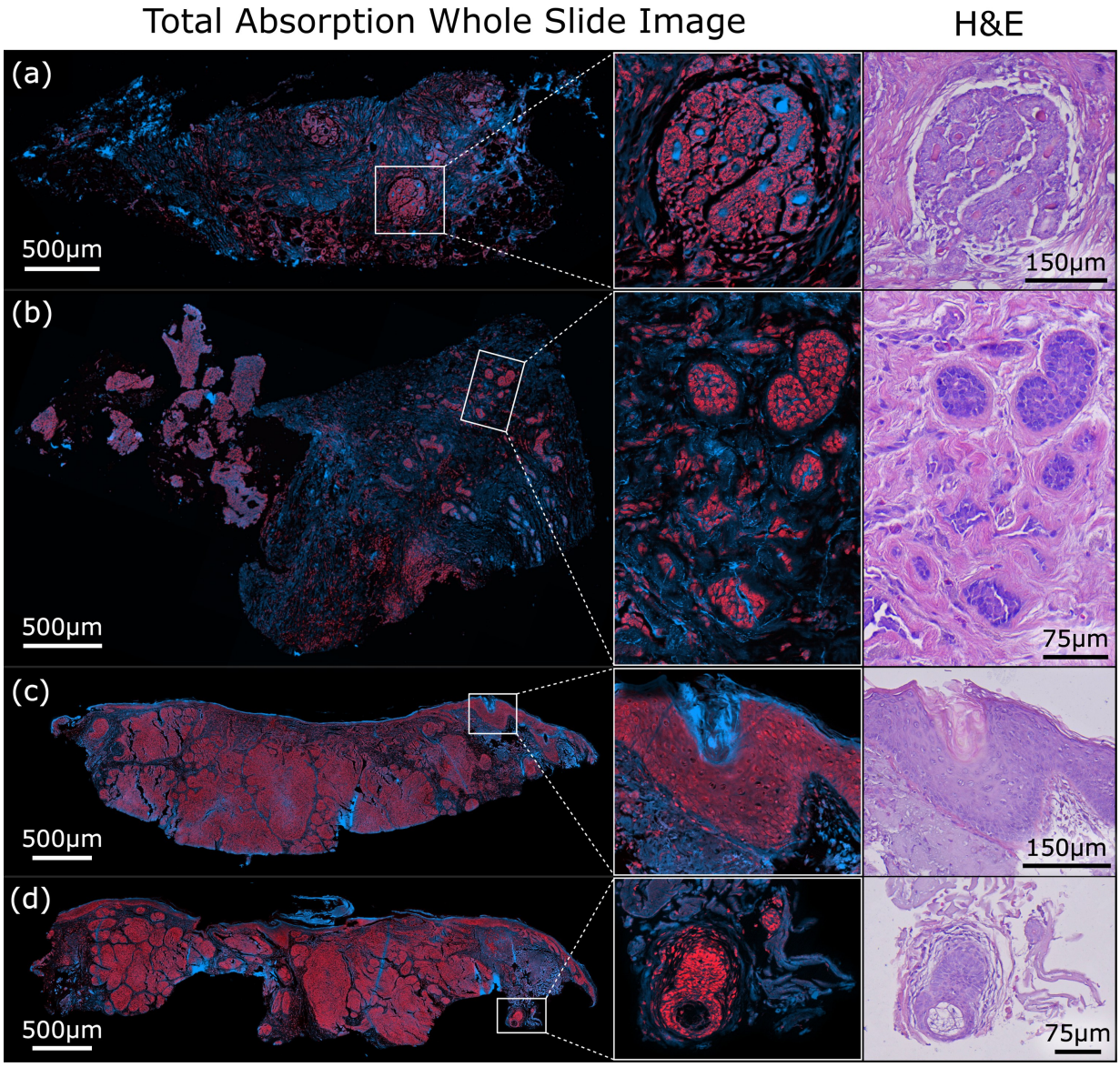

Figure 3.12: Four whole slide PARS TA images presented at low and high magnifications with corresponding high magnification H&E images. Parts (a) and (b) show two WSIs of malignant human breast tissue. Parts (c) and (d) show three PARS WSIs of malignant human skin tissue.

whole slide sections of human breast tissue exhibiting invasive mucinous carcinoma and ductal carcinoma, respectively. At both low and high magnifications, irregular and poorly organised ductal structures can be seen in the breast tissue samples, indicative of a pathologic process [12]. Figure 3.12(c) and (d) show whole slide sections of human skin tissue exhibiting basal cell carcinoma. At low magnifications, the tumour nodules are easily identifiable in both skin tissue samples as dense nests of basaloid cells primarily below the skin surface with some extending from the epidermis. Of note, the TA colourization heatmap strongly corresponds to and facilitates identifying abnormal areas quickly in comparison to standard H&E images. For reference, the normal epidermis of the skin can be seen at high magnification in Figure 3.12(c) along with high resolution details of cell arrangements, nuclei and subnuclear structures. The stratum cornea can be seen primarily with the blue radiative contrast. Furthermore, the high magnification view of Figure 3.12(d) shows a sebaceous gland in the tissue sample.

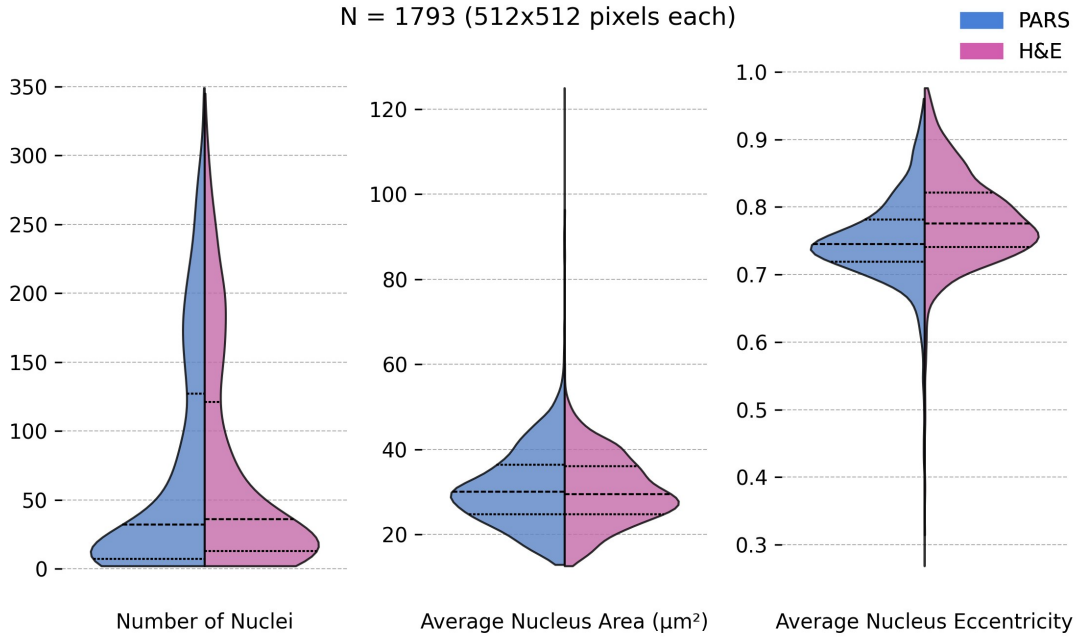

Figure 3.13: Feature-based quantitative comparison of the raw PARS images to standard H&E images. A total of N=1793 image pairs (512×512 pixels each) compared based on three metrics (a) Number of nuclei (b) Mean nuclear area and (c) Mean nuclear eccentricity. The dashed horizontal lines in each violin plot indicate the quartiles of the distributions.

To reinforce the observed visual similarities between the PARS and H&E images, a feature-based quantitative analysis was conducted on a dataset comprising 1793 image

pairs, each measuring 512×512 pixels. Images pairs were selected from both breast and skin tissue samples used in this study. Nuclear features, including nuclear count, average nuclear area, and average nuclear eccentricity, were quantified for each image pair (see methods section 3.2.6).

Figure 3.13 illustrates the distributions of these nuclear metrics for both raw PARS and H&E images. The analysis reveals close symmetry in the distributions between each image type, and closely matched median values (center dashed line). Specifically, the median nuclear count, area, and eccentricity for PARS were 32, 30.0 μm^2 and 0.74, respectively, while for H&E, these values were 34, 29.5 μm^2, and 0.78. The close statistical agreement in nuclear features provides a quantitative assessment specific to histology, suggesting similarity in diagnostically relevant content related to nuclear morphology.

The whole slide scanning times for the PARS point scanning system is primarily a function of the excitation pulse repetition rate and the desired pixel spacing (250 nm/pixel), which relates to image magnification. Here, the imaging speed was defined by the 50 kHz UV source, resulting in a theoretical limit of 5 min/mm^2 for standard 40× high magnification imaging. Other common magnifications used by pathologists, such as 20x and 10x, correspond to pixel spacings of 500 nm/pixel and 1 um/pixel, respectively, which have theoretical imaging times of 1.3 min/mm^2 and 20 s/mm^2, respectively. With this setup, the total scan time for a WSI is simply the total scan and autofocus time per section multiplied by the number of sections. Here, each section is of size 0.5 mm x 0.5 mm and takes approximately 4.7 minutes to scan. This is taking into account the additional time needed for the mechanical stages to accelerate and decelerate while turning around for each row. All 10 axials scans for autofocusing take ∼15 seconds per section, representing ∼6% of the total section imaging time.

While these imaging times are relatively slow and represent a disadvantage of the current system, there is future possibility for improvement. This can be done with faster repetition rate UV lasers and hybrid optomechanical scanning configurations. For instance, there exist 5.5 MHz pulsed 257 nm UV excitation lasers that could potentially provide up to a ∼100x increase in imaging speeds. Future and ongoing work aims to enhance these imaging speeds further with a hybrid optomechanical scanning setup and a similar MHz-range UV excitation source.

3.3.4 Whole Slide Virtual H&E Staining

Pathologists are trained to analyze tissue sections stained in the style of H&E, and while the whole slide TA images in Figure 3.14 show analogous contrast, emulation of H&E stain-

ing style can facilitate a better interpretation experience. Furthermore, machine learning techniques for disease classification and image segmentation have mostly been focused on H&E staining styles [148]. Recently our group has shown such H&E emulation by using the generative machine learning model Pix2Pix to intelligently combine the radiative, non-radiative and scattering contrast channels [33]. With the automated whole slide scanning system and raw data quality improvements presented here, we are now able to virtually stain WSIs with H&E. A section of malignant breast tissue, shown in Figure 3.14(b), was scanned, and then virtually stained to resemble standard H&E. The virtual H&E model for this sample was trained on a separate WSI of breast tissue. Visually, at low magnifications we can see an almost identical WSI and are able to make out the same ductal and lobular structures as well as areas of fatty tissue. At high magnifications the virtual H&E staining compares very well to the gold standard, as determined by our clinical colleagues.

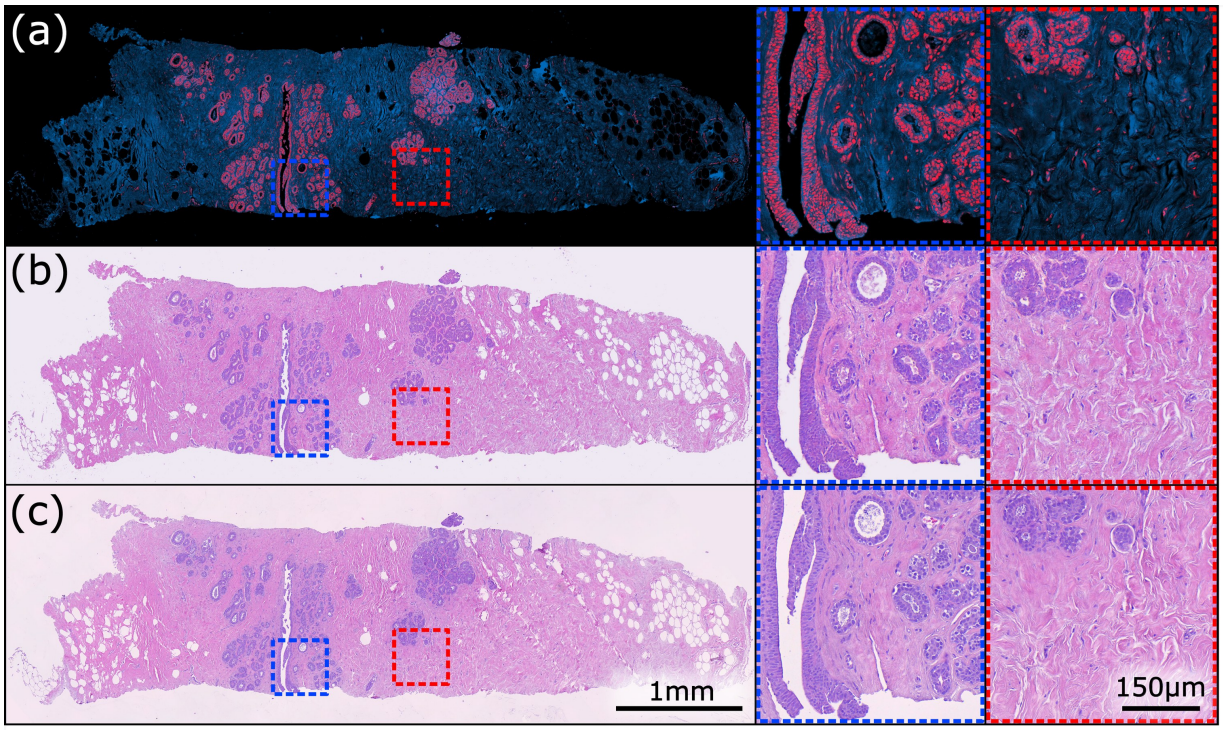

Figure 3.14: Comparison between the PARS TA, virtual H&E, and corresponding ground truth H&E WSIs of a breast NCB. (a) Shows a raw TA WSI. (b) Shows the PARS TA WSI virtually stained with H&E. (c) Shows the ground truth H&E WSI. Two example areas are shown in higher magnification.

As a means of quantitative comparison, the same nuclear features computed in Figure 3.13 were calculated here to measure similarity of the virtual and ground truth H&E im-

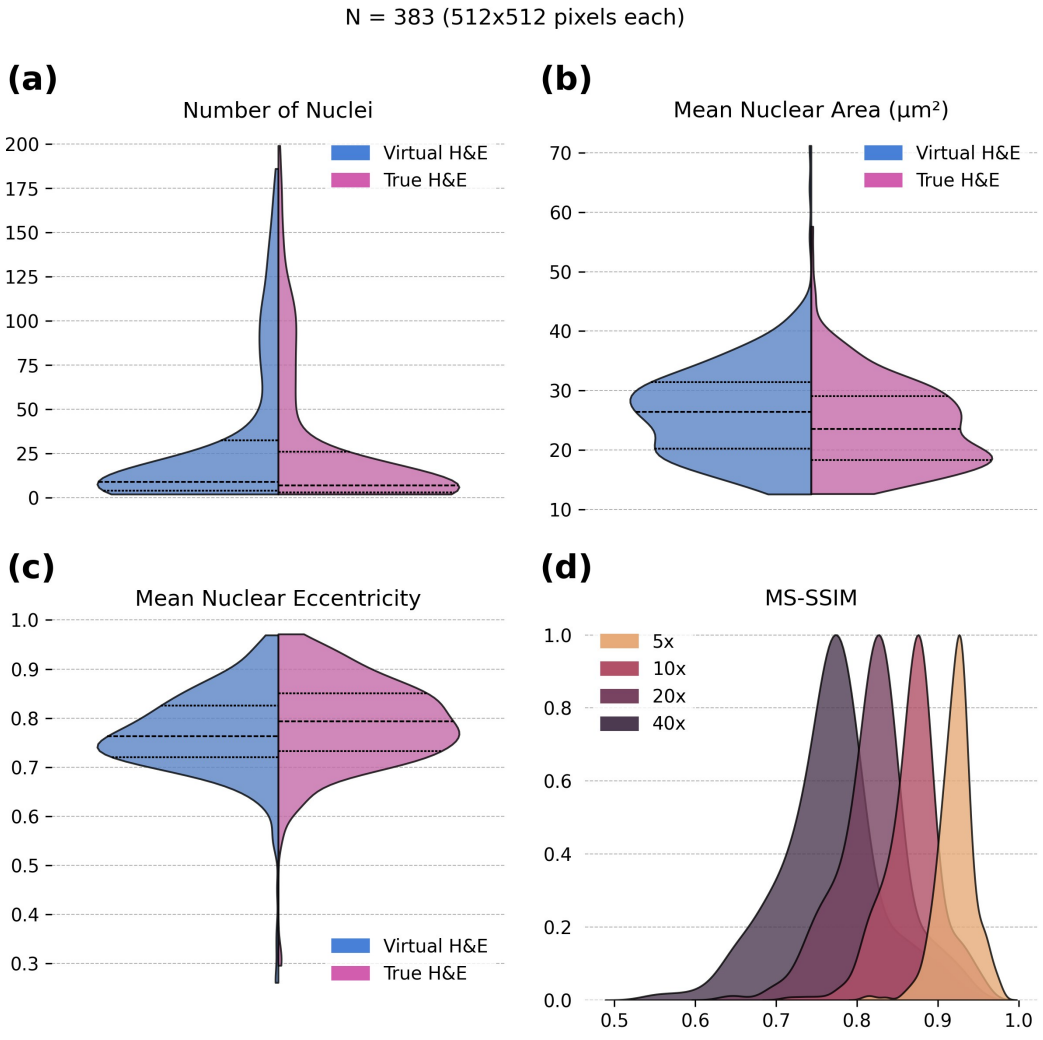

Figure 3.15: Quantitative comparison of the virtual H&E and corresponding ground truth H&E WSIs. A feature-based analysis of (a) Number of nuclei (b) Mean nuclear area and (c) Mean nuclear eccentricity is shown. (d) Normalized MS-SSIM distributions computed at increasing magnifications (5x, 10x, 20x and 40×) to provide pixel-level quantitative measure of agreement. The dashed horizontal lines in each violin plot indicate the quartiles of the distributions.

ages. The analysis in Figure 3.15(a)-(c) reveals close symmetry in feature distributions and median values for the real and virtual H&E images. Here, the median nuclear count, area, and eccentricity for virtual H&E were 9, 26.36 μm^2 and 0.76, respectively, while for H&E, these values were 7, 23.56 μm^2, and 0.79. Following this, an MS-SSIM metric was computed to measure the pixel-level similarity between the images, shown in Figure 3.15(d). MS-SSIM was computed at 40× (native PARS resolution), 20x, 10x, and 5x magnification equivalents with resulting median scores of 0.77, 0.82, 0.87 and 0.92. While these values suggest good structural correspondence between the images, image registration errors and tissue alterations from the staining process may lead to lower values, independent of inherent differences in image modalities. To reliably assess similarity, one must establish diagnostic equivalence through masked clinical concordance studies. The presented platform and workflow has facilitated such studies [3], by providing pathologists with PARS WSIs with matching magnification ranges and analogous contrasts to the gold standard H&E.

3.4 Conclusion

Here we present an automated PARS whole slide scanning microscope with a refined optics architecture for imaging thin, transmissible samples. The system performs label-free automated whole slide scanning using the autofocus workflow and contrast levelling algorithms presented here. WSIs of all three contrast channels (scattering, radiative and non-radiative) were shown in malignant human breast and skin tissue samples. Slides were viewable at magnifications up to 40× and recovered high-resolution subcellular diagnostic details. Clinically relevant features were identified in both the radiative and non-radiative contrast channels as well as in the combined TA WSIs. We demonstrated the close correspondence and analogous contrast of the label-free TA images to gold standard H&E staining. Previously reported Pix2Pix virtual H&E model was applied to an entire breast tissue section, highlighting the system's potential for label-free WSI H&E emulation. Visual similarities between the PARS, virtual H&E and real H&E images were reinforced with quantitative metrics comparing nuclear features and similarity of structural information. We demonstrated that PARS imaging is non-destructive, permitting standard diagnostic quality H&E staining to be performed sequentially. This ability to capture and virtually stain one-to-one whole slide PARS images is crucial for the masked clinical pathology validation studies in Chapter 5 comparing PARS virtual H&E images to ground truth H&E.

Building on this automated whole slide PARS imaging platform and its demonstrated compatibility with virtual H&E workflows, Chapter 4 explores alternative, unpaired deep

learning strategies for virtual staining of PARS WSIs. The motivation for these approaches and their advantages in are discussed in detail in the next chapter.

Chapter 4

Virtual Whole Slide H&E Histology with PARS using CycleGAN with Weakly Registered Pairs

4.1 Introduction and Motivations

With the automated PARS histology scanner from the previous chapter, high-SNR WSIs of entire unstained FFPE sections can now be acquired at 40× magnification. These scans provide H&E-analogous contrast at clinical scale and resolution while remaining non-destructive, leaving samples available for downstream staining. Building on this work, in this chapter we present the first application of an unpaired CycleGAN framework for virtual H&E staining of PARS WSIs. This approach advances the modality toward clinical usability by transforming label-free contrasts into the familiar colour domain of standard H&E pathology, while avoiding the registration challenges and blurring artifacts associated with strictly pixel-aligned training in previous methods [33].

Although the 266 nm excitation wavelength targets histologically relevant biomolecules (e.g. DNA, collagen, and elastin) [59, 69, 70] to provide contrast of nuclear structures and connective tissues, pathologists are trained to interpret tissue sections in the familiar colour style of H&E. Therefore, transforming these raw contrasts to emulate the H&E staining style can facilitate a more familiar interpretation experience.

The straightforward approach to H&E emulation with PARS data involves applying a fixed-colour transform to the non-radiative and radiative channels, as demonstrated in

[32]. In this work, the non-radiative nuclear contrast was rendered purple to mimic hematoxylin, while the radiative connective tissue contrast was rendered pink to mimic eosin staining. While this provides a more familiar colour scheme, employing Convolutional Neural Networks (CNNs) and deep learning algorithms for virtual staining offers several advantages. These networks can take structural features into account when combining contrast channels into an H&E representation. This is especially helpful when the raw input data deviates from or lacks the exact biomolecular specificity of the target stain. For example, autofluorescence imaging is unable to directly measure nuclear contrast and instead relies on deep learning-based virtual staining algorithms to infer nuclear structures based on other contrasts and surrounding structures [26, 64, 65, 66, 67, 68]. Similarly, despite the close correspondence between PARS contrasts and H&E, the use of deep learning models is preferable, as they can better accommodate potential differences between the image domains.

The most recent work in PARS virtual H&E staining employed the Pix2Pix I2I translation model [33]. As discussed in Section 2.1.5, this supervised approach requires exact pixel-to-pixel matched ground truth data for emulation. However, achieving perfect alignment between images captured with different modalities (i.e., PARS and brightfield) is inherently difficult and, in many cases, unattainable due to deformations or tissue degradation caused by the staining process. Alignment is further complicated by fundamental differences between modalities: PARS is a laser-scanning, absorption-based technique, whereas brightfield microscopy relies on wide-field white light illumination and a camera sensor. As a result, subtle mismatches in resolution and acquisition style (e.g., differences in optical sectioning, illumination, and other imaging conditions) between the two imaging systems are particularly difficult to resolve at the pixel level, reducing the effectiveness of strict paired training schemes.

In the context of PARS virtual staining, misaligned inputs severely impact virtual staining performance and result in blurring or smudging of tissue structures that were originally well-resolved before translation. Such errors are particularly problematic for diagnostic tasks requiring fine detail. For example, mitotic count (a common cancer grading) demands a high resolution assessment of tumor cells to identify and count which ones are actively dividing [11]. For this reason, there is a need to improve current PARS virtual staining performance and ensure the generated images preserve the same fine detail and diagnostic fidelity as the input data.

4.1.1 Study Overview and Contributions

An improved virtual staining and image processing workflow is presented to advance PARS histology toward clinical-grade emulation of H&E staining. The CycleGAN [114]) architecture, detailed in Section 2.1.5, was implemented for virtual staining, representing the first application of an unpaired framework to PARS WSIs. Unlike prior Pix2Pix-based approaches [33], CycleGAN is more flexible to misalignments, as it does not depend on pixel-perfect registration. In this study, because PARS permits subsequent H&E staining, the model was trained with loosely registered pairs to provide a balance of histological features in both domains, mitigating the risk of hallucination artifacts [149]. Matching feature distributions, combined with the strong structural similarity between PARS contrasts and H&E, helps ensure that the virtual stains remain faithful to underlying tissue morphology.

Earlier work [33] demonstrated feasibility using cropped test regions from WSIs drawn from within the training dataset. In contrast, this study extends virtual staining to entirely unseen full slides held out from both training and validation, providing a more clinically realistic test scenario.

Alongside the staining framework, the PARS preprocessing pipeline was enhanced with self-supervised Noise2Void denoising [150] and a custom algorithm to correct mechanical scanning jitter artifacts. Together, these refinements improve the clarity of fine subcellular features (e.g., nucleoli, intercellular junctions) and provide higher-quality inputs for the virtual staining network.

Virtual H&E performance was compared for Pix2Pix, entirely unpaired CycleGAN, and CycleGAN trained with semi-registered pairs, with the latter producing the highest quality results. Applied to malignant human breast and skin tissue, the generated virtual H&E images faithfully reproduced detailed subcellular and subnuclear diagnostic features, and are difficult to distinguish from gold-standard staining. Overall, this work represents a significant advancement toward a fully label-free virtual H&E microscope capable of delivering clinical-quality histology whole slide H&E images directly from unstained samples.

4.2 Materials and Methods

4.2.1 Description of PARS Tissue Imaging Process

The label-free images acquired for this study were captured using the whole slide scanning PARS system developed in Chapter 3 [1]. In short, a 400 ps pulsed 50 kHz 266 nm

UV laser (Wedge XF 266, RPMC) is used to excite the sample, simultaneously inducing non-radiative and radiative relaxation processes. The non-radiative relaxation processes are sampled as time-resolved photothermal, and photoacoustic signals probed with a continuous wave 405 nm detection beam (OBIS-LS405, Coherent). This detection beam is co-aligned and focused onto the sample with the excitation light using a 0.42 NA UV objective lens (NPAL-50-UV-YSTF, OptoSigma). The radiative emissions (>266 nm) from the radiative relaxation process, as well as the transmitted detection light, are collected using a 0.7 NA objective lens (278-806-3, Mitutoyo). The 405 nm detection wavelength and the radiative emissions are spectrally separated, and each directed toward an avalanche photodiode (APD130A2, Thorlabs). Refer to Chapter 3, Section 3.2.1, Figure 3.1 for more detail.

To form an image, mechanical stages move the sample in an "s"-like scanning pattern to laterally separate the excitation events on the sample (∼250 nm/pixel). At each excitation pulse, several hundred nanoseconds of time-resolved signal from each system photodiode is digitized at a 200 MHz rate (CSE1442, RZE-004-200, Gage Applied). A portion of the collected signal is pre-excitation and is used to form the scattering image of the sample in its unperturbed state. The non-radiative image pixels are then derived as a percentage modulation in the detection scattering (post-excitation). Next, the radiative image pixels are obtained from the peak emission amplitude recorded after each excitation event. Pixels are then arranged in a cartesian grid based on the stage position feedback, forming a stack of three co-registered label-free image contrasts: non-radiative, radiative, and scattering. Finally, the excitation pulse energy and detection power, recorded throughout imaging, are used to correct image noise caused by laser power and pulse energy variability. Refer to Chapter 3, Section 3.2.4, Figure 3.3 for more detail.

Whole slide samples can be scanned using the workflow detailed in Chapter 3, Section 3.2.2. In brief, the entire tissue area is divided into subsections (500×500µm), each individually scanned at their optimal focus position. Using their relative stage positions and small amount of overlap (∼5%), these sections are stitched and blended into a single WSI.

4.2.2 PARS Data Preprocessing

In addition to the correction of noise due to laser power and pulse variability (see Chapter 3, Section 3.3.1, Figure 3.6), the Noise2Void (N2V) framework developed by Krull et al. [150] is used to further denoise the raw PARS images. Unlike many other traditional CNN-based denoising methods, N2V does not require paired training data with both a noisy and clean image target. It assumes that image noise is pixel-wise independent, while the underlying

image signal contains statistical dependencies. As such, it facilitates a simple approach for denoising PARS images, and was used to train a denoising CNN for the radiative and non-radiative contrast channels, separately. Models were trained on a body of raw data taken from both human skin and breast WSIs. A series of 125 PARS tiles was used to generate a model for each of the radiative and non-radiative images. Each model was trained over a series of 300 epochs, with 500 steps per epoch, using 96 pixel neighbourhoods.

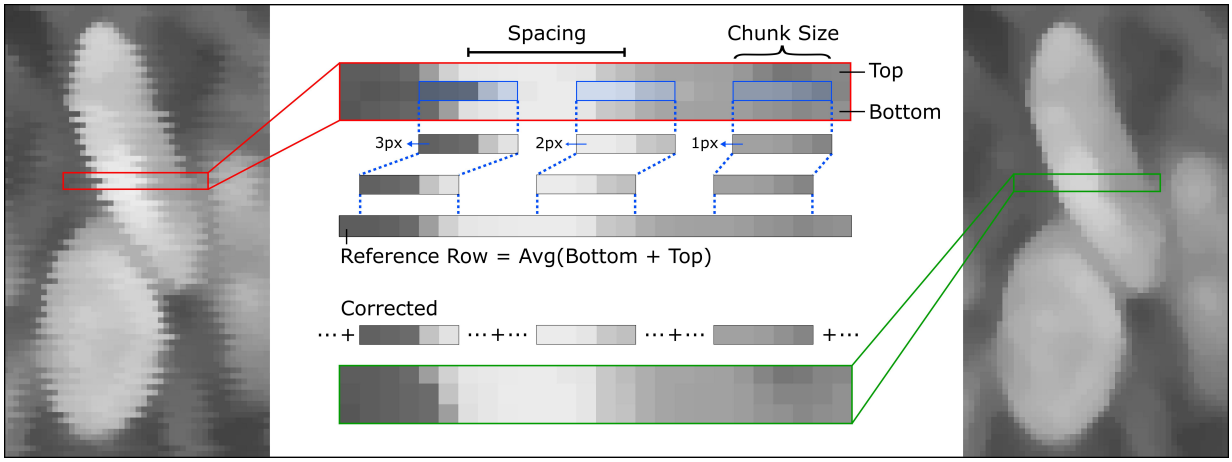

Figure 4.1: Algorithm used for jitter correction of denoised images. Each line of the image is broken into subsegments, which are correlated to the row above and below. Based on the correlation, the segment is shifted laterally to align the edges of image structures. Shifted segments are then averaged together to form a corrected line.

The final processing step before training the virtual staining model is to correct a scanning-related image artifact, which is uncovered after denoising the raw data. When the data stream acquired during scanning is shaped into an image section, pixels are evenly spaced in the cartesian grid. In reality, the spatial sampling is not perfectly even, owing to slight inconsistencies in stage velocity. This results in "jitter" artifacts which are then corrected using the custom algorithm shown in Figure 4.1. The artifacts and images shown in Figure 4.1 are exaggerated for the purpose of demonstrating the algorithm's working principles. The algorithm determines the optimal pixel shifts for a series of chunks spaced across a given row, with overlap. Chunks are then moved to their appropriate locations and summed together into a corrected row, with areas of overlapping chunks averaged. Figure 4.1 illustrates three example chunks and their optimal pixel shifts. These shifts are determined by moving a chunk left and right until a minimal mean square error is reached between the chunk and a reference row. This reference is calculated as the average between the top and bottom rows for the given row being corrected. The algorithm relies on the

assumption that the fast axis speed profile differs mostly for velocity sweeps in opposing directions and minimally for velocity sweeps in matching directions. As such, the top and bottom rows were captured in the same direction and averaging them together provides a suitable in-between row to use as reference for correction.

4.2.3 Dataset Preparation for Model Training

In this work, a CycleGAN image translation model was used for virtual staining. This model's working principles in detailed in background Section 2.1.5. While CycleGAN is able to learn an image domain mapping with unpaired data, it can be advantageous to provide the model with semi or loosely registered images, as a form of high-level labeling to better guide the training process and strengthen the model. As one-to-one H&E and PARS WSI pairs are obtainable, it seems most appropriate to prepare the dataset accordingly. However, the two datasets are not intrinsically registered, so a simple affine transform is used. Affine transforms allow for shearing and scaling, as well as rotation and translation [151]. In general, it is sufficient for the alterations of tissue layout on the slide which occur during the staining process. The affine transform is determined using the geometric relationship between three registration points. This found relation, or transformation matrix, is then applied to the entire WSI for both the non-radiative and radiative channels [151].

After the whole slide PARS TA image and H&E image are registered, the entire image is sliced into small tiles (512×512) which are paired together as shown in Figure 4.2(a). The TA image shows the radiative (blue) and non-radiative (red) raw images in a combine single coloured image. However, during training, the network uses inverted TA patches, in which the radiative and non-radiative image pixel intensities are inverted before they are stacked into a coloured image. Inverting these channels provides a coloured image where the white background in the PARS data maps to the white background in the H&E data. After training is complete, the model can be applied to larger images, such as entire WSIs, by virtually staining 512×512 tiles in parts. This process is shown in Figure 4.2(b). When applying the model, the virtually stained tiles overlap, and these overlap regions are averaged together in the final virtually stained image. Here an overlap of 50% was used.

In this study two CycleGAN models were trained on loosely paired data using the registration and dataset preparation methods described earlier. One model was trained on human skin tissue and another on human breast tissue. For each model, the training sets were composed of 5000 training pairs of size 512×512 px (128×128 µm) sourced from standard $40\times$ magnification (250 nm/pixel) WSIs of each tissue type. The model generators

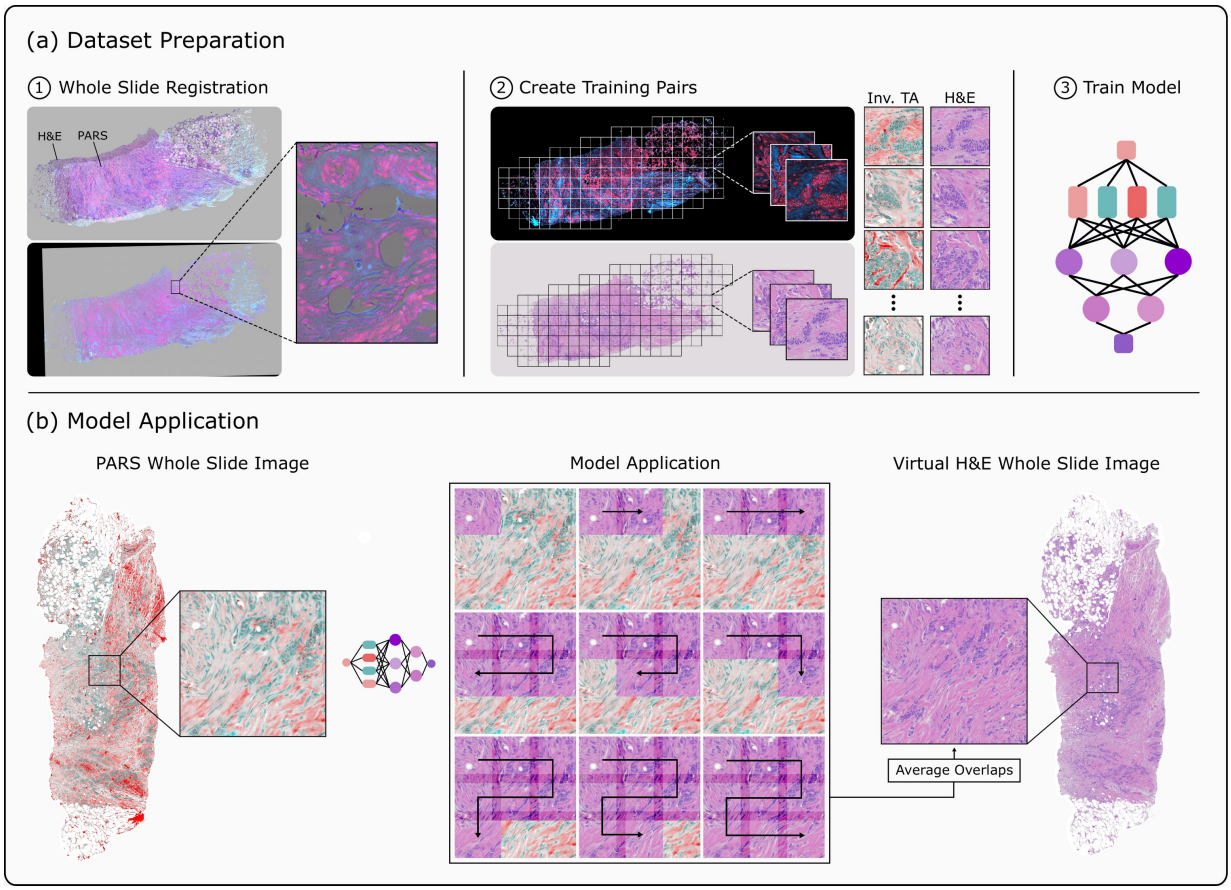

Figure 4.2: Visualization of data preparation process and inversion. (a) The total-absorption and H&E images registered and then cut into matching tiles, to generate a loosely registered dataset. The pixel intensities of the total-absorption images are then inverted, to provide a better initialization for training. Finally, the datasets are used to train the virtual colourization model. (b) To form images, the model is repeatedly applied to overlapping tiles of the TA images. The overlapping tiles are subsequently averaged to form the final virtual colourization.

were trained for 500 epochs with an early stopping criteria to terminate training when losses stopped improving. The model was trained with a learning rate of 0.0002, batch size of 1 and an 80/20% split of training and validation pairs. For comparison purposes, a Pix2Pix model and standard unpaired CycleGAN model were also trained for each tissue type. The Pix2Pix models were trained on the same dataset as the paired CycleGAN model, however with the more rigorous registration process and the same model parameters previously described by Boktor *et al.* [33]. For the unpaired training of CycleGAN models, the same number of training pairs were used, however the TA and H&E domains were sourced from different WSIs of the same tissue type.

4.2.4 Sample Preparation

Tissue samples were first fixed in formalin solution for a period of 24 to 48 hours, within 20 minutes of excision. Samples were then dehydrated with ethanol and treated with xylene to eliminate residual ethanol and fats. The samples were subsequently embedded in paraffin wax, creating FFPE blocks. A microtome was then used to cut thin tissue sections (∼4-5 μm) from the FFPE blocks. Tissue sections were placed on glass microscope slides and baked at 60 °C for approximately 60 minutes to evaporate excess paraffin. The unstained samples were first imaged at 40× with the PARS microscope and then directly stained with H&E. H&E-stained slides were then imaged at 40× (Morpholens 1, Morphle Digital Pathology). This process was performed on a variety of malignant human skin and breast tissue samples and direct one-to-one WSIs were acquired for model training.

Tissues were provided by clinical collaborators at the Cross-Cancer Institute (Edmonton, Alberta, Canada) from anonymous patient donors with all patient identification removed from the samples. Patient consent was waived by the ethics committee because these archival tissues were no longer required for patient diagnostics. No information regarding patient identity was provided to the researchers. Samples were collected under protocols approved by the Research Ethics Board of Alberta (Protocol ID: HREBA.CC-18-0277) and the University of Waterloo Health Research Ethics Committee (Photoacoustic Remote Sensing Microscopy of Surgical Resection, Needle Biopsy, and Pathology Specimens; Protocol ID: 40275). All human tissue experiments were conducted in accordance with the government of Canada guidelines and regulations, including "Ethical Conduct for Research Involving Humans (TCPS 2)".

4.3 Results and Discussion

A current shortcoming of the PARS raw images is the presence of measurement noise. In Chapter 3 [1] significant improvements in PARS image quality were achieved by measuring detection power and excitation pulse energy. Image noise was then corrected based on the laser energy variability. Even with the energy reference correction, measurement noise is still present in the non-radiative signals. This additive noise disproportionately impacts signals which exhibit low non-radiative relaxation since they generate smaller non-radiative perturbations in the detection beam. Figure 4.3 shows an example of the raw non-radiative and radiative image channels after reconstruction and laser power reference correction. At high magnification, significant noise can be seen in the raw data channels. This motivates denoising as a preprocessing step. However, noiseless PARS image targets were not available for training a traditional denoising CNN. Hence, the N2V framework, described in Section 4.2.2 is an ideal method as it allows effective denoising without a clean image target. Figure 4.3 shows results after denoising with clear improvements in image quality for both the non-radiative and radiative channels. After removing noise from the raw data, the jitter artifacts mentioned in Section 4.2.2 are uncovered and become the main source of noise in the images. While these sub-resolution shifts and distortions between the rows of the image can be seen embedded within the noise, they are difficult to resolve and correct. Denoising not only helps improve raw data quality but helps make the jitter correction possible. As shown in Figure 4.3, most of the artifacts are removed after applying the jitter correction algorithm.

After denoising and jitter correcting the raw data, the whole slide radiative and non-radiative images are registered to the ground truth H&E image. As mentioned in Section 4.2.3 a simple affine transform is effective for registration. For an affine transform, a geometric relationship is determined for three registration points between the two image datasets. This found relationship can then be applied to the entire WSI. This provides the necessary transformations to account for most of the tissue layout alterations accrued during the staining process. An example of a WSI before and after registration is shown in Figure 4.4. Registration results are shown for a small size breast tissue sample with an inverted TA image overlayed with ground truth H&E image. A close alignment can be seen between the PARS and H&E ground truth images at both low and high magnifications.

The three-point affine registration is less rigorous compared to the methods employed by Boktor *et al.* [33] for Pix2Pix virtual staining. However, it is significantly faster and may generate upwards of 6000 closely registered 512×512 training pairs for a single $40\times$, $1\,\text{cm}^2$, WSI. In some cases, alignment between these training pairs may be sufficient for error metrics specific to supervised learning, such as MSE, or SSIM. In the future this may

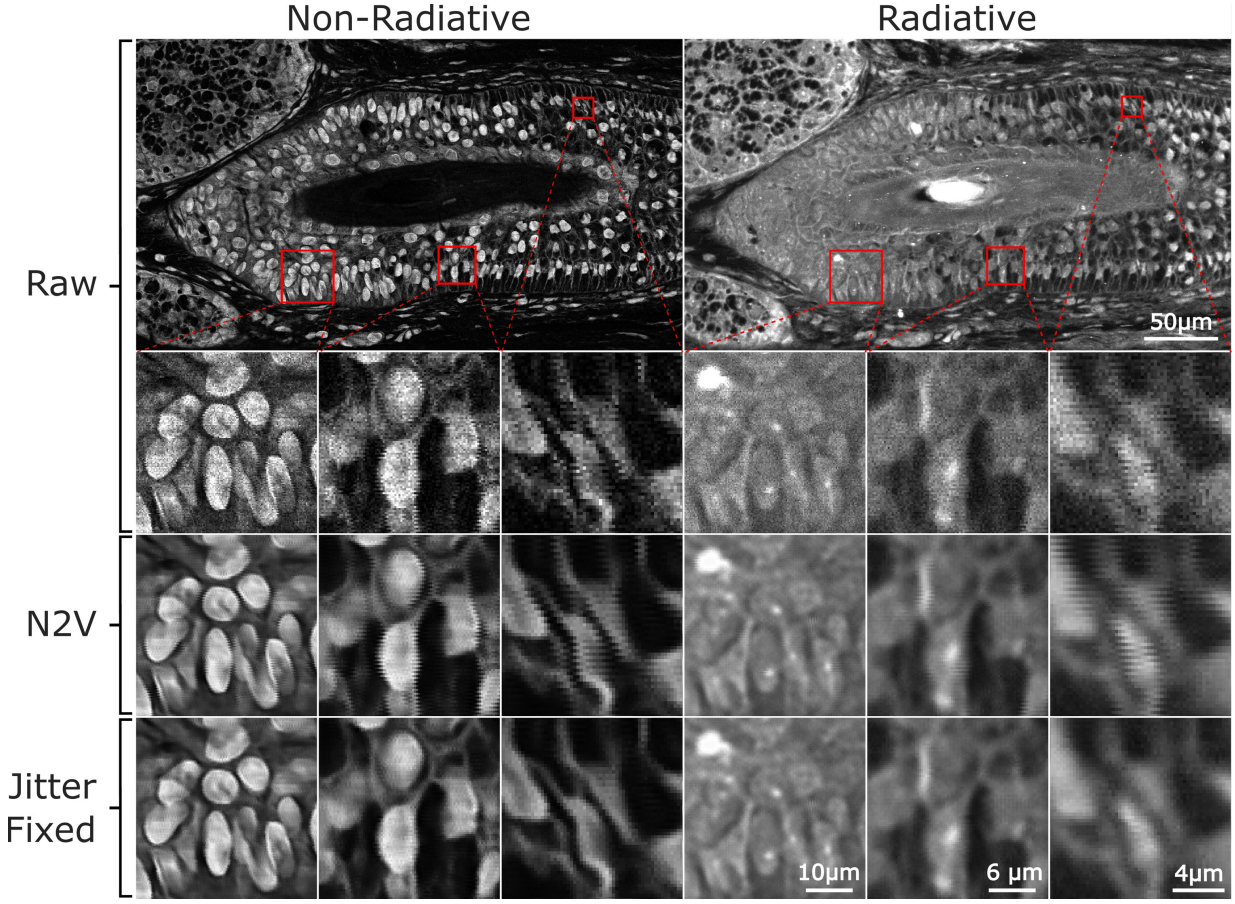

Figure 4.3: Denoising results with the N2V-based denoising CNN and subsequent jitter correction algorithm applied to both the raw non-radiative and radiative image channels. Three example regions are shown at higher magnification to see the effect of the denoising and jitter correction algorithms. The structure imaged here shows a hair follicle capture from human skin tissue.

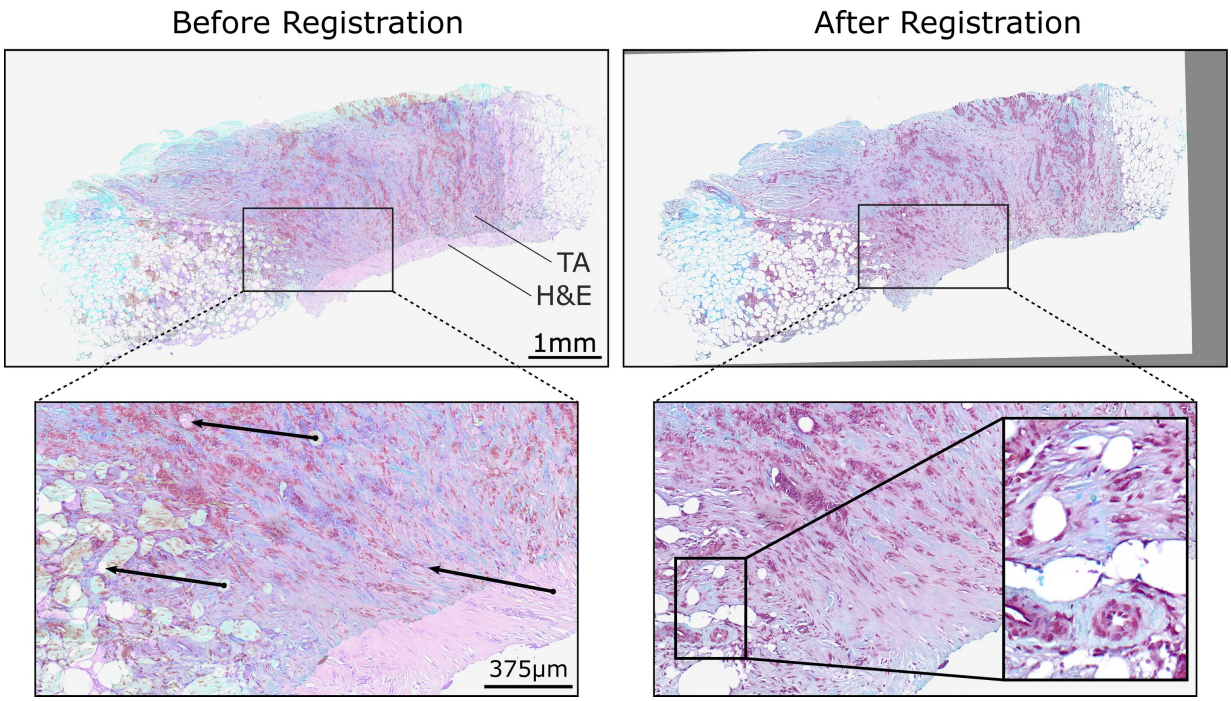

Figure 4.4: Example showing the before and after results of a three-point affine transform applied to an entire WSI. Three example points are shown as well as a high magnification close-up of the registration performance. Here the H&E and inverted TA images are overlayed.

enable hybrid training schemes which combine paired and unpaired data. Previous works in hybrid I2I translation have shown improve performance over purely unsupervised methods, even with a small amount of additional paired data [152], [153]. Although supervised error metrics were not explicitly employed on the loosely paired CycleGAN presented here, the results demonstrate a potential advantage over strictly supervised Pix2Pix, and over CycleGAN trained entirely on unpaired data.

Next, a comparison between previous Pix2Pix based colourizations [33], unpaired CycleGAN, and the proposed paired CycleGAN was conducted. Figure 4.5 shows this comparison for unseen data from a variety of skin tissue structures. The Pix2Pix model was trained on the same PARS images used for the paired CycleGAN, however, registration was performed according to the previously reported process [33]. While the Pix2Pix model performs quite well, the transform tends to blur very fine structures. This artifact is observed in all four skin tissue examples. This blurring is likely caused by slight imperfections in alignment and registration between the training H&E and TA images, which severely weaken model performance. Achieving perfect alignment between the label-free images and H&E data is challenging as certain structures are very susceptible to staining artifacts. For example, lipid areas or regions with loose connective tissue may be severely altered, or even washed away during the deparaffinization and staining processes. This leads to inconsistencies between datasets which cannot be accounted for through registration. Subsequently, even if the label-free and H&E-stained images are aligned, there may still be variation or uncertainty in the data which affect translation quality. This highlights the importance of a more flexible model such as CycleGAN which can handle variation and uncertainty in the input data.

As expected, both unpaired and paired CycleGAN implementations provide sharper virtual H&E (Figure 4.5). However, the model trained on an unpaired dataset shows some examples of mis-colourization. For example, Figure 4.5 panel 1 shows a cluster of cell nuclei which, in the unpaired model, have been tainted red and look to be colourized as RBCs instead of cell nuclei. Conversely, panel 2 shows a crop of the skin's epidermis layer with some background whitespace. The unpaired CycleGAN adds texture to the outermost stratum coronium layer of the tissues. In addition, a hallucination structure is seen in the bottom right of the background, which is not seen in the TA image, or in the H&E. In panel 3, which shows part of a sebaceous gland, the unpaired CycleGAN overemphasizes the red colouration in certain regions. In panel 4, a similar overemphasis of red colours is observed. The red incorrectly implies the presence of RBCs, in the connective tissue. In unpaired scenarios, CycleGAN is a highly under-constrained model, which has been known to create hallucinations. Hallucinations occur when spurious structures are added or features are removed during the image domain transfer [149]. This problem usually arises when the

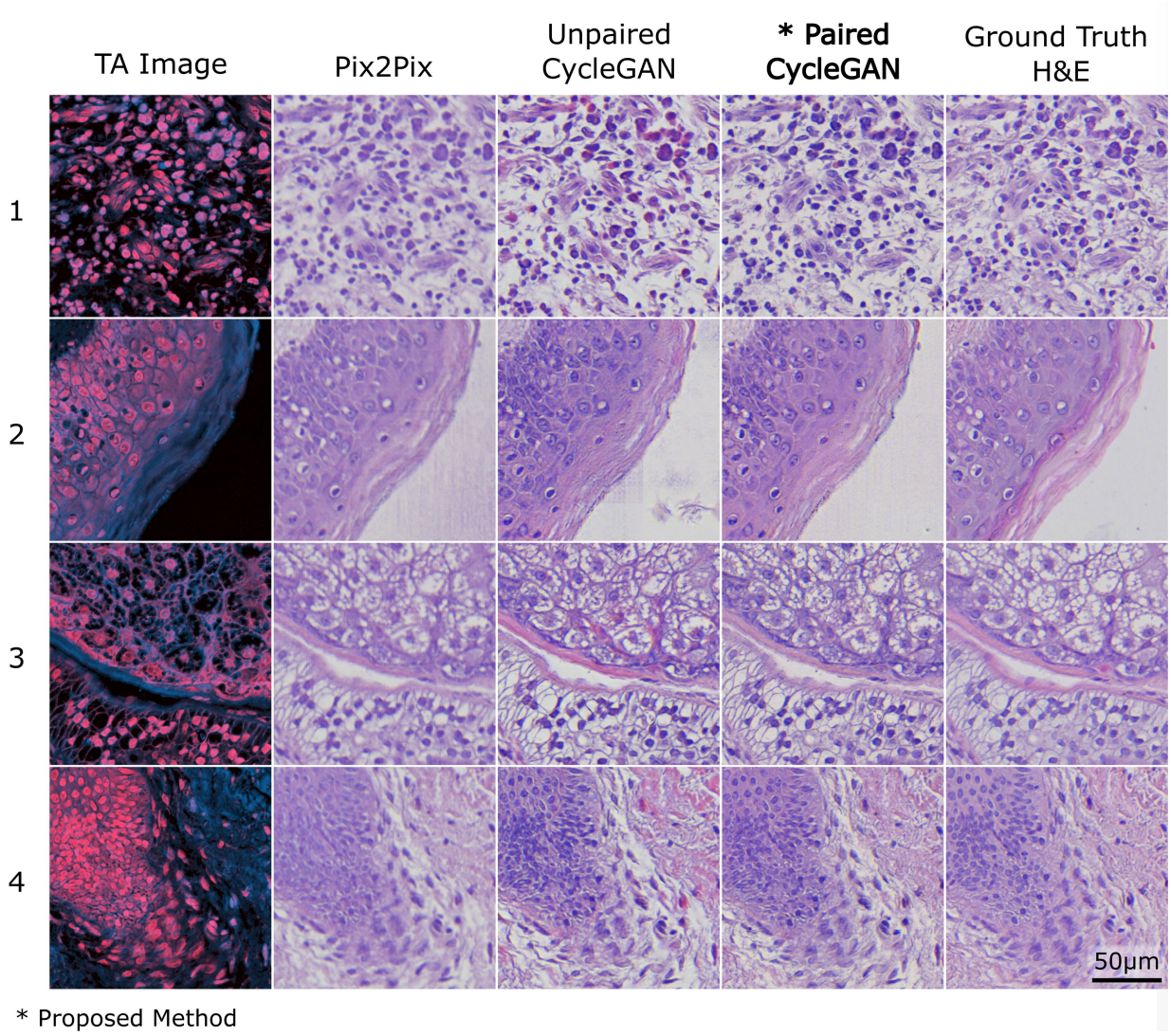

Figure 4.5: Comparison of Pix2Pix as well as paired and unpaired CycleGAN implementation with the gold standard H&E and PARS TA acquisitions of skin tissue.

data provided in the target domain has under or over representation, or bias, towards certain image features. Providing the CycleGAN model with loosely paired training data can strengthen the model during training by ensuring an equal representation of features in both image domains (TA and H&E). Hence, in all four diverse tissue structure examples, the paired CycleGAN does not exhibit the same artifacts as the unpaired version. It is clear the CycleGAN implementation trained with paired data has superior performance, avoiding the hallucination of structures seen with the unpaired CycleGAN model.

The same comparison between colourization models was also performed on unseen malignant breast tissue areas, showing mainly glandular structures and connective tissues. These comparisons can be seen in Figure 4.6. As with the skin tissue examples, the data used for training was taken from separate WSIs of the same tissue type. Overall, similar trends in the model performances are seen in the breast tissue structures. The Pix2Pix model applies a slight blur during the transformation and important nuclear details appear smudged. The unpaired CycleGAN implementation again produces hallucinations in the translation process. In all four examples, these hallucinations cause mis-colourization of the hematoxylin stain. Emulated hematoxylin stain is incorrectly spattered across areas of the connective tissue, falsely indicating the potential presence of nuclei. Abnormal nuclear morphology, such as increased nuclear size and irregular shape, organization, and patterning are all valuable details in cancer diagnosis and prognosis. Hence, these nuclear hallucinations are problematic. In contrast, the paired CycleGAN implementation avoids these hallucinations, and the virtual H&E closely resembles the ground truth.

WSIs provide pathologists with critical access to both low and high magnifications of tissue structures. This enables them informed diagnostic decisions. At low magnification, pathologists can overview the tissue structure, identify areas of concern, and contextualize high magnification analysis. High magnifications allow for in-depth examination of tissue structure and cellular morphology which is vital for precise diagnoses. As such, demonstrating virtual staining on an entire WSI is an essential goal. In Figure 4.7 the semi-registered CycleGAN virtual staining model is applied to an entire malignant skin tissue sample. This tissue contains a diverse set of structures to assess the model's performance. Both low and high magnification images are shown and compared against the corresponding one-to-one H&E WSI. Figure 4.7(a) shows a low magnification depiction of the entire slide where a variety of structures can be identified including an artery, smooth muscle structures, and a basaloid tumor extending from the epidermis. This indicates a primary diagnosis of basal cell carcinoma for the skin sample.

Figure 4.7(b) shows virtually stained sebaceous gland and hair follicle structures, stemming from the epidermis layer of the tissue. The virtual stain closely resembles the gold standard H&E. However, in the ground truth H&E, a blue colour can be seen at the edge

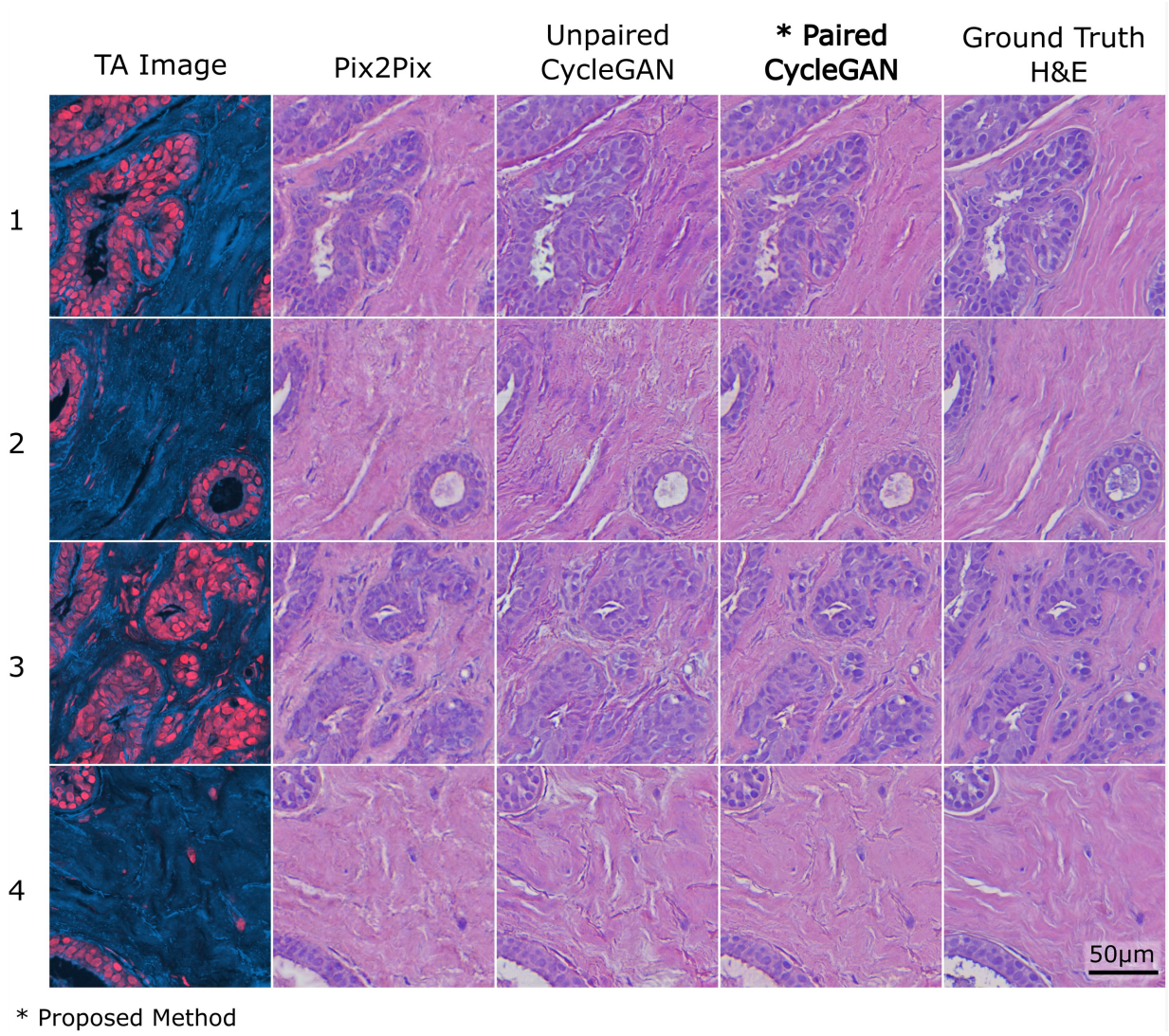

Figure 4.6: Comparison of Pix2Pix as well as paired and unpaired CycleGAN implementation with the gold standard H&E and PARS TA acquisitions of malignant breast tissue.

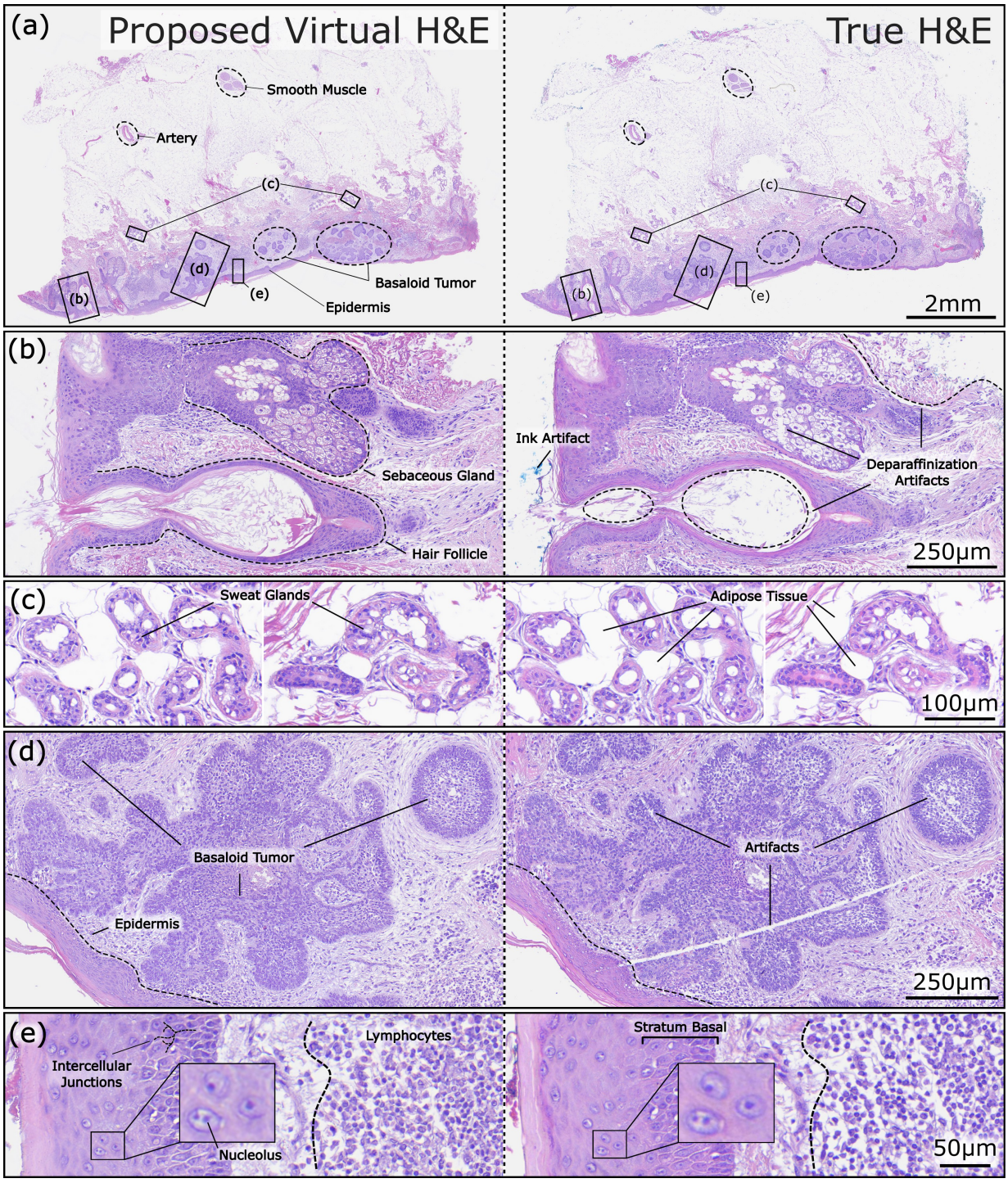

Figure 4.7: Comparison of paired CycleGAN virtual staining with H&E for malignant skin tissue. (a) Whole slide view. High-resolution view of: (b) sebaceous gland and hair follicle; (c) sweat glands and adipose tissue; (d) basaloid cells and tumor; (e) epidermis with lymphocytes and subcellular details.

of the epidermis which is not shown in the virtually stained image. This blue inking is an artifact of the markings drawn on the tissue specimen by a surgeon during the resection process. Furthermore, part of the connective structures inside the void in the hair follicle bulb have been washed away during the deparaffinization and staining process. A similar removal of connective tissue can be in the upper right corner of the H&E image. As well, a few of the secretory cells in the sebaceous gland have been removed and appear fragmented. Notably, in Figure 4.7(d) the H&E image exhibits slash marks which are not present in the virtual H&E. In contrast, all these damaged structures are intact in the PARS virtual H&E. These artifacts exhibit why perfect registration is not always possible in certain parts of the tissue specimen. Additionally, they are prime examples of artifacts which may occur during histochemical processing. A potential advantage of implementing virtual staining is reducing such sample processing artifacts.

Figure 4.7(c) also shows the excellent performance of the semi-registered CycleGAN virtual staining model on a group of sweat glands. Here, the cytoplasmic membrane of the surrounding adipose tissue remains intact, and the lipid cell nuclei are recovered with clarity and colour resembling the gold standard ground truth. Figure 4.7(d) shows a higher magnification view of the basaloid tumor which stems from the epidermis layer of the skin. The virtual H&E accurately mimics the staining colour of the basaloid cell nests of the tumour, which are important clinical features for diagnosis of basal cell carcinoma. Lastly, Figure 4.7(e) shows a close-up of the epidermal layers. Important diagnostic details can be seen in both the virtual and real H&E image, including subcellar structures such as nucleoli. Furthermore, within the stratum basale of the epidermis, a distinct network of thin lines and gaps is observed between the densely packed cells. These spaces are known as intercellular junctions which form intricate and essential networks of connections within the epidermis. These junctions help promote cell adhesion, facilitate intercellular communication, and maintain structural integrity in the epidermis. Proper observation of these structures is crucial during diagnostic evaluations. Disruptions or disorganization in these junctions can be indicative of cancer and potential invasiveness. Therefore, preserving the sharpness and quality of the input data, along with accurate staining colour, is of utmost importance in the virtual staining model. The paired CycleGAN model properly colourizes these smaller features and retains the input resolution of the raw data. This ensures that pathologists can effectively examine and evaluate these crucial aspects, leading to more accurate and reliable diagnoses.

As initially reported by Ecclestone *et al.* [32], the non-radiative and radiative label-free PARS contrasts tend to match the chemical staining contrast of H&E respectively. However, there can still be notable distinctions in the chemical H&E staining and PARS visualizations. PARS may recover additional details and emphasize structures which are

not highlighted by traditional H&E stains. In an example shown in Figure 4.8, the raw PARS image highlights the inner wall of an artery. Specifically, the internal elastic membrane, which provides elasticity and support to the artery, is emphasized in blue (radiative channel). This structure can be visualized with UV excitation due to the presence of certain fluorophores contained in the elastin fibres, one of which is a cross-linking tricarboxylic amino acid with a pyridinium ring [154]. In contrast, H&E is unable to show as clear a distinction between the layers of the artery. As such, PARS provides greater specificity to this structure compared to H&E. However, to accurately reflect the staining patterns of H&E, the virtual staining model deliberately supresses the intrinsic contrast to minimize the prominence of the internal elastic membrane.

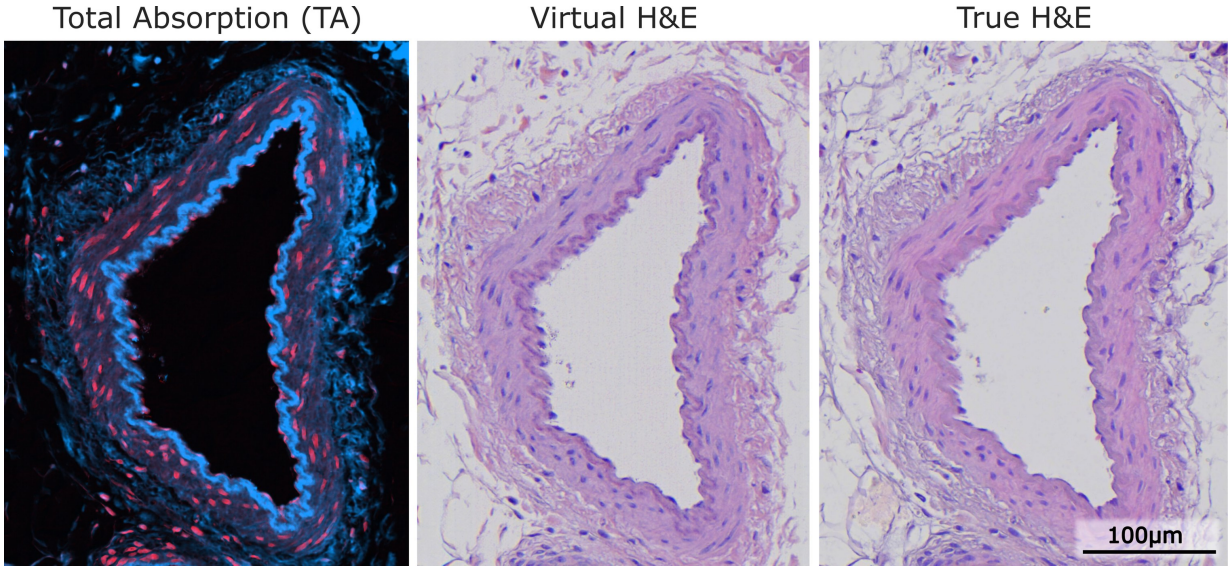

Figure 4.8: Example of the differences in the intrinsic PARS contrast, and chemical H&E staining. The PARS TA image highlights the inner wall of the artery or the internal elastic membrane. This feature is not highlighted in the H&E image.

Traditionally a stain such as Verhoeff-Van Gieson (VVG), which highlights normal or pathologic elastic fibers, would be required to visualize the internal elastic membrane of arteries [155]. In clinical applications, VVG stain is sometimes combined with Masson's trichrome stain [156], to differentiate collagen and muscle fibers within tissue samples. This is performed to visualize potential increases in collagen associated with diseases like cirrhosis and assess muscle tissue morphology for pathological conditions affecting muscle fibers. In contrast, all these structures are well highlighted in the PARS raw data. Currently, the H&E virtual staining model flattens these structures during the image translation process.

However, this highlights the potential use of the rich PARS raw data to replicate various clinically relevant contrasts beyond H&E staining.

4.4 Conclusion

In summary, a PARS data pre-processing and unpaired virtual staining pipeline is shown and applied to malignant human tissue samples. Here, measurement reference correction, and Noise2Void based image denoising, are successfully applied to improve image quality. Finally, a new algorithm is presented to reduce pixel level mechanical scanning position artifacts, which blur submicron scale features. These enhancements afford marked improvements in the clarity of small tissue structures, such as nucleoli and chromatin distribution. In conjunction, virtual staining pipeline is presented which uses a semi-registered CycleGAN model. While CycleGAN does not strictly require registration like Pix2Pix, providing the semi-registered data may enhances the colourization quality by reducing the presence of hallucination artifacts. Presented here, emulated H&E images are produced from label-free PARS images with quality and contrast that compare favorably to traditional H&E staining. The colourization performance represents the current best PARS virtual staining implementation. Applied to entire sections of unstained human tissues, the presented method enables accurate recovery of subtle structural and subnuclear details. With these improvements, the PARS virtual H&E images, may be effectively indistinguishable from gold standard chemically stained H&E scans. This represents an essential milestone in developing a new clinically ready label-free virtual staining microscope.

With a virtual staining pipeline capable of generating diagnostic-quality H&E WSIs from unstained PARS data now established, the next step is to evaluate whether these images support accurate clinical interpretation. As such, Chapter 5 addresses this question through a masked clinical concordance study comparing PARS virtual H&E images with gold-standard H&E pathology.

Chapter 5

Clinical Concordance and Masked Validation of PARS Virtual H&E with Gold-Standard Pathology in Breast Needle Core Biopsies

5.1 Introduction and Motivations

With the automated whole slide PARS imaging platform (Chapter 3) and the Cycle-GAN-based virtual H&E staining framework (Chapter 4), it is now possible to generate diagnostic-quality whole slide virtual H&E images directly from unstained FFPE sections. The next step toward clinical translation is to determine whether these virtual stains are suitable for pathologists to perform an accurate diagnosis. In this chapter, the diagnostic fidelity of PARS virtual H&E images is evaluated through the first masked clinical concordance study using one-to-one WSI pairs of breast tissue NCBs spanning a spectrum of known histologic findings.

In addition to qualitative comparisons between virtual and chemically stained images, quantitative evaluation is important for assessing virtual staining performance. When paired data are available, full-reference metrics such as SSIM [130] are commonly used to benchmark virtual staining quality [15]. However, such metrics do not reflect similarity of higher-level clinical features, nor do they capture diagnostic utility. Moreover, tissue alterations introduced during the staining process inevitably cause misalignments between the virtual and chemical references. Since these metrics operate at the pixel level, they

are sensitive to registration errors, and such misalignments can lead to worsened scores independent of the actual performance of the virtual staining. Therefore, while valuable, these metrics have clear limitations and provide an imperfect standard of comparison.

A more reliable way to demonstrate diagnostic equivalence is to quantify the level of agreement between the virtual and real H&E images through masked clinical concordance studies. In these studies, certified pathologists independently review virtual and standard slides without knowledge of their origin. In effect, this tests whether the virtual stains can substitute for conventional H&E in a clinical workflow. This type of comparison has not yet been done with PARS virtual H&E images, partly because damage-free whole slide imaging capabilities were previously unavailable. As such, prior to Chapters 3 and 4, virtual H&E staining of an entire PARS WSI had never been demonstrated, and a true comparison with the H&E diagnostic process at the WSI level was not possible.

5.1.1 Specific Background

A breast NCB is a medical procedure in which a small, cylindrical piece of breast tissue is removed for examination and diagnosis, typically with the aid of imaging guidance (e.g., ultrasound) [157]. The procedure is performed when an abnormality is found in the breast, such as a palpable mass, or an area of suspicious tissue seen on a mammogram or other imaging tests. It is an established standard of care for obtaining accurate preoperative histological diagnosis of suspicious breast lesions [158, 159, 160, 161, 162, 163]. In addition, it offers numerous advantages, including reduced cost and complication rates, over surgical biopsies primarily due its minimally invasive approach [164, 165, 166, 167].

Following the NCB procedure, the samples undergo standard processing into thin FFPE tissue sections, which are then stained for histological analysis. H&E staining is the primary means by which pathologists assess breast NCBs to distinguish between malignant and benign tissue, as well as to determine cancer type and grade [168].

Concordance rates refer to the degree of agreement between two or more pathologists who independently review the same tissue sample. Variability in the interpretation of breast core biopsies among pathologists can arise due to several contributing factors. These factors include the quality of the tissue sample obtained during the biopsy procedure and the level of experience of the pathologist. In addition, the amount of tissue available for histologic examination plays a role, wherein higher numbers of cores and longer cores tend to improve concordance among pathologists [169]. Therefore, in the context of breast NCBs, concordance rates are important to define because they reflect the diagnostic accuracy of

the procedure, which typically informs subsequent surgical treatment decisions. In comparing PARS virtual H&E and true H&E, a high concordance rate would indicate a strong agreement, suggesting that the virtual histology method is successfully replicating the diagnostic information present in the traditional H&E staining. Evaluating concordance rates is crucial for validating PARS virtual H&E as a viable alternative to traditional H&E staining techniques in diagnostic applications.

5.1.2 Study Overview and Contributions

This study presents the first masked clinical concordance analysis of PARS virtual H&E imaging compared with the gold standard chemical H&E. While other virtual staining works have incorporated pathologist evaluations, these have typically been focused on region-level assessments and more cursory questionnaires such as ranking overall diagnostic quality [15]. To the best of our knowledge, this study is the first to evaluate virtual H&E staining through full masked diagnoses and gradings performed on 40× magnification WSIs, as would be done in routine clinical practice.

In this work, a prospective study was conducted on seven independent breast NCBs representing a spectrum of histologic findings, including normal breast, Ductal Carcinoma In Situ (DCIS), IDC, and Invasive Lobular Carcinoma (ILC). Unstained tissue was scanned via PARS microscopy to generate virtual H&E images, and then standard H&E staining of these same seven core biopsies was performed. The diagnostic characteristics of these images were assessed by seven breast cancer expert pathologists, masked as to the origin of the images. A concordance analysis was performed to define the diagnostic performance of the two imaging modalities, standard H&E and PARS.

The study results demonstrated that PARS virtual H&E images were deemed to be of diagnostic quality, and pathologists were unable to distinguish the image origin, above that expected by chance. The diagnostic concordance on cancer vs. benign was high between PARS and conventional H&E (98% agreement) and there was complete agreement for within-PARS images. Similarly, agreement was substantial (kappa > 0.6) for specific cancer subtypes. PARS virtual H&E inter-rater reliability was broadly consistent with the published literature on diagnostic performance of conventional histology NCBs across all tested histologic features.

5.2 Methods

This study was approved by the Research Ethics Board of Alberta (Protocol ID: HREBA.CC-18-0277) and the University of Waterloo Health Research Ethics Committee (Protocol ID: 40275; Photoacoustic Remote Sensing Microscopy of Surgical Resection, Needle Biopsy, and Pathology Specimens). The ethics committees waived the need for patient consent as these archival tissues were no longer necessary for patient diagnostics. Researchers were not provided with any information pertaining to the identity of the patients. All human tissue experiments were conducted in accordance with the government of Canada guidelines and regulations, including "Ethical Conduct for Research Involving Humans (TCPS2)".

5.2.1 Patient Materials

Tissues were acquired from the Cross-Cancer Institute (Edmonton, AB, Canada) through collaboration with clinical partners. The samples were obtained from anonymous patient donors, with all patient identifiers removed to ensure anonymity. The seven independent breast tissue core biopsies used in this study represented a spectrum of known histologic findings. Specifically, three of the breast core biopsy samples had IDC only, two samples had both IDC and DCIS, one sample had ILC, and one was normal glandular tissue.

5.2.2 Sample Preparation Prior to PARS Imaging and Gold Standard H&E Staining

The breast core biopsy samples were obtained from patients using a hollow core needle and processed in a dedicated core facility. Immediately after excision, the collected tissue samples were placed in a formalin solution for fixation and preservation of the fresh tissue. The samples were stored in the formalin solution for a period of 24 to 28 h to ensure proper fixation. Following fixation, a skilled laboratory histotechnician performed a series of preparation steps. First, the samples were dehydrated using ethanol and then treated with xylene to remove any residual ethanol and fats. The samples were then subsequently embedded in paraffin wax, creating standard FFPE blocks. A microtome was then used to cut thin tissue sections ($\sim$4-5 μm) from the FFPE blocks. Tissue sections were placed on glass microscope slides and briefly baked at 60 °C to evaporate excess paraffin.

5.2.3 PARS Microscope Imaging

Whole slide label-free PARS images were acquired from the unstained tissue sections using the custom-built PARS microscope system presented in Chapter 3. A more detailed recount of the PARS optical design, system schematic, and imaging process is reported in Chapter 3, Section 3.2. In brief, the sample is precisely targeted with focused excitation pulses from a 50 kHz 400 ps 266 nm UV laser (Wedge XF 266, RPMC; Bright Solutions, Pavia, Italy). To achieve 40× imaging magnification, these excitation events are spaced 250 nm apart, while three-axis mechanical stages move the sample across the objective lens in an 's'-shaped scanning pattern. At each excitation event, time-resolved radiative, non-radiative relaxation, and scattering signals are measured and compressed into single pixel intensity values. These intensity values collectively form the three co-registered label-free images.

To measure the radiative signal intensity, the spectrum of emitted photons is broadly collected with an avalanche photodiode (APD130A2; Thorlabs, Newton, NJ, USA) and the peak amplitude value is recorded. To measure the non-radiative relaxation effect, time-domain photothermal and photoacoustic signals are recorded. This is performed using a 405 nm continuous-wave probe beam (OBIS-LS405; Coherent, Santa Clara, CA, USA) which is coaxially aligned with the excitation spot. From this, a single non-radiative intensity value is extracted as the percentage modulation of the transmitted probe beam intensity before and after excitation. The scattering intensity of the sample is determined by calculating the average probe transmission intensity prior to excitation. Both the excitation and detection beams are focused onto the sample using a 0.42 NA UV objective lens (NPAL-50-UV-YSTF; OptoSigma, Santa Ana, CA, USA). The transmitted probe light and radiative photons are collected using a 0.7 NA objective lens (278-806-3; Mitutoyo, Aurora, IL, USA). The radiative spectrum (>266 nm) and 405 nm detection wavelength are then spectrally separated prior to measurement.

The entire sample is scanned in $500 \times 500\,\mu$m parts which are later stitched back together into a single WSI. The 405 nm scattering contrast is primarily used to find and maintain sharp focus across the sample while the radiative and non-radiative images are primarily used for virtual staining.

5.2.4 Gold Standard H&E Staining and Digital Image Acquisition

After all samples were imaged with the PARS microscope, standard H&E staining was performed on each of the seven core biopsies. Digital whole slide H&E images were then

acquired at 40× resolution using a standard brightfield microscope (Morpholens 1; Morphle Digital Pathology, New York, NY, USA).

5.2.5 PARS Virtual H&E Colourization

The CycleGAN virtual H&E staining model presented in Chapter 4 was employed in this study to convert the PARS label-free data to virtual H&E images. While fixed-colour relationships have previously been applied to PARS data for emulating H&E staining [32], there are several advantages to using a deep learning-based virtual colouring process. For instance, a virtual staining algorithm can adaptively suppress data that is not directly necessary for generating a virtual H&E, as demonstrated in the previous Chapter 4, Figure 4.8. Additionally, the virtual colouring process has the capability to consider structural information when combining the raw PARS contrasts into a colourized H&E.

The CycleGAN virtual staining model in this study was trained using the same workflow and data preparation process as in the previous Chapter 4, with the exception of the Noise2Void denoising algorithm. The virtual H&E model was trained using a distinct set of WSI pairs that were not involved in the masked pathologist study. These additional training samples underwent the same tissue processing, imaging, and staining procedures as the core needle biopsies.

In brief, the PARS label-free WSIs are first loosely registered to their corresponding ground truth H&E pairs using a simple affine transform with three registration points. Images are then cut into 512×512 px ($128 \times 128\,\mu$m) tile pairs for use in model training. Prior to slicing, the PARS label-free contrasts are combined into a single TA coloured image where the radiative channel is blue, and the non-radiative channel is red. An example TA WSI and corresponding training pairs can be seen in Figure 5.1 alongside its corresponding ground truth H&E image. The virtual staining model in this study was trained on roughly 1000 training pairs. Once the virtual staining model is trained, the same model was then applied to all seven breast core needle biopsies, forming the virtual and real H&E pairs.

5.2.6 Evaluation by Expert Pathologists

The PARS virtual H&E and true H&E images were randomly oriented and displayed in a pre-specified, custom random order generation algorithm designed to maximize the distance between the two image pairs (PARS and true H&E) for each individual sample. Each of the 14 images were placed on a customized web-based histology visualizing software platform without any identification except core biopsy #1 through core biopsy #14. The order of

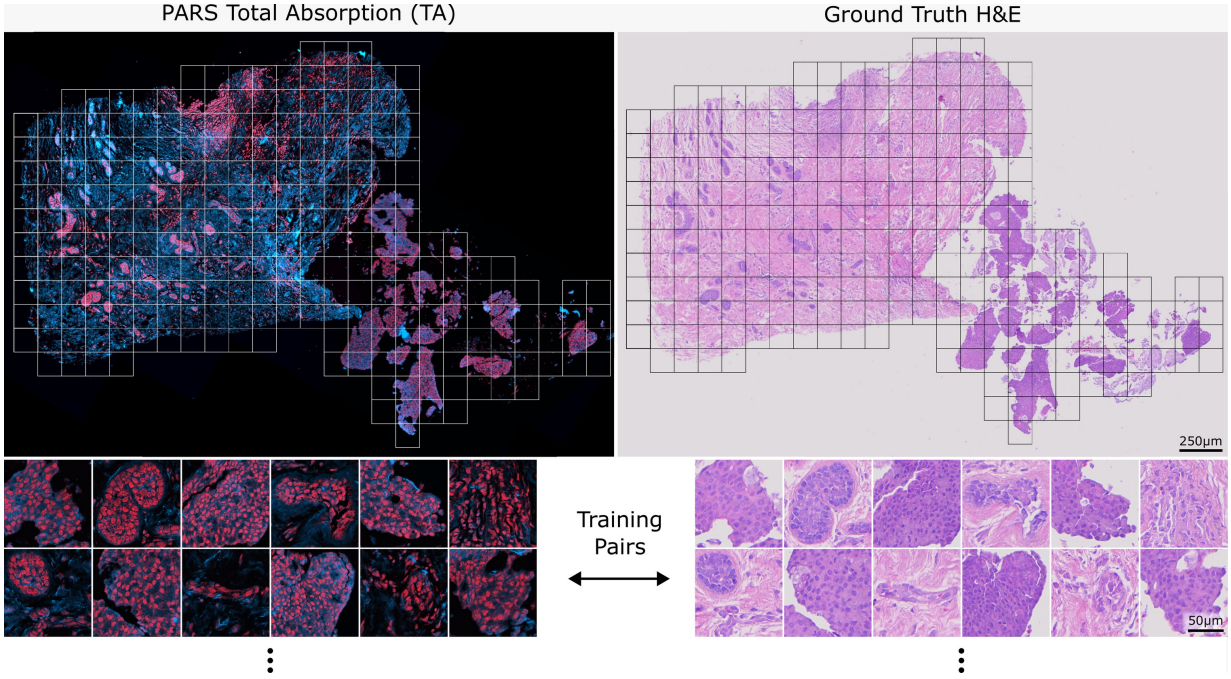

Figure 5.1: An example PARS TA image side-by-side with its corresponding ground truth H&E WSI. Example 512×512 px pairs that can be used to train the model can be seen below each image.

Table 5.1: Survey questionnaire given to pathologists for each of the 14 total images.

1. The primary tissue diagnosis is:

Invasive ductal carcinoma	Invasive lobular carcinoma	DCIS	Normal glandular tissue	Image inadequate for diagnosis
◯	◯	◯	◯	◯

2. DCIS necrotic score:

No in situ disease present	Grade 1	Grade 2	Grade 3	Not assessable
◯	◯	◯	◯	◯

3. DCIS nuclear grade:

No in situ disease present	Grade 1	Grade 2	Grade 3	Not assessable
◯	◯	◯	◯	◯

4. Evaluation for invasive disease:

	No invasive disease	Score 1	Score 2	Score 3	Not assessable
Tubule formation	◯	◯	◯	◯	◯
Nuclear pleomorphism	◯	◯	◯	◯	◯
Mitotic rate	◯	◯	◯	◯	◯

5. Type of image: Is this image from FFPE H&E-stained tissue?

Yes, this is H&E	No, this is not H&E	Uncertain
◯	◯	◯

IDC, invasive ductal carcinoma; ILC, invasive lobular carcinoma; DCIS, ductal carcinoma in situ.
◯ Symbol indicates the options provided to pathologists for each question

sample display was P2, P5, T1, T4, T3, T6, T2, P1, P7, P4, T5, T7, P3, and P6, where 'P' corresponds to PARS virtual H&E and 'T' corresponds to true H&E. Each of 14 images were provided independently to breast cancer focused board-certified anatomic pathologists, and 7 surveys were completed. The pathologists were masked to the clinicopathologic details of the cases and the origin of the digital images (either true H&E or PARS virtual H&E). Each pathologist was asked to score each image on the parameters shown in Table 5.1, including histologic diagnosis, grade of in situ disease, grade of invasive disease, and the origin of the digital image (Table 5.1).

5.2.7 Statistical Analysis

Concordance analysis is a statistical method used to measure the agreement between two or more raters or observers in their interpretation or classification of a set of data. Concordance may be measured through Cohen and Fleiss kappa coefficients. Cohen's kappa coefficient is a measure of inter-rater reliability that takes into account the possibility of agreement occurring by chance [170]. It is used to determine whether two raters agree beyond what would be expected by chance alone. Fleiss' kappa is an extension of Cohen's kappa to compare more than two raters [171].

Kappa values range from -1 to 1, with a value of 1 indicating perfect agreement and a value of 0 indicating agreement no better than chance. Negative values indicate agreement worse than chance. Interpretation of kappa values vary, but a value in excess of 0.6 is considered "substantial" [172] or "good" [173].

This method has several advantages over other measures of agreement, including its ability to account for chance agreement and its robustness to variations in the prevalence of different categories of data [170]. All calculations were performed in R statistical software (version 4.2.0) [174].

5.3 Results

5.3.1 Example Whole Slide Image Pairs

Figure 5.2 and 5.3 show two exemplary sets of PARS virtual H&E and real H&E images employed in this study. At the top of each figure is the raw TA PARS image serving as the input to the virtual staining algorithm. Both of these figures show examples of

invasive ductal carcinomas, with higher magnification regions showcasing irregular malignant glandular structures infiltrating a fibrofatty stroma, characteristic of invasive breast carcinoma. One benefit to the virtual H&E stains is that they all share consistent stain colouring, which matches the colouring of the training dataset. In contrast, staining colours for true H&E images can vary depending on specifics of the preparation, digitization and storage of the tissue samples [175]. As such, the virtual H&E images in Figure 5.2 and 5.3 share similar staining colours, whereas their true H&E counterparts exhibit a slight difference in colours. Nonetheless, both the virtual and H&E images achieve excellent epithelial and stromal contrast and highlight the same tissue structures.

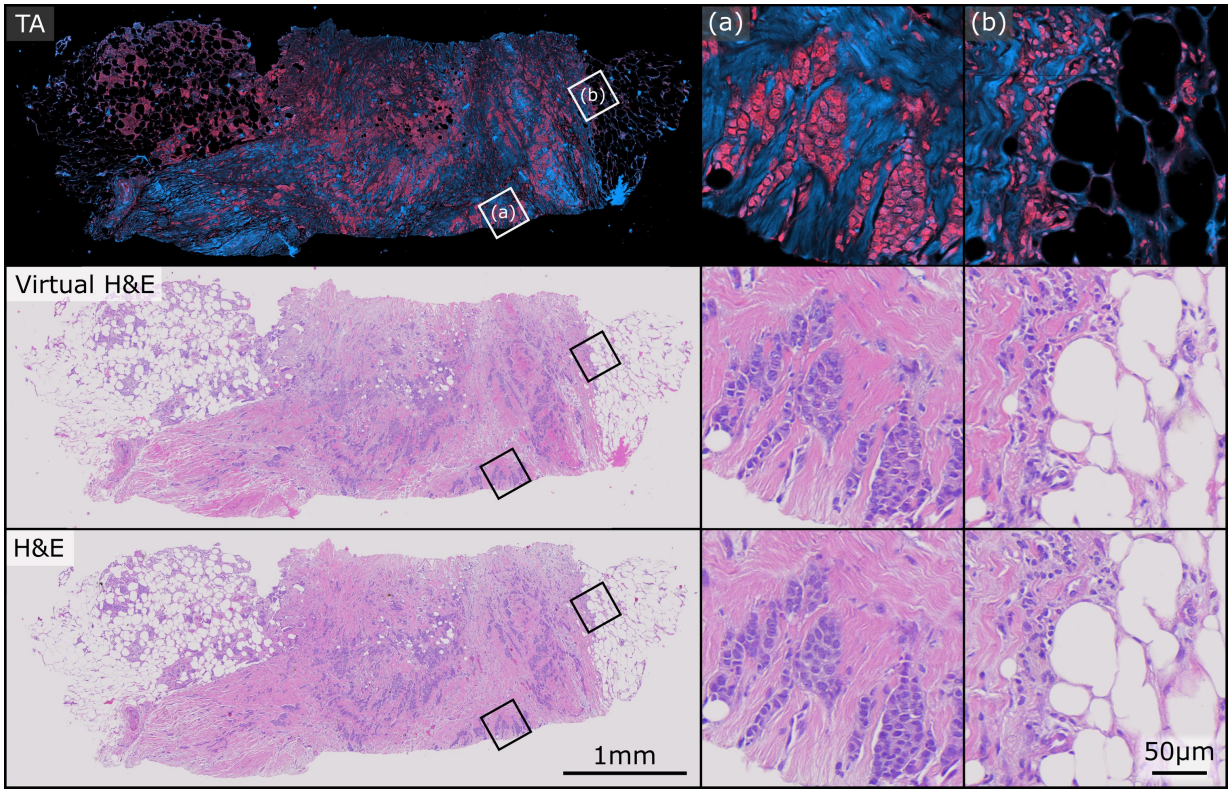

Figure 5.2: Example PARS TA, virtual H&E, and true H&E pair used in this study. The sample exhibits closely matched staining colours between the virtual and real representations. (a) and (b) depict two regions of higher magnification on the sample.

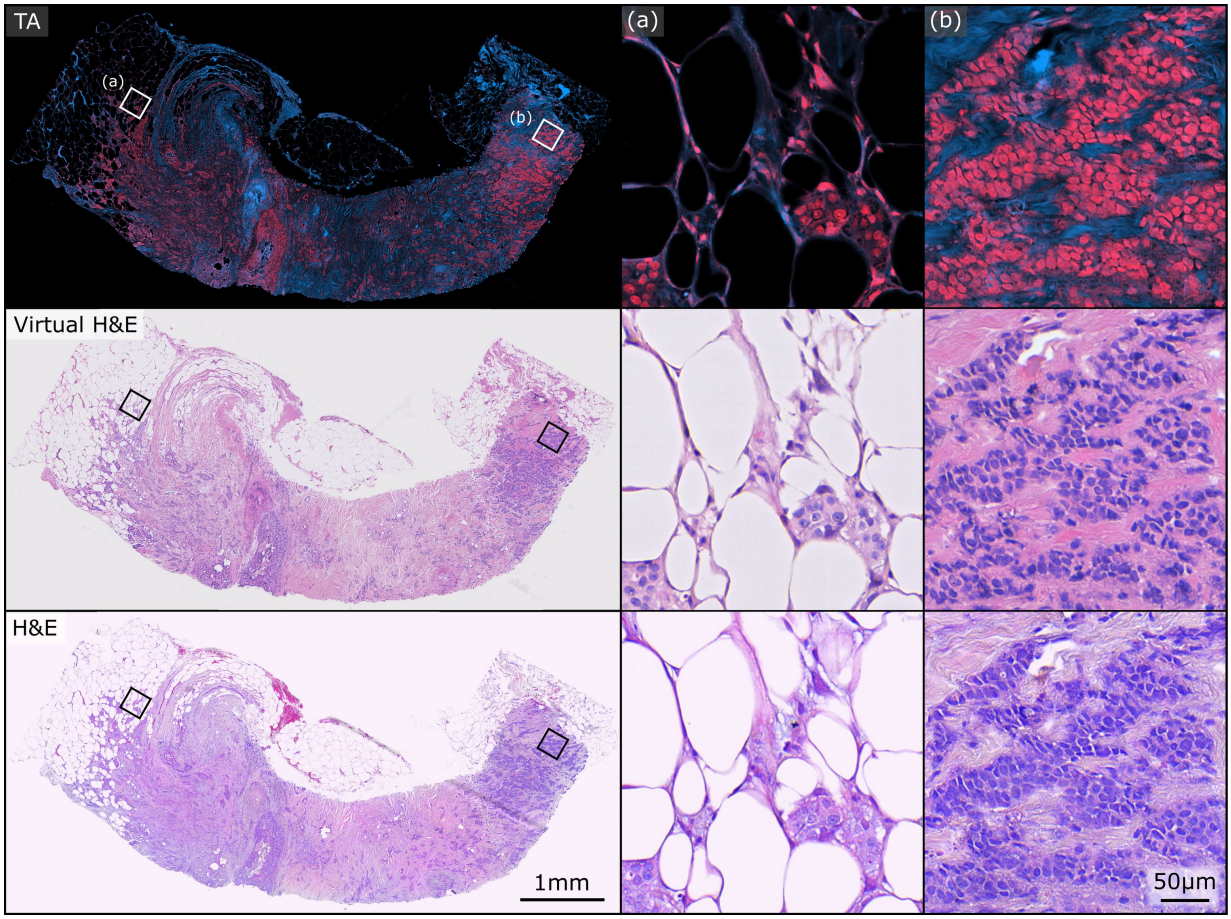

Figure 5.3: Example PARS TA, virtual H&E, and true H&E pair used in this study. Both the virtual and real H&E images exhibit excellent epithelial and stromal contrast and highlight the same tissue structures. (a) and (b) depict two regions of higher magnification on the sample.

5.3.2 Image Origin

For each image, either true H&E or PARS virtual H&E, respondents were asked to identify the origin of each image, whether it was a true FFPE H&E-stained slide (yes), not a true FFPE H&E-stained slide (no), or uncertain. Three raters responded 'Yes' when asked if a PARS image was a true H&E image for all seven images. The fourth respondent reported 'Uncertain' for all seven PARS and H&E images. For the remaining three pathologists, PARS images were misidentified as true H&E images 0/7, 1/7, 3/6 times and true H&E images were misidentified as virtual H&E images 1/7, 3/7, 3/6 times (the final pathologist only responded to this question for six image pairs). These results show that masked pathologists were unable to reliably distinguish between conventional H&E and PARS virtual H&E.

5.3.3 Primary Diagnosis

Respondents were asked to make a primary diagnosis for both the PARS virtual H&E images as well as the true H&E images. All respondents were able to make a primary diagnosis for each WSI with the exception of the fourth respondent, who selected 'Image inadequate for diagnosis' precisely once.

If all primary diagnosis responses are combined into either a high-level 'cancer' or 'benign' category, out of the 48 image-pair assessments (excluding one diagnosis of 'image inadequate'), there was only one disagreement between an H&E and PARS pair (kappa = 0.921). In total, 40 image pairs were both assessed as cancerous, while the remaining 7 image pairs were both assessed as benign. This indicates there was reliable discrimination between cancerous and benign cases. Here, 'cancer' comprises the diagnosis of ILC, IDC, and DCIS.

For the specific cancer subtypes, a concordance analysis for the primary diagnosis among the seven pathologists was performed for both true H&E only and PARS virtual H&E only. The Fleiss' kappa value for agreement between rater for true H&E images was 0.639. The Fleiss' kappa value for agreement between rater for PARS virtual H&E images was 0.620. Next, a pairwise comparison was conducted, calculating Cohen's kappa, to assess the concordance of the primary diagnosis between the PARS virtual H&E and true H&E images. Four of the seven pathologists (raters 3, 5, 6, 7) agreed on the primary diagnosis for all seven image pairs (kappa = 1). The first respondent disagreed on the primary diagnosis for a single image pair (kappa = 0.611). The second and fourth respondents disagreed on the primary diagnosis for two image pairs (rater 2, kappa = 0.364; rater 4,

kappa = 0.417). Table 5.2 shows a comparison between the primary diagnosis given to the H&E and PARS image pairs.

Table 5.2: Summary of pathologist responses to question "the primary tissue diagnosis is".

	H&E Diagnosis					
PARS Diagnosis	IDC	ILC	DCIS	Benign	Image Inadequate	Total
IDC	36	0	1	1	0	38
ILC	1	1	0	0	0	2
DCIS	1	0	0	0	0	1
Benign	0	0	0	7	0	7
Image Inadequate	1	0	0	0	0	1
Total	39	1	1	8	0	49

Note: IDC, invasive ductal carcinoma; ILC, invasive lobular carcinoma; DCIS, ductal carcinoma in situ.

5.3.4 Evaluation of Tissue Gradings

A similar analysis to the primary diagnosis response was performed to assess the concordance for the evaluation of invasive tissue components: tubule formation score, nuclear pleomorphism score, and mitotic rate score. This analysis was also performed on the final Nottingham histological grade. In Table 5.3, a Fleiss' kappa coefficient was computed for the within-H&E-only invasiveness gradings and the within-PARS-only invasiveness gradings. This was performed to first observe the concordance among pathologists for H&E only and for PARS only and contrast it with the concordance result for a pairwise comparison of concordance between H&E and PARS. For the pairwise comparison, a Cohen's kappa coefficient was computed for each rater and the average coefficient is reported in Table 5.3. The kappa coefficients were computed from responses of all image pairs excluding image pair six. Image pair six was not involved because it was given the primary diagnosis of 'normal glandular tissue' from all raters except one (rater 2, PARS image).

In some cases, for both true H&E and PARS images, pathologists were unable to assess or submit a grading between 1 and 3. Table 5.4 summarizes the total number of 'not assessable' responses for each image type across all 49 image pair assessments. 'Both' is the number where the rater categorized both H&E and PARS images in the same pair as not assessable for that evaluation.

For each rater, there was widespread agreement between which images were assessable or not. The accessibility was highest for the tubule formation score (48/49 H&E, 48/49 PARS), slightly lower for nuclear pleomorphism score (44/49 H&E, 43/49 PARS), and much lower for the mitotic rate score and the Nottingham histological grade (34/49 H&E, 35/49 PARS). Additionally, the number of image pairs where pathologists agreed that both PARS and H&E was either assessable or not assessable followed the same trend. Agreement was observed in 47/49 image pairs for the tubule formation score, 44/49 for nuclear pleomorphism score, and 36/49 for the mitotic rate score and Nottingham histological grade.

Table 5.3: Inter-rater reliability of invasive cancer scores.

Evaluation Component	**Comparison**	**Kappa Coefficient***
Invasive Tubule Formation Score	Within H&E	0.553
	Within PARS	0.300
	H&E–PARS	0.420
Invasive Nuclear Pleomorphism Score	Within H&E	0.051
	Within PARS	0.058
	H&E–PARS	0.188
Invasive Mitotic Rate Score	Within H&E	0.125
	Within PARS	0.148
	H&E–PARS	0.032
Nottingham Histological Grade	Within H&E	0.161
	Within PARS	0.126
	H&E–PARS	0.073

* The pairwise H&E–PARS comparisons are the mean Cohen's kappa coefficient values among raters.

5.4 Discussion

5.4.1 Study Summary and Key Findings

In this pilot validation study, seven pairs of PARS virtual and conventional H&E images were assessed by seven pathologists masked with respect to the origin of the images. Comparative analysis of PARS and H&E using the standardized synoptic reporting of the single

Table 5.4: Distribution of "not assessable" responses.

	DCIS Necrotic	DCIS Nuclear	Invasive Tubule Formation	Invasive Nuclear Pleomorphism	Invasive Mitotic Rate	Nottingham Histological Grade *
H&E	1	7	1	5	15	15
PARS	2	4	1	6	14	14
Both	1	3	0	3	8	8

* Nottingham grade "not assessable" if any of the invasive components are "not assessable".

core biopsy images demonstrated several key findings. Both PARS virtual and conventional H&E images were of diagnostic quality, and reliably allowed the discrimination of cancer (the aggregate diagnoses of IDC, ILC, and DCIS) from benign breast tissue. With respect to the primary diagnostic categories above, the raters showed almost identical agreement across H&E images as they did across PARS images. Furthermore, the diagnoses made by our pathologists viewing conventional H&E were comparable to the diagnoses of pathologists viewing PARS virtual H&E; with the granular categorization of each image into the five primary diagnostic results, overall concordance among pathologists was substantial (kappa >0.6) and was not meaningfully higher with conventional H&E images rather than the PARS virtual H&E images. Four of the seven pathologists agreed on the primary diagnosis for all seven image pairs, one pathologist disagreed on the primary diagnosis for a single image pair, and two pathologists disagreed on the primary diagnosis for two image pairs.

5.4.2 Interpretation of Findings in Context

Diagnostic reproducibility in breast cancer histology remains suboptimal and underpins the difficult of evaluating new histologic techniques. Within the context of our study, PARS-based breast core biopsy imaging was equivalent to more traditional digital histopathology using H&E-stained slides. Inter-observer discordance appeared lower than previously reported intra-observer discordance. For example, pathologists given the same breast cancer biopsy material on which they had previously issued a diagnostic report, separated by a six month interval, exhibit surprisingly low intra-observer agreement rates of 92% for invasive breast cancer, 84% for DCIS, and 53% for benign with atypia [176]. Similarly, a pathology review of the original breast cancer NCB in a pre-operative quality assurance process identified 403 discordance cases out of 4950 (∼8%) [177]. Furthermore, histologic interpre-

tation and grading of core needle biopsies is dependent on the quantity of available tissue, which in our study was limited to a single core biopsy per case. The authors could find no published literature on the inter-rater reliability of breast cancer core biopsy gradings, so it is difficult to put the grading data we generated in context, other than to state that grading concordance was poor (0.6 or less) with both conventional and PARS virtual H&E. As determination of mitotic rate requires the counting of mitoses in 10 high-power fields with invasive cancer, single core biopsies can have insufficient tissue for reliable assessment of mitotic rate. Consequently, in clinical practice, core biopsy pathology reports frequently omit overall grade [167, 168], deferring definitive grading to the larger, surgical excision specimens.

5.4.3 Strengths and Limitations

Among the strengths of this study was the use of masked pathologists, the use of 40× digital scanning equivalent to standard digitized conventional H&E images, and efforts to reduce confounding observer recognition of serially presented images by re-orienting pairs of biopsies and maximizing their sequence separations. Furthermore, our study used the identical tissue for the two images, rather than adjacent slides, allowing direct cell-to-cell concordance of the images. Limitations of our study include its relatively small sample size, and the selection of tissues representing only the most common histologic findings on breast biopsy. Future research should aim to conduct larger studies with additional samples to substantiate and build upon our findings.

5.5 Conclusion

This prospective cohort study provides evidence supporting the effectiveness of PARS microscopy for the diagnostic interpretation of human breast tissue core biopsies. The images were deemed to be of diagnostic quality by expert breast cancer pathologists. The key consideration of cancer vs. benign tissue was reliably distinguished in both conventional and PARS virtual H&E histology images. Similarly, cancer subtypes were reliably distinguished with both techniques.

While the initial diagnosis of breast cancer is typically made via conventional H&E evaluation of core biopsies, the complexity of the tissue preparation and staining frequently requires one week or more before the pathology report is available. PARS is an imaging technique that can be applied not only to fixed, unstained tissues, as in this specific study,

but also to freshly resected specimens and in vivo examination of tissue. As such, PARS has the potential to dramatically reduce diagnostic timelines.

Finally, PARS is a non-destructive process that generates a rich dataset suitable for analysis by artificial intelligence algorithms, which are being successfully applied to cancer diagnosis of digital histology [178, 179]. The virtual colourization process already leverages in-house developed AI algorithms, and analysis via AI would be a natural extension of this process. The unstained tissue remains suitable for any additional subsequent analyses, which allows downstream standard-of-care processing of samples to be unaffected. Consequently, PARS virtual histology has the potential to both improve the speed and the accuracy of diagnostic interpretation of breast histology, reduces the consumption of limited biopsy tissue, and is, in principle, widely applicable to histologic evaluation of benign and malignant tissues of any origin. Moreover, this study was limited to human breast cancers but should be directly applicable to all other types of biopsied organs since tissue preservation and H&E staining are the same procedure for all types of tissues.

Chapter 6

Label-Free Whole Slide Virtual Multi-Staining Using Dual-Excitation Photon Absorption Remote Sensing Microscopy

6.1 Introduction and Motivations

The previous Chapters 3 to 5 established a PARS whole slide imaging platform, a CycleGAN-based virtual staining framework, and a masked clinical concordance study confirming the diagnostic equivalence of PARS virtual H&E to chemical H&E in breast NCB samples. These efforts focused on H&E only, the gold standard and most widely used stain in histology. In this chapter, PARS virtual staining is extended beyond H&E to multiple specialized histochemical stains, and a 355 nm excitation source is introduced to capture complementary biomolecular contrasts for model input. Additionally, a new virtual staining model is employed, designed to better utilize loosely registered pairs and strike a balance between the paired Pix2Pix and unpaired CycleGAN approaches previously covered.

Motivation for Multiplexed Staining

While H&E is the most widely used and indispensable stain in pathology, it is not the only routinely used stain in diagnostic workflows. There exist specialized stains to provide more targeted contrast (see Section 2.1.2), such as Masson's trichrome for collagen analysis, PAS for carbohydrate-rich structures, and JMS stain for highlighting glomerular and tubular

membranes in renal pathology [6], [9]. On their own, each of these stains provides complementary diagnostic information not available from H&E alone. However, their combined visualization on the same tissue sample would be especially valuable, as findings from one stain can be focal, whereas multiple stains together provide stronger diagnostic confidence [45, 108].

However, conventional staining protocols are destructive, require new sections for each stain, and are time- and labor-intensive [15, 13]. In practice, stain multiplexing is limited: tissue sections cannot typically be stained, destained, and re-stained for different protocols, and cutting multiple sections is not always possible for valuable or scarce biopsies (e.g., core biopsies, brain tissue) [15]. These limitations, combined with the costs, toxic reagents, and turnaround delays of chemical staining, create a strong motivation for label-free virtual multiplexed staining. Such methods would emulate multiple histochemical stains from a single unstained section while leaving tissue available for downstream assays if needed.

Secondary Excitation Laser for Additional Label-Free Contrast

The effectiveness of a virtual histochemical staining algorithm depends, in part, on the contrast that the label-free platform is able to provide to the staining algorithm. Ideally, a given modality is able to recover sufficient biomolecular-specific contrast to closely match the desired chemical contrast. As previously discussed, with the 266 nm excitation wavelength, excellent nuclear specificity and broad connective tissue contrast can be achieved. However, supplying additional information to the virtual staining model could aid in distinguishing between different structures and improve its capacity to learn the relationship between the PARS raw data and the given chemical stain. This is particularly important when extending beyond H&E to other virtual stains, though it is also likely to yield benefits for H&E emulation.

For this reason, a secondary excitation wavelength at 355 nm is proposed to provide an additional set of non-radiative and radiative contrasts. Like 266 nm (UVC), longer-wave ultraviolet (UVA) wavelengths such as 355 nm exhibit broad absorption across various chromophores in cell and tissue samples [17, 69, 70]. On the radiative relaxation side, 355 nm provides visualizations of collagen and elastin structures in the ECM [17], in different proportions to 266 nm, which may help strengthen discernibility between collagen, muscle tissue, and other ECM components during the virtual staining process. Additionally, the 355 nm wavelength targets autofluorescence of biomolecules involved in cellular metabolic processes [180], such as the redox ratio (the ratio of coenzymes NADH and FAD), which is heightened during carcinogenesis [181, 182, 183]. While this work does not encompass fresh tissue or live cell imaging, the integration of 355 nm into a PARS system will support future efforts in this domain.

On the non-radiative side, 355 nm provides visualization of RBCs through hemoglobin absorption, and also offers contrast of melanin absorbers [136]. Specificity toward these biomolecules is currently lacking, and therefore 355 nm may assist in colourizing RBCs in tissues and melanin pigments in skin, for example.

Striking a Balance Between Paired and Unpaired Training Schemes

While Pix2Pix, CycleGAN, and their variants are among the most widely used models for medical I2I translation [15], both have inherent trade-offs and neither is ideal. In Chapter 4, CycleGAN was employed to better accommodate misalignment in the image pairs, and its performance was compared with Pix2Pix. However, the disadvantage of CycleGAN is that it operates in an entirely unpaired regime and is therefore less constrained, despite the cycle consistency loss.

As additional histochemical stains are explored in this chapter, the direct mapping of contrast between domains may not be as straightforward as with the H&E stain. This creates motivation to adopt a more constrained model, one that uses a supervised learning approach while remaining robust to small misalignments in the paired training data. A recent I2I translation model, RegGAN ("registration" GAN) [34], addresses this by treating misalignments in the target image as a form of "noisy" labeling. To accommodate the noisy labels, it employs an additional registration network to adaptively fit the misalignment noise distribution during training. This model has not yet been applied to virtual staining, and its applicability in this context is investigated in this research module.

6.2 Study Overview and Contributions

This work presents the first demonstration of PARS virtual staining across multiple specialized stains, including Masson's trichrome, PAS, and JMS, in addition to H&E. This advance is achieved with a newly developed dual-excitation PARS system, representing the first application of long-wave UVA 355 nm excitation alongside the established 266 nm UVC source. The addition of 355 nm extends PARS contrast beyond the nuclear and connective tissue signals of 266 nm, enhancing visualization of stromal architecture (e.g., collagen, elastin) and capturing RBCs, melanin-containing elements, and other tissue features through complementary radiative and non-radiative absorption. The system is designed to interlace the 266 nm and 355 nm pulses on the sample, enabling concurrent acquisition without compromising imaging speed.

Virtual staining is demonstrated in unseen WSIs across a diverse set of tissues and disease contexts, including human kidney with Clear Cell Renal Cell Carcinoma (ccRCC),

human skin with nodular melanoma and fungal infection, and multiple murine organs such as kidney, Gastrointestinal (GI), and brain, using large datasets that enable robust evaluation in both healthy and pathological conditions. An improved virtual staining model, RegGAN [34], is used. This supervised framework integrates a registration network, combining the accuracy of paired approaches with the misalignment tolerance of unpaired methods, and is shown to outperform Pix2Pix and CycleGAN across all tissue types and disease cases. Furthermore, results demonstrate that the dual-excitation input consistently outperforms 266 nm or 355 nm alone, with quantitative improvements in similarity and perceptual metrics and improved reconstruction of histology-specific features, such as nuclei, collagen, RBCs, and fungal hyphae. Importantly, masked evaluation by three expert pathologists confirmed that virtual stains achieve comparable diagnostic quality to their chemical counterparts and that pathologists were unable to reliably determine whether a given image was chemically or virtually stained. For each tissue–stain combination, corresponding chemical and virtual WSIs are publicly available at the BioImage Archive [184], under accession number *S-BIAD2232*, accessible at https://doi.org/10.6019/S-BIAD2232. All uploaded WSIs were entirely held out from the training and validation sets. Data are provided in OME-TIFF format and can be viewed with standard pathology software such as QuPath.

Having demonstrated strong diagnostic agreement between PARS virtual H&E and conventional H&E in this masked clinical study, Chapter 6 extends this framework beyond H&E alone. Specifically, it explores the generation of multiple virtual histochemical stains from a single label-free PARS image, along with system and model developments required to support this broader staining capability.

6.3 Methods

6.3.1 Dual-Excitation PARS System Architecture and Configuration

The dual-excitation PARS histology microscope system used in this study is illustrated in Figure 6.1a. The system includes two excitation sources: a 400 ps pulsed 266 nm UVC laser (Wedge XF 266, Bright Solutions) and a 1.5 ns pulsed 355 nm UVA laser (ULPN-355-10-1-10-M, IPG Photonics), both operating at a 50 kHz pulse repetition rate. These excitation wavelengths were selected to provide complementary contrast for virtual staining. As shown in Chapters 3 and 4 and previous works [32], 266 nm offers strong absorption

of nucleic acids, providing important nuclear-specific non-radiative contrast, along with radiative emissions from ECM structures. The 355 nm source is similarly broadly absorbed, providing complementary autofluorescence from ECM components such as collagen and elastin [17], along with non-radiative signals from absorbers like hemoglobin for RBC visualization, melanin, and other pigments [136].

The output from the 266 nm source first passes through a CaF_2 prism (PS862, Thorlabs) to spectrally separate residual 532 nm green light, which is directed to a beam trap (BT: BT610, Thorlabs). The 266 nm beam is then 3× expanded using a variable beam expander (3×VBE: BE03-266, Thorlabs). The adjustable collar of the expander allows for collimation control of the 266 nm laser for axial beam alignment. The expanded beam is directed toward a Nd:YAG harmonic separator (HS_2: 37-721, Edmund Optics) where it is combined with the 355 nm source.

The output from the 355 nm source is first condensed by 2× and then re-expanded with a 2× variable expander (2×VBE: BE02-355, Thorlabs), resulting in an overall magnification of 1X. As with the 266 nm, this is done so the adjustable collar of the expander can be used to fine-tune the collimation of the 355 nm laser for axial alignment purposes. The 355 nm beam is then reflected off a second Nd:YAG harmonic separator (HS_1: 37-721, Edmund Optics) and transmitted through HS_2 to align with the 266 nm path.

A continuous wave 405 nm detection source (OBIS-LS 405, Coherent) is used to probe the sample for scattering signals and non-radiative contrast. The fiber-coupled laser is first collimated (Col.: C40APC-A, Thorlabs) and directed through both HS_1 and HS_2 to co-align with the two excitation beams.

All three beams (266 nm, 355 nm, 405 nm) are then co-focused onto the sample using a 0.42NA UV objective lens (OL_1: NPAL-50-UV-YSTF, OptoSigma). The forward-propagating light, including scattered 405 nm and 355 nm and radiative emission from both UV sources, is collected using a 0.7 NA top objective lens (OL_2: 278-806-3, Mitutoyo). The collected light is coupled into a multimode optical fiber (MMF: M133L01, Thorlabs) using a high-NA achromatic coupler (AC_1: F950FC-A, Thorlabs), and then re-collimated into free space by AC_2 for downstream spectral separation.

The scattered 355 nm light is immediately sent into a beam trap using a 355 nm notch filter (NF_1: 39-387, Edmund Optics). The transmitted 405 nm beam is then separated from the radiative emissions using a 405 nm notch filter (NF_2: NF405-13, Thorlabs). The radiative emissions and non-radiative scattering modulation are each recorded on avalanche photodetectors (PD: APD130A2, Thorlabs) following condenser lenses (Cond.: ACL25416U-A, Thorlabs). An additional avalanche photodetector is used in the forward path to record the 266 nm pulse amplitude and 405 nm power level; the 355 nm source was not recorded

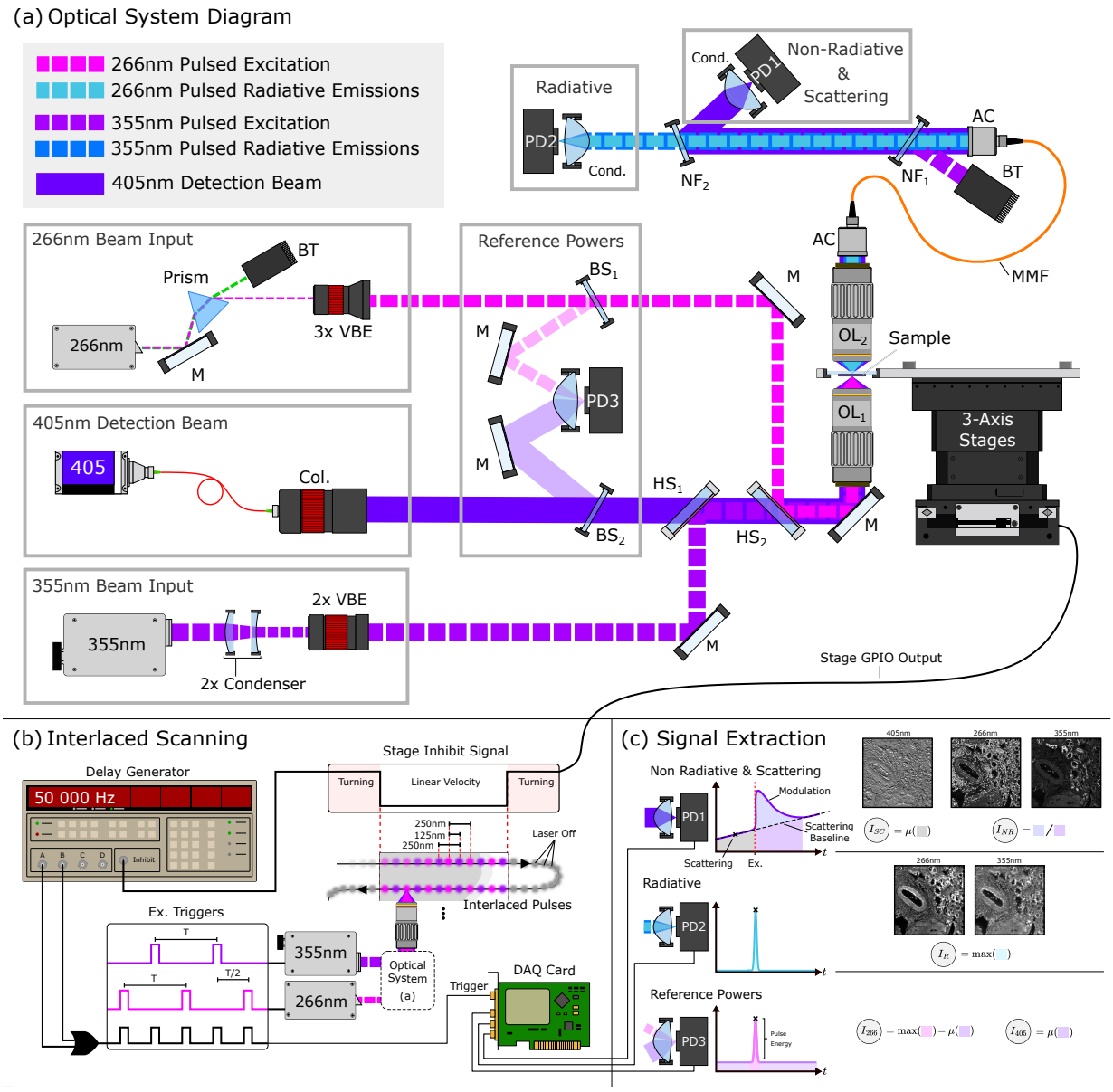

Figure 6.1: Dual-excitation PARS architecture, interlaced scanning pattern, and signal extraction. (a) Simplified PARS optical diagram. Components: AC (achromatic collimator), BT (beam trap), BS (beam sampler), Col. (collimator), HS (harmonic separator), MMF (multi-mode fiber), M (mirror), NF (notch filter), OL (objective lens), PD (photodiode detector), VBE (variable beam expander), Cond. (condenser). (b) Interlaced excitation scan pattern. A delay generator alternately triggers 266 nm and 355 nm pulses to create interlaced pattern on the sample. Pulses are inhibited during stage turnaround via a programmed stage GPIO signal. An acquisition card is triggered at each pulse to collect time-series data. (c) Signal extraction from system photodetectors. ∼500 ns segments are recorded from three photodetectors and compressed into pixel values for each contrast. Non-radiative contrast is calculated as the modulation from the scattering baseline; radiative signal is defined as the peak value; and reference powers (266 nm pulse amplitude and 405 nm power) are extracted for post-acquisition power correction.

given its lower pulse variability. These beams are sampled using beam samplers (BS1: BSF10-UV and BS2: BSF10-A, Thorlabs) for post-acquisition power correction.

To estimate the effective spot sizes of the detection and excitation beams at the focal plane, Edge Spread Functions (ESFs) were collected, sampled densely at 50 nm/pixel, across sharp edge features. From this, the FWHM of the resulting Line Spread Functions (LSFs) were calculated, and the beam waist ($1/e^2$ width) was used to estimate peak fluence based on the pulse energies used during imaging.

6.3.2 Interlaced Scanning, Signal Acquisition, and Image Reconstruction

An overview of the scanning process, signal acquisition, and image reconstruction pipeline is illustrated in Figure 6.1b and 6.1c. A programmable delay generator (DG645, Stanford Research Systems) is used to alternately trigger the 266 nm and 355 nm lasers, each at 50 kHz, producing spatially interlaced excitation spots along the scan trajectory. By interlacing the pulses rather than performing two sequential scans, the dual-excitation system acquires radiative and non-radiative contrast from both excitation sources essentially simultaneously, without compromising imaging speed.

During a scan, the mechanical stages move the samples in an S-shaped raster pattern. In the linear velocity regions, the stages move at 12.5 mm/s, spacing the alternating 266 nm and 355 nm pulses by 125 nm, and maintaining a 250 nm step between successive pulses of the same wavelength.

During the turnaround (non-linear) regions, both excitation lasers are disabled to avoid high-density UV pulses and potential photobleaching. A TTL high signal from the stage is used to inhibit the delay generator, effectively gating off the laser triggers during these periods.

At each excitation pulse, a high-speed digitizer (Gage CSE1442, 200 MS/s) captures a $\sim$500 ns time segment from each system photodetector, as shown in Figure 6.1c. In total, three photodetectors (PDs) are used to collect signals that produce a total of five distinct PARS contrasts in a single pass: 405 nm scattering, 266 nm and 355 nm non-radiative (PD1), and 266 nm and 355 nm radiative, along with 266 nm and 405 nm input reference powers (PD3).

PD1 captures the forward-scattered 405 nm signal and non-radiative response. The scattering contrast is calculated as the average pre-excitation scattering intensity. These scattering images are extracted during the autofocus phase of the whole slide scan to ensure

high-SNR acquisition. Non-radiative contrast is computed from the transient modulation of the scattering signal relative to a predicted baseline following excitation. As described in [93], the scattering baseline is estimated using a first-order linear fit of the scattering signal before and after excitation. The non-radiative signal is then calculated as the percentage deviation from this predicted baseline. This approach has been shown to improve SNR [93], particularly at structural edges where scattering intensity varies rapidly, by reducing error from motion-induced baseline shifts.

PD2 captures the radiative emission signals from both excitation wavelengths. The radiative contrast is extracted by taking the peak signal amplitude within the acquisition window. PD3 measures the 266 nm and 405 nm input reference powers. The average scattering input power is estimated from the pre-excitation signal level, while the 266 nm pulse energy is calculated as the difference between the peak signal amplitude and the scattering power reference.

Following the extraction of pixel intensities for each excitation pulse, the 266 nm and 355 nm pixel values are deinterlaced and reconstructed into separate images by mapping each pixel onto a cartesian grid based on their stage positions. Due to the alternating excitation sequence, the two wavelength channels are sampled on grids offset by 125 nm along the fast-scan (column) direction, corresponding to a half-step lateral shift between the 266 nm and 355 nm channels. During reconstruction, a half-pixel resampling was applied to align the two channels onto a common Cartesian grid prior to downstream processing. Each reconstructed image represents a single 500 µm x 500 µm field of view. Using the automated workflow detailed in Chapter 3, Section 3.2.2, whole slide imaging is performed by autofocusing across the sample using the scattering signal and capturing a series of overlapping sections. These sections are then stitched and blended to form a WSI of each contrast.

6.3.3 Deep Learning Based Virtual Staining

Whole Slide Preprocessing, Artifact Annotation, and Whole Slide Inference

The process used to prepare the training data for the virtual staining model and to perform WSI inference is illustrated in Figure 6.2. Following PARS imaging, the same unstained tissue sections were subsequently stained and brightfield scanned. Due to the differences in the imaging modalities and tissue deformation during the staining, spatial misalignments between the PARS and stained images were then corrected using the Warpy registration pipeline [185]. Warpy applies a combination of rigid and non-rigid transformations to closely align the two WSI pairs, a necessary starting point for the model training. All

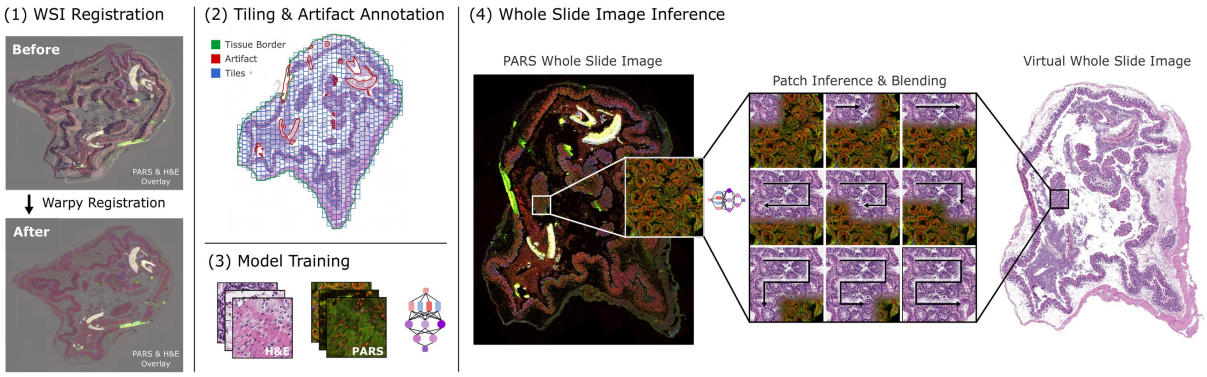

Figure 6.2: Workflow for preparing training data and performing whole slide virtual staining. (1) PARS and stained WSIs are aligned using the Warpy registration framework. (2) Tissue borders and artifacts are annotated in QuPath, and the slides are tiled into artifact-free patches. (3) These patches are used to train the virtual staining model. (4) Virtual staining is applied to full PARS WSIs using overlapping patch-wise inference, followed by linear blending and tissue masking to produce the final virtual stained slide. The example shown depicts mouse H&E gastrointestinal tissue.

virtual staining models evaluated in this study (RegGAN, Pix2Pix, and CycleGAN) were trained and evaluated using the same conventionally registered WSI pairs generated via the Warpy pipeline.

After registration, QuPath was used to annotate the tissue borders and label artifacts across the tissue. These artifacts include tissue tears, cover-slip bubbles, folds, and out-of-focus areas in the stained images, as well as paraffin obstructions and dust artifacts in the PARS images. Annotations were exported in GeoJSON format and processed by a custom Python script, which excluded the artifact regions and tiled the WSIs into smaller, co-registered patches. Tiling was required to divide the high-resolution slides into manageable chunks for training.

The resulting datasets were used to train the virtual staining model, described in the following section. Once trained, the model was applied to the entire PARS WSIs using a patch-based inference with 40% overlap between adjacent tiles. Overlapping patch regions were linearly blended to ensure visual continuity, resulting in a virtual WSI resembling a conventional stained slide. Following inference, a tissue mask was applied to remove any background artifacts. The mask was generated by thresholding the 355 nm radiative contrast channel from the PARS image, and the background regions were smoothly faded to white.

Model Architecture and Training Scheme

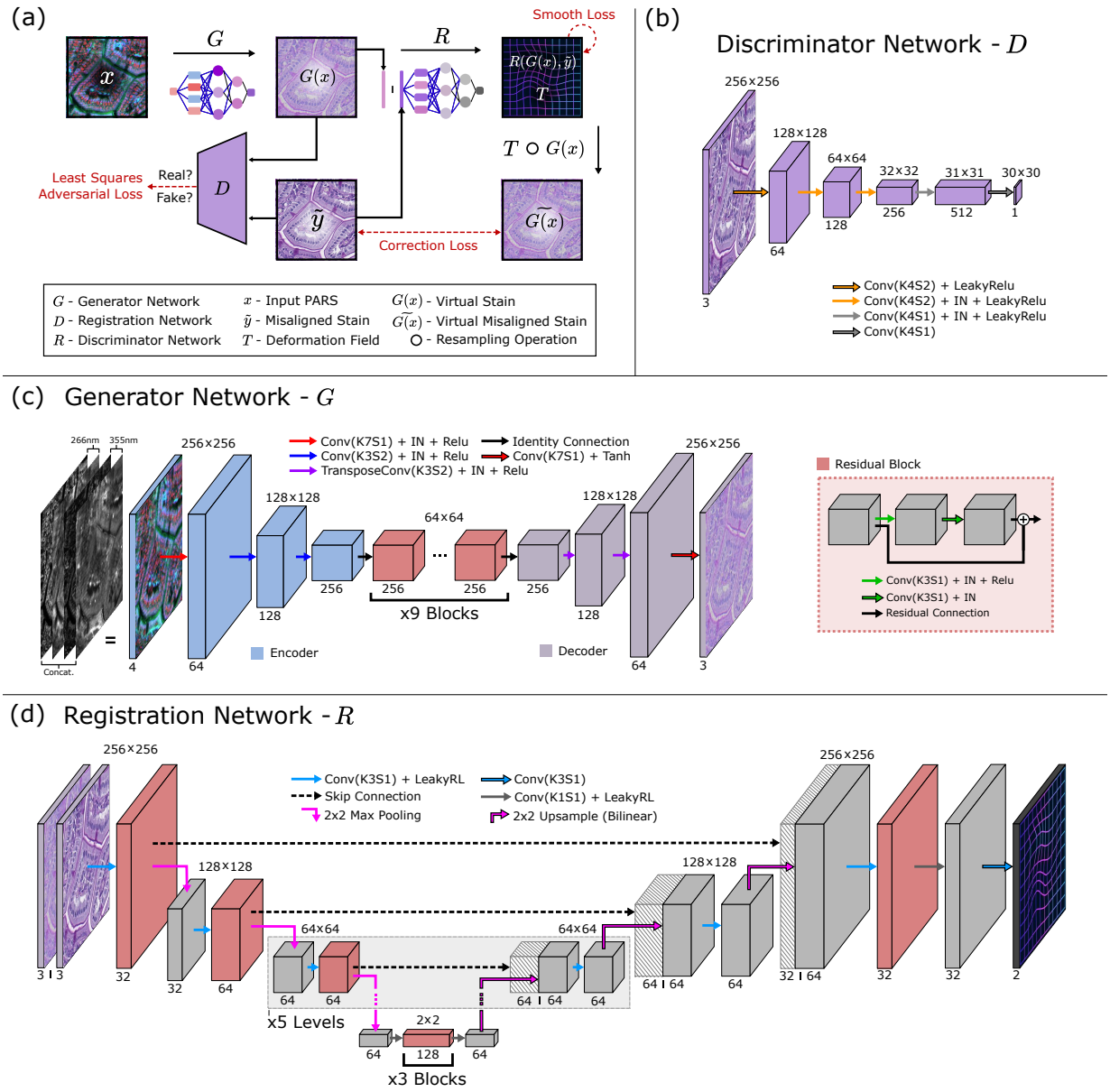

Figure 6.3: Overview of the RegGAN-based virtual staining framework and network architectures. (a) RegGAN training workflow with generator G, registration network R, and discriminator D. (b) Architecture of Discriminator D: 70×70 PatchGAN for patch-wise real/fake classification. (c) Generator G: ResNet encoder-decoder processing four-channel 266 nm & 355 nm inputs to RGB output. (d) Registration network R: ResUNet predicting 2D deformation field from six-channel input. IN = Instance Normalization; ReLU = Rectified Linear Unit.

Virtual staining employs I2I translation models, most of which follow one of two training paradigms: supervised approaches like Pix2Pix and variants [113], [186], and unsupervised methods such as CycleGAN [114]. Both approaches have been widely used in virtual staining, with unpaired methods more common due to general scarcity and difficulty in obtaining perfectly registered training data [187].

Supervised models like Pix2Pix are effective when training pairs are precisely aligned, however, achieving such alignment is particularly difficult in high-resolution, cross-modality tasks like PARS to brightfield translation. Even with registration pipelines like Warpy, small residual misalignments exist due to differences in the optical systems, imaging conditions, and local tissue deformation during staining. These inconsistencies introduce label "noise" that can result in blurred or smeared output quality. Pix2Pix has previously been applied to PARS data for H&E emulation in [33], [103], demonstrating strong performance and high concordance under carefully registered conditions; however, at the cost of labor-intensive preprocessing and time-consuming annotation to identify and exclude poorly aligned regions, which also reduced the effective dataset size.

CycleGAN-based models avoid the alignment issue by eliminating the need for paired training data. However, the lack of pixel-level supervision results in weaker constraints on both contrast translation and structural preservation. CycleGAN was previously been applied to loosely paired PARS data for virtual H&E staining in Chapter 4, successfully avoiding the blurring observed with Pix2Pix under misalignment. While this worked well for PARS to H&E, where the mapping between modalities was more direct, the stains explored in this work involve more complex or subtle structural and contrast relationships, making a supervised approach better suited to learn these mappings.

For these reasons, the virtual staining model used in this work is based on RegGAN [34], which offers a more effective balance between the paired and unpaired training regimes. RegGAN treats misalignments in the target image as a form of noisy labelling and incorporates a learnable registration network into the training process. This network adaptively estimates deformation fields that align the generated image to the target domain. As such, the model retains the benefits of paired supervision while remaining robust to residual misalignment, making it well suited for high-resolution virtual staining across imaging modalities.

The RegGAN training scheme is illustrated in Figure 6.3a. The generator network (G) receives a multichannel PARS input patch (x) and produces a virtual stained output ($G(x)$). This output, along with its corresponding misaligned real stain image ($\tilde{y}$), is concatenated and passed through the registration network (R). The registration network predicts a deformation field (T), which is applied to $G(x)$) to generate a registered virtual

output $G(\widetilde{x})$ that is more closely aligned with the real stain. An L1 correction loss is computed between the registered virtual output and the real stain image to encourage structural and visual similarity in the generated output. A more detailed report of the RegGAN working principles is presented in Section 2.1.5.

In parallel, the discriminator (D) learns to distinguish between real and virtual images, while the generator works to fool the discriminator by producing increasingly realistic virtual stains. To improve training stability, a least squares adversarial loss is used, per the LSGAN framework [188]. Additionally, a smoothness loss is applied to the predicted deformation field, encouraging spatial smoothness by penalizing large spatial gradients.

Figure 6.3(b-d) detail the convolutional architectures of the discriminator (D), generator (G), and registration (R) networks, respectively. Full layer configurations, including convolutional kernel sizes, strides, and feature dimensions, are provided within the figure. The discriminator network, shown in Figure 6.3b, follows the 70×70 PatchGAN architecture which outputs a patch-wise classification map, where each value reflects the likelihood of a local region being real or generated. The localized feedback helps the generator in producing realistic fine-scale texture and structural detail.

The generator network, illustrated in Figure 6.3c, adopts a ResNet-based encoder-decoder structure, commonly used in I2I translation tasks [114]. The inputs to the generator are the concatenated non-radiative and radiative contrasts from both the 266 nm and 355 nm wavelengths. The network consists of an encoder with two downsampling layers, a bottleneck with nine residual blocks, and a decoder that upsamples the features and outputs a three-channel RGB virtual stain image.

The registration network, shown in Figure 6.3d, is a ResUNet-style architecture from [189]. It receives a six-channel input formed by concatenating the virtual and real stain images. The architecture consists of seven downsampling levels, a central bottleneck with three residual blocks, and a symmetric decoder with bilinear upsampling and skip connections from the encoder. The final output is a two-channel deformation field representing the predicted x and y displacements.

Training Parameters and Implementation Details

An overview of the tissue types, stains, and dataset sizes used in this study is provided in Table 6.1. The datasets include mouse GI, kidney, and brain tissues; human kidney samples with ccRCC; human skin with fungal infection; and human skin with nodular melanoma. The stains used include H&E, Masson's trichrome, PAS, and JMS.

For each tissue and stain combination, the dataset was split into 80% training and 20% validation patches. In addition, multiple WSIs were held out entirely for testing for

each virtual staining model. WSI-based evaluation provided a realistic and stringent test scenario, as these slides were never seen during training or validation. For each WSI, a global mean and standard deviation were computed for each contrast channel, and each PARS input patch was normalized by subtracting this mean and dividing by the standard deviation.

Table 6.1: Training and validation sample summary by tissue type and stain.

Tissue Type	**Histochemical Stain**	**Training Samples**
Human kidney (ccRCC)	Hematoxylin and eosin	72,749
Human skin (melanoma)	Hematoxylin and eosin	26,066
Human skin (fungal disease)	Periodic acid–Schiff	21,030
Human kidney (ccRCC)	Masson's trichrome	88,769
Mouse kidney	Jones methenamine silver	27,157
Mouse kidney	Hematoxylin and eosin	16,524
Mouse kidney	Periodic acid–Schiff	22,586
Mouse kidney	Masson's trichrome	28,117
Mouse gastrointestinal	Hematoxylin and eosin	9,481
Mouse gastrointestinal	Periodic acid–Schiff	29,568
Mouse gastrointestinal	Masson's trichrome	33,425
Mouse brain	Hematoxylin and eosin	21,103

Note: Samples are 256×256 px patches.

All models were trained using the Adam optimizer with betas (0.5, 0.999). The generator and registration networks used a learning rate of $2{\times}10^{-4}$, while the discriminator used a lower learning rate of $2{\times}10^{-5}$. The generator was set to update four times for every update of the discriminator and registration networks. A batch size of 1 and a fixed patch size of 256×256 pixels was used. All LeakyReLU activations had a negative slope of 0.2. The smooth loss, correction loss, and adversarial loss were weighted by 10, 20, and 1, respectively. Data augmentation included random horizontal and vertical flips, along with 90° rotations.

Training was conducted for up to 70 epochs or until validation losses plateaued. The discriminator was updated using a history buffer containing the 50 most recent generated images, rather than relying solely on the latest outputs, as suggested in [190]. All models were implemented in Python 3.11.9 using PyTorch 2.4.1+cu118, and training was performed on a single NVIDIA RTX 4070 Super GPU using mixed-precision computation.

In addition to the primary models with all contrasts, ablation experiments were con-

ducted to evaluate how different subsets of PARS contrast channels affect virtual staining performance. Separate models were trained using only 266 nm radiative and non-radiative inputs, as well as only 355 nm radiative and non-radiative inputs. All training parameters remained consistent with the primary models. Some contrast configurations had more limited input information, and the generator update frequency was initially increased during the first ∼10 epochs to improve early training stability, after which the standard 4:1 generator to discriminator and registration network update ratio was resumed.

6.3.4 Sample Preparation

Tissue samples were sectioned at ∼5 μm thickness onto microscope slides from FFPE blocks prepared using standard histological methods. Freshly resected tissues were fixed in formalin within 20 minutes of excision and stored for 24 to 48 hours. Samples were then dehydrated in ethanol, cleared with xylene, and embedded in liquid paraffin wax at 60 °C. Slides were baked at a low temperature (50–55 ^{o}C) to smooth the paraffin surface for PARS imaging.

After PARS imaging, tissues were stained with one of the following: H&E, Masson's trichrome, PAS, or JMS, and scanned at 40× magnification using a brightfield microscope (Leica Aperio AT2, Robarts Research Institute).

The ccRCC human kidney samples were provided by the Ontario Tumour Bank. Human skin tissues (nodular melanoma and fungal infection) were provided by collaborators at the Cross Cancer Institute (Edmonton, Alberta, Canada). Murine tissues were resected in-house and sent to the Robarts Research Institute (University of Western Ontario) for FFPE processing.

Human samples were from anonymous patient donors and no information regarding patient identity was provided to the researchers. Patient consent was waived by the ethics committee because these archival tissues were no longer required for patient diagnostics. Samples were collected under protocols approved by the Research Ethics Board of Alberta (Protocol ID: HREBA.CC-18- 0277) and the University of Waterloo Health Research Ethics Committee (Photoacoustic Remote Sensing Microscopy of Surgical Resection, Needle Biopsy, and Pathology Specimens; Protocol ID: 40275). All human tissue experiments were conducted in accordance with the government of Canada guidelines and regulations, such as "Ethical Conduct for Research Involving Humans (TCPS 2)"

6.3.5 Masked Pathologist Evaluation

To obtain an initial assessment of diagnostic quality and visual similarity between chemical and virtual stains, a masked image evaluation was performed with three board-certified pathologists. A total of 20 tissue images were evaluated, consisting of 10 chemically stained images and 10 corresponding virtual stains acquired from exactly matching fields of view of the same tissue sample.

Each image was presented at both low-magnification (overview) and high-magnification (cellular detail). The survey images included all stain types used in this study and incorporated both healthy and disease cases across multiple tissue types. The image order was randomized, rotated, and flipped to minimize recognition of paired samples, and pathologists were masked to image origin.

Pathologists were asked to provide a score for the diagnostic quality of each image on a three-point scale (1 = poor, 2 = good, 3 = excellent). They were also asked to identify whether the image was chemically stained or not, with the options "yes," "no," or "uncertain." Responses were collected independently for all participants. The agreement in diagnostic quality between paired chemical and virtual images was quantified using linear weighted Cohen's kappa, and image origin classification accuracy was evaluated using binomial confidence intervals.

6.4 Results and Discussion

6.4.1 Expanded Contrast and Biomolecular Specificity with Addition of 355 nm Excitation

The dual-excitation PARS microscope captures label-free contrast through complementary radiative and non-radiative mechanisms at two UV excitation wavelengths. To illustrate the distinct features captured with each wavelength, Figure 6.4 overviews images from human skin, human kidney, and mouse kidney samples, and demonstrates the value of combining these contrasts in a single visualization. Across all samples, the 266 nm and 355 nm pulse energies were kept low and measured at 163pJ and 808pJ, respectively, generate strong signal without tissue damage visible in any of the stained samples. Similar to previous work [1], the system achieves a spatial resolution in the 500 nm range, comparable to that of a 40× brightfield scanner [47], allowing detailed subcellular visualizations. The system achieved lateral spatial resolutions (FWHM) of 563.8 nm for the 405 nm detection

beam, 370.8 nm for the 266 nm excitation and 520.3 nm for the 355 nm excitation (see Figure 6.5), enabling clear visualization of cellular details comparable to a 40x brightfield scanner [47]. Across all samples, the measured pulse energies were 163 pJ (266 nm) and 808 pJ (355 nm), with a peak optical fluence at the focal plane estimated to be 1.05 nJ/μm^2 and 2.64 nJ/μm^2, respectively, assuming a Gaussian profile using the 1/e^2 spot size radius. These fluence values are approximately two orders of magnitude below reported deep-UV photodamage thresholds measured in living cells ($\sim$0.5–2 μJ/μm^2) under deep-UV illumination [191] and provide a useful order-of-magnitude reference for fixed FFPE tissue. Consistent with this comparison, no histochemical artifacts or observable tissue damage was detected in the samples imaged.

Figure 6.4(a-b) presents representative images acquired from human skin tissue diagnosed with nodular melanoma. Figure 6.4a shows a breakdown of the contrast channels obtained at 266 nm (left) and 355 nm (right), with each wavelength producing both non-radiative and radiative signals. This yields four distinct contrast channels per scan, each reflecting different structural and biochemical properties within the tissue. Importantly, because the 266 nm and 355 nm excitations are interlaced within a single scan trajectory, these four contrasts are captured essentially simultaneously, without compromising imaging speed. The 266 nm excitation provides strong nuclear contrast through non-radiative absorption of nucleic acids, and radiative signals from connective tissues and fluorophores in the ECM, providing clear visualization of surrounding tissue structures such as sweat glands.

In contrast, 355 nm excitation reveals biologically meaningful tissue features that are less prominent or absent under 266 nm. The non-radiative contrast strongly highlights RBCs through hemoglobin absorption [136] and also provides signal in surrounding tissue structures not as well emphasized with 266 nm non-radiative. The radiative emissions at 355 nm similarly highlights many fluorophores and structures of the ECM (e.g., collagen and elastin), but with different spectral weightings than 266 nm radiative. For example, basement membranes of sweat glands are more pronounced in the 355 nm radiative channel, reflecting differences in absorption and emission efficiencies.

Figure 6.4b shows the composite PARS image from all four channels, alongside the corresponding H&E-stained section from the same malignant human skin sample. In Figure 6.4(b-ii), a region of melanoma was selected to demonstrate the strong 355 nm non-radiative sensitivity to melanin. The 355 nm non-radiative signal (blue), clearly outlines heavily pigmented tumour cells, corresponding to dark melanin regions in the H&E image, highlighting the diagnostic value of 355 nm excitation.

Figure 6.4(b-iii) shows a nodular tumour with characteristic morphology, including

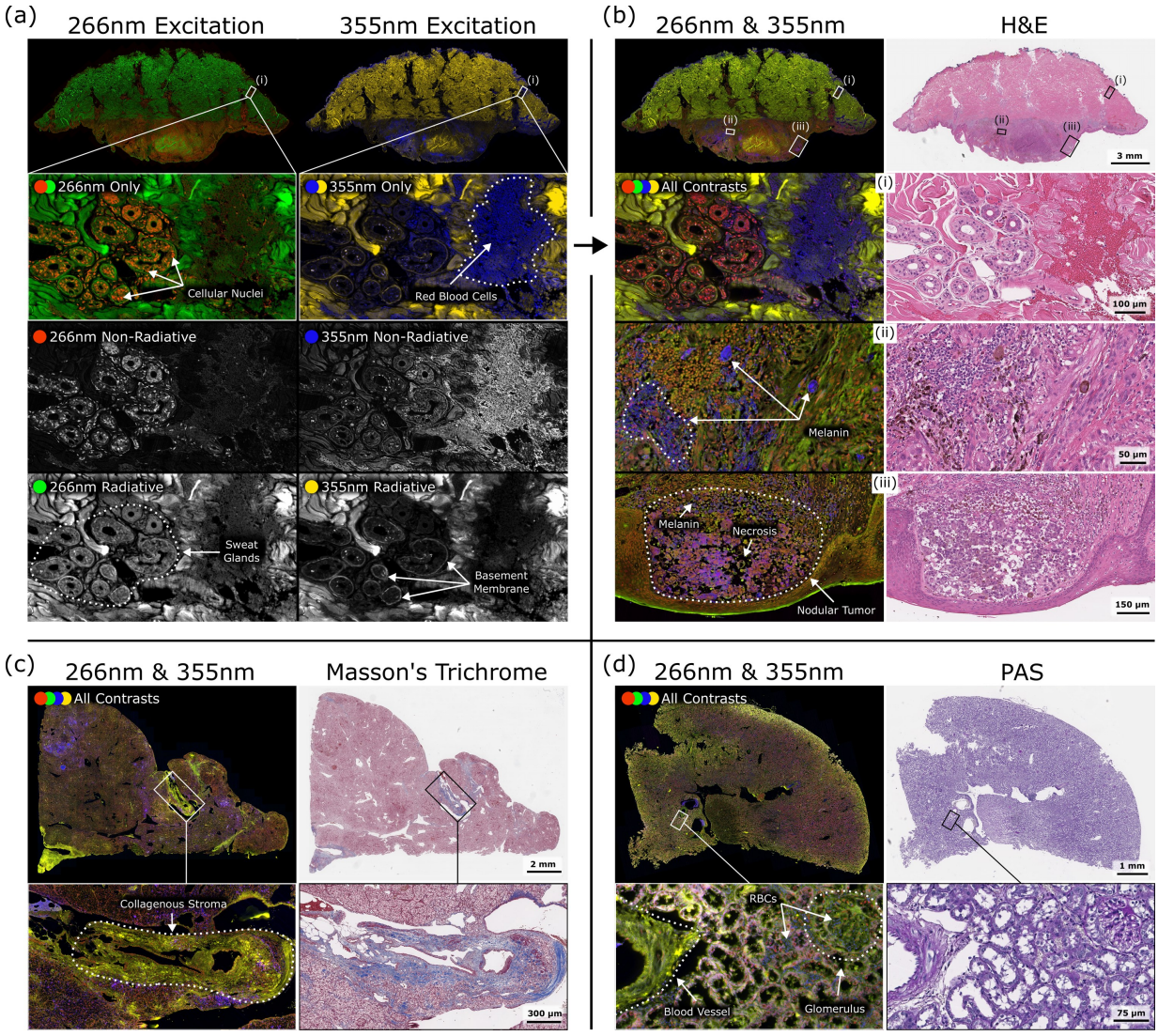

Figure 6.4: Summary of label-free contrasts from 266 nm and 355 nm excitation in the PARS system, compared with H&E and specialized stains. (a) Malignant skin (nodular melanoma) with separate non-radiative (NR) and radiative (R) contrasts: 266 nm NR highlights nuclei; 355 nm NR emphasizes RBCs and tissue detail; R signals outline connective tissue, with 355 nm highlighting basement membranes. (b) Composite PARS and matching H&E section. (b-ii) Superficial spreading melanoma with 355 nm NR sensitivity to melanin; (b-iii) tumor with melanin, necrosis, and vertical growth. (c) Human kidney with ccRCC, compared to Masson's trichrome stain; 355 nm R signal matches collagen-rich stroma. (d) Healthy mouse kidney with PAS stain showing carbohydrate-rich structures; PARS reveals similar features, including nuclei, RBCs, reticular fibres, and basement membranes.

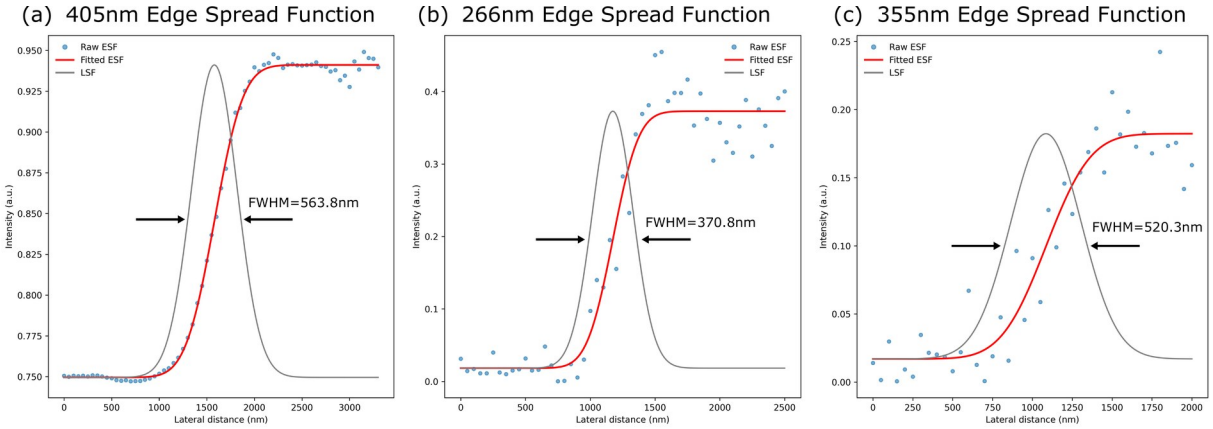

Figure 6.5: Edge-based spatial resolution measurements for the three wavelengths used in the system. ESF (red) were extracted from scans sampled at 50 nm/pixel and fitted to raw edge data (blue dots) to derive LSF (grey) for (a) 405 nm measured from the scattering contrast channel using an edge phantom, (b) 266 nm measured from the non-radiative contrast channel using a nuclear edge, and (c) 355 nm measured from the non-radiative contrast channel using an RBC edge. The measured FWHM values are: 563.8 nm (405 nm), 370.8 nm (266 nm) and 520.3 nm (355 nm).

nuclear pleomorphism, necrosis, and extensive melanin deposition. The epidermis is clearly delineated, and the tumour mass appears to press against it, consistent with the vertical growth patterns typical of nodular melanoma [192]. The combined 266 nm and 355 nm contrasts align closely with the H&E reference but 355 nm enhances visibility of tumour architecture and melanin accumulation.

Figure 6.4c shows a human kidney sample with ccRCC and compares the composite PARS image to the corresponding Masson's trichrome-stained section. Masson's trichrome selectively stains collagen-rich regions in blue, helping identify areas of fibrosis and stromal remodeling [9]. These same collagen rich regions are clearly visible in the radiative channels of the PARS image, particularly in the 355 nm autofluorescence response (yellow). While collagen exhibits autofluorescence under both excitation wavelengths, the 355 nm response is more prominent, while the 266 nm radiative signal appears more uniform across the tissue.

Figure 6.4d shows a healthy mouse kidney sample imaged with PARS and compared to the corresponding PAS-stained section. The PAS stain highlights carbohydrate-rich structures, such as polysaccharides (e.g., glycogen), glycoproteins, and mucosubstances. It is commonly used in kidney pathology to delineate the basement membranes of glomerular capillary loops and renal tubules, which appear magenta [193]. In the PARS image, both radiative channels show the tubule structures, and the capillary loops of the glomerulus

correspond to the pink-stained regions in the PAS image. Nuclei in the glomerulus are shown in red (266 nm, non-radiative), and RBCs in the capillaries are visible in blue (355 nm non-radiative). A blood vessel on the left is outlined in yellow and green from both radiative signals and aligns well with the pink reticular fibers outlined in the PAS image.

Overall, the addition of 355 nm excitation expands the structural and biomolecular contrast available in the PARS system, complementing the contrast provided by 266 nm. In many cases, the two wavelengths highlight common tissue features, doing so with different intensity distributions, offering an alternate visualization of shared structures. Together, the combined contrasts correspond well with the patterns seen in both routine H&E and more specialized stains, suggesting their potential utility as input for label-free multi-stain virtual histology.

6.4.2 High-Fidelity Virtual Staining of Diverse Histochemical Stains

The complementary radiative and non-radiative contrasts captured by the 266 nm and 355 nm excitation wavelengths provide diverse and diagnostically relevant structural and biochemical information within the tissue, forming a strong input foundation for virtual staining. Building on the previous section, the following demonstrates the system's ability to replicate a range of histochemical stains across both healthy and diseased samples, using the RegGAN-based staining framework described in Section 6.3.3 and the full dual-excitation input.

In evaluating the virtual staining performance of the models, three key aspects of the experimental design should be highlighted. First, all testing results presented in this work were generated from entirely unseen WSIs that were held out during model training and validation. This approach tests the model's generalization performance on new tissue sections, mirroring a real-world clinical use case for such a system, and avoiding potential biases from having seen training pairs from the same sample.

Second, because PARS imaging is label-free and operates at low pulse energies that do not visibly damage the tissue, the same slides were chemically stained after imaging. This was core to the training process but is also important for evaluation because it allows direct one-to-one comparisons with the exact chemical counterpart, which is not always feasible in virtual staining studies.

Lastly, histochemically stained WSIs exhibit a wide range of complex tissue structures across many scales, from global patterns to fine cellular details and layouts. It can be

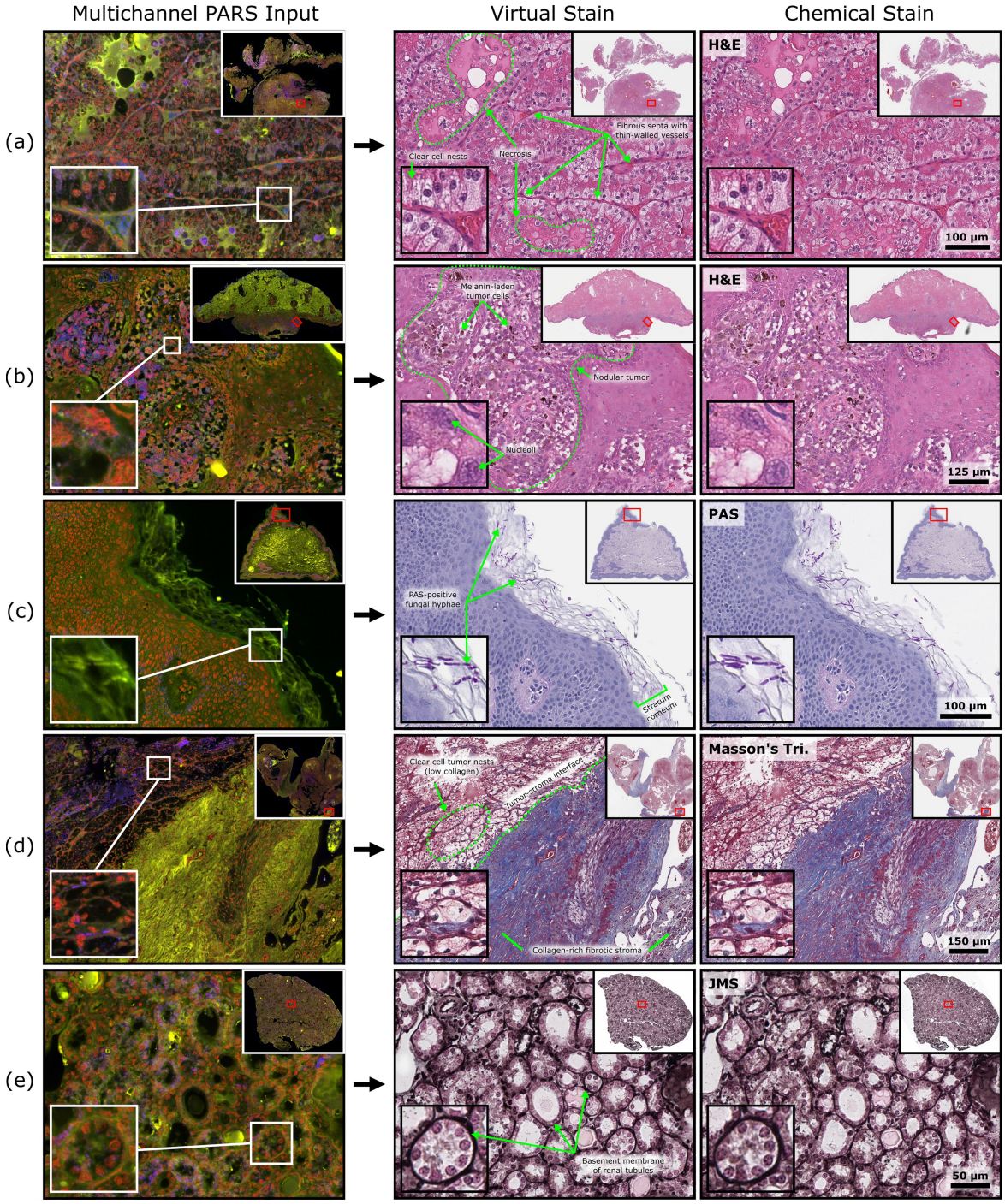

Figure 6.6: Virtual staining results using dual-excitation PARS input and RegGAN model across healthy and diseased tissues with H&E and specialized stains. (a) H&E of human kidney with ccRCC. (b) H&E of human skin with melanoma. (c) PAS of human skin with fungal infection highlighting PAS-positive hyphae. (d) Masson's trichrome of ccRCC kidney. (e) JMS stain of healthy mouse kidney.

challenging to convey staining performance across these scales through isolated crops alone. For this reason, in addition to showing representative areas, WSI virtual and chemical pairs have been made publicly available at the BioImage Archive. Slides are standard OME-TIFF format and can be viewed and compared with standard pathology viewing software such as QuPath

Figure 6.6 presents representative virtual staining results across five stain-tissue combinations. Each example includes the label-free PARS input (left), virtual stain (middle), and chemical reference (right), with a zoomed-out whole slide view and high-resolution crop to demonstrate performance across scales. The figure includes human kidney and skin tissues, primarily from disease cases such as ccRCC, melanoma, and fungal infection, along with one mouse kidney example. Standard H&E staining is shown first, followed by three specialized stains (PAS, Masson's trichrome, and JMS) to demonstrate more specific structural and biochemical features. Alongside these disease-focused cases, Figure 6.7 provides addition supporting results in healthy mouse tissues, highlighting model performance and PARS contrasts across organs such as brain, GI tract, and kidney.

The first two rows of Figure 6.6 present H&E-stained sections of human kidney and skin. In both cases, the virtual outputs closely resemble their chemical counterpart, properly staining nuclear structures in purple and cytoplastic content and surrounding connective tissue pink. In the malignant kidney tissue (Figure 6.6a), the virtual stain accurately reproduces the ccRCC tumor architecture, including nests of cells with distinct cell borders and abundant clear cytoplasm (high power area) [193]. The presence of necrosis is clearly visible in the PARS input and is accurately replicated in the virtual stain. This finding is associated with disease aggressiveness. In addition, the thin fibrous septa that separate the tumor nests are clearly visualized in the virtual stain and the fine vascular structures and RBCs within the capillary lumens are well rendered. In the human skin tissue with nodular melanoma (Figure 6.6b), the virtual stain accurately captures the melanin-laden tumor cells and architecture of the tumor nodule [192]. Within the tumor, the nuclei display marked pleomorphism, and the model is able to reproduce the small nucleoli inside these cells (higher power area). The distribution and localization of melanin within the tumor closely matches the chemical stain, aided by the 355 nm non-radiative absorption contrast input.

The third row, Figure 6.6c, presents a case of dermatophytosis, a superficial fungal infection of the skin commonly diagnosed using the PAS stain, which highlights polysaccharides in fungal cell walls (e.g., chitin) [46]. In the virtual stain, PAS-positive fungal hyphae are clearly visible as thin magenta-coloured filaments clustered along the stratum corneum. The distribution and localization of these fungal organisms accurately match the chemical reference, as do their colour and orientation. The virtual output also faithfully re-

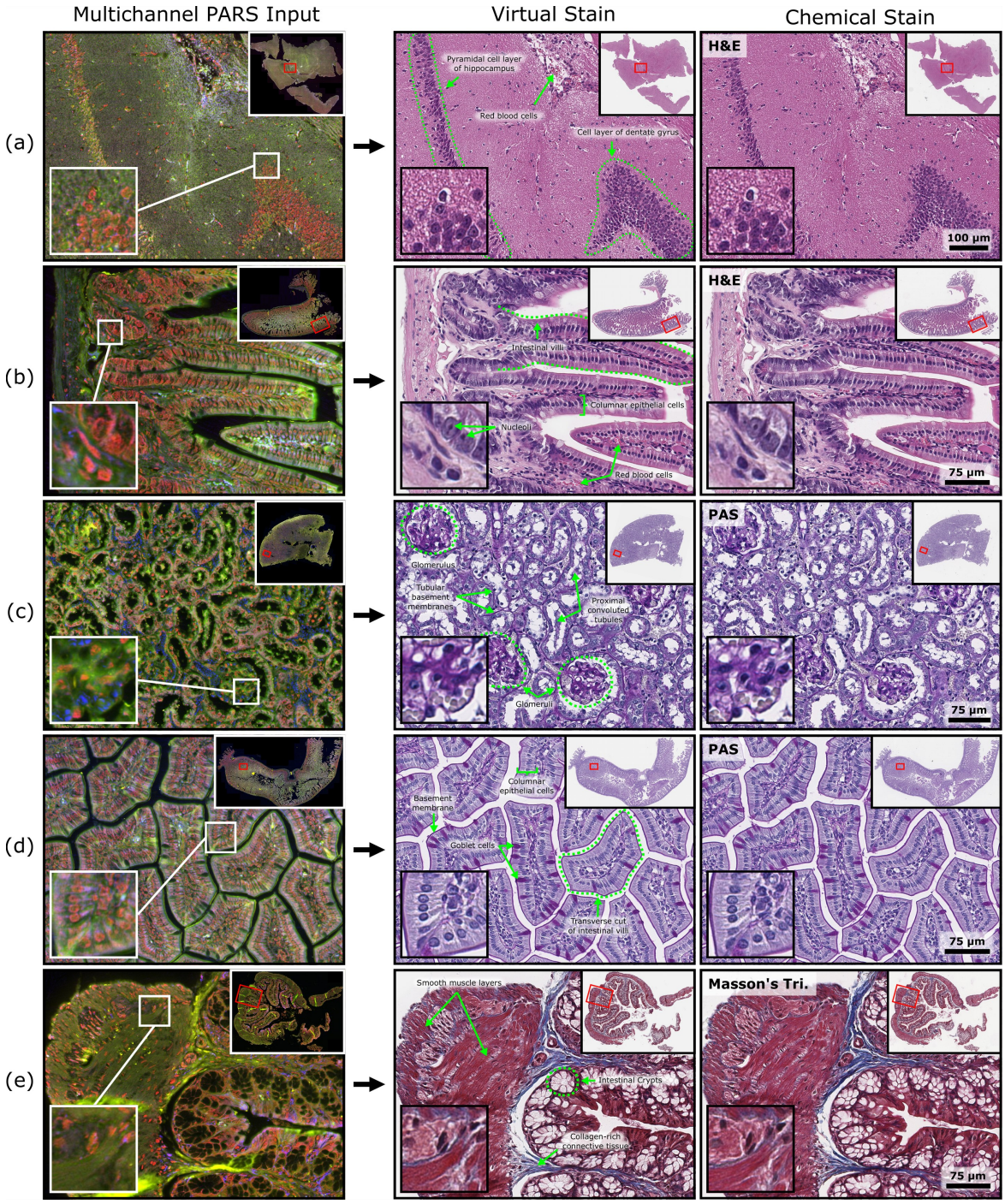

Figure 6.7: Virtual staining results using dual-excitation PARS input and RegGAN model across healthy mouse tissues with multiple stains; annotations highlight key structures. (a) H&E brain: hippocampal pyramidal layer, dentate gyrus, RBCs. (b) H&E intestine: villi, columnar epithelium, nucleoli (zoom-in). (c) PAS kidney: tubules and glomerular basement membranes (magenta). (d) PAS intestine: transverse villi and goblet cells. (e) Masson's trichrome intestine: smooth muscle, collagen-rich connective tissue (blue), intestinal crypts.

produces the structure and organization of the surrounding epidermis layers. Notably, the fungal elements are discernible in the label-free PARS input, providing valuable contrast that supports accurate virtual staining of these diagnostically important structures.

In the ccRCC kidney stained with Masson's trichrome (Figure 6.6d), the virtual output closely matches the chemical reference and enables accurate assessment of the fibrosis surrounding the invasive tumor. The intricate blue and red staining in the collagen-rich area at the bottom right is accurately translated in detail in the virtual stain. In contrast, the tumor growth in the upper left has minimal collagen content, and the virtual stain also accurately reflects this, providing clear visualization of the tumor-stroma interface. The higher power region further highlights the model's sensitivity to subtle collagen cues within the tumor nests, which could aid the evaluation of tumor-driven stromal remodelling.

The last row, Figure 6.6e, shows the JMS stain applied to healthy mouse kidney tissue. This stain highlights glomerular and tubular basement membranes in black and is invaluable for the assessment of non-neoplastic kidney biopsies [45]. Overall, the virtual output closely matches the chemical reference, sharply staining the basement membranes between tubules black and accurately colouring the pink nuclear and background counterstain (Nuclear Fast Red). The higher magnification area showcases a distal tubule structure with a well-defined black border and clearly resolved epithelial nuclei, matching well with its chemical reference.

To further highlight the utility of the virtual staining models, Figure 6.8 presents simultaneous virtual H&E, Masson's trichrome, PAS, and JMS generated from a single multichannel PARS input in mouse kidney tissue. Figure 6.8a highlights a region containing both abnormal glomeruli and surrounding normal structures, while Figure 6.8b shows a normal glomerulus for comparison. The observations in Figure 6.8a were made in an aging mouse, where spontaneous, age-related glomerular alterations are not uncommon [194, 195].

The two glomeruli in Figure 6.8a show globally disrupted architecture, with disrupted and compressed capillary networks due to mesangial area expansion by pale-staining, amorphous material. Each of the virtual stains contributes information about the nature of the glomerular alteration. In the virtual H&E, the glomeruli appear pale pink. The virtual Masson's trichrome shows the mesangial nodules to appear pale blue-gray (versus the darker blue colour typical of collagen). The virtual PAS and JMS stains display reduced staining of the amorphous material, with PAS appearing pale and JMS a pink-gray colour, lacking the strong magenta colour of PAS or the sharply defined black staining of JMS seen in the normal glomerulus in Figure 6.8b. These combined staining insights are most consistent with glomerular amyloidosis [196], a condition involving extracellular protein

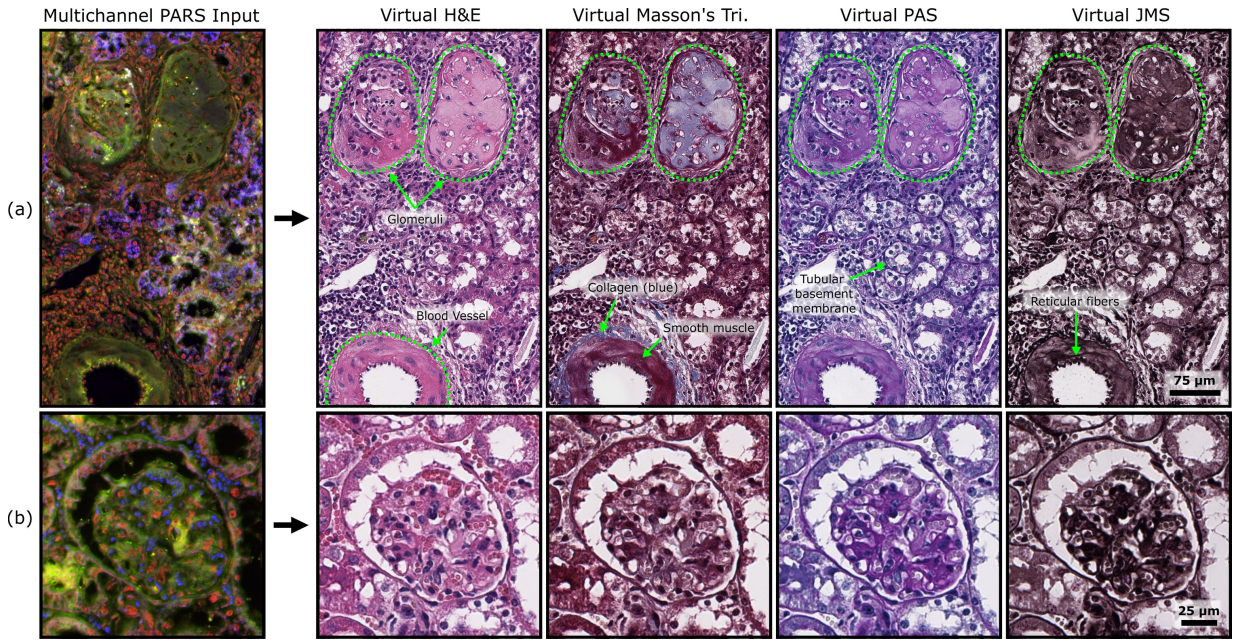

Figure 6.8: Simultaneous virtual H&E, Masson's trichrome, PAS, and JMS staining of mouse kidney tissue from a single PARS input. (a) Region containing two abnormal glomeruli with nodular expansion of mesangial areas, along with a blood vessel and surrounding renal tubules. (b) Normal glomerular architecture from another mouse kidney section, shown in the same four virtual stains for comparison.

deposits (i.e., amyloid) within glomeruli that disrupts glomerular filtration barrier and impairs selective permeability.

The region in Figure 6.8a also includes several well-preserved normal structures. A blood vessel with clearly defined smooth muscle is visible across all stains, with surrounding collagen clearly identifiable in the virtual Masson's trichrome. Reticular fibers can also be seen within the vessel wall in the virtual JMS (and PAS). The surrounding renal tubules are also properly stained and sharply outlined with the virtual PAS and JMS. In addition to this example, Figures 6.9 and 6.10 provide further examples of simultaneous virtual multi-staining in healthy mouse GI tissue and human ccRCC kidney tissue, respectively, where the multiple stains offer complementary views of tissue structure and pathology.

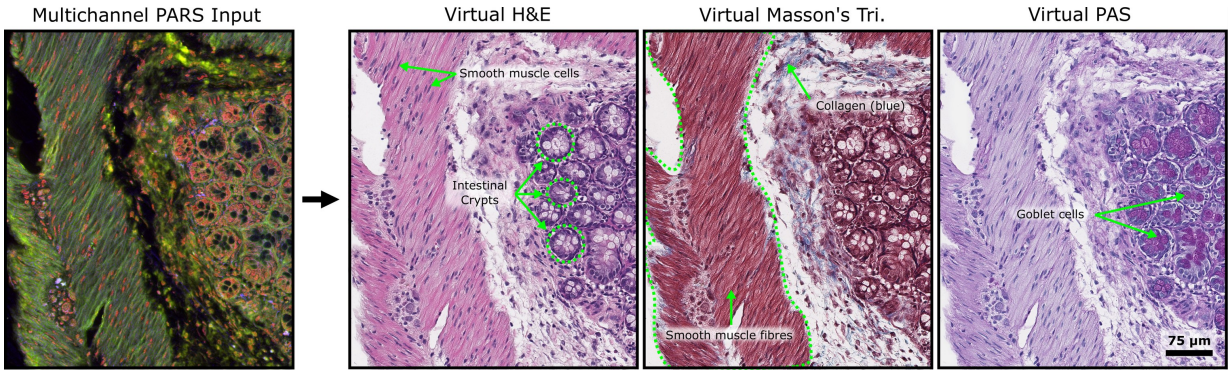

Figure 6.9: Virtual histochemical multi-staining of mouse intestine tissue from a single multichannel PARS input. The single PARS image (left) is used to generate three virtual stains: H&E, Masson's trichrome, and PAS. The virtual H&E highlights smooth muscle cells and intestinal crypts. Masson's trichrome shows collagen (blue) and smooth muscle fibers, while PAS reveals magenta-stained goblet cells.

Together, the example demonstrates how each virtual stain contributes distinct structural and biochemical information that, when combined, allows for a more complete interpretation of the glomerular pathology than routine H&E or any single stain alone could provide. For example, work by Haan et al. demonstrated that virtual multi-staining, achieved through stain-to-stain transformations, can improve diagnostic accuracy in renal pathology, supporting the value of combining multiple stain types [108]. In addition to the virtual stains, the label-free PARS input here offers an additional distinct visualization of tissue structures, with a unique contrast mechanism independent from chemical staining. Moreover, because the sample remains unaltered, subsequent staining with other specialized markers can be performed. For example, to definitively confirm amyloid deposition in Figure 6.8a, the same kidney section could be chemically stained with Congo red and imaged under polarized light microscopy [196].

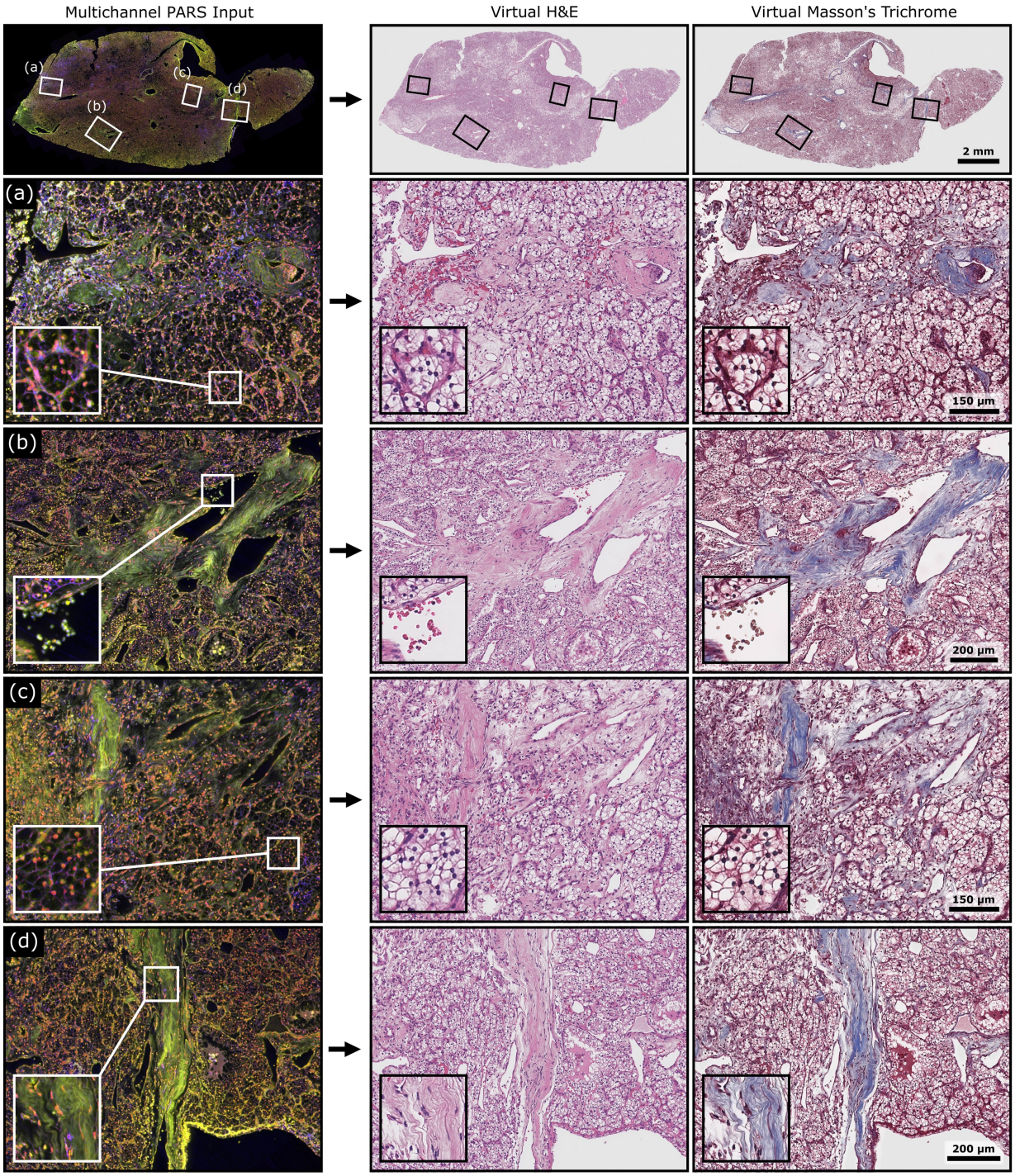

Figure 6.10: Virtual histochemical multi-staining of human kidney tissue with ccRCC. A single multi-channel PARS image is used to generate two virtual stains: H&E and Masson's trichrome. WSI virtual stains are shown at the top, with four representative regions (i)-(iv) selected for detailed viewing. In the virtual H&E, clear cell tumor nests are visible across the sampled regions, showing characteristic cytoplasmic clearing and nested morphology. The corresponding Masson's trichrome images highlight tumor-driven stromal remodeling, with collagen deposition (blue) surrounding the tumor regions.

In addition to demonstrating cases where the virtual staining closely resembles the chemical reference, it is also helpful to highlight situations where the output deviates from the ground truth to better understand model behavior. Accordingly, a qualitative assessment of some representative failure cases observed across the virtual staining results is provided in Figure 6.11. Firstly, virtual staining failures often occur in areas where there are slide artifacts or acquisition-related issues, such as tissue folds, out-of-focus areas, or debris on the sample (e.g., dust or hair). These artifacts typically generate strong radiative signals which locally dominates the PARS input and wash out other non-radiative contrasts, reducing the available structural cues, leading to weakened or missing structures or local miscoloration in the virtual stain (Figure 6.11a-e).

Additional examples are shown where the virtual staining deviates from the chemical reference. In Figure 6.11f, blue surgical margin ink appears blue in the chemical stain but is not rendered as blue in the virtual output, instead appearing eosin-like or RBC–like coloring. Notably, the margin ink is present in the raw PARS input and produces signal in the 355 nm non-radiative channel (blue), a channel that also typically highlight RBC structures in the tissue. In Figure 6.11g, fungal hyphae in PAS-stained skin are generally detected in the virtual output but appear incompletely stained or fragmented in some regions. In addition, Figure 6.11h shows an example of a hair follicle base where the hair shaft is miscolored with dark eosin-like staining that does not match the chemical reference, potentially reflecting limited representation of such structures in the training data.

In addition to these failure examples, the overall global color was assessed using L*a*b* color space histograms comparing virtual and chemical stains. Figure 6.12 shows overlaid distributions of the L* (lightness), a* (green-red axis), and b* (blue-yellow axis) channels for virtual and corresponding chemical stains, aggregated across randomly sampled image patches for each stain type (N=5000). This analysis provides an overall, global view of color consistency and is intended to assess whether systematic color shifts are present.

Across all stains, the virtual staining outputs exhibit close overlap with the chemical reference distributions in each channel, indicating good overall agreement in luminance and chromatic components. Minor distributional differences are observed, but do not suggest widespread or systematic color or intensity bias. This consistency is likely aided by the fact that chemical staining was performed within a single facility using standardized protocols, reducing inter-slide variability during training.

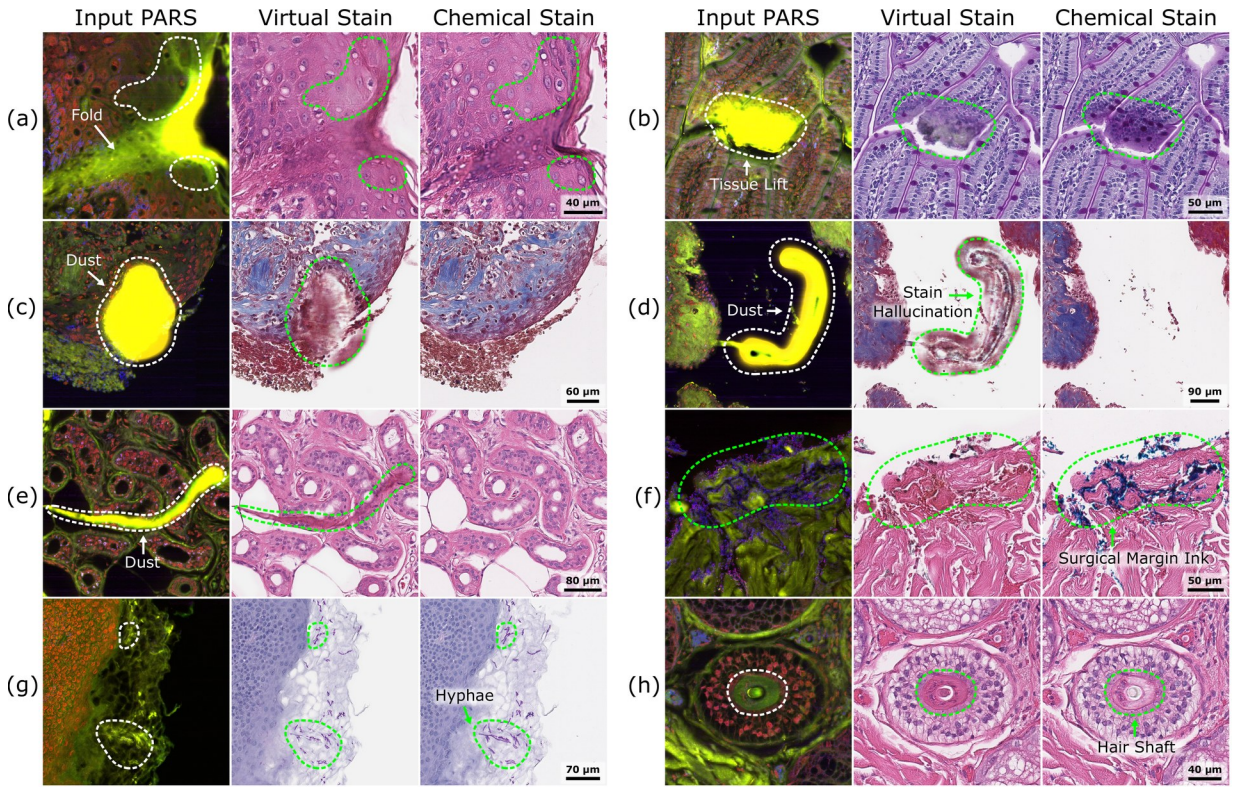

Figure 6.11: Representative failure cases observed in the virtual staining results across tissue types and histochemical stains. Each example shows the multichannel PARS input (left), virtual stain (middle), and chemical reference (right). Dashed outlines indicate regions of interest. (a) Human skin (H&E): A tissue fold produces strong radiative signal and attenuates local non-radiative nuclear contrast, leading to weakened or missing nuclear staining adjacent to the fold. (b) Mouse GI tissue (PAS): Partial tissue lift and defocus result in washed-out input contrast and inconsistent coloration in the virtual stain. (c) Human kidney (Masson's trichrome): Dust present on the slide results in red stain-like coloration in the virtual output. (d) Human kidney (Masson's trichrome): Debris on the slide background results in spurious staining in the virtual output. (e) Human skin (H&E): Dust overlying glandular structures disrupts local virtual staining, resulting in eosin-like miscoloration while surrounding glandular morphology remains largely preserved. (f) Human skin (H&E): Blue surgical margin ink does not appear blue in the virtual output and instead appears as eosin-like or RBC–like features inconsistent with the chemical reference. (g) Human skin with fungal infection (PAS): Fungal hyphae are detected in the virtual stain but appear faint, fragmented, or incompletely stained relative to the chemical reference. (h) Human skin (H&E): A hair follicle exhibits miscoloration of the hair shaft, appearing dark eosin-like in the virtual output compared to the chemical reference.

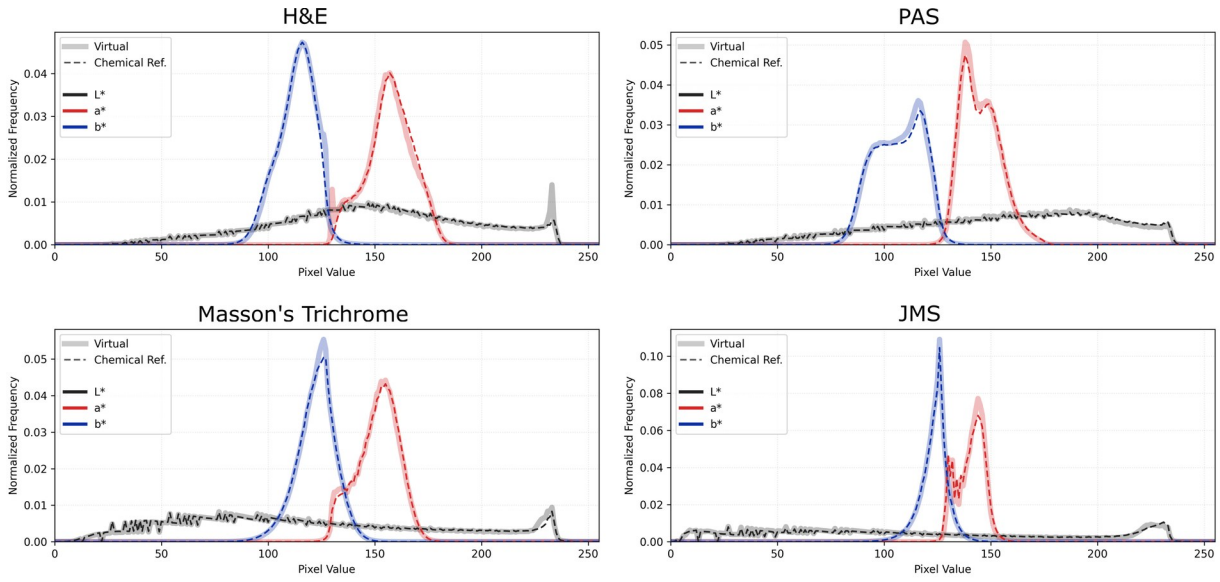

Figure 6.12: L*a*b* color distribution comparison between virtual and chemical stains. Overlaid histograms show the distributions of the L* (lightness), a* (green–red), and b* (blue–yellow) channels for virtual stains (dashed lines) and corresponding chemical references (solid lines) for H&E, PAS, Masson's trichrome, and JMS. For each stain, histograms were generated by aggregating 5000 randomly sampled image patches drawn from representative test images. The substantial overlap across channels indicates overall color consistency between virtual and chemical stains, while minor distributional differences reflect subtle global color differences.

6.4.3 Pathologist Validation Results

The results from the masked pathologist evaluation further demonstrate the close correspondence between chemical and virtual stains. As detailed in section 6.3.5, expert pathologists, masked to the image origin, reviewed a set of randomized chemical and virtual image pairs spanning all stain types, tissue types, and disease contexts included in this study.

Table 6.2: Summary of masked pathologist evaluation of chemical and virtual stains.

Image Origin	Avg. DQ (± Std)	Rated Chemical	Rated Virtual	Uncertain
Chemical	2.600 ± 0.306	17	1	12
Virtual	2.667 ± 0.314	18	1	11

DQ = Diagnostic Quality (1: poor, 2: good, 3: excellent).

A summary of diagnostic quality scores and image original classification is provided in Table 6.2, with the full responses presented in Table 6.3. For each pathologist, diagnostic quality scores assigned to chemical and virtual image pairs were similar, with both image types consistently rated as "good" or "excellent". Diagnostic quality scoring is inherently subjective and was used here as a coarse measure to assess relative agreement rather than specific diagnostic performance. To quantify the agreement in diagnostic quality scores between the paired chemical and virtual images, a linear weighted Cohen's kappa was used. Pathologist 1 showed substantial agreement (κ=0.615), pathologist 2 showed moderate agreement (κ=0.483), and pathologist 3 showed complete agreement (κ=1.000).

When asked to classify image origin, pathologists were unable to reliably distinguish chemical from virtual images under masked conditions. When excluding responses marked as "uncertain", image origin classification accuracy was 50.0% (95% CI: 27.2–72.8%) for pathologist 1 (who classified 100% of images as chemical) and 47.1% (95% CI: 23.0–72.2%) for pathologist 2, while pathologist 3 marked all responses as uncertain. When pooled across pathologists ($n = 37$ "yes" or "no" responses), overall origin classification accuracy was 48.6% (95% CI: 31.9–65.6%), suggesting that image origin was not reliably distinguishable in this evaluation. A substantial fraction of responses were marked as "uncertain" (38.3% of all classifications), which reflects the difficulty of confidently distinguishing chemical from virtual images under masked conditions. While uncertainty responses were excluded from the primary accuracy analysis, treating these responses as incorrect would further reduce observed classification accuracy.

Overall, within the limits of the small sample size used here, several observations can be

made. Diagnostic quality scores assigned to virtual images were generally similar to those assigned to chemical stains across the images evaluated, with no obvious or systematic differences observed. In addition, under masked conditions, pathologists were not able to reliably distinguish virtual images from chemical images, with a substantial proportion of responses marked as uncertain. These observations provide supportive evidence of visual similarity between virtual and chemical images; however, future work involving larger studies with increased sample size and more structured diagnostic tasks that are specific to tissue type and stain would be required for a rigorous assessment of diagnostic equivalence and comparative performance.

6.4.4 Contribution of Individual Excitation Channels to Virtual Staining Performance

To evaluate the individual and combined contributions of 266 nm and 355 nm excitation contrasts, additional models were trained using only 266 nm input and only 355 nm input. These were compared to the dual excitation models presented in the previous section for all tissue and stain combinations used in this study (Table 6.1). Relative performance was then quantified using two metrics: (1) MS-SSIM [197], which captures pixel-level structural similarity across scales, with higher values indicating better similarity; and (2) DISTS [135], which captures perceptual similarity based on structural and textural fidelity, with lower values indicating better similarity. The overall aggregated results across all tissue and stain combinations, together with the detailed per–tissue–stain–combination breakdowns for every dataset in this study, are shown in Table 6.4 for the DISTS metric and Table 6.5 for the MS-SSIM metric.

In all cases, models trained with both excitation contrasts achieved improved scores (higher for MS-SSIM and lower for DISTS) compared to those trained with either wavelength alone. These results are consistent with the idea that the complementary contrast from both wavelengths provides more biochemical specificity and structural information to the model, supporting improved virtual staining performance. In general, 266 nm models outperformed 355 nm models for most tissue-stain combinations, likely attributed to the essential nuclear contrast present in the 266 nm non-radiative channel. One notable exception was observed in the skin melanoma sample, where the 355 nm model achieved a better DISTS score, reflecting improved replication of melanoma texture from the 355 nm non-radiative channel.

While these metrics help assess overall staining quality, further analysis was done to assess how the addition of 266 nm or 355 nm affects the virtual staining of more specific

Table 6.3: Results of masked pathologist evaluation showing responses for diagnostic quality (DQ) and image origin (IO).

	Type – Stain – Sample	Path. 1		Path. 2		Path. 3		Avg. DQ
		DQ	IO	DQ	IO	DQ	IO	
1.	C – H&E – Kidney ccRCC	3	Y	2	U	3	U	2.67
1.	V – H&E – Kidney ccRCC	3	Y	2	Y	3	U	2.67
2.	C – MT – Kidney ccRCC	2	Y	2	Y	3	U	2.33
2.	V – MT – Kidney ccRCC	2	Y	2	U	3	U	2.33
3.	C – PAS – Mouse Kidney	3	Y	1	N	3	U	2.33
3.	V – PAS – Mouse Kidney	3	Y	2	Y	3	U	2.67
4.	C – JMS – Mouse Kidney	3	Y	1	Y	2	U	2.00
4.	V – JMS – Mouse Kidney	2	Y	2	Y	2	U	2.00
5.	C – H&E – Skin Melanoma	3	Y	3	Y	3	U	3.00
5.	V – H&E – Skin Melanoma	3	Y	3	Y	3	U	3.00
6.	C – PAS – Mouse GI	3	Y	2	U	3	U	2.67
6.	V – PAS – Mouse GI	3	Y	2	N	3	U	2.67
7.	C – MT – Kidney ccRCC	3	Y	2	Y	3	U	2.67
7.	V – MT – Kidney ccRCC	3	Y	3	Y	3	U	3.00
8.	C – PAS – Skin Fungal	3	Y	3	Y	3	U	3.00
8.	V – PAS – Skin Fungal	3	Y	3	Y	3	U	3.00
9.	C – H&E – Kidney ccRCC	3	Y	2	Y	3	U	2.67
9.	V – H&E – Kidney ccRCC	3	Y	2	Y	3	U	2.67
10.	C – MT – Kidney ccRCC	3	Y	2	Y	3	U	2.67
10.	V – MT – Kidney ccRCC	3	Y	2	Y	3	U	2.67

DQ = Diagnostic Quality (1: poor, 2: good, 3: excellent).
IO = Image Origin (Y: Yes, N: No, U: Uncertain).
C = Chemical stain. **V** = Virtual stain. **MT** = Masson's Trichrome;

Table 6.4: DISTS (↓) scores across datasets for different excitation wavelength input combinations. Each cell reports the Avg. ± Std results.

Dataset	Test Samples	DISTS (↓)		
		Dual Excitation	**266 nm Only**	**355 nm Only**
Kidney ccRCC (H&E)	60,531	0.126 ± 0.023	0.136 ± 0.023	0.136 ± 0.023
Skin Melanoma (H&E)	21,739	0.135 ± 0.021	0.151 ± 0.022	0.149 ± 0.022
Skin Fungal Disease (PAS)	11,406	0.142 ± 0.032	0.150 ± 0.032	0.154 ± 0.033
Kidney ccRCC (Masson's)	66,672	0.139 ± 0.022	0.142 ± 0.022	0.150 ± 0.022
Mouse Kidney (JMS)	16,473	0.168 ± 0.023	0.174 ± 0.023	0.174 ± 0.024
Mouse Kidney (H&E)	17,821	0.129 ± 0.020	0.136 ± 0.018	0.147 ± 0.020
Mouse Kidney (PAS)	21,594	0.128 ± 0.018	0.135 ± 0.017	0.139 ± 0.017
Mouse Kidney (Masson's)	18,867	0.158 ± 0.032	0.163 ± 0.032	0.169 ± 0.033
Mouse GI (H&E)	7,768	0.127 ± 0.028	0.136 ± 0.026	0.149 ± 0.028
Mouse GI (PAS)	28,345	0.145 ± 0.025	0.152 ± 0.024	0.160 ± 0.025
Mouse GI (Masson's)	12,996	0.148 ± 0.042	0.158 ± 0.041	0.164 ± 0.042
Mouse Brain (H&E)	8,452	0.130 ± 0.023	0.139 ± 0.023	0.144 ± 0.024
All Datasets	292,664	0.138 ± 0.027	0.145 ± 0.027	0.150 ± 0.027

Note: GI, gastrointestinal. Metric are computed on 256×256 px patches.

Table 6.5: MS-SSIM (↑) scores across datasets for different excitation wavelength input combinations. Each cell reports the Avg. ± Std results.

Dataset	Test Samples	MS-SSIM (↑)		
		Dual Excitation	**266 nm Only**	**355 nm Only**
Kidney ccRCC (H&E)	60,531	0.939 ± 0.044	0.914 ± 0.051	0.910 ± 0.055
Skin Melanoma (H&E)	21,739	0.870 ± 0.072	0.812 ± 0.082	0.811 ± 0.082
Skin Fungal Disease (PAS)	11,406	0.869 ± 0.066	0.843 ± 0.068	0.827 ± 0.084
Kidney ccRCC (Masson's)	66,672	0.913 ± 0.049	0.896 ± 0.054	0.882 ± 0.060
Mouse Kidney (JMS)	16,473	0.836 ± 0.069	0.797 ± 0.078	0.802 ± 0.075
Mouse Kidney (H&E)	17,821	0.926 ± 0.025	0.907 ± 0.029	0.857 ± 0.051
Mouse Kidney (PAS)	21,594	0.914 ± 0.039	0.890 ± 0.041	0.867 ± 0.047
Mouse Kidney (Masson's)	18,867	0.896 ± 0.061	0.876 ± 0.066	0.851 ± 0.074
Mouse GI (H&E)	7,768	0.920 ± 0.039	0.894 ± 0.047	0.843 ± 0.080
Mouse GI (PAS)	28,345	0.864 ± 0.075	0.842 ± 0.078	0.803 ± 0.098
Mouse GI (Masson's)	12,996	0.893 ± 0.067	0.873 ± 0.069	0.855 ± 0.077
Mouse Brain (H&E)	8,452	0.929 ± 0.058	0.909 ± 0.051	0.893 ± 0.058
All Datasets	292,664	0.904 ± 0.063	0.879 ± 0.070	0.862 ± 0.078

Note: GI, gastrointestinal. Metric are computed on 256×256 px patches.

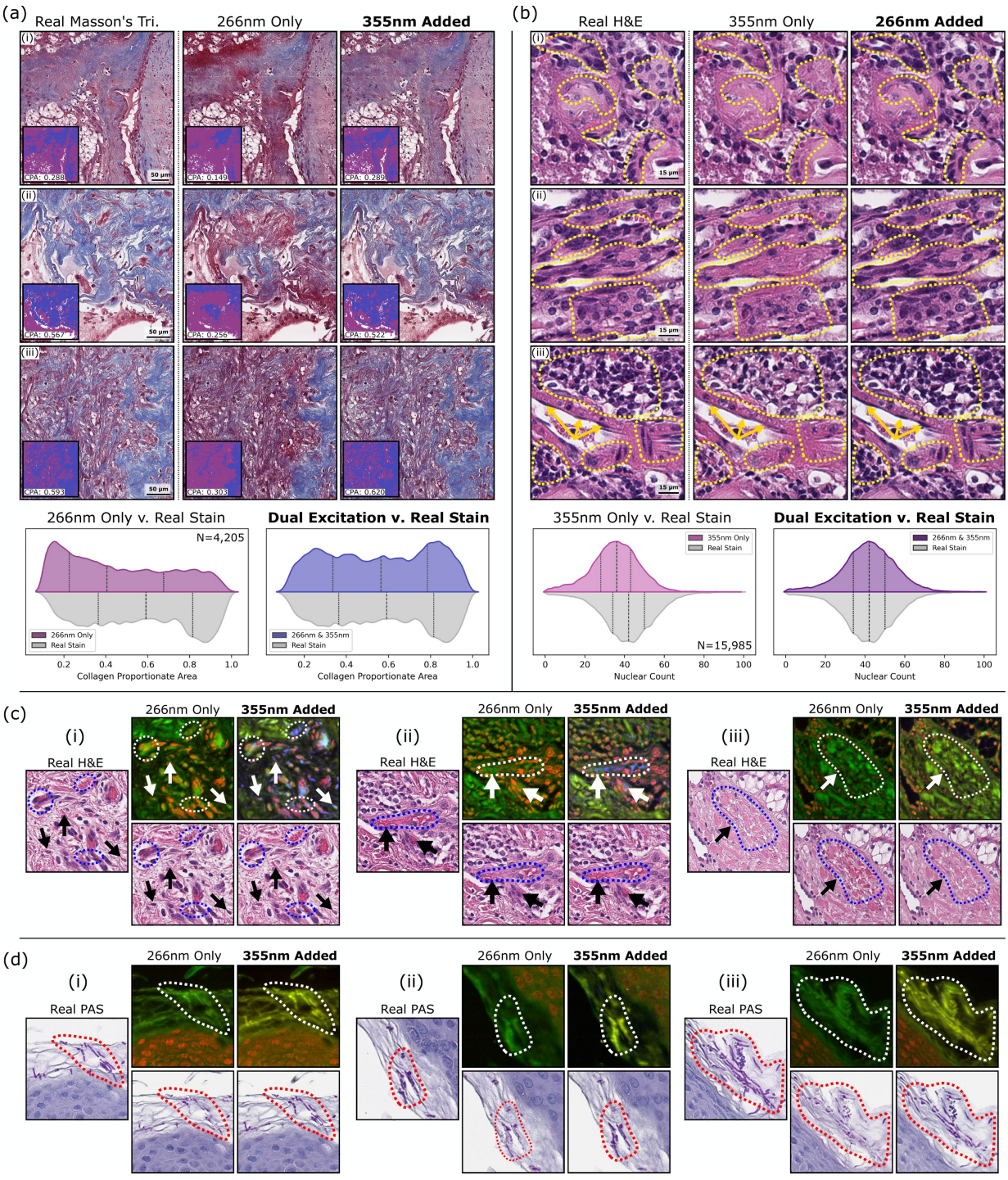

Figure 6.13: Dual-excitation virtual staining improves reconstruction of histological features across multiple stains, with visual and quantitative comparisons. (a) Masson's trichrome of ccRCC kidney: addition of 355 nm improves collagen staining. (b) H&E of mouse kidney: addition of 266 nm adds nuclear contrast, improving nuclear staining. (c) Addition of 355 nm improves RBC staining accuracy. (d) Dual excitation improves PAS staining of fungal hyphae.

histological features. Figure 6.13 presents three representative examples, collagen in Masson's trichrome, nuclei in H&E, RBCs, and fungal hyphae in PAS-stained skin, with each demonstrating how dual excitation improves staining of clinically relevant features.

Figure 6.13a compares virtual Masson's trichrome staining of ccRCC kidney tissue using models trained with 266 nm only versus dual excitation input. Using QuPath digital pathology software, a pixel classifier was trained to segment collagen-positive pixels. The collagen proportionate area (CPA), defined as the fraction of tissue area classified as collagen, was computed across 256×256 px patches in regions with at least 5% collagen. While CPA is primarily used in liver biopsies to assess fibrosis and clinical outcomes [198], here it serves as a quantitative proxy for evaluating collagen staining accuracy. Three example regions are shown in Figure 6.13a, in order of increasing CPA values. In each example, the 266 nm model underestimates collagen presence, mis-staining collagen areas in red, leading to significantly reduced CPA values. By adding the 355 nm channels, the model more closely matches the reference stain, as reflected in the segmentation maps (bottom left), which show a similar distribution of collagen. These qualitative findings are further supported in the violin plots below, which show CPA distributions across N = 4,205 patches. The dual excitation model achieves an almost symmetric distribution (median 0.57 ± 0.25), closely matching the ground truth (0.59 ± 0.25). In contrast, the 266 nm model exhibits a skewed distribution (median 0.40 ± 0.25), reflecting an overall underestimation of collagen. The improvement likely results from the addition of the 355 nm radiative channel, which provides complementary autofluorescence contrast to 266 nm. While collagen fluoresces under both excitations, many surrounding structures do as well. Access to both radiative channels allow the model to better stain collagen based on learned differences in emission intensities across tissue structures. Surrounding tissue structures also exhibit non-radiative contrast at 355 nm, which may further aid in distinguishing collagen.

Figure 6.13b demonstrates the benefits of including 266 nm input for nuclear staining. Examples are shown in H&E mouse kidney and compare the 355 nm only model to the dual excitation output. In each case, the 355 nm model struggles to accurately reconstruct nuclei, and several nuclear structures are missed entirely and replaced by pink eosin staining. Although 355 nm lacks nuclear contrast, the model does successfully infer some nuclear structures from the surrounding tissue, but this is not always reliable. In contrast, by adding 266 nm excitation, the model consistently identifies and correctly stains nuclei. The quantitative nuclear counts reinforce this difference. Using StarDist [144] for segmentation, nuclear counts were computed for N=17,821 patches. The dual excitation model closely matches the chemical H&E distribution (median 42.00 ± 14.50 vs. real 41.57 ± 14.23), while the 355 nm model shows a similar distribution shape but with a shifted center, reflecting the overall undercounting of nuclei (34.95 ± 12.54).

Figure 6.13c shows three examples of how the addition of 355 nm channels improves staining of RBCs. While the 266 nm model can often identify RBCs using structural cues, it lacks hemoglobin-specific contrast which can lead to errors. In Figure 6.13 examples (c-i) and (c-ii), RBCs are either missed or incorrectly stained purple as nuclei. While in Figure 6.13(c-iii), the 266 nm model hallucinates red RBC-looking structures where none exist. In contrast, the 355 nm non-radiative channel (shown in blue) captures hemoglobin absorption, providing both positive and negative cues that help the model more accurately identify RBCs and avoid such false positives.

Lastly, Figure 6.13d shows three examples of PAS staining of fungal hyphae in skin tissue. The 266 nm model identifies some fungal structures but often underrepresents or only partially stains them. With both excitation contrasts, the model more accurately stains the fungal elements, aided by the 355 nm radiative channel (shown in yellow), which enhances their visibility and allows for more complete staining. In each case, the dual excitation output more closely matches the reference PAS stain. While some deviations remain and the staining is not perfect, the addition of 355 nm contrast leads to a noticeably improved staining of fungal hyphae.

6.4.5 Comparative Performance of Virtual Staining Models

The RegGAN model was chosen for virtual staining because it enables supervised training while remaining robust to imperfect alignments by integrating a registration network during training. This makes it well-suited for cross-modality tasks where precise pixel-level alignment is difficult to achieve. To evaluate its effectiveness, RegGAN was benchmarked against two commonly used approaches: Pix2Pix (paired) and CycleGAN (unpaired). Figure 6.14 presents qualitative and quantitative comparisons across the models, using a subset of examples that highlight each stain applied to a relevant tissue type or disease case featured in this study. Figure 6.14(a-e) show: (a) H&E-stained human kidney with ccRCC (N=60,531), (b) H&E-stained human skin with nodular melanoma (N=21,739), (c) PAS-stained human skin with fungal infection (N=11,406), (d) Masson's trichrome-stained kidney with ccRCC (N=66,672), and (e) JMS-stained healthy mouse kidney (N=16,473). Each row in the figure includes the 266 nm and 355 nm PARS input, the corresponding chemical stain, and outputs from the three models. In addition, violin plots showing the relative performance of each model are provided for both the DISTS (perceptual similarity) and MS-SSIM (structural similarity) metrics. The quantitative scores for RegGAN, Pix2Pix, and CycleGAN across all tissue–stain combinations, including both the overall aggregated metrics and the per–tissue–stain–combination breakdowns for every dataset in

this study, are presented in Table 6.6 for the DISTS metric and Table 6.7 for the MS-SSIM metric.

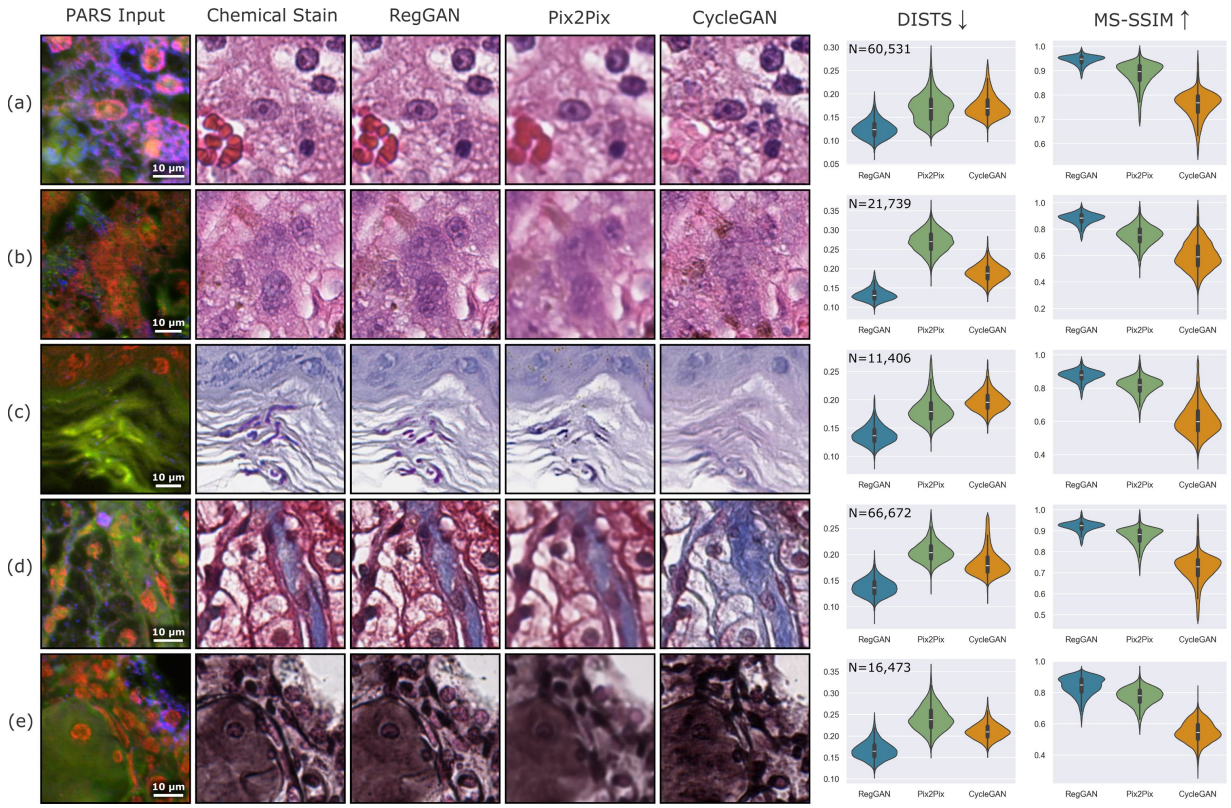

Figure 6.14: Visual and quantitative comparison of virtual staining performance for RegGAN, Pix2Pix, and CycleGAN models. Each example shows the PARS input image, ground truth chemical stain, and outputs from all three models, along with distributions of quantitative metrics (DISTS and MS-SSIM). The comparison covers all stains used in this study and includes representative disease cases where possible: (a) H&E-stained human kidney with ccRCC, (b) H&E-stained human skin with nodular melanoma, (c) PAS-stained human skin with fungal infection, (d) Masson's trichrome-stained human kidney with ccRCC, and (e) JMS-stained healthy mouse kidney.

The Pix2Pix model, a strictly supervised model trained on aligned pairs, accurately captures the overall stain colour and tissue structure. However, in each example in Figure 6.14, it consistently generates overly smoothed and blurry outputs, failing to reproduce the correct textures and structural detail. While it may be sufficient for low magnifications, the blurring limits diagnostic utility at higher magnifications, where features like mitotic figures, nuclear atypia, and subtle architectural cues are important. These limitations are evident in the loss of nuclear detail in Figure 6.14b, poorly defined glomerulus basement

Table 6.6: Quantitative comparison of RegGAN, Pix2Pix, and CycleGAN for each dataset using DISTS (↓). Each cell reports the Avg. ± Std results.

Dataset	Test Samples	DISTS (↓)		
		RegGAN	**Pix2Pix**	**CycleGAN**
Kidney ccRCC (H&E)	60,531	0.126 ± 0.023	0.171 ± 0.034	0.176 ± 0.031
Skin Melanoma (H&E)	21,739	0.135 ± 0.021	0.271 ± 0.030	0.191 ± 0.024
Skin Fungal Disease (PAS)	11,406	0.142 ± 0.032	0.187 ± 0.068	0.199 ± 0.034
Kidney ccRCC (Masson's)	66,672	0.139 ± 0.022	0.207 ± 0.024	0.190 ± 0.036
Mouse Kidney (JMS)	16,473	0.168 ± 0.023	0.242 ± 0.030	0.213 ± 0.025
Mouse Kidney (H&E)	17,821	0.129 ± 0.020	0.186 ± 0.030	0.179 ± 0.019
Mouse Kidney (PAS)	21,594	0.128 ± 0.018	0.152 ± 0.023	0.188 ± 0.015
Mouse Kidney (Masson's)	18,867	0.158 ± 0.032	0.195 ± 0.050	0.191 ± 0.031
Mouse GI (H&E)	7,768	0.127 ± 0.028	0.175 ± 0.050	0.191 ± 0.026
Mouse GI (PAS)	28,345	0.145 ± 0.025	0.182 ± 0.033	0.222 ± 0.037
Mouse GI (Masson's)	12,996	0.148 ± 0.042	0.208 ± 0.068	0.236 ± 0.051
Mouse Brain (H&E)	8,452	0.130 ± 0.023	0.184 ± 0.031	0.191 ± 0.023
All Datasets	292,664	0.138 ± 0.027	0.194 ± 0.047	0.193 ± 0.035

Note: GI, gastrointestinal. Metric are computed on 256×256 px patches.

Table 6.7: Quantitative comparison of RegGAN, Pix2Pix, and CycleGAN for each dataset using MS-SSIM (↑). Each cell reports the Avg. ± Std results.

Dataset	Test Samples	MS-SSIM (↑)		
		RegGAN	**Pix2Pix**	**CycleGAN**
Kidney ccRCC (H&E)	60,531	0.939 ± 0.044	0.873 ± 0.077	0.750 ± 0.079
Skin Melanoma (H&E)	21,739	0.870 ± 0.072	0.744 ± 0.088	0.594 ± 0.112
Skin Fungal Disease (PAS)	11,406	0.869 ± 0.066	0.808 ± 0.080	0.613 ± 0.109
Kidney ccRCC (Masson's)	66,672	0.913 ± 0.049	0.864 ± 0.062	0.707 ± 0.090
Mouse Kidney (JMS)	16,473	0.836 ± 0.069	0.771 ± 0.065	0.547 ± 0.071
Mouse Kidney (H&E)	17,821	0.926 ± 0.025	0.856 ± 0.042	0.656 ± 0.081
Mouse Kidney (PAS)	21,594	0.914 ± 0.039	0.871 ± 0.046	0.667 ± 0.070
Mouse Kidney (Masson's)	18,867	0.896 ± 0.061	0.875 ± 0.067	0.743 ± 0.097
Mouse GI (H&E)	7,768	0.920 ± 0.039	0.871 ± 0.055	0.732 ± 0.098
Mouse GI (PAS)	28,345	0.864 ± 0.075	0.806 ± 0.090	0.476 ± 0.163
Mouse GI (Masson's)	12,996	0.893 ± 0.067	0.837 ± 0.085	0.641 ± 0.168
Mouse Brain (H&E)	8,452	0.929 ± 0.058	0.848 ± 0.089	0.592 ± 0.100
All Datasets	292,664	0.904 ± 0.063	0.843 ± 0.082	0.663 ± 0.134

Note: GI, gastrointestinal. Metric are computed on 256×256 px patches.

membranes in the JMS-stained kidney (Figure 6.14d), and incomplete PAS fungal staining in Figure 6.14c. Despite careful registration using tools like Warpy, Pix2Pix remains sensitive to slight misalignments and differences between imaging modalities, which are inevitable in real-world datasets. As well, its performance would likely degrade significantly with noisier or less curated inputs.

The CycleGAN model, trained in an unpaired fashion, produces sharper images and retains textural detail more effectively. However, its less constrained training approach limits its ability to learn more complex contrast mappings. For example, RBCs are poorly reproduced in the H&E kidney (Figure 6.14a); the blue collagen stain is exaggerated and poorly localized in the trichrome example (Figure 6.14d); fungal elements are entirely missed in the PAS skin (Figure 6.14c); and melanin and nuclei are poorly rendered in the H&E melanoma case (Figure 6.14b). In the JMS-stained kidney (Figure 6.14e), CycleGAN roughly applies the correct stain colour and texture but fails to accurately stain the real basement membrane structures.

In contrast, by incorporating a registration network into the training process, RegGAN benefits from paired training feedback while being robust to data misalignments. It preserves high-resolution texture and structure better than Pix2Pix, particularly evident in the accurate rendering of nuclear detail (Figure 6.14b) and basement membranes (Figure 6.14e), while also achieving more faithful stain translation than CycleGAN. It successfully captures collagen in the trichrome example (Figure 6.14d), the PAS-stained fungal elements (Figure 6.14c), and melanin in the skin example (Figure 6.14b), producing the most consistent alignment with the chemical reference across all examples.

These qualitative observations are supported by the quantitative metrics. RegGAN achieves the best performance across all stain–tissue combinations under the DISTS metric, which captures perceptual similarity based on structural and textural fidelity (lower values reflect better similarity). CycleGAN generally achieves better DISTS scores than Pix2Pix, particularly in Figure 6.14 (b), (d), and (e), where Pix2Pix exhibits more pronounced blurring and textural loss. However, CycleGAN underperforms in specialized staining tasks such as PAS fungal staining (Figure 6.14c), where it fails to capture key features that Pix2Pix more accurately reproduces.

When evaluated with MS-SSIM, which captures pixel-level structural similarity across scales (higher values reflect better similarity), RegGAN again outperforms both models. CycleGAN performs the worst in all MS-SSIM examples, reflecting its failure to accurately map certain structural features and stain distributions, despite its sharper overall appearance and textural similarity.

RegGAN demonstrated the strongest performance in virtual staining; however, the

results highlight the broader utility of incorporating registration directly into a training pipeline. Its ability to handle small but unavoidable misalignments reduces the time burden of precise data curation. It also helps mitigate challenges in cross-modality learning tasks, particularly those involving mismatched resolutions or differences in acquisition, such as optical sectioning, illumination, or other imaging conditions. By addressing these discrepancies as part of the training and optimization process, registration-aware approaches enable more scalable and robust use of imperfectly paired data. Beyond virtual staining, this strategy may benefit a range of cross-modality learning tasks in biomedical imaging where alignment is a limiting factor.

6.5 Conclusion

This study presents a dual-excitation PARS microscopy system for label-free virtual multi-stain histology, combining 266 nm and 355 nm UV excitations to capture complementary radiative and non-radiative contrasts. The addition of 355 nm expands the range of histological features that can be distinguished, including RBCs and melanin-containing elements, and enhances visualization of stromal architecture including collagen and elastin, while 266 nm excitation provides important nuclear contrast and surrounding connective tissue structures. Using the RegGAN image-translation framework, this study presents the first PARS virtual staining of specialized stains such as Masson's trichrome, PAS, and JMS, alongside H&E, across healthy and pathological human and murine tissues, including kidney, skin, brain, and gastrointestinal tract. Evaluation on unseen WSIs showed close correspondence between virtual and chemical stains, with improved similarity metrics, perceptual metrics, and more accurate reconstruction of histology-specific features when both excitation wavelengths were used. A masked pathologist evaluation further demonstrated that virtual stains preserved diagnostic quality comparable to their chemical counterparts, and pathologists were unable to reliably determine image origin. Together, these results establish dual-excitation PARS virtual staining as a non-destructive addition to the histopathology workflow, enabling pre-stain histology imaging that preserves tissue for conventional histology and downstream molecular analyses, while expanding diagnostic insight.

Chapter 7

Conclusions and Future Work

This thesis presented the development of a whole slide PARS microscopy platform and virtual staining framework capable of capturing label-free WSIs and generating multiple histochemical stains from a single unstained FFPE tissue section. The system produces WSIs in the same formats and magnifications expected in clinical practice, allowing the acquired images to be reviewed and compared directly against conventional chemically stained slides. Importantly, the system provides diagnostic-quality visualization without consuming or altering the tissue, leaving the original specimen intact and available for downstream assays or specialized stains. Consequently, the framework can either replace complex and time-consuming staining or serve as a nondestructive pre-scan prior to conventional processing, depending on clinical or research needs. In addition, because the PARS and chemically stained WSIs can be matched in a true one-to-one manner, this work was able to assess diagnostic similarity, and overall demonstrated that pathologists could not reliably distinguish traditional stains from the virtual stains generated here, within the scope of the tissue types, disease contexts, stains, and cohort sizes evaluated.

Across the research modules in this thesis (Chapters 3–6), the presented work encompasses contributions to the PARS imaging system, the implementation, evaluation, and comparison of deep learning–based virtual staining models, a first masked clinical concordance study, and finally extending the PARS imaging and virtual staining capabilities beyond H&E.

The first component of this thesis introduced an automated, high-resolution, whole slide PARS microscope capable of imaging standard thin, transmissible FFPE tissue sections. This system addresses key limitations of earlier PARS prototypes, including restricted field-of-view and prohibitively slow, manual operation. The work establishes a repeatable PARS

imaging workflow capable of producing label-free WSIs in the magnification and format required for clinical review. Quantitative and qualitative evaluations show that essential histologic features, such as nuclear morphology, are faithfully reproduced compared to gold-standard H&E staining.

Building on this hardware foundation, this thesis implements the first WSI virtual H&E staining for PARS using an the unpaired CycleGAN framework. By training on loosely paired data and enforcing balanced feature distributions across domains, the approach produces virtual H&E slides that preserve fine architectural details at clinical magnifications. Together with the PARS imaging system and virtual staining model, true diagnostic review of the virtually stained PARS images was possible. Subsequently, this enabled the first masked diagnostic concordance study of PARS virtual H&E which was performed on one-to-one whole slide pairs of human breast NCBs. Board-certified pathologists independently assessed each slide, and the results showed strong agreement across a broad range of histologic findings. These outcomes provide the first evidence that PARS virtual H&E can support clinical interpretation at a level comparable to conventional staining.

The final module expanded the virtual staining framework beyond H&E through two important advances: the introduction of a secondary 355 nm excitation source to complement PARS's established 266 nm contrasts, and the application of a new registration-guided translation model (RegGAN) for virtual multi-staining. Together, these developments enabled the first demonstrations of PARS virtual staining of secondary specialized stains including Masson's Trichrome, PAS, and JMS (in addition to H&E) from a single unstained section. Expert pathologists judged these virtual stains to be diagnostically equivalent to their chemical counterparts. This module also resulted in the public release of virtual staining results on held-out WSIs spanning all tissue stains presented in this thesis, including both healthy and diseased cases. This module also included a robust comparison of RegGAN against CycleGAN and Pix2Pix across all stains and tissue types employed in this work.

Overall, this thesis demonstrates that PARS, combined with virtual staining algorithms, can deliver clinically interpretable WSIs and faithfully reproduce several of the most commonly used histochemical stains. Importantly, this approach preserves the original tissue slide, enabling additional assays or specialized stains that would otherwise require serial sections. This work advances PARS histology toward practical integration with pathology workflows and provides a foundation for future developments in PARS label-free digital histology.

Discussion on Future Directions

While this work demonstrates the feasibility and diagnostic utility of a multi-wavelength PARS whole slide imaging system and virtual multi-staining framework, several opportunities remain to advance both the PARS modality and the downstream computational pipeline. These future directions fall into two areas: (1) advancements in the PARS system architecture and (2) developments in virtual staining and evaluation strategies.

On the system architecture side, a main limitation of the PARS system presented here is total scan time. While the imaging speeds achieved in this work were sufficient for proof-of-concept whole-slide acquisition, virtual staining model development, and pathologist concordance studies, substantially higher throughput will be required for practical use in routine clinical workflows, particularly for routine stains such as H&E. Chapter 3 (Section 3.3.3) provides a breakdown of PARS whole slide imaging speed (also applies to the dual-excitation system in Ch 6). As a point-scanning modality, PARS speed is primarily dictated by the excitation laser repetition rate (50 kHz here) and the mechanics of the scanning process. Increasing the repetition rate is the first step toward faster imaging. Multi-megahertz deep-UV sources can be custom made through fourth-harmonic generation of 1030 or 1064 nm pump lasers, or such systems can now be purchased commercially (for example, Amplitude's Satsuma deep-UV laser offers single-shot rates up to 40 MHz). Moving from 50 kHz to even a 1 to 5 MHz source would offer one to two orders of magnitude theoretical speed improvement (for example, approximately 8.8 hours versus 5 minutes for a $1\,cm^2$ area at 250 nm/pixel under ideal scanning efficiency). However, practically achieving these speeds requires moving the excitation beam across the sample fast enough to space out the high-repetition-rate pulses, which is not feasible with the current mechanical stage scanning architecture. As such, fast mirror-based beam scanning is required instead. MEMS mirrors, which can swing at multi-kilohertz frequencies, can support the line rates needed for high-repetition-rate excitation. In fact, concurrent work from our group has already demonstrated a hybrid opto-mechanical scanning approach using both MEMS mirrors and stage translation to achieve approximately 1 MHz PARS imaging, showing that substantial speed improvements are achievable and continue to be improved and developed [105].

In addition to speed improvements, there are clear opportunities to further expand the biomolecular contrast captured by the PARS histology system. This work showed that adding a 355 nm excitation channel meaningfully broadened the available biomolecular contrast and improved virtual staining performance. Two main future developments could push this further. The most immediate improvement, which requires no additional wavelengths, would be to spectrally separate the radiative PARS channel, which is currently

collected as a single broadband intensity. In reality, this signal contains molecule-specific spectral information, and spectral binning would provide a richer radiative contrast set while only requiring relatively modest changes to the radiative measurement module. Beyond this, additional excitation wavelengths or a tunable source could be introduced to further diversify non-radiative and radiative contrasts. While feasible, expanding the wavelength range introduces challenges such as chromatic aberrations, and different spectral bands (e.g., UV, visible, infrared) would require distinct optical pathways with appropriate substrates, coatings, mirrors, objectives, and scanning heads. Depending on the wavelengths involved, this can represent a substantially larger architectural change.

On the computational side, opportunities exist to advance virtual staining algorithms. The majority of current methods operate in a patch-based training framework, which is necessary because WSIs are too large to process directly. However, strictly patch-based methods miss slide-level global context and can produce patch-to-patch inconsistencies. Other areas of computational pathology, such as WSI classification and segmentation, have developed strategies to incorporate broader or longer-range context, including multi-scale or pyramidal architectures [199, 200] and graph-based WSI representations [201, 202]. Adapting similar strategies for virtual staining could allow models to better capture global tissue structure and improve coherence across WSI outputs. In addition, it may be valuable to explore architectures beyond GANs. For example, one recent study demonstrated that diffusion models can outperform GAN-based approaches when used for pixel super-resolution virtual staining [68], where a lower-resolution input is upsampled and virtually stained at 40×. This approach also offers potential speed benefits, since a faster lower-resolution PARS acquisition (e.g., 10×) could still yield high-resolution virtual stains.

However, improvements in virtual staining algorithms must be accompanied by improvements in how these algorithms are evaluated. Although masked concordance studies remain the most reliable way to assess diagnostic equivalence, they are constrained by pathologist time, inter-reader variability, and logistical constraints that make large-scale evaluation difficult. As virtual staining progresses, there is a need for quantitative, pathology-aware metrics that reflect clinically meaningful tissue features rather than general image-similarity or perceptual measures (e.g., MS-SSIM, DISTS). Developing such metrics is important because full pathology review is not always feasible. Automated or AI-assisted diagnostic tools offer a natural complement to expert assessment; classifiers or segmentation models trained on chemical stains could be applied to virtual stains to quantify agreement at structural or diagnostic levels, providing objective measures not restricted by human throughput. Such frameworks would allow rapid testing and iteration on virtual staining methods without relying exclusively on expert review.

While the work presented in this thesis focuses on transmission-mode imaging of thin,

fixed tissue sections, extending PARS microscopy to freshly resected specimens and in vivo tissue imaging represents an important direction with significant clinical applications. Proof-of-concept demonstrations of PARS imaging on thick and freshly resected tissues have already been reported [32], showing that both radiative and non-radiative contrasts can be detected without histochemical staining. However, several technical and practical challenges remain for routine application in these settings.

From an optical standpoint, imaging thick or in vivo tissues requires transitioning from the transmission-mode configuration used in this work to reflection-mode operation. Because biological tissues scatter light predominantly in the forward direction, reflection-mode operation returns less signal to the detection optics, making it more difficult to achieve sufficient SNR for the non-radiative PARS signal. Potential solutions include improved collection efficiency of the backscattered probe light, optimized detection geometries, and higher repetition-rate excitation sources that enable signal averaging without significantly increasing acquisition time. In addition, because bulk tissue cannot be physically sectioned prior to imaging, optical sectioning must be performed during acquisition, for example using confocal pinholing as demonstrated in previous reflection-mode PARS systems [32]. Furthermore, surface morphology presents another challenge. Because fresh and in vivo tissues are not uniformly flat like thin histological sections, compression mounts or index-matching media may be required to maintain an optically smooth imaging surface.

Practical considerations related to sample handling and clinical workflow must also be addressed. When imaging freshly resected tissue, acquisition speed becomes important, as imaging must occur before significant autolysis or degradation of the specimen. For in vivo imaging, additional challenges arise in stabilizing the imaging site and maintaining consistent tissue positioning during acquisition. Finally, an additional challenge in extending PARS microscopy to freshly resected or in vivo tissues is the absence of an established histological gold standard for direct comparison. Conventional histopathology relies on fixed, sectioned, and chemically stained tissue, whereas fresh tissue imaging captures the specimen in its native state. One possible validation strategy is to image the exposed surface of freshly resected tissue and then process the same specimen through conventional fixation, sectioning, and staining, enabling comparison with adjacent histological sections. Developing robust validation protocols will be important for evaluating diagnostic performance and facilitating broader adoption of PARS-based imaging approaches.

Letter of Copyright Permission

Figure 2.11 – Springer Nature License

This Agreement between James Tweel (University of Waterloo) ("You") and Springer Nature ("Springer Nature") consists of your license details and the terms and conditions provided by Springer Nature and the Copyright Clearance Center.

License Number	6225631204695
License date	Mar 10, 2026
Licensed Content Publisher	Springer Nature
Licensed Content Publication	Nature Biomedical Engineering
Licensed Content Title	Virtual histological staining of unlabelled tissue-autofluorescence images via deep learning
Licensed Content Author	Yair Rivenson et al
Licensed Content Date	Mar 4, 2019
Type of Use	Thesis/Dissertation
Format	Print and electronic
Portion	Figures/Tables/Illustrations
Number of figures	1
Institution name	University of Waterloo
Portions	Fig. 3 and Fig. 4

References

[1] James E.D. Tweel, Benjamin R. Ecclestone, Marian Boktor, Deepak Dinakaran, John R. Mackey, and Parsin Haji Reza. Automated Whole Slide Imaging for Label-Free Histology Using Photon Absorption Remote Sensing Microscopy. *IEEE Transactions on Biomedical Engineering*, 71(6):1901–1912, June 2024.

[2] James ED Tweel, Benjamin R Ecclestone, Marian Boktor, James Alexander Tummon Simmons, Paul Fieguth, and Parsin Haji Reza. Virtual histology with photon absorption remote sensing using a cycle-consistent generative adversarial network with weakly registered pairs. *arXiv preprint arXiv:2306.08583*, 2023.

[3] James E. D. Tweel, Benjamin R. Ecclestone, Hager Gaouda, Deepak Dinakaran, Michael P. Wallace, Gilbert Bigras, John R. Mackey, and Parsin Haji Reza. Photon Absorption Remote Sensing Imaging of Breast Needle Core Biopsies Is Diagnostically Equivalent to Gold Standard H&E Histologic Assessment. *Current Oncology*, 30(11):9760–9771, November 2023. Publisher: Multidisciplinary Digital Publishing Institute.

[4] James ED Tweel, Benjamin R Ecclestone, James A Tummon Simmons, and Parsin Haji Reza. Label-free whole slide virtual multi-staining using dual-excitation photon absorption remote sensing microscopy. *arXiv preprint arXiv:2509.05085*, 2025.

[5] John D Bancroft and Marilyn Gamble. *Theory and practice of histological techniques*. Elsevier health sciences, 2008.

[6] Christina E. Day, editor. *Histopathology: Methods and Protocols*, volume 1180 of *Methods in Molecular Biology*. Springer, New York, NY, 2014.

[7] Fatemeh Ghezloo, Pin-Chieh Wang, Kathleen F. Kerr, Tad T. Brunyé, Trafton Drew, Oliver H. Chang, Lisa M. Reisch, Linda G. Shapiro, and Joann G. Elmore. An

analysis of pathologists' viewing processes as they diagnose whole slide digital images. *Journal of Pathology Informatics*, 13:100104, January 2022.

[8] Neeta Kumar, Ruchika Gupta, and Sanjay Gupta. Whole Slide Imaging (WSI) in Pathology: Current Perspectives and Future Directions. *Journal of Digital Imaging*, 33(4):1034–1040, August 2020. tex.pmcid: PMC7522141.

[9] Tatyana S. Gurina and Lary Simms. Histology, Staining. In *StatPearls*. StatPearls Publishing, Treasure Island (FL), 2023. tex.copyright: Copyright © 2023, StatPearls Publishing LLC. tex.lccn: NBK557663.

[10] Mousa A. Al-Abbadi. Basics of cytology. *Avicenna Journal of Medicine*, 1(1):18–28, 2011. tex.pmcid: PMC3507055.

[11] Ian A. Cree, Puay Hoon Tan, William D. Travis, Pieter Wesseling, Yukako Yagi, Valerie A. White, Dilani Lokuhetty, and Richard A. Scolyer. Counting mitoses: SI(ze) matters! *Modern Pathology: An Official Journal of the United States and Canadian Academy of Pathology, Inc*, 34(9):1651–1657, September 2021. tex.pmcid: PMC8376633.

[12] Elizabeth Mallon, Pinchas Osin, Nasar Nasiri, Iain Blain, Beatrice Howard, and Barry Gusterson. The Basic Pathology of Human Breast Cancer. *Journal of Mammary Gland Biology and Neoplasia*, 5(2):139–163, April 2000.

[13] Larry E. Morrison, Mark R. Lefever, Heather N. Lewis, Monesh J. Kapadia, and Daniel R. Bauer. Conventional histological and cytological staining with simultaneous immunohistochemistry enabled by invisible chromogens. *Laboratory Investigation*, 102(5):545–553, May 2022. Publisher: Nature Publishing Group tex.copyright: 2021 The Author(s).

[14] Nicola Michielli, Alessandro Caputo, Manuela Scotto, Alessandro Mogetta, Orazio Antonino Maria Pennisi, Filippo Molinari, Davide Balmativola, Martino Bosco, Alessandro Gambella, Jasna Metovic, Daniele Tota, Laura Carpenito, Paolo Gasparri, and Massimo Salvi. Stain normalization in digital pathology: Clinical multicenter evaluation of image quality. *Journal of Pathology Informatics*, 13:100145, September 2022. tex.pmcid: PMC9577129.

[15] Bijie Bai, Xilin Yang, Yuzhu Li, Yijie Zhang, Nir Pillar, and Aydogan Ozcan. Deep learning-enabled virtual histological staining of biological samples. *Light: Science & Applications*, 12(1):57, March 2023. Publisher: Nature Publishing Group tex.copyright: 2023 The Author(s).

[16] G. Popescu. *Quantitative Phase Imaging of Cells and Tissues*. McGraw-Hill biophotonics Quantitative phase imaging of cells and tissues. McGraw Hill LLC, 2011.

[17] Frédéric Jamme, Slavka Kascakova, Sandrine Villette, Fatma Allouche, Stéphane Pallu, Valérie Rouam, and Matthieu Réfrégiers. Deep UV autofluorescence microscopy for cell biology and tissue histology. *Biology of the Cell*, 105(7):277–288, 2013.

[18] Da-Kang Yao, Ruimin Chen, Konstantin Maslov, Qifa Zhou, and Lihong V. Wang. Optimal ultraviolet wavelength for in vivo photoacoustic imaging of cell nuclei. *Journal of Biomedical Optics*, 17(5):056004, May 2012. tex.pmcid: PMC3602808.

[19] Takayoshi Kobayashi, Kazuaki Nakata, Ichiro Yajima, Masashi Kato, and Hiromichi Tsurui. Label-Free Imaging of Melanoma with Confocal Photothermal Microscopy: Differentiation between Malignant and Benign Tissue. *Bioengineering*, 5(3):67, August 2018. tex.pmcid: PMC6163989.

[20] Giulia Borile, Deborah Sandrin, Andrea Filippi, Kurt I Anderson, and Filippo Romanato. Label-free multiphoton microscopy: much more than fancy images. *International Journal of Molecular Sciences*, 22(5):2657, 2021.

[21] Yanping Li, Binglin Shen, Shaowei Li, Yihua Zhao, Junle Qu, and Liwei Liu. Review of stimulated raman scattering microscopy techniques and applications in the biosciences. *Advanced Biology*, 5(1):2000184, 2021.

[22] Shaowei Li, Yanping Li, Rongxing Yi, Liwei Liu, and Junle Qu. Coherent anti-stokes raman scattering microscopy and its applications. *Frontiers in Physics*, 8:598420, 2020.

[23] Leena Latonen, Sonja Koivukoski, Umair Khan, and Pekka Ruusuvuori. Virtual staining for histology by deep learning. *Trends in Biotechnology*, 42(9):1177–1191, 2024.

[24] Steven L. Jacques. Optical properties of biological tissues: a review. *Physics in Medicine and Biology*, 58(11):R37–61, June 2013.

[25] Jun Xia, Junjie Yao, and Lihong V. Wang. Photoacoustic tomography: Principles and advances. *Electromagnetic waves (Cambridge, Mass.)*, 147:1–22, 2014. tex.pmcid: PMC4311576.

[26] Yair Rivenson, Hongda Wang, Zhensong Wei, Kevin de Haan, Yibo Zhang, Yichen Wu, Harun Günaydın, Jonathan E. Zuckerman, Thomas Chong, Anthony E. Sisk, Lindsey M. Westbrook, W. Dean Wallace, and Aydogan Ozcan. Virtual histological staining of unlabelled tissue-autofluorescence images via deep learning. *Nature Biomedical Engineering*, 3(6):466–477, June 2019. Publisher: Nature Publishing Group tex.copyright: 2019 The Author(s), under exclusive licence to Springer Nature Limited.

[27] Mustafa H Chowdhury, Krishanu Ray, Michael L Johnson, Stephen K Gray, James Pond, and Joseph R Lakowicz. On the feasibility of using the intrinsic fluorescence of nucleotides for dna sequencing. *The Journal of Physical Chemistry C*, 114(16):7448–7461, 2010.

[28] Qiang Wang, Ahsan R. Akram, David A. Dorward, Sophie Talas, Basil Monks, Chee Thum, James R. Hopgood, Malihe Javidi, and Marta Vallejo. Deep learning-based virtual H& E staining from label-free autofluorescence lifetime images. *npj Imaging*, 2(1):1–11, June 2024. Publisher: Nature Publishing Group tex.copyright: 2024 The Author(s).

[29] Marian Boktor, James E. D. Tweel, Benjamin R. Ecclestone, Jennifer Ai Ye, Paul Fieguth, and Parsin Haji Reza. Multi-channel feature extraction for virtual histological staining of photon absorption remote sensing images. *Scientific Reports*, 14(1):2009, January 2024. Publisher: Nature Publishing Group tex.copyright: 2024 The Author(s).

[30] Benjamin R Ecclestone, James A Tummon Simmons, James ED Tweel, Channprit Kaur, Aria Hajiahmadi, and Parsin Haji Reza. Photon absorption remote sensing (pars): A comprehensive approach to label-free absorption microscopy across biological scales. *arXiv preprint arXiv:2403.04229*, 2024.

[31] Benjamin R. Ecclestone, James A. Tummon Simmons, James E. D. Tweel, Deepak Dinakaran, and Parsin Haji Reza. Photon Absorption Remote Sensing (PARS): Comprehensive Absorption Imaging Enabling Label-Free Biomolecule Characterization and Mapping, June 2025. arXiv: 2506.20069 [physics] Number: arXiv:2506.20069.

[32] Benjamin R. Ecclestone, Kevan Bell, Sarah Sparkes, Deepak Dinakaran, John R. Mackey, and Parsin Haji Reza. Label-free complete absorption microscopy using second generation photoacoustic remote sensing. *Scientific Reports*, 12(1):8464, May 2022. Publisher: Nature Publishing Group tex.copyright: 2022 The Author(s).

[33] Marian Boktor, Benjamin R. Ecclestone, Vlad Pekar, Deepak Dinakaran, John R. Mackey, Paul Fieguth, and Parsin Haji Reza. Virtual histological staining of label-free total absorption photoacoustic remote sensing (TA-PARS). *Scientific Reports*, 12(1):10296, June 2022. Publisher: Nature Publishing Group tex.copyright: 2022 The Author(s).

[34] Lingke Kong, Chenyu Lian, Detian Huang, Zhenjiang Li, Yanle Hu, and Qichao Zhou. Breaking the Dilemma of Medical Image-to-image Translation, November 2021. arXiv: 2110.06465 [cs, eess] Number: arXiv:2110.06465.

[35] Hani A Alturkistani, Faris M Tashkandi, and Zuhair M Mohammedsaleh. Histological Stains: A Literature Review and Case Study. *Global Journal of Health Science*, 8(3):72–79, March 2016. tex.pmcid: PMC4804027.

[36] Alan P Brown, Philip Drew, Brian Knight, Philippe Marc, Sean Troth, Kuno Wuersch, and Joyce Zandee. Graphical display of histopathology data from toxicology studies for drug discovery and development: An industry perspective. *Regulatory toxicology and pharmacology*, 82:167–172, 2016.

[37] Jaafar S. Makki. Diagnostic Implication and Clinical Relevance of Ancillary Techniques in Clinical Pathology Practice. *Clinical Medicine Insights. Pathology*, 9:5–11, March 2016. tex.pmcid: PMC4807883.

[38] Laurence Brown. Improving histopathology turnaround time: a process management approach. *Current Diagnostic Pathology*, 10(6):444–452, December 2004.

[39] Saeed Alshieban and Khaled Al-Surimi. Reducing turnaround time of surgical pathology reports in pathology and laboratory medicine departments. *BMJ quality improvement reports*, 4(1), 2015.

[40] Kenneth PH Pritzker and Heikki J Nieminen. Needle biopsy adequacy in the era of precision medicine and value-based health care. *Archives of pathology & laboratory medicine*, 143(11):1399–1415, 2019.

[41] Timothy M Pawlik, Charles R Scoggins, Daria Zorzi, Eddie K Abdalla, Axel Andres, Cathy Eng, Steven A Curley, Evelyne M Loyer, Andrea Muratore, Gilles Mentha, et al. Effect of surgical margin status on survival and site of recurrence after hepatic resection for colorectal metastases. *Annals of surgery*, 241(5):715–724, 2005.

[42] Makoto Ohori, Thomas M Wheeler, Michael W Kattan, Yasuki Goto, and Peter T Scardino. Prognostic significance of positive surgical margins in radical prostatectomy specimens. *The Journal of urology*, 154(5):1818–1824, 1995.

[43] Yair Rivenson, Tairan Liu, Zhensong Wei, Yibo Zhang, Kevin de Haan, and Aydogan Ozcan. PhaseStain: The digital staining of label-free quantitative phase microscopy images using deep learning. *Light: Science & Applications*, 8(1):23, February 2019. Publisher: Nature Publishing Group tex.copyright: 2019 The Author(s).

[44] John KC Chan. The wonderful colors of the hematoxylin–eosin stain in diagnostic surgical pathology. *International journal of surgical pathology*, 22(1):12–32, 2014.

[45] Xin J Zhou, Zoltan G Laszik, Tibor Nadasdy, Vivette D D'Agati, et al. *Silva's diagnostic renal pathology*. Cambridge University Press, 2017.

[46] Taekwoon Kim, Jeongsoo Lee, and Joonsoo Park. Dermatomycosis from the perspective of dermatopathology (version 1.1). *Journal of*, 26(3), 2021.

[47] Tiffany L. Sellaro, Robert Filkins, Chelsea Hoffman, Jeffrey L. Fine, Jon Ho, Anil V. Parwani, Liron Pantanowitz, and Michael Montalto. Relationship between magnification and resolution in digital pathology systems. *Journal of Pathology Informatics*, 4(1):21, January 2013.

[48] Andrew H Song, Guillaume Jaume, Drew FK Williamson, Ming Y Lu, Anurag Vaidya, Tiffany R Miller, and Faisal Mahmood. Artificial intelligence for digital and computational pathology. *Nature Reviews Bioengineering*, 1(12):930–949, 2023.

[49] Ming Y Lu, Bowen Chen, Drew FK Williamson, Richard J Chen, Melissa Zhao, Aaron K Chow, Kenji Ikemura, Ahrong Kim, Dimitra Pouli, Ankush Patel, et al. A multimodal generative ai copilot for human pathology. *Nature*, 634(8033):466–473, 2024.

[50] Marcel Streit, Made Budiarta, Marvin Jungblut, and Gerti Beliu. Fluorescent labeling strategies for molecular bioimaging. *Biophysical Reports*, 5(1), 2025.

[51] Natan T Shaked, Stephen A Boppart, Lihong V Wang, and Jürgen Popp. Label-free biomedical optical imaging. *Nature photonics*, 17(12):1031–1041, 2023.

[52] Yoav N Nygate, Mattan Levi, Simcha K Mirsky, Nir A Turko, Moran Rubin, Itay Barnea, Gili Dardikman-Yoffe, Miki Haifler, Alon Shalev, and Natan T Shaked. Holographic virtual staining of individual biological cells. *Proceedings of the National Academy of Sciences*, 117(17):9223–9231, 2020.

[53] Tanishq Mathew Abraham, Paloma Casteleiro Costa, Caroline Elizabeth Serafini, Zhe Guang, Zhaobin Zhang, Stewart Neill, Jeffrey J Olson, Richard Levenson, and Francisco E Robles. Label-and slide-free tissue histology using 3d epi-mode quantitative phase imaging and virtual hematoxylin and eosin staining. *Optica*, 10(12):1605–1618, 2023.

[54] M Wolman and FH Kasten. Polarized light microscopy in the study of the molecular structure of collagen and reticulin. *Histochemistry*, 85(1):41–49, 1986.

[55] David Keefe, Lin Liu, Wei Wang, and Celso Silva. Imaging meiotic spindles by polarization light microscopy: principles and applications to ivf. *Reproductive biomedicine online*, 7(1):24–29, 2003.

[56] FG Bechara, T Gambichler, MAOA Stücker, A Orlikov, S Rotterdam, P Altmeyer, and K Hoffmann. Histomorphologic correlation with routine histology and optical coherence tomography. *Skin Research and Technology*, 10(3):169–173, 2004.

[57] T Maier, M Braun-Falco, T Hinz, MH Schmid-Wendtner, T Ruzicka, and C Berking. Morphology of basal cell carcinoma in high definition optical coherence tomography: en-face and slice imaging mode, and comparison with histology. *Journal of the European Academy of Dermatology and Venereology*, 27(1):e97–e104, 2013.

[58] Lida P Hariri, Mari Mino-Kenudson, Michael Lanuti, Alyssa J Miller, Eugene J Mark, and Melissa J Suter. Diagnosing lung carcinomas with optical coherence tomography. *Annals of the American Thoracic Society*, 12(2):193–201, 2015.

[59] Soheil Soltani, Ashkan Ojaghi, and Francisco E. Robles. Deep UV dispersion and absorption spectroscopy of biomolecules. *Biomedical Optics Express*, 10(2):487–499, February 2019. Publisher: Optica Publishing Group tex.copyright: © 2019 Optical Society of America.

[60] Junjie Yao and Lihong V Wang. Sensitivity of photoacoustic microscopy. *Photoacoustics*, 2(2):87–101, 2014.

[61] Stephen E Bialkowski, Nelson GC Astrath, and Mikhail A Proskurnin. *Photothermal spectroscopy methods*. John Wiley & Sons, 2019.

[62] Subhasis Adhikari, Patrick Spaeth, Ashish Kar, Martin Dieter Baaske, Saumyakanti Khatua, and Michel Orrit. Photothermal microscopy: imaging the optical absorption of single nanoparticles and single molecules. *ACS nano*, 14(12):16414–16445, 2020.

[63] John C Lindon, George E Tranter, and David Koppenaal. *Encyclopedia of spectroscopy and spectrometry*. Academic Press, 2016.

[64] Yijie Zhang, Kevin de Haan, Yair Rivenson, Jingxi Li, Apostolos Delis, and Aydogan Ozcan. Digital synthesis of histological stains using micro-structured and multiplexed virtual staining of label-free tissue. *Light: Science & Applications*, 9(1):78, May 2020. Publisher: Nature Publishing Group tex.copyright: 2020 The Author(s).

[65] Xinyang Li, Guoxun Zhang, Hui Qiao, Feng Bao, Yue Deng, Jiamin Wu, Yangfan He, Jingping Yun, Xing Lin, Hao Xie, Haoqian Wang, and Qionghai Dai. Unsupervised content-preserving transformation for optical microscopy. *Light: Science & Applications*, 10(1):44, March 2021. Publisher: Nature Publishing Group tex.copyright: 2021 The Author(s).

[66] Artzai Picon, Alfonso Medela, Luisa F. Sánchez-Peralta, Riccardo Cicchi, Roberto Bilbao, Domenico Alfieri, Andoni Elola, Ben Glover, and Cristina L. Saratxaga. Autofluorescence Image Reconstruction and Virtual Staining for In-Vivo Optical Biopsying. *IEEE access : practical innovations, open solutions*, 9:32081–32093, 2021.

[67] Xiangyu Meng, Xin Li, and Xun Wang. A Computationally Virtual Histological Staining Method to Ovarian Cancer Tissue by Deep Generative Adversarial Networks. *Computational and Mathematical Methods in Medicine*, 2021(1):4244157, 2021. tex.copyright: Copyright © 2021 Xiangyu Meng et al.

[68] Yijie Zhang, Luzhe Huang, Nir Pillar, Yuzhu Li, Hanlong Chen, and Aydogan Ozcan. Pixel super-resolved virtual staining of label-free tissue using diffusion models. *Nature Communications*, 16(1):5016, May 2025. Publisher: Nature Publishing Group tex.copyright: 2025 The Author(s).

[69] A.C. Croce and G. Bottiroli. Autofluorescence Spectroscopy and Imaging: A Tool for Biomedical Research and Diagnosis. *European Journal of Histochemistry : EJH*, 58(4):2461, December 2014. tex.pmcid: PMC4289852.

[70] Monica Monici. Cell and tissue autofluorescence research and diagnostic applications. In *Biotechnology Annual Review*, volume 11, pages 227–256. Elsevier, January 2005.

[71] Yu-Cheng Chen, Xiaotian Tan, Qihan Sun, Qiushu Chen, Wenjie Wang, and Xudong Fan. Laser-emission imaging of nuclear biomarkers for high-contrast cancer screening and immunodiagnosis. *Nature Biomedical Engineering*, 1(9):724–735, September 2017. Publisher: Nature Publishing Group tex.copyright: 2017 The Author(s).

[72] Martin Schnell, Shachi Mittal, Kianoush Falahkheirkhah, Anirudh Mittal, Kevin Yeh, Seth Kenkel, Andre Kajdacsy-Balla, P. Scott Carney, and Rohit Bhargava. All-digital histopathology by infrared-optical hybrid microscopy. *Proceedings of the National Academy of Sciences of the United States of America*, 117(7):3388–3396, February 2020. tex.pmcid: PMC7035604.

[73] Rui Cao, Scott D. Nelson, Samuel Davis, Yu Liang, Yilin Luo, Yide Zhang, Brooke Crawford, and Lihong V. Wang. Label-free intraoperative histology of bone tissue via deep-learning-assisted ultraviolet photoacoustic microscopy. *Nature Biomedical Engineering*, 7(2):124–134, February 2023. Publisher: Nature Publishing Group tex.copyright: 2022 The Author(s), under exclusive licence to Springer Nature Limited.

[74] Chi Zhang, Yu Shrike Zhang, Da-Kang Yao, Younan Xia, and Lihong V. Wang. Label-free photoacoustic microscopy of cytochromes. *Journal of Biomedical Optics*, 18(2):020504, February 2013. tex.pmcid: PMC3560837.

[75] Nathaniel J. M. Haven, Kevan L. Bell, Pradyumna Kedarisetti, John D. Lewis, and Roger J. Zemp. Ultraviolet photoacoustic remote sensing microscopy. *Optics Letters*, 44(14):3586–3589, July 2019. Publisher: Optica Publishing Group tex.copyright: © 2019 Optical Society of America.

[76] Saad Abbasi, Martin Le, Bazil Sonier, Deepak Dinakaran, Gilbert Bigras, Kevan Bell, John R Mackey, and Parsin Haji Reza. All-optical reflection-mode microscopic histology of unstained human tissues. *Scientific reports*, 9(1):13392, 2019.

[77] Parsin Hajireza, Wei Shi, Kevan Bell, Robert J. Paproski, and Roger J. Zemp. Non-interferometric photoacoustic remote sensing microscopy. *Light: Science & Applications*, 6(6):e16278–e16278, June 2017. Publisher: Nature Publishing Group tex.copyright: 2017 The Author(s).

[78] Brendon S. Restall, Nathaniel J. M. Haven, Pradyumna Kedarisetti, and Roger J. Zemp. In vivo combined virtual histology and vascular imaging with dual-wavelength photoacoustic remote sensing microscopy. *OSA Continuum*, 3(10):2680–2689, October 2020. Publisher: Optica Publishing Group tex.copyright: © 2020 Optical Society of America.

[79] Zohreh Hosseinaee, Nima Abbasi, Nicholas Pellegrino, Layla Khalili, Lyazzat Mukhangaliyeva, and Parsin Haji Reza. Functional and structural ophthalmic imaging using noncontact multimodal photoacoustic remote sensing microscopy and op-

tical coherence tomography. *Scientific Reports*, 11(1):11466, June 2021. Publisher: Nature Publishing Group tex.copyright: 2021 The Author(s).

[80] Zohreh Hosseinaee, Benjamin Ecclestone, Nicholas Pellegrino, Layla Khalili, Lyazzat Mukhangaliyeva, Paul Fieguth, and Parsin Haji Reza. Functional photoacoustic remote sensing microscopy using a stabilized temperature-regulated stimulated Raman scattering light source. *Optics Express*, 29(19):29745–29754, September 2021. Publisher: Optica Publishing Group tex.copyright: © 2021 Optical Society of America.

[81] Lyazzat Mukhangaliyeva, Samed Kocer, Alkris Warren, Kevan Bell, Marian Boktor, Mustafa Yavuz, Eihab Abdel-Rahman, and Parsin Haji Reza. Deformable mirror-based photoacoustic remote sensing (PARS) microscopy for depth scanning. *Biomedical Optics Express*, 13(11):5643–5653, November 2022. Publisher: Optica Publishing Group tex.copyright: © 2022 Optica Publishing Group.

[82] Kevan Bell, Saad Abbasi, Deepak Dinakaran, Muba Taher, Gilbert Bigras, Frank K. H. van Landeghem, John R. Mackey, and Parsin Haji Reza. Reflection-mode virtual histology using photoacoustic remote sensing microscopy. *Scientific Reports*, 10(1):19121, November 2020. Publisher: Nature Publishing Group tex.copyright: 2020 The Author(s).

[83] Benjamin R. Ecclestone, Kevan Bell, Saad Abbasi, Deepak Dinakaran, Frank K. H. van Landeghem, John R. Mackey, Paul Fieguth, and Parsin Haji Reza. Improving maximal safe brain tumor resection with photoacoustic remote sensing microscopy. *Scientific Reports*, 10(1):17211, October 2020. Publisher: Nature Publishing Group tex.copyright: 2020 The Author(s).

[84] Kevan Bell, Kevan Bell, Lyazzat Mukhangaliyeva, Layla Khalili, and Parsin Haji Reza. Hyperspectral absorption microscopy using photoacoustic remote sensing. *Optics Express*, 29(15):24338–24348, July 2021. Publisher: Optical Society of America tex.copyright: © 2021 Optical Society of America.

[85] Pradyumna Kedarisetti, Nathaniel J. M. Haven, Brendon S. Restall, Matthew T. Martell, and Roger J. Zemp. Label-free lipid contrast imaging using non-contact near-Infrared photoacoustic remote sensing microscopy. *Optics Letters*, 45(16):4559–4562, August 2020.

[86] EA Shirshin, BP Yakimov, ME Darvin, NP Omelyanenko, SA Rodionov, Yu I Gurfinkel, J Lademann, VV Fadeev, and AV Priezzhev. Label-free multiphoton

microscopy: the origin of fluorophores and capabilities for analyzing biochemical processes. *Biochemistry (Moscow)*, 84(Suppl 1):69–88, 2019.

[87] Arash Aghigh, Stéphane Bancelin, Maxime Rivard, Maxime Pinsard, Heide Ibrahim, and François Légaré. Second harmonic generation microscopy: a powerful tool for bio-imaging. *Biophysical Reviews*, 15(1):43–70, 2023.

[88] Paul J Campagnola and C-Y Dong. Second harmonic generation microscopy: principles and applications to disease diagnosis. *Laser & Photonics Reviews*, 5(1):13–26, 2011.

[89] Delphine Débarre, Willy Supatto, Ana-Maria Pena, Aurélie Fabre, Thierry Tordjmann, Laurent Combettes, Marie-Claire Schanne-Klein, and Emmanuel Beaurepaire. Imaging lipid bodies in cells and tissues using third-harmonic generation microscopy. *Nature methods*, 3(1):47–53, 2006.

[90] Bettina Weigelin, Gert-Jan Bakker, and Peter Friedl. Third harmonic generation microscopy of cells and tissue organization. *Journal of Cell Science*, 129(2):245–255, 2016.

[91] Chi-Kuang Sun, Cheng-Chi Chen, Shi-Wei Chu, Tsung-Han Tsai, Yung-Chih Chen, and Bai-Ling Lin. Multiharmonic-generation biopsy of skin. *Optics letters*, 28(24):2488–2490, 2003.

[92] Terence TW Wong, Ruiying Zhang, Pengfei Hai, Chi Zhang, Miguel A Pleitez, Rebecca L Aft, Deborah V Novack, and Lihong V Wang. Fast label-free multilayered histology-like imaging of human breast cancer by photoacoustic microscopy. *Science advances*, 3(5):e1602168, 2017.

[93] James A. Tummon Simmons, Sarah J. Werezak, Benjamin R. Ecclestone, James E. D. Tweel, Hager Gaouda, and Parsin Haji Reza. Label-Free Non-Contact Vascular Imaging Using Photon Absorption Remote Sensing. *IEEE Transactions on Biomedical Engineering*, 72(3):1160–1169, March 2025.

[94] Knut Rurack. Fluorescence quantum yields: methods of determination and standards. In *Standardization and quality assurance in fluorescence measurements I: techniques*, pages 101–145. Springer, 2008.

[95] Thomas Gustavsson and Dimitra Markovitsi. Fundamentals of the intrinsic dna fluorescence. *Accounts of Chemical Research*, 54(5):1226–1235, 2021.

[96] Anil B Shrirao, Rene S Schloss, Zachary Fritz, Mayur V Shrirao, Robert Rosen, and Martin L Yarmush. Autofluorescence of blood and its application in biomedical and clinical research. *Biotechnology and bioengineering*, 118(12):4550–4576, 2021.

[97] Stephen P Nighswander-Rempel, Jennifer Riesz, Joel Gilmore, and Paul Meredith. A quantum yield map for synthetic eumelanin. *The Journal of chemical physics*, 123(19), 2005.

[98] Paul Beard. Biomedical photoacoustic imaging. *Interface focus*, 1(4):602–631, 2011.

[99] Lihong V Wang and Hsin-i Wu. *Biomedical optics: principles and imaging*. John Wiley & Sons, 2007.

[100] Nicholas Pellegrino, Benjamin R Ecclestone, Deepak Dinakaran, Frank van Landeghem, Paul Fieguth, and Parsin Haji Reza. Time-domain feature extraction for target specificity in photoacoustic remote sensing microscopy. *Optics Letters*, 47(15):3952–3955, 2022.

[101] Benjamin Ecclestone, Deepak Dinakaran, and Parsin Haji Reza. Single acquisition label-free histology-like imaging with dual-contrast photoacoustic remote sensing microscopy. *Journal of Biomedical Optics*, 26(5):056007–056007, 2021.

[102] Benjamin R Ecclestone, Zohreh Hosseinaee, Nima Abbasi, Kevan Bell, Deepak Dinakaran, John R Mackey, and Parsin Haji Reza. Three-dimensional virtual histology in unprocessed resected tissues with photoacoustic remote sensing (pars) microscopy and optical coherence tomography (oct). *Scientific Reports*, 11(1):13723, 2021.

[103] Benjamin R Ecclestone, James ED Tweel, Marie Abi Daoud, Hager Gaouda, Deepak Dinakaran, Michael P Wallace, Ally Khan Somani, Gilbert Bigras, John R Mackey, and Parsin Haji Reza. Photon absorption remote sensing virtual histopathology: Diagnostic equivalence to gold-standard h&e staining in skin cancer excisional biopsies. *arXiv preprint arXiv:2504.18737*, 2025.

[104] Marian Boktor, James ED Tweel, Benjamin R Ecclestone, Jennifer Ai Ye, Paul Fieguth, and Parsin Haji Reza. Multi-channel feature extraction for virtual histological staining of photon absorption remote sensing images. *Scientific Reports*, 14(1):2009, 2024.

[105] Benjamin Ecclestone. *Label-free optical microscopy: Photon Absorption Remote Sensing (PARS) and other methods for label-free histopathological imaging of tissues*. Doctoral thesis, University of Waterloo, Waterloo, Ontario, Canada, 2026.

[106] Brendyn D. Cikaluk, Brendon S. Restall, Nathaniel J. M. Haven, Matthew T. Martell, Ewan A. McAlister, and Roger J. Zemp. Rapid ultraviolet photoacoustic remote sensing microscopy using voice-coil stage scanning. *Optics Express*, 31(6):10136–10149, March 2023. Publisher: Optica Publishing Group tex.copyright: © 2023 Optica Publishing Group.

[107] Matthew T. Martell, Nathaniel J. M. Haven, Brendyn D. Cikaluk, Brendon S. Restall, Ewan A. McAlister, Rohan Mittal, Benjamin A. Adam, Nadia Giannakopoulos, Lashan Peiris, Sveta Silverman, Jean Deschenes, Xingyu Li, and Roger J. Zemp. Deep learning-enabled realistic virtual histology with ultraviolet photoacoustic remote sensing microscopy. *Nature Communications*, 14(1):5967, September 2023. Publisher: Nature Publishing Group tex.copyright: 2023 The Author(s).

[108] Kevin de Haan, Yijie Zhang, Jonathan E. Zuckerman, Tairan Liu, Anthony E. Sisk, Miguel F. P. Diaz, Kuang-Yu Jen, Alexander Nobori, Sofia Liou, Sarah Zhang, Rana Riahi, Yair Rivenson, W. Dean Wallace, and Aydogan Ozcan. Deep learning-based transformation of H&E stained tissues into special stains. *Nature Communications*, 12(1):4884, August 2021. Publisher: Nature Publishing Group tex.copyright: 2021 The Author(s).

[109] Erik A Burlingame, Mary McDonnell, Geoffrey F Schau, Guillaume Thibault, Christian Lanciault, Terry Morgan, Brett E Johnson, Christopher Corless, Joe W Gray, and Young Hwan Chang. Shift: speedy histological-to-immunofluorescent translation of a tumor signature enabled by deep learning. *Scientific reports*, 10(1):17507, 2020.

[110] Nassim Bouteldja, Barbara M Klinkhammer, Tarek Schlaich, Peter Boor, and Dorit Merhof. Improving unsupervised stain-to-stain translation using self-supervision and meta-learning. *Journal of pathology informatics*, 13:100107, 2022.

[111] Ian J Goodfellow, Jean Pouget-Abadie, Mehdi Mirza, Bing Xu, David Warde-Farley, Sherjil Ozair, Aaron Courville, and Yoshua Bengio. Generative adversarial nets. *Advances in neural information processing systems*, 27, 2014.

[112] Olaf Ronneberger, Philipp Fischer, and Thomas Brox. U-net: Convolutional networks for biomedical image segmentation. In *International Conference on Medical image computing and computer-assisted intervention*, pages 234–241. Springer, 2015.

[113] Phillip Isola, Jun-Yan Zhu, Tinghui Zhou, and Alexei A Efros. Image-to-image translation with conditional adversarial networks. In *Proceedings of the IEEE conference on computer vision and pattern recognition*, pages 1125–1134, 2017.

[114] Jun-Yan Zhu, Taesung Park, Phillip Isola, and Alexei A. Efros. Unpaired Image-to-Image Translation using Cycle-Consistent Adversarial Networks, August 2020. arXiv: 1703.10593 [cs] Number: arXiv:1703.10593.

[115] Mehdi Mirza and Simon Osindero. Conditional generative adversarial nets. *arXiv preprint arXiv:1411.1784*, 2014.

[116] Yaniv Taigman, Adam Polyak, and Lior Wolf. Unsupervised cross-domain image generation. *arXiv preprint arXiv:1611.02200*, 2016.

[117] Guha Balakrishnan, Amy Zhao, Mert R Sabuncu, John Guttag, and Adrian V Dalca. Voxelmorph: a learning framework for deformable medical image registration. *IEEE transactions on medical imaging*, 38(8):1788–1800, 2019.

[118] Dan Li, Hui Hui, Yingqian Zhang, Wei Tong, Feng Tian, Xin Yang, Jie Liu, Yundai Chen, and Jie Tian. Deep Learning for Virtual Histological Staining of Bright-Field Microscopic Images of Unlabeled Carotid Artery Tissue. *Molecular Imaging and Biology*, 22(5):1301–1309, October 2020.

[119] Guanghao Zhang, Bin Ning, Hui Hui, Tengfei Yu, Xin Yang, Hongxia Zhang, Jie Tian, and Wen He. Image-to-Images Translation for Multiple Virtual Histological Staining of Unlabeled Human Carotid Atherosclerotic Tissue. *Molecular Imaging and Biology*, 24(1):31–41, February 2022.

[120] Yoav N. Nygate, Mattan Levi, Simcha K. Mirsky, Nir A. Turko, Moran Rubin, Itay Barnea, Gili Dardikman-Yoffe, Miki Haifler, Alon Shalev, and Natan T. Shaked. Holographic virtual staining of individual biological cells. *Proceedings of the National Academy of Sciences*, 117(17):9223–9231, April 2020. Publisher: Proceedings of the National Academy of Sciences.

[121] Jingxi Li, Jason Garfinkel, Xiaoran Zhang, Di Wu, Yijie Zhang, Kevin De Haan, Hongda Wang, Tairan Liu, Bijie Bai, Yair Rivenson, et al. Biopsy-free in vivo virtual histology of skin using deep learning. *Light: Science & Applications*, 10(1):233, 2021.

[122] Yuzhu Li, Nir Pillar, Jingxi Li, Tairan Liu, Di Wu, Songyu Sun, Guangdong Ma, Kevin de Haan, Luzhe Huang, Yijie Zhang, et al. Virtual histological staining of unlabeled autopsy tissue. *Nature communications*, 15(1):1684, 2024.

[123] Yuzhu Li, Nir Pillar, Tairan Liu, Guangdong Ma, Yuxuan Qi, Yijie Zhang, Xilin Yang, Adrian J Correa, Guangqian Xiao, Kuang-Yu Jen, et al. Label-free evaluation of lung and heart transplant biopsies using tissue autofluorescence-based virtual staining. *BME frontiers*, 6:0151, 2025.

[124] Bijie Bai, Hongda Wang, Yuzhu Li, Kevin de Haan, Francesco Colonnese, Yujie Wan, Jingyi Zuo, Ngan B. Doan, Xiaoran Zhang, Yijie Zhang, Jingxi Li, Xilin Yang, Wenjie Dong, Morgan Angus Darrow, Elham Kamangar, Han Sung Lee, Yair Rivenson, and Aydogan Ozcan. Label-free virtual HER2 immunohistochemical staining of breast tissue using deep learning. *BME Frontiers*, 2022:9786242, 2022. tex.eprint: https://spj.science.org/doi/pdf/10.34133/2022/9786242.

[125] Lei Kang, Xiufeng Li, Yan Zhang, and Terence T. W. Wong. Deep learning enables ultraviolet photoacoustic microscopy based histological imaging with near real-time virtual staining. *Photoacoustics*, 25:100308, March 2022.

[126] Chiho Yoon, Eunwoo Park, Sampa Misra, Jin Young Kim, Jin Woo Baik, Kwang Gi Kim, Chan Kwon Jung, and Chulhong Kim. Deep learning-based virtual staining, segmentation, and classification in label-free photoacoustic histology of human specimens. *Light: Science & Applications*, 13(1):226, September 2024. Publisher: Nature Publishing Group tex.copyright: 2024 The Author(s).

[127] Pranita Pradhan, Tobias Meyer, Michael Vieth, Andreas Stallmach, Maximilian Waldner, Michael Schmitt, Juergen Popp, and Thomas Bocklitz. Computational tissue staining of non-linear multimodal imaging using supervised and unsupervised deep learning. *Biomedical Optics Express*, 12(4):2280–2298, March 2021. tex.pmcid: PMC8086483.

[128] Kianoush Falahkheirkhah, Sudipta S. Mukherjee, Sounak Gupta, Loren Herrera-Hernandez, Michael R. McCarthy, Rafael E. Jimenez, John C. Cheville, and Rohit Bhargava. Accelerating Cancer Histopathology Workflows with Chemical Imaging and Machine Learning. *Cancer Research Communications*, 3(9):1875–1887, September 2023. tex.pmcid: PMC10506535.

[129] Zhijie Liu, Lingchao Chen, Haixia Cheng, Jianpeng Ao, Ji Xiong, Xing Liu, Yaxin Chen, Ying Mao, and Minbiao Ji. Virtual formalin-fixed and paraffin-embedded staining of fresh brain tissue via stimulated Raman CycleGAN model. *Science Advances*, 10(13):eadn3426, March 2024. Publisher: American Association for the Advancement of Science.

[130] Zhou Wang, Alan C Bovik, Hamid R Sheikh, and Eero P Simoncelli. Image quality assessment: from error visibility to structural similarity. *IEEE transactions on image processing*, 13(4):600–612, 2004.

[131] Martin Heusel, Hubert Ramsauer, Thomas Unterthiner, Bernhard Nessler, and Sepp Hochreiter. Gans trained by a two time-scale update rule converge to a local nash equilibrium. *Advances in neural information processing systems*, 30, 2017.

[132] Gabriel Popescu. *Quantitative Phase Imaging of Cells and Tissues*. McGraw-Hill Education, 1st edition edition, 2011.

[133] Laura Marcu. Fluorescence lifetime techniques in medical applications. *Annals of biomedical engineering*, 40(2):304–331, 2012.

[134] Rupsa Datta, Tiffany M Heaster, Joe T Sharick, Amani A Gillette, and Melissa C Skala. Fluorescence lifetime imaging microscopy: fundamentals and advances in instrumentation, analysis, and applications. *Journal of biomedical optics*, 25(7):071203–071203, 2020.

[135] Keyan Ding, Kede Ma, Shiqi Wang, and Eero P. Simoncelli. Image Quality Assessment: Unifying Structure and Texture Similarity. *IEEE Transactions on Pattern Analysis and Machine Intelligence*, pages 1–1, 2020. arXiv: 2004.07728 [cs].

[136] Junjie Yao and Lihong V. Wang. Photoacoustic Microscopy. *Laser & photonics reviews*, 7(5):10.1002/lpor.201200060, September 2013. tex.pmcid: PMC3887369.

[137] Navid Borhani, Andrew J. Bower, Stephen A. Boppart, and Demetri Psaltis. Digital staining through the application of deep neural networks to multi-modal multi-photon microscopy. *Biomedical Optics Express*, 10(3):1339–1350, March 2019. Publisher: Optica Publishing Group tex.copyright: © 2019 Optical Society of America.

[138] Warren R Zipfel, Rebecca M Williams, and Watt W Webb. Nonlinear magic: multiphoton microscopy in the biosciences. *Nature biotechnology*, 21(11):1369–1377, 2003.

[139] Ji-Xin Cheng and X Sunney Xie. Coherent anti-stokes raman scattering microscopy: instrumentation, theory, and applications, 2004.

[140] Winfried Denk, James H Strickler, and Watt W Webb. Two-photon laser scanning fluorescence microscopy. *Science*, 248(4951):73–76, 1990.

[141] Ezgi Mercan, Selim Aksoy, Linda G. Shapiro, Donald L. Weaver, Tad Brunye, and Joann G. Elmore. Localization of Diagnostically Relevant Regions of Interest in Whole Slide Images. In *2014 22nd International Conference on Pattern Recognition*, pages 1179–1184, August 2014. ISSN: 1051-4651.

[142] Da-Kang Yao, Konstantin Maslov, Kirk K. Shung, Qifa Zhou, and Lihong V. Wang. *In vivo* label-free photoacoustic microscopy of cell nuclei by excitation of DNA and RNA. *Optics Letters*, 35(24):4139–4141, December 2010. Publisher: Optica Publishing Group tex.copyright: © 2010 Optical Society of America.

[143] Tte Yeo, Sh Ong, Jayasooriah, and R Sinniah. Autofocusing for tissue microscopy. *Image and Vision Computing*, 11(10):629–639, December 1993.

[144] Uwe Schmidt, Martin Weigert, Coleman Broaddus, and Gene Myers. Cell Detection with Star-Convex Polygons. In Alejandro F. Frangi, Julia A. Schnabel, Christos Davatzikos, Carlos Alberola-López, and Gabor Fichtinger, editors, *Medical Image Computing and Computer Assisted Intervention – MICCAI 2018*, Lecture Notes in Computer Science, pages 265–273, Cham, 2018. Springer International Publishing.

[145] Gabriel Landini, Giovanni Martinelli, and Filippo Piccinini. Colour deconvolution: Stain unmixing in histological imaging. *Bioinformatics (Oxford, England)*, 37(10):1485–1487, June 2021.

[146] Stephan Preibisch, Stephan Saalfeld, and Pavel Tomancak. Globally optimal stitching of tiled 3d microscopic image acquisitions. *Bioinformatics*, 25(11):1463–1465, 2009.

[147] Colin H Richards, Zahra Mohammed, Tahir Qayyum, Paul G Horgan, and Donald C McMillan. The prognostic value of histological tumor necrosis in solid organ malignant disease: a systematic review. *Future Oncology*, 7(10):1223–1235, October 2011. Publisher: Future Medicine.

[148] Jeroen van der Laak, Geert Litjens, and Francesco Ciompi. Deep learning in histopathology: The path to the clinic. *Nature Medicine*, 27(5):775–784, May 2021. Publisher: Nature Publishing Group tex.copyright: 2021 Springer Nature America, Inc.

[149] Joseph Paul Cohen, Margaux Luck, and Sina Honari. Distribution Matching Losses Can Hallucinate Features in Medical Image Translation, October 2018. arXiv: 1805.08841 [cs] Number: arXiv:1805.08841.

[150] Alexander Krull, Tim-Oliver Buchholz, and Florian Jug. Noise2Void - Learning Denoising from Single Noisy Images, April 2019. arXiv: 1811.10980 [cs] Number: arXiv:1811.10980.

[151] A. Ardeshir Goshtasby. *Image Registration*. Advances in Pattern Recognition. Springer, London, 2012.

[152] Samarth Shukla, Luc Van Gool, and Radu Timofte. Extremely Weak Supervised Image-to-Image Translation for Semantic Segmentation, September 2019. arXiv: 1909.08542 [cs] Number: arXiv:1909.08542.

[153] Soumya Tripathy, Juho Kannala, and Esa Rahtu. Learning image-to-image translation using paired and unpaired training samples, May 2018. arXiv: 1805.03189 [cs] Number: arXiv:1805.03189.

[154] Z. Deyl, K. Macek, M. Adam, and O. Vancíková. Studies on the chemical nature of elastin fluorescence. *Biochimica Et Biophysica Acta*, 625(2):248–254, October 1980.

[155] Meghan A. Piccinin and Janice Schwartz. Histology, Verhoeff Stain. In *StatPearls*. StatPearls Publishing, Treasure Island (FL), 2024. tex.copyright: Copyright © 2024, StatPearls Publishing LLC. tex.lccn: NBK519050.

[156] William N. O'connor and Sylvia Valle. A Combination Verhoeffs Elastic and Masson's Trichrome Stain for Routine Histology. *Stain Technology*, 57(4):207–210, January 1982. Publisher: Taylor & Francis.

[157] Ulrich Bick, Rubina M. Trimboli, Alexandra Athanasiou, Corinne Balleyguier, Pascal A. T. Baltzer, Maria Bernathova, Krisztina Borbély, Boris Brkljacic, Luca A. Carbonaro, Paola Clauser, Enrico Cassano, Catherine Colin, Gul Esen, Andrew Evans, Eva M. Fallenberg, Michael H. Fuchsjaeger, Fiona J. Gilbert, Thomas H. Helbich, Sylvia H. Heywang-Köbrunner, Michel Herranz, Karen Kinkel, Fleur Kilburn-Toppin, Christiane K. Kuhl, Mihai Lesaru, Marc B. I. Lobbes, Ritse M. Mann, Laura Martincich, Pietro Panizza, Federica Pediconi, Ruud M. Pijnappel, Katja Pinker, Simone Schiaffino, Tamar Sella, Isabelle Thomassin-Naggara, Anne Tardivon, Chantal Van Ongeval, Matthew G. Wallis, Sophia Zackrisson, Gabor Forrai, Julia Camps Herrero, Francesco Sardanelli, and European Society of Breast Imaging (EUSOBI), with language review by Europa Donna–The European Breast Cancer Coalition. Image-guided breast biopsy and localisation: Recommendations for information to women and referring physicians by the European Society of Breast Imaging. *Insights into Imaging*, 11(1):12, February 2020. tex.pmcid: PMC7002629.

[158] H. M. Verkooijen, P. H. Peeters, E. Buskens, V. C. Koot, I. H. Borel Rinkes, W. P. Mali, and T. J. van Vroonhoven. Diagnostic accuracy of large-core needle biopsy for

nonpalpable breast disease: a meta-analysis. *British Journal of Cancer*, 82(5):1017–1021, March 2000. tex.pmcid: PMC2374424.

[159] S. H. Parker, F. Burbank, R. J. Jackman, C. J. Aucreman, G. Cardenosa, T. M. Cink, J. L. Coscia, G. W. Eklund, W. P. Evans, and P. R. Garver. Percutaneous large-core breast biopsy: a multi-institutional study. *Radiology*, 193(2):359–364, November 1994.

[160] Joseph P. Crowe, Alice Rim, Rebecca J. Patrick, Lisa A. Rybicki, Sharon F. Grundfest-Broniatowski, Julian A. Kim, and Katherine B. Lee. Does core needle breast biopsy accurately reflect breast pathology? *Surgery*, 134(4):523–526; discussion 526–528, October 2003.

[161] Helena M. Verkooijen. Diagnostic accuracy of stereotactic large-core needle biopsy for nonpalpable breast disease: Results of a multicenter prospective study with 95% surgical confirmation. *International Journal of Cancer*, 99(6):853–859, 2002. tex.copyright: Copyright © 2002 Wiley-Liss, Inc.

[162] R. J. Jackman, K. W. Nowels, J. Rodriguez-Soto, F. A. Marzoni, S. I. Finkelstein, and M. J. Shepard. Stereotactic, automated, large-core needle biopsy of nonpalpable breast lesions: False-negative and histologic underestimation rates after long-term follow-up. *Radiology*, 210(3):799–805, March 1999.

[163] Ji Hyun Youk, Eun-Kyung Kim, Min Jung Kim, and Ki Keun Oh. Sonographically Guided 14-Gauge Core Needle Biopsy of Breast Masses: A Review of 2,420 Cases with Long-Term Follow-Up. *American Journal of Roentgenology*, 190(1):202–207, January 2008. Publisher: American Roentgen Ray Society.

[164] Allison R. Hatmaker, Rafe M. J. Donahue, John L. Tarpley, and A. Scott Pearson. Cost-effective use of breast biopsy techniques in a veterans health care system. *The American Journal of Surgery*, 192(5):e37–e41, November 2006.

[165] Wendy Bruening, Joann Fontanarosa, Kelley Tipton, Jonathan R. Treadwell, Jason Launders, and Karen Schoelles. Systematic review: Comparative effectiveness of core-needle and open surgical biopsy to diagnose breast lesions. *Annals of Internal Medicine*, 152(4):238–246, February 2010.

[166] Rebekah R. White, Terri J. Halperin, John A. Olson, Mary S. Soo, Rex C. Bentley, and Hilliard F. Seigler. Impact of Core-Needle Breast Biopsy on the Surgical Management of Mammographic Abnormalities. *Annals of Surgery*, 233(6):769–777, June 2001. tex.pmcid: PMC1421319.

[167] D. N. Smith, R. Christian, and J. E. Meyer. Large-core needle biopsy of nonpalpable breast cancers. The impact on subsequent surgical excisions. *Archives of Surgery (Chicago, Ill.: 1960)*, 132(3):256–259; discussion 260, March 1997.

[168] T'ng Chang Kwok, Emad A. Rakha, Andrew H. S. Lee, Matthew Grainge, Andrew R. Green, Ian O. Ellis, and Desmond G. Powe. Histological grading of breast cancer on needle core biopsy: The role of immunohistochemical assessment of proliferation. *Histopathology*, 57(2):212, August 2010. Publisher: Wiley-Blackwell.

[169] Cornelia M. Focke, Thomas Decker, and Paul J. van Diest. The reliability of histological grade in breast cancer core needle biopsies depends on biopsy size: a comparative study with subsequent surgical excisions. *Histopathology*, 69(6):1047–1054, December 2016.

[170] Mary L. McHugh. Interrater reliability: The kappa statistic. *Biochemia Medica*, 22(3):276–282, October 2012. tex.pmcid: PMC3900052.

[171] Joseph L. Fleiss. Measuring nominal scale agreement among many raters. *Psychological Bulletin*, 76(5):378–382, 1971. Place: US Publisher: American Psychological Association.

[172] Jacob Kohen. A coefficient of agreement for nominal scale. *Educational and psychological measurement*, 20:37–46, 1960.

[173] Practical Statistics for Medical Research.

[174] R: a language and environment for statistical computing.

[175] Thaína A. Azevedo Tosta, Paulo Rogério de Faria, Leandro Alves Neves, and Marcelo Zanchetta do Nascimento. Color normalization of faded H&E-stained histological images using spectral matching. *Computers in Biology and Medicine*, 111:103344, August 2019.

[176] Sara L. Jackson, Paul D. Frederick, Margaret S. Pepe, Heidi D. Nelson, Donald L. Weaver, Kimberly H. Allison, Patricia A. Carney, Berta M. Geller, Anna N. A. Tosteson, Tracy Onega, and Joann G. Elmore. Diagnostic Reproducibility: What Happens When the Same Pathologist Interprets the Same Breast Biopsy Specimen at Two Points in Time? *Annals of Surgical Oncology*, 24(5):1234–1241, May 2017.

[177] Catarina Calle, Elaine Zhong, Matthew G. Hanna, Katia Ventura, Maria A. Friedlander, Monica Morrow, Hiram Cody, and Edi Brogi. Changes in the Diagnoses

of Breast Core Needle Biopsies on Second Review at a Tertiary Care Center: Implications for Surgical Management. *The American Journal of Surgical Pathology*, 47(2):172–182, February 2023.

[178] António Polónia, Sofia Campelos, Ana Ribeiro, Ierece Aymore, Daniel Pinto, Magdalena Biskup-Fruzynska, Ricardo Santana Veiga, Rita Canas-Marques, Guilherme Aresta, Teresa Araújo, Aurélio Campilho, Scotty Kwok, Paulo Aguiar, and Catarina Eloy. Artificial Intelligence Improves the Accuracy in Histologic Classification of Breast Lesions. *American Journal of Clinical Pathology*, 155(4):527–536, March 2021.

[179] Yueping Liu, Dandan Han, Anil V. Parwani, and Zaibo Li. Applications of Artificial Intelligence in Breast Pathology. *Archives of Pathology & Laboratory Medicine*, February 2023.

[180] Jenu V Chacko and Kevin W Eliceiri. Autofluorescence lifetime imaging of cellular metabolism: Sensitivity toward cell density, ph, intracellular, and intercellular heterogeneity. *Cytometry Part A*, 95(1):56–69, 2019.

[181] Olivia I Kolenc and Kyle P Quinn. Evaluating cell metabolism through autofluorescence imaging of nad (p) h and fad. *Antioxidants & redox signaling*, 30(6):875–889, 2019.

[182] Melissa C Skala, Kristin M Riching, Annette Gendron-Fitzpatrick, Jens Eickhoff, Kevin W Eliceiri, John G White, and Nirmala Ramanujam. In vivo multiphoton microscopy of nadh and fad redox states, fluorescence lifetimes, and cellular morphology in precancerous epithelia. *Proceedings of the National Academy of Sciences*, 104(49):19494–19499, 2007.

[183] Shulian Wu, Yudian Huang, Qinggong Tang, Zhifang Li, Hannah Horng, Jiatian Li, Zaihua Wu, Yu Chen, and Hui Li. Quantitative evaluation of redox ratio and collagen characteristics during breast cancer chemotherapy using two-photon intrinsic imaging. *Biomedical Optics Express*, 9(3):1375–1388, 2018.

[184] Matthew Hartley, Gerard J Kleywegt, Ardan Patwardhan, Ugis Sarkans, Jason R Swedlow, and Alvis Brazma. The bioimage archive–building a home for life-sciences microscopy data. *Journal of Molecular Biology*, 434(11):167505, 2022.

[185] Nicolas Chiaruttini, Olivier Burri, Peter Haub, Romain Guiet, Jessica Sordet-Dessimoz, and Arne Seitz. An Open-Source Whole Slide Image Registration Work-

flow at Cellular Precision Using Fiji, QuPath and Elastix. *Frontiers in Computer Science*, 3, January 2022. Publisher: Frontiers.

[186] Ting-Chun Wang, Ming-Yu Liu, Jun-Yan Zhu, Andrew Tao, Jan Kautz, and Bryan Catanzaro. High-Resolution Image Synthesis and Semantic Manipulation with Conditional GANs, August 2018. arXiv: 1711.11585 [cs] Number: arXiv:1711.11585.

[187] Weiping Lin, Yihuang Hu, Runchen Zhu, Baoshun Wang, and Liansheng Wang. Virtual staining for pathology: Challenges, limitations and perspectives. *Intelligent Oncology*, 1(2):105–119, April 2025.

[188] Xudong Mao, Qing Li, Haoran Xie, Raymond Y. K. Lau, Zhen Wang, and Stephen Paul Smolley. Least Squares Generative Adversarial Networks, April 2017. arXiv: 1611.04076 [cs] Number: arXiv:1611.04076.

[189] Moab Arar, Yiftach Ginger, Dov Danon, Ilya Leizerson, Amit Bermano, and Daniel Cohen-Or. Unsupervised Multi-Modal Image Registration via Geometry Preserving Image-to-Image Translation, March 2020. arXiv: 2003.08073 [cs] Number: arXiv:2003.08073.

[190] Ashish Shrivastava, Tomas Pfister, Oncel Tuzel, Josh Susskind, Wenda Wang, and Russ Webb. Learning from Simulated and Unsupervised Images through Adversarial Training, July 2017. arXiv: 1612.07828 [cs] Number: arXiv:1612.07828.

[191] Viswanath Gorti, Kaitlyn McCubbins, Daniel Houston, Aaron D Silva Trenkle, Abigail Holberton, Caroline E Serafini, Levi Wood, Gabriel Kwong, and Francisco E Robles. Quantifying uv-induced photodamage for longitudinal live-cell imaging applications of deep-uv microscopy. *Biomedical Optics Express*, 16(1):208–221, 2024.

[192] *Weedon's Skin Pathology*. November 2024.

[193] J. Charles Jennette MD and Vivette D. D'Agati MD. *Heptinstall's Pathology of the Kidney*. Wolters Kluwer, Philadelphia, 2024.

[194] Laëtitia Elies, Elise Guillaume, Mathilde Gorieu, Patricia Neves, and Frédéric Schorsch. Historical control data of spontaneous pathological findings in c57bl/6j mice used in 18-month dietary carcinogenicity assays. *Toxicologic Pathology*, 52(2-3):99–113, 2024.

[195] Ying Li, Jian Dai, Fuyuki Kametani, Masahide Yazaki, Akihito Ishigami, Masayuki Mori, Hiroki Miyahara, and Keiichi Higuchi. Renal function in aged c57bl/6j mice

is impaired by deposition of age-related apolipoprotein a-ii amyloid independent of kidney aging. *The American Journal of Pathology*, 193(6):725–739, 2023.

[196] Jessica S. Hoane, Crystal L. Johnson, James P. Morrison, and Susan A. Elmore. Comparison of Renal Amyloid and Hyaline Glomerulopathy in B6C3F1 Mice: An NTP Retrospective Study. *Toxicologic pathology*, 44(5):687–704, July 2016. tex.pmcid: PMC4912446.

[197] Z. Wang, E.P. Simoncelli, and A.C. Bovik. Multiscale structural similarity for image quality assessment. In *The Thrity-Seventh Asilomar Conference on Signals, Systems & Computers, 2003*, volume 2, pages 1398–1402 Vol.2, November 2003.

[198] Elena Buzzetti, Andrew Hall, Mattias Ekstedt, Roberta Manuguerra, Marta Guerrero Misas, Claudia Covelli, Gioacchino Leandro, TuVinh Luong, Stergios Kechagias, Emanuel K. Manesis, Massimo Pinzani, Amar P. Dhillon, and Emmanuel A. Tsochatzis. Collagen proportionate area is an independent predictor of long-term outcome in patients with non-alcoholic fatty liver disease. *Alimentary Pharmacology & Therapeutics*, 49(9):1214–1222, May 2019.

[199] Chetan L Srinidhi, Ozan Ciga, and Anne L Martel. Deep neural network models for computational histopathology: A survey. *Medical image analysis*, 67:101813, 2021.

[200] Zixu Zhao, Huangjing Lin, Hao Chen, and Pheng-Ann Heng. Pfa-scannet: Pyramidal feature aggregation with synergistic learning for breast cancer metastasis analysis. In *International Conference on Medical Image Computing and Computer-Assisted Intervention*, pages 586–594. Springer, 2019.

[201] David Ahmedt-Aristizabal, Mohammad Ali Armin, Simon Denman, Clinton Fookes, and Lars Petersson. A survey on graph-based deep learning for computational histopathology. *Computerized Medical Imaging and Graphics*, 95:102027, 2022.

[202] Siemen Brussee, Giorgio Buzzanca, Anne MR Schrader, and Jesper Kers. Graph neural networks in histopathology: Emerging trends and future directions. *Medical Image Analysis*, page 103444, 2025.